Original paper

Arc-like magmatism in syn- to post-collisional setting: the Ediacaran Angra Fria Magmatic Complex (NW Namibia) and its cross-Atlantic correlatives in the south Brazilian Florianópolis Batholith

Vojtěch Janoušek[a,b*], Luana Florisbal[c], Jiří Konopásek[a,d], Petr Jeřábek[b], Maria de Fátima Bitencourt[e], Petr Gadas[a], Vojtěch Erban[a,†], Veronika Kopačková-Strnadová[a]

[a] *Czech Geological Survey, Klárov 3, 118 21 Prague 1, Czech Republic*

[b] *Institute of Petrology and Structural Geology, Charles University, Albertov 6, 128 43 Prague 2, Czech Republic*

[c] *Centro de Filosofia e Ciências Humanas, Departamento de Geologia, Universidade Federal de Santa Catarina, Campus Universitário Trindade, Florianópolis, SC 88.010-970, Brazil*

[d] *Department of Geosciences, UiT The Arctic University of Norway, Dramsveien 201, N-9037 Tromsø, Norway*

[e] *Programa de Pós-graduação em Geociências, Instituto de Geociências, Universidade Federal do Rio Grande do Sul, Av. Bento Gonçalves, 9500, Porto Alegre, RS 91500-000, Brazil*

[†] *Present address: Pragolab Ltd., Nad Krocínkou 55, 190 00 Prague 9, Czech Republic*

* *Corresponding author*

tel. (+420) 251 085 229, fax (+420) 251 818 748; vojtech.janousek@geology.cz

Intended for *Journal of Geodynamics*

Abstract

Ediacaran syn-tectonic plutonic rocks (amphibole gabbros, quartz diorites/tonalites to biotite- and muscovite-bearing granites) of the Angra Fria Magmatic Complex (Kaoko Belt, north-western Namibia) belong to two compositionally similar, magnesian, transitional tholeiitic–calc-alkaline suites, the Older (~625–620 Ma) and the Younger (~585–575 Ma). Both have counterparts in the broadly contemporaneous Florianópolis Batholith (southern Brazil), from which they were separated during the Cretaceous opening of the southern Atlantic. In the Angra Fria Magmatic Complex, the only unequivocal mantle contributions are identified in mingling zones of the Younger Suite and hybrid mafic–intermediate dykes of uncertain age. Previously published Hf-in-zircon isotopic data, together with new whole-rock geochemical and Sr–Nd isotopic signatures, underline an important role of crustal anatexis of a material with late Palaeoproterozoic to early Mesoproterozoic mean crustal residence (1.9–1.5 Ga). This interval resembles some of the published Nd model ages for Tonian 'Adamastor Rift'-related felsic magmatic rocks in the Namibian Coastal and Uruguayan Punta del Este terranes. In detail, the Older Suite probably originated mainly by fluid-present melting of metabasalts and metatonalites, followed by (near) closed-system fractional crystallization (with or without accumulation) of amphibole ± plagioclase. For the Younger Suite, the principal process was the dehydration melting of relatively felsic lower crustal protoliths (metagreywackes or intermediate–acid orthogneisses >> metapelites), leaving garnet in the residue. Based on the geological context, the conspicuous enrichment of hydrous-fluid-mobile large ion lithophile over the conservative high field strength elements is not interpreted through a classic model of oceanic plate subduction, devolatilization, and fluxed-melting of the overriding mantle wedge. Instead, it is thought to reflect high-grade metamorphism of deeply buried continental crust and attendant water-fluxed melting of the overlying crustal lithologies, connected with inversion of the Tonian 'Adamastor Rift'.

Research Highlights

- Ediacaran magmatism in Angra Fria Complex is correlated with Florianópolis Batholith
- Mature crustal material (1.9–1.5 Ga model ages) remelted with limited mantle input
- Syn- to post-collisional intracontinental setting, unrelated to oceanic subduction
- Arc-like LILE/HFSE enrichment may reflect H_2O-fluxed melting in the crust

Keywords

whole-rock geochemistry; Sr–Nd isotopes; Kaoko Belt; Florianópolis Batholith; Kaoko–Dom Feliciano–Gariep orogenic system

1. Introduction

The whole-rock geochemical and radiogenic isotopic signatures of igneous rocks are capable of constraining mantle or crustal sources, melting conditions, differentiation mechanisms as well as the likely geotectonic setting of ancient magmatic activity (e.g., Brown and Rushmer, 2006; Janoušek et al., 2016; Taylor and McLennan, 2009; Wilson, 1989). In particular, whole-rock geochemical studies of granitoids provide snapshots of the compositions of their lower/middle crustal and/or mantle sources and conditions (P–T, aH_2O…) prevailing at the time of magma generation (Brown, 2013; Clemens, 2003; Jacob et al., 2021; Kemp and Hawkesworth, 2003; Moyen et al., 2021). In turn, such information is indispensable for any trustworthy geodynamic reconstruction and correlation of dismembered crustal units.

An often-cited example of large-scale correlations between now widely dispersed plates comes from the southern Atlantic realm (de Wit et al., 2008; Porada, 1979). There, the coastal parts of Namibia, southern Brazil and Uruguay represent remnants of the high-grade hinterland of the Neoproterozoic Kaoko–Dom Feliciano–Gariep orogenic system hosting large volumes of syn-orogenic igneous rocks (e.g. Bitencourt and Nardi, 1993; Chemale Jr. et al., 2012; Florisbal et al., 2012a; Goscombe and Gray, 2007; Kröner et al., 2004; Lara et al., 2020; Masberg et al., 2005; Oyhantçabal et al., 2007; Philipp and Machado, 2005; Seth et al., 1998). In particular, the plutonic rocks of the Angra Fria Magmatic Complex in the Kaoko Belt (NW Namibia) seem to have counterparts in the broadly contemporaneous Florianópolis Batholith (Santa Catarina, southern Brazil) (Fig. 1; Konopásek et al., 2016).

Although most of the late Neoproterozoic igneous rocks in the hinterland part of the Kaoko–Dom Feliciano–Gariep orogenic system have been interpreted as resulting from arc magmatism above subducting oceanic plate (Basei et al., 2000, 2018; Goscombe and Gray, 2007), numerous arguments presented in the recent literature speak against their subduction-related origin. These arguments were summarized by Konopásek et al. (2020) and include the

syn- to post-collisional nature of the plutonic bodies (Bitencourt and Nardi, 1993; Oyhantçabal et al., 2007), estimated timing for the end of rifting coinciding with the onset of orogenesis and coeval flysch sedimentation (Hoffman et al., 2021; Konopásek et al., 2017), as well as the beginning of thrusting of orogenic hinterland over the foreland at the time of, or even before, the intrusion of the supposed arc magmas (Battisti et al., 2018; De Toni et al., 2020a; Percival et al., 2022). Yet, as we will show in this contribution, some of the late Neoproterozoic magmatic rocks in the hinterland indeed show geochemical features apparently typical of arc magmatism, calling for an alternative petrogenetic model for their origin through (fluid-present) melting in an orogenic setting away from any possible influence of an active subduction of oceanic lithosphere.

The newly acquired mineral chemistry, as well as whole-rock geochemical major-, trace- and Sr–Nd isotopic data, complemented by the geochronological and Sr–Nd isotopic set of Konopásek et al. (2016), provides a fresh insight into the nature, prospective sources, evolution and geodynamic causes of plutonic activity in the Angra Fria Magmatic Complex. These data are then correlated with the available information from the selected magmatic units of the Florianópolis Batholith in southern Brazil.

The current paper indicates that the commonly encountered enrichment of hydrous-fluid-mobile Large Ion Lithophile Elements (LILE) over the conservative High Field Strength Elements (HFSE) in granitic suites does not need to be interpreted in terms of a classic model of oceanic plate subduction, devolatilization, fluxed-melting of the overriding mantle wedge and differentiation of the metasomatized mantle wedge-derived basic magmas. Instead, it may reflect the water-fluxed melting of a mature continental crust, whether it was arc-related or not. These findings bear important consequences for the apparently straightforward interpretation of the above-mentioned whole-rock geochemical features in terms of tectonic setting of the magma origin, as well as for the geodynamic evolution of the Kaoko–Dom Feliciano–Gariep.

2. Geological setting

2.1 Kaoko–Dom Feliciano–Gariep orogenic system

The Kaoko Belt forms the northeastern part of the Kaoko–Dom Feliciano–Gariep orogenic system developed from ca. 650 to 550 Ma as a result of the convergence of Paleoproterozoic–Mesoproterozoic foreland crustal blocks: the Congo Craton, the Kalahari Craton + the Namaqua Belt, the Río de la Plata Craton and the Nico Pérez–Luis Alves Terrane/Craton (Fig. 1a).

At the onset of convergence, these orogenic foreland domains were covered by relics of Mesoproterozoic volcano-sedimentary units, as well as by sedimentary and volcanic sequences related to extensive, and probably episodic, Neoproterozoic (ca. 840–660 Ma) rifting (Konopásek et al., 2018; Percival et al., 2021). During the orogenic evolution, the pre-Neoproterozoic basement and its volcano-sedimentary cover were deformed and metamorphosed to various degrees; nowadays, they represent the foreland fold-and-thrust belt (Basei et al., 2000; De Toni et al., 2020a; Goscombe and Gray, 2008; Percival et al., 2022; Ulrich et al., 2011) (Fig. 1a).

The internal, hinterland part of the orogenic system is exposed as low- to medium-pressure, high-temperature metamorphic rocks and plutonic rocks of the Coastal Terrane (Goscombe and Gray, 2007) in the Kaoko Belt, the Porto Belo Complex in the northern (De Toni et al., 2020a, b), and the Punta del Este Terrane (Oyhantçabal et al., 2009) in the southern Dom Feliciano Belt (Fig. 1a). The Coastal Terrane of the hinterland is built of metamorphosed supracrustal associations of clastic sedimentary rocks intercalated with bimodal metavolcanic rocks of early Neoproterozoic age (ca. 820–785 Ma; Konopásek et al., 2008, 2018). The western (South American) hinterland is an infracrustal association of mostly magmatic rocks of similar age as the metavolcanic rocks of the Coastal Terrane (ca. 800–770 Ma) metamorphosed at granulite-facies conditions (De Toni et al., 2020b; Lenz et al., 2011; Masquelin et al., 2012;

Oyhantçabal et al., 2009; Will et al., 2019). Xenoliths and roof pendants of orthogneisses with similar protolith ages are found within the late Neoproterozoic granitoids of the entire hinterland domain (Koester et al., 2016; Martil et al., 2017). There is no consensus about the tectonic setting of the early Neoproterozoic magmatism. Although some researchers interpret it as an oceanic subduction-related magmatic arc (De Toni et al., 2020b; Koester et al., 2016; Martil et al., 2017), others favour rifting-related melting of the lower crust and uppermost mantle (Konopásek et al., 2018; Will et al., 2019).

Along the boundaries with the foreland domains, the hinterland of the Kaoko–Dom Feliciano–Gariep orogenic system contains large volumes of igneous rocks. The magmatic province along the western edge of the foreland is known as the Granite Belt (Basei et al., 2000), and it is formed, from south to north, by the Aiguá, Pelotas, and Florianópolis batholiths (Fig. 1a). The Granite Belt reached the maximum magmatic activity between ca. 630 and 580 Ma (see summaries in Lara et al. (2020) for the Aiguá Batholith, Philipp and Machado (2005) for the Pelotas Batholith, and Florisbal et al. (2012b) with ESM 1 for the Florianópolis Batholith).

The magmatic province along the eastern edge of the hinterland in the Kaoko Belt was named Boundary Igneous Complex (Fig. 1a) (Konopásek et al., 2008). Its magmatic activity dated between ca. 580 and 550 Ma reflected the tectonic evolution. (1) The early magmatism at ca. 580–570 Ma accompanying the onset of thickening in the Kaoko Belt was followed by (2) numerous broadly granitic intrusions into the Coastal Terrane hinterland and culminated by (3) the emplacement of a sheet-like body of a strongly porphyritic Amspoort melagranite at ca. 550 Ma (Seth et al., 1998; Janoušek et al., 2010).

The Granite Belt has always played a central role in interpreting the early tectonic evolution of the Kaoko–Dom Feliciano–Gariep orogenic system. Numerous authors (e.g., Basei et al., 2018; Caxito et al., 2021; Chemale Jr. et al., 2012; Fernandes et al., 1992) viewed the Granite Belt as a magmatic arc related to the subduction of the so-called Adamastor Ocean. In

contrast to that, several studies emphasized the syn-collisional character of the early granitic intrusions (Bitencourt and Nardi, 1993; De Toni et al., 2020a; Florisbal et al., 2012b; Oyhantçabal et al., 2007), as well as the fact that the magmatic activity in the Granite Belt started ca. 20–30 million years after the thrusting of the Granite Belt's host rocks over the Dom Feliciano Belt foreland (e.g., Battisti et al., 2018; De Toni et al., 2020a; Percival et al., 2022).

2.2 Angra Fria Magmatic Complex

The Angra Fria Magmatic Complex (AFMC; Fig. 1a; Fig. 2), defined by Konopásek et al. (2016) as a bimodal plutonic rock association, forms an integral part of the Coastal Terrane of the Namibian Kaoko Belt. It can be subdivided into two distinct suites.

The **Older Suite** was dated at ca. 626–620 Ma. It is represented by gabbroic–granitic rocks variably deformed at the transition from magmatic to solid-state conditions or entirely in the solid state. Although some authors discussed the possible correlation of magmatic rocks exposed in the coastal parts of the Kaoko and Dom Feliciano belts, these correlations were mainly based on common intrusion ages without discussion of spatial distribution and composition of coeval intrusions (e.g., Basei et al., 2018). Magmatic rocks with ages corresponding to the AFMC Older Suite have not been recognized in any other part of the Coastal Terrane, but they were coeval with the earliest magmatic activity in the Florianópolis Batholith of the Dom Feliciano Belt in Brazil (Fig. 1b). Based on the intrusion ages, matching Sr–Nd isotopic signatures and position in the Coastal Terrane, Konopásek et al. (2016) interpreted the AFMC as a direct continuation of the Brazilian Florianópolis Batholith isolated on the African side of the orogenic system by the Mesozoic opening of the Atlantic Ocean.

The diorites–granites of the AFMC **Younger Suite**, dated at ca. 586–574 Ma, are the earliest products of magmatic processes associated with the thrusting of the Coastal Terrane over the Kaoko Belt foreland (Goscombe and Gray, 2008; Ulrich et al., 2011) (Fig. 1b). The

nature and genesis of the AFMC and its relation to the northern part of the South American Granite Belt (the Florianópolis Batholith) are the main topics of the current contribution.

2.3 Florianópolis Batholith

Magmatic rocks of compositions similar to those of the Namibian AFMC are known from two regions of the Florianópolis Batholith in southern Brazil: the southerly Garopaba and the northerly Porto Belo–Bombinhas regions. In the south occur mostly little deformed early granitoids with coeval mafic magmatic rocks (630–620 Ma) – the **Paulo Lopes** (porphyritic Bt monzo- and syenogranite; the mineral names' abbreviations follow those of Whitney and Evans 2010) and **Garopaba** (Hbl–Bt granodiorite) types. The granitoids of the Porto Belo–Bombinhas region represent products of a protracted magmatic activity. During the early, syn-collisional phase intruded the magmas parental to the **Quatro Ilhas** (coarsely porphyritic Bt (± Ms) granites and granodiorites that interacted with coeval mafic magmas producing various hybrid rock types; 625–614 Ma) and the **Mariscal** (fine–medium-grained peraluminous Ms–Bt granite, 609 Ma) plutons. The least deformed syn-tectonic granites and hypabyssal rocks of the **Zimbros Intrusive Suite** (ca. 590 Ma) were emplaced either within the shear zone (Zimbros Granite with mafic microgranular enclaves (MME) and composite mafic–felsic dykes) or outside the main deformation site **(Morro dos Macacos Granite)**.

3. Field relations

The studied AFMC consists of alternating, generally N–S trending lithological belts (Fig. 2) dominated by magmatic rocks of the Older (Fig. 3a–e) and Younger (Fig. 3d–g) suites, which show clear cross-cutting relationships (Fig. 3d–e). Magmas parental to both suites intruded the host gneisses (ca. 800–650 Ma), which are more abundant towards the east of the studied area. Orthogneiss and gabbro/diorite to granite of the Older Suite occur in the west, while the

Younger Suite, represented by granodiorite–diorite and granite bodies and dykes dominates in the east. Beyond the mapped area, the extent of both magmatic suites is currently unknown.

In both magmatic suites, the intensely folded host gneisses are locally preserved as xenoliths, several metres (or more) in size. The gabbroic–granitic rocks of the Older Suite were variably deformed at the transition from magmatic to solid state or entirely in the solid state (Fig. 3a, b, e). The magmatic/subsolidus fabrics are steep and N–S striking. In one outcrop, we observed a modally layered sequence, in which Pl-rich bands alternated with Amp-rich ones at the hand-specimen scale. In orthogneiss, this fabric is defined by the shape-preferred orientation of K-feldspar porphyroclasts and folded by upright, N–S trending folds. The orthogneiss is locally cut by thin microdiorite dykes of unclear age, which are also weakly deformed (Fig. 3h).

Similarly, the Younger Suite also shows steep N–S striking magmatic fabrics, with the best examples demonstrated by the elongation and preferred orientation of dioritic MME in granodiorite in the domains of mingling (Fig. 3f). Microstructures show that the high-temperature magmatic/subsolidus fabrics of both suites were locally intensely overprinted under greenschist-facies conditions. Field evidence shows that the overprinting low-temperature fabric is still steep and N–S trending in both suites.

4. Petrology and mineral chemistry

The samples studied for petrology and mineral chemistry (ESM 2; see ESM 3 for analytical details) include orthogneiss (NP-018), gabbro (NP-020) and quartz diorite to tonalite (NP-011, NP-012), hornblendite (NP-013) of the Older Suite, as well as tonalite–granodiorite (NP-007, NP-009), granite (NP-021) and leucogranite (NP-010) of the Younger Suite and mafic tonalite dyke (NP-017) of ambiguous age.

4.1 Older Suite

The biotite augen orthogneiss **NP-018** consists of plagioclase, K-feldspar, quartz, biotite, titanite, and epidote, as well as accessory apatite, zircon, magnetite and Ti-oxide (Fig. 4a). The magmatic assemblage is overprinted by a greenschist-facies fabric defined by the shape-preferred orientation of feldspar porphyroclasts, biotite, and recrystallized quartz aggregates. During this overprint, K-feldspar is, in places, replaced by myrmekite, while andesine porphyroclasts are locally recrystallized to fine-grained oligoclase. Biotite is green and shows high X_{Fe} ~0.47 (ESM 4).

The gabbro **NP-020** shows coarse- to finer-grained domains consisting of tschermakitic amphibole (Fig. 5a), plagioclase and locally biotite, chlorite, epidote, and apatite. Large amphibole grains contain inclusions of ilmenite, magnetite, pyrite, pyrrhotite, chalcopyrite, and rare rutile, which also occur as individual grains in the finer-grained domains. Plagioclase is bytownite ($An_{76–87}$), and biotite is characterized by X_{Fe} of ~0.39.

The coarse-grained hornblendite **NP-013** contains two varieties of amphibole, plagioclase, biotite (X_{Fe} ~0.36), and accessory epidote, titanite and apatite. Large amphibole grains of Si-poor magnesiohornblende are heterogeneously replaced by Si-rich magnesiohornblende–actinolite (Fig. 4b and Fig. 5a), which locally also forms small grains. The replacement zones occupied by the Si-rich amphibole are sometimes associated with small relics of diopsidic clinopyroxene. Plagioclase of andesine composition is locally affected by sericitization, and the rock contains alteration zones represented by nests of prehnite, albite, K-feldspar, chlorite and calcite (Fig. 4b).

The medium-grained Amp–Bt quartz diorite **NP-012** with weak magmatic fabric contains two amphibole varieties, plagioclase, quartz, biotite (X_{Fe} ~0.42) and accessory titanite, apatite, zircon and allanite (Fig. 4c). Similarly to NP-013, large amphibole grains of Si-poor magnesiohornblende are heterogeneously replaced by Si-rich magnesiohornblende–actinolite

(Fig. 4c and Fig. 5a). Andesine ($An_{31–46}$) is locally sericitized and replaced by secondary oligoclase–albite, while Fe-sulphides, calcite, and chlorite are rarely present.

Medium- to fine-grained Bt–Amp tonalite to quartz diorite **NP-011** shows a weak subsolidus fabric and contains plagioclase, tschermakitic to pargasitic/Mg-hastingsitic amphibole, quartz, biotite, epidote and accessory apatite, allanite, titanite, magnetite and zircon (Fig. 4d and Fig. 5a–b). Plagioclase of andesine composition ($An_{40–45}$) is locally sericitized and replaced by oligoclase–albite, while calcite, K-feldspar, and chlorite are rarely present. Biotite is green and shows X_{Fe} of 0.45–0.56.

4.2 Younger Suite

The medium-grained Amp–Bt tonalite **NP-009** with relatively strong, probably magmatic fabric contains plagioclase, ferrohornblende, biotite (X_{Fe} ~0.56), chlorite and quartz, with accessory titanite, apatite, ilmenite, epidote and pyrite (Fig. 4e and Fig. 5a). Plagioclase composition ranges from andesine to labradorite with relic, anorthite-rich cores, which are intensely sericitized (Fig. 4e).

The medium-grained Amp–Bt granodiorite **NP-007** with a strong magmatic–subsolidus fabric contains plagioclase, quartz, K-feldspar, biotite (X_{Fe} ~0.66), chlorite, ferropargasite/hastingsite, titanite and accessory zircon, apatite and ilmenite (Fig. 4f and Fig. 5b). Plagioclase of andesine composition is locally recrystallized and subsequently intensely sericitized and replaced by oligoclase–albite (Fig. 4f). K-feldspar is locally replaced by myrmekite.

The Ms–Bt granite **NP-021** with magmatic or high-temperature subsolidus fabric contains plagioclase, K-feldspar, quartz, biotite (X_{Fe} ~0.73), muscovite, apatite and accessory zircon (Fig. 4g). K-feldspar is locally replaced by myrmekite, while plagioclase of the oligoclase–andesine composition is locally sericitized and replaced by albite (Fig. 4g).

The Ms–Bt leucogranite **NP-010** with weak fabric contains oligoclase, K-feldspar, quartz, biotite (X_{Fe} ~0.7), muscovite, chlorite and apatite (Fig. 4h). Biotite is partly replaced by chlorite, K-feldspar by myrmekite, and plagioclase by sericite.

4.3 Rocks of ambiguous age

The Bt microtonalite **NP-017** has been collected from a fine-grained mafic dyke crosscutting the augen orthogneiss of the Older Suite in the west of the studied area. The sample shows weak subsolidus fabric and contains plagioclase, quartz, large amounts of biotite (X_{Fe} ~0.53–0.56), magnetite and accessory zircon, as well as secondary muscovite, K-feldspar, titanite, epidote, and apatite (Fig. 4g). Plagioclase of andesine composition is locally intergrown with quartz and shows sericitization and replacement by albite (Fig. 4g).

5. Amphibole chemistry as a proxy of parental magma composition

In the basic–intermediate granitic rocks, the composition of calcic amphibole can be used to constrain physico-chemical conditions of crystallization (P–T, oxygen fugacity, water activity in the magma). In particular, hornblende-based geobarometry has attracted much attention (Anderson, 1996; Anderson et al., 2008; Yavuz and Döner, 2017 and references therein). Unfortunately, the chemistry of calcic amphiboles appears to be intrinsically more sensitive to temperature and coexisting liquid composition than to pressure; consequently, amphibole-based pressure estimates are typically subject to errors in order of several kbar (Putirka, 2016). Moreover, many of the empirical hornblende geobarometers rely on the presence of the low-variance mineral assemblage Hbl + Bt + Pl + Kfs + Qtz + Ttn + Fe–Ti oxides + melt, which is generally absent in the AFMC rocks.

For these reasons, we gave up any attempts to calculate the depth of Amp crystallization. Instead, we have focussed on the empirical Amp-based geothermometry of Ridolfi and Renzulli (2012) that should yield reasonable results (Erdmann et al., 2014; Putirka, 2016). The advantage

is that it should be applicable to a broad range of Amp compositions, it does not require a particular mineral assemblage, and it also yields estimates of oxygen fugacity and water contents of the parental magma (Table 1).

5.1 Older Suite (OS)

For the primary amphiboles, the mean temperatures range from ca. 800 to 730 °C. The estimated oxygen fugacity (fO_2) is variable, –13.5 to –15.2. In the T vs. log(fO_2) diagram (Fig. 5c), the primary, high-T amphiboles in samples NP 011, NP 012, and NP 013 indicate more oxidized magmas, evolving from the NNO + 2 to the NNO buffer. The amphiboles of gabbro NP 020 point to significantly more reduced conditions, clustering at about the NNO buffer, or slightly below. The inferred average H_2O contents, starting from 16 wt. % in the gabbro, and going down to 11.3–9.7 wt. % in the rest of the OS, demonstrate that the parental magmas were water-rich (Fig. 5d).

5.2 Younger Suite (YS)

Amphibole is comparably rare in the YS dataset, and thus only two samples could have been studied. The mean estimated temperatures for the YS amphiboles are ca. 730–740 °C. Compared to the Older Suite, the average oxygen fugacities (fO_2) derived from the amphiboles of the samples NP-009 and NP-007 are low, –16.3 and –15.6, respectively. This implies conditions ranging from NNO to FMQ buffers and even below (Fig. 5c). At first glance, the average calculated H_2O contents in coexisting magmas are high and very different from OS: 10.8 wt. % (NP-009) and 13.0 wt. % (NP-007). Especially for the sample NP-009, however, the reconstructed H_2O contents in magma increase from those comparable to the primary, high-T OS amphiboles (NP-011, NP-012 and NP-013) to almost 14 wt. % H_2O in amphiboles crystallized at the lowest T (Fig. 5d).

6. Whole-rock geochemistry

The Namibian dataset consists of 23 newly obtained whole-rock geochemical analyses of plutonic rocks from the Angra Fria Magmatic Complex (see ESM 5 for major-, and ESM 6 for trace-element data). Of these, six were carried out on samples whose Sr–Nd–Hf isotopic compositions and ages were determined by Konopásek et al. (2016). Most major- and trace-element analyses were carried out in the ACME Labs/Bureau Veritas Commodities Canada Ltd. (Vancouver) by ICP-ES and ICP-MS; only three at the University of Bergen, Norway by a combination of XRF and ICP-MS (ESM 3). The data set is split into three temporal groups: the Old Suite (OS, n = 8), the Young Suite (YS, 6) and samples of ambiguous age (9).

As some samples show signs of greenschist-facies overprint, we have tested the possible elemental mobility using the ternary plot F–M–W (fresh felsic igneous, fresh mafic igneous and chemical weathering principal components) of Ohta and Arai (2007). In this projection, chemically weathered igneous rocks can be easily identified as they tend to be displaced from the fresh igneous rocks trend (dashed) towards the W apex. Based on this projection for the AFMC data (ESM 7a), as well as the fact that the whole dataset (altered or not) behaves coherently in all classification diagrams, it can be argued that the LILE (including the K and Na) mobility, if any, was negligible. For these reasons, we assume that using the complete set of major- and trace elements is justifiable.

The Brazilian dataset contains in total 80 selected analyses from the Florianópolis Batholith as follows: Paulo Lopes (n = 6) and Garopaba (5) (Florisbal et al., 2009), Quatro Ilhas (22) and Mariscal (12) (Florisbal et al., 2012a), Zimbros mafic dykes (26) and Zimbros MME (9) (Nardi and Bitencourt, 1993; Bitencourt, 1996 and unpublished data). Their compositions are also plotted onto whole-rock geochemical diagrams, along with the AFMC data, but the rigorous comparison is left to the Discussion.

6.1 Major- and minor-element composition

In the TAS diagram of Cox et al. (1979), all but one of the AFMC samples are classified as subalkaline gabbros to granites (SiO_2 = 49.2–76.0 wt. %). The only ultrabasic, Amp-rich sample NP-020 plots outside the diagram bounds (SiO_2 = 40.7 wt. %; Fig. 6a). In the AFM diagram of Irvine and Baragar (1971) (Fig. 6b), the AFMC analyses form a more or less continuous, steep trend transitional between calc-alkaline and tholeiitic. The SiO_2 vs. K_2O diagram (Peccerillo and Taylor, 1976) classifies the basic–intermediate rocks further as mostly high-K calc-alkaline; the acid samples are even richer in K_2O, straddling the boundary of the shoshonitic domain (Fig. 6c).

As argued by Bonin et al. (2020), useful information is provided by the multicationic scheme of Debon and Le Fort (1983, 1988). It is based on millications and hence, unlike the schemes based on weight percentages, it better reflects the stoichiometry of individual rock-forming minerals. In the P–Q (‘nomenclature‘) diagram of Debon and Le Fort (1988), the AFMC rocks range from gabbro, through quartz diorite, tonalite, granodiorite, to ‘adamellite’ (= monzogranite) and ‘granite’ (= syenogranite) (Fig. 6d). The B–A (‘characteristic minerals’) plot of the same authors portrays the evolution of the alumina balance (i.e. aluminosity) as a function of maficity (B = Fe + Mg +Ti) (Fig. 6e). The AFMC rocks are mostly metaluminous (A/CNK down to 0.45; ESM 5), falling into sector IV of the diagram, with the characteristic ferromagnesian mineral assemblage of Bt + Amp ± Cpx. Only the most felsic rock types become variably peraluminous (A/CNK up to 1.27), eventually straddling the boundary of sector I (Ms > Bt) and reaching leucogranitic compositions. In the modified version of this diagram (Villaseca et al., 1998) (ESM 7b), the felsic samples can be further classified as low- to moderately peraluminous. In the PQ and BA diagrams (Fig. 6d–e), the studied magmatic suite forms a trend that can be described as a calc-alkaline subtype of Debon and Le Fort’s cafemic association. The K/(K + Na) vs. B plot of Debon and Le Fort (1988) (Fig. 6f) shows

that most of the dataset is sodic, and only the most felsic members attain a potassic character. In Debon and Le Fort's B vs. Mg/(Mg + Fe) (i.e., mg#) diagram (ESM 7c), AFMC rocks straddle the boundary between magnesian and ferriferous associations. The mg# shows negative correlation with silica, dropping from ca. 50 in the mafic to 28 in the most felsic samples (ESM 5). Conspicuously, out of this range, elevated mg# values show the likely cumulative character of samples NP-012 and NP-013 (tonalite and hornblendite from a modally layered sequence) and NJ-58 (hornblendite) (mg# = 62–69).

In contrast to the millications-based scheme of Debon and Le Fort, in the (wt. %) SiO_2 vs. FeOt/(FeOt + MgO) diagram of Frost et al. (2001) (Fig. 7a), virtually the entire AFMC falls into the magnesian domain. In their SiO_2 vs. MALI diagram (Fig. 7b), the trend seems mostly calc–alkalic; however, the most basic samples are calcic, and most of the acidic YS samples alkali–calcic.

Harker plots (Fig. 8a–e) for most of the AFMC are characterized by a more or less monotonous decrease in FeOt, MgO, and CaO with silica. On the other hand, K_2O rises rather sharply (Fig. 6c). Trends for Al_2O_3 and, in particular, Na_2O are inflexed at SiO_2 ~ 65 wt. %, convex upward (Fig. 8a, e). The presumed cumulates (NP-020, NJ-58, and NP-013) often plot off these trends (e.g., Al_2O_3, MgO, and Na_2O).

6.2 Trace elements

The presumed cumulates are rich in transition metals (ESM 6). Otherwise, the contents of these elements in the basic–intermediate rocks of the Older Suite rise with rising silica (e.g., V; Fig. 8f) and then drop again in acid types. Similarly inflexed trends are also seen for Ba and Ga, while Rb increases monotonously in all rock types (Fig. 8g–i).

Spider plots normalized to Normal Mid-Ocean Ridge Basalt (NMORB) (Sun and McDonough, 1989) are plotted separately for each of the three age groups (Fig. 9a–c). Most OS

and YS samples show common features, in particular characteristic strong enrichments in LILE (Cs, Rb, Ba, and K), Th, U, and Pb. Typical are also deep troughs in HFSE (Nb, Ta and Ti, the latter getting deeper with increasing SiO_2), as well as negative, albeit weaker, P anomalies. Normalized heavy REE (HREE) contents are typically close to unity within the two main suites. Exceptions are the felsic samples NJ-57 (OS), NJ-62, and NP-010 (both YS) that are significantly depleted in the HREE (Fig. 9a–b). Strong HREE depletion is also a characteristic feature of all samples of uncertain age, no matter whether mafic or felsic (Fig. 9c). Compared to the rest of the dataset, mafic cumulates (NJ-58, NP-013, NP-020) are characterized by significantly lower concentrations of Rb, Ba, U, Th, Nb, Ta, Zr, Hf, LREE and HREE.

Chondrite-normalized (Boynton, 1984) HREE contents of the AFMC never drop below unity (Fig. 10). Within the OS (Fig. 10a), the amphibole-rich gabbro NP-020 shows a slightly convex upward, middle-REE (MREE) enriched pattern with a negligible Eu anomaly (Eu/Eu* = 0.92; ESM 6). The amphibole cumulates NP-013 and NJ-58 yield mutually comparable convex-upward patterns, richer in all REE and with a deeper Eu anomaly if compared to NP-020. Quartz diorite NP-012 also shares analogous features. The patterns of the three remaining intermediate samples are essentially straight and fairly fractionated, with a negative Eu anomaly (Eu/Eu* = 0.88–0.72). Finally, the Eu/Eu* parameter in acid members of the OS (orthogneisses) drops to 0.42 (in NK-29), but the total REE contents are the highest in the dataset. As an exception, the NJ-57 orthogneiss shows much lower ΣREE and a strong positive Eu anomaly.

The two basic–intermediate samples of the YS (Fig. 10b) yield mutually contrasting REE distributions, while the pattern of the mafic dyke NK-28 is steep, with a slight positive Eu anomaly (La_N/Yb_N = 28.0; Eu/Eu* = 1.15), that for the tonalite NP-009 is rather flat with notable Eu depletion (La_N/Yb_N = 4.9; Eu/Eu* = 0.78). Most of the acid YS samples possess negative Eu anomalies deepening with increasing SiO_2 from Eu/Eu* of 1.07 and 0.95 (NP-008

and NP-007 with flat patterns) to 0.47 and 0.36 (NP-010 and NJ-62 with kinked, depleted HREE segments).

As noted above, all samples with uncertain age (Fig. 10c) are depleted in HREE and show steep patterns (La_N/Yb_N = 20.1–41.9). While the mafic dykes have slightly positive, if any, Eu anomalies, these anomalies become deep in the two acidic samples (Eu/Eu* = 0.45 and 0.40).

7. Isotope geochemistry

7.1 Hafnium isotopic data in zircon

The Hf isotopic compositions from AFMC zircons analysed (but not discussed) by Konopásek et al. (2016) are shown in the form of a two-stage Hf evolution diagram (Fig. 11a). Although zircons from these five samples yielded consistent crystallization ages, they exhibit large variations in initial ε_{Hf}^{t} values and crustal Hf model ages (T_{DM}^{HfC}). Within the Older Suite, the hornblendite NJ-58 shows more radiogenic Hf (ε_{Hf}^{t} = –2.6 to –3.2, T_{DM}^{HfC} = 1.72–1.76 Ga) than the mutually comparable Bt orthogneiss NJ-57 and quartz diorite NJ-59 (ε_{Hf}^{t} = –4.5 to –5.5, T_{DM}^{HfC} = 1.84–1.90 Ga). In the Younger Suite, Ms–Bt granite NJ-62 is surprisingly unevolved (ε_{Hf}^{t} = –0.7 to –1.1, T_{DM}^{HfC} = 1.55–1.58 Ga), in contrast to the mafic dyke NJ-05 (ε_{Hf}^{t} = –7.7 to –8.2). The latter yields Eburnean crustal Hf model ages (T_{DM}^{HfC} = 2.01–2.04 Ga).

7.2 Whole-rock Sr–Nd isotopic data

Seventeen newly acquired Sr–Nd isotopic compositions for AFMC, determined by Thermal Ionization Mass Spectrometry (TIMS) at Radiogenic Isotope Laboratory of the Czech Geological Survey in Prague (see ESM 3 for analytical details), have been supplemented by six Sr–Nd pairs from Konopásek et al. (2016) (Table 2). Whenever practicable, the isotopic data were age-corrected to the intrusive ages, measured, or inferred from the field relations. The

same value of 580 Ma was assumed for all samples of ambiguous age. The AFMC data are compared with whole-rock Sr–Nd isotopic data from selected rock types of the Florianópolis Batholith adopted from Florisbal et al. (2009) (Paulo Lopes and Garopaba), Florisbal et al. (2012a) (Quatro Ilhas and Mariscal), and Chemale Jr. et al. (2012) (Zimbros, Quatro Ilhas and Mariscal) (Fig. 11b–f).

Typical samples from the Older Suite contain a relatively unevolved Sr ($^{87}Sr/^{86}Sr_i$ = 0.7054–0.7078) and radiogenic Nd (ε_{Nd}^{i} = –3.0 to –5.1) (Fig. 11b) translating to rather low two-stage Depleted Mantle Nd model ages ($T_{Nd.2stg}^{DM}$ = 1.51–1.67 Ga; Fig. 11c). The Sr–Nd isotopic compositions of the ultrabasic–intermediate samples and acidic orthogneisses are mutually well comparable.

The YS granitoids are characterized by significantly higher $^{87}Sr/^{86}Sr_i$ of 0.7103–0.7127 (but keep in mind the much younger ages used for age corrections) and lower ε_{Nd}^{i} values of –3.9 to –8.4 ($T_{Nd.2stg}^{DM}$ = 1.54–1.78 Ga) if compared to the OS (Fig. 11b–c, e–f). Interestingly, the dyke NJ-05 shows a mature-crust-like Sr–Nd isotopic signature ($^{87}Sr/^{86}Sr_i$ = 0.7118, ε_{Nd}^{i} = –8.4) and, accordingly, yields the highest Nd model age ($T_{Nd.2stg}^{DM}$ = 1.90 Ga).

The granite samples NP-016 and NJ-54 of uncertain age gave crust-like Sr–Nd isotopic compositions ($^{87}Sr/^{86}Sr_{580}$ = 0.7078 and 0.7124, ε_{Nd}^{580} = –4.6 and –6.8, $T_{Nd.2stg}^{DM}$ = 1.60 and 1.77 Ga, respectively). Their Sr–Nd isotopic signatures thus resemble the OS (NP-016, an affinity that would be further strengthened if older than 580 Ma) or YS (NJ-54). In contrast, the two mafic dykes NP-017 and NK-28 are the most primitive in the dataset, with CHUR-like Sr–Nd isotopic signatures, if corrected for an assumed age of 580 Ma ($^{87}Sr/^{86}Sr_{580}$ = 0.7047 and 0.7052, ε_{Nd}^{580} = –0.3 and –0.8, $T_{Nd.2stg}^{DM}$ = 1.26 and 1.30 Ga).

8. Discussion

8.1 Amphibole-derived crystallization conditions of the magmas parental to the AFMC granitoids

Oxygen fugacities of the magma, calculated using the empirical approach of Ridolfi and Renzulli (2012), differ strikingly for the Older and Younger suites of the AFMC (Fig. 5c). For the OS are inferred variable but comparably oxidized conditions (between NNO + 2 and NNO buffer itself). In contrast, the average oxygen fugacity derived from the YS amphiboles is relatively low (ranging from NNO to FMQ, and often even below the latter).

Furthermore, the OS amphibole compositions (Ridolfi and Renzulli, 2012) indicate that the coexisting magmas were likely water-rich (~16 wt. % H_2O in the gabbro, 11.3 to 9.7 wt. % H_2O in the remaining samples), and this is in line with the inferred relatively oxidized conditions and the presence of magnetite, often abundant. The melt's water contents calculated from the YS amphiboles are also high (Fig. 5f), even though the parental magma was relatively reduced.

In any case, the water contents obtained from cumulate gabbro NP-020 appear too high and may be substantially compromised by re-equilibration with highly fractionated, water-rich interstitial liquid. Without another suitable hygrometer, it is difficult to assess the reliability and significance of our results from the AFMC. The validity of the Ridolfi and Renzulli's (2012) amphibole hygrometer has been questioned by Erdmann et al. (2014), and the effects of H_2O on amphibole stability are indeed complex and poorly understood (Putirka, 2016).

Still, our results can be taken at least to indicate that we are dealing with superhydrous magmas (> 8 wt. % H_2O), like in the Adamello Pluton, eastern Alps (Müntener et al., 2021). Indeed, based on a recent study of fluid inclusions from lower crustal cumulates of the Kohistan

Arc, Urann et al. (2022) inferred up to 10 wt. % H_2O in primary melts. According to these authors, subsequent fractional crystallization could have led to magmas with 12–20 wt. % H_2O.

8.2 Petrogenetic model for the AFMC

In principle, there are two end-member models invoked for the genesis of intermediate–acid I-type granitoids: (1) fractionation of mantle-derived magmas, and (2) crustal anatexis of acid–intermediate metaigneous protoliths (e.g., Castro, 2020; Moyen et al. 2021 and references therein). The results of the current work are compatible with a dominantly intracrustal, anatectic origin of the AFMC magmatic rocks. This concerns not only the felsic types; even the most mafic rocks of the OS (gabbros, hornblendites) are likely Amp ± Pl cumulates from crustally derived intermediate parental magmas. The strongest argument comes from whole-rock Sr–Nd and zircon Hf isotopic compositions – especially for the OS, where isotopic signatures of the (ultra-) basic–intermediate vs. acidic rock types (including orthogneisses) all match and fall within the continental crust realm (Fig. 11).

Therefore, in our view, only a handful of the rock types studied from the AFMC could potentially be of mantle origin. First of all, this likely concerns some of the mafic dykes of ambiguous age. Moreover, in the YS, mafic, probably mantle-derived melts show significant evidence for comingling with felsic, crustal magmas (Fig. 3f).

8.2.1 Possible mantle sources for the AFMC magmatism

The two samples of discrete basic–intermediate dykes of unknown age from the northwestern tip of the study area show the most primitive (CHUR-like) Sr–Nd isotopic signatures in our dataset (NP-017, NK-28: SiO_2 = 58.33 and 62.35 wt. %; ε_{Nd}^{580} = –0.3 and –0.8, $T_{Nd.2stg}^{DM}$ = 1.26 and 1.30 Ga; Fig. 11b–c, e–f). Analogous isotopic data were acquired by Janoušek et al. (2010) for Opx–Cpx dolerite (SiO_2 = 48.8 wt. %) dyke NI-012 from the Nadas Valley ca. 10 km further

ESE (ε_{Nd}^{550} = +0.1, $T_{Nd.2stg}^{DM}$ = 1.21 Ga). Similarly to the AFMC dykes (Fig. 3h), the NI-012 dyke was folded jointly with its metagranitoid host belonging to the ~550 Ma Amspoort magmatic suite of the Boundary Igneous Complex (see fig. 2f of Janoušek et al., 2010). Therefore, all three occurrences seem to belong to the same basic–intermediate dyke swarm, whereby the individual dykes tapped similar sources but did not necessarily share the same age.

Given the fairly primitive Sr–Nd isotopic signature of these dykes, it is tempting to assume their origin by fractional crystallization, with or without crustal assimilation, of CHUR-like (or slightly depleted) mantle-derived magmas. If true, the strong depletion in HREE (Fig. 9c) would point to melting within the Grt stability field, and thus at depths exceeding ca. 85 km for typical dry peridotite solidus temperatures (Robinson and Wood, 1998). Indeed, the Zr/Nb ratios of the dykes are relatively low (NK-28: 7.8, NP-017: 18.8, NI-012: 8.4), resembling average OIB (5.8) or EMORB (8.8), rather than NMORB (31.8) (Sun and McDonough, 1989). On the whole-rock geochemical grounds, we thus prefer an origin from asthenosphere-derived (or at least asthenosphere-influenced) primary basaltic magmas, strongly fractionated and contaminated upon their ascent and emplacement into the crust (primary I-type granitoids *sensu* Castro, 2020).

Still, as an alternative petrogenetic model for the dykes, we cannot fully exclude a putative deep-seated metabasic source of primitive elemental and isotopic geochemistry. The crustal residence ages ($T_{Nd.2stg}^{DM}$) of 1.21–1.30 Ga partly overlap with those of 0.94–1.23 Ga determined for the mafic member of the Bimodal Suite that has intruded the Coastal Terrane of the Kaoko Belt during the ~800 Ma rifting (Konopásek et al., 2008, 2018). If present at lower crustal depths, well within the garnet stability field, Ediacaran partial melting of such primitive metabasic rocks (or their cumulates) could theoretically yield magmas of composition not unlike that of Angra Fria mafic dykes. The most probable mechanism would be fluid-fluxed

melting, possibly with attendant entrainment of peritectic phases. In this alternative scenario, the studied dykes would be secondary I-type granitoids *sensu* Castro (2020).

During our sampling campaign, we could not find any larger and reasonably homogeneous mafic bodies within, or close to, the mingling zones in the YS (Fig. 3f) that would be, with a great degree of confidence, spared of likely re-equilibration with their tonalitic host (e.g., Elburg, 1996; Pin et al., 1990). Thus, the mafic, potentially mantle-derived plutonic rocks of the YS are underrepresented in our dataset. The only exception remains the peculiar quartz dioritic dyke NJ-05 that, however, shows Eburnean whole-rock Nd model ages ($T_{Nd.2stg}^{DM}$) of 1.95 Ga and crustal Hf-in-zircon model ages (T_{DM}^{HfC}) of 2.01–2.04 Ga. The rock is fairly fractionated (SiO_2 ~ 52 wt. %, MgO ~ 3 wt. %, mg# = 34; see also low contents of transition metals). Thus, possible genetic scenarios comprise: (1) strong contamination of a 'standard' (primitive or depleted) mantle-derived magma by ancient (Nd and Hf crustal residence >> 2 Ga) crustal material, (2) fractionation of a primary mafic magma coming from an enriched (metasomatized) lithospheric mantle domain, or (3) remelting of juvenile metabasic crust derived directly from a depleted-mantle source in Eburnean times.

Regarding the first hypothesis, the presence of xenocrysts captured from the Eburnean (or older) basement is ruled out, as the same zircon grains as used for the Hf isotopic work have been dated *in situ* by U–Pb method at 584 ± 7 Ma and no inheritance has been detected (Konopásek et al., 2016). Even if it had escaped unnoticed, it still could not fully explain the good correspondence between the Hf-in-zircon and whole-rock Nd model ages, as the latter element is also hosted by phases other than zircon. Hence, if crustal contamination of a mantle-derived magma was operative, it had to have occurred prior to the onset of zircon growth. Still, the Nd isotopic composition of the NJ-05 dyke is the least radiogenic within the entire AFMC data set, dominated by granitoids thought to represent partial melts of the local crust. Also, the

comparably less evolved isotopic signature of the putative crustal contaminant(s) argues stoutly against the contamination hypothesis (ad 1).

In case of origin by extensive fractionation of an enriched mantle-derived magma (ad 2), the mantle metasomatism would have to be ancient in order to yield the strongly unradiogenic Nd–Hf isotopic signature. Given the low LILE contents (Rb = 49 ppm, K_2O contents of mere 1.35 wt. %: see ESM 5, ESM 6), the source would have to be only a modestly overprinted lithospheric mantle domain. If true, the normalized HREE contents just slightly below unity could indicate shallow melting of the lithospheric mantle source, clearly in the spinel peridotite stability field.

However, the most likely appears to be the third hypothesis, which invokes remelting of the juvenile Eburnean-age basement, as it easily reconciles the ~2 Ga Nd and Hf model ages, as well as the rather fractionated whole-rock composition (elevated silica, low mg# and transition metal contents). Indeed, a review of experimental data confirms that partial melting of Amp-rich metabasic rocks can yield basic melts with a whole-rock composition comparable to NJ-05, including similar SiO_2, MgO, and CaO contents (Gao et al., 2016). Melts with less than 55 wt. % SiO_2 can be produced by fluid-absent melting under lower crustal conditions (Rapp and Watson, 1995; Rapp et al., 1991; Wolf and Wyllie, 1994) or water-saturated melting at variable pressures (Sisson and Grove, 1993; Xiong et al., 2005). In either case, peritectic phase entrainment may have further decreased the silica contents and aluminosity and increased the maficity (Mg + Fe + Ti) of the magmas (Castro, 2020; García-Arias and Stevens, 2017).

8.2.2 The role of intracrustal melting

The crustal sources of intermediate–acid members (SiO_2 > 52 wt. %) of the individual AFMC suites can be constrained by major-element diagrams based on the results of experimental partial melting of contrasting protoliths. In the binary plot CaO/(MgO + FeOt) vs. Al_2O_3/(MgO

+ FeOt) of Gerdes et al. (2000) (Fig. 12a), the samples of the OS correspond to partial melts of metabasalts–metatonalites, while the most siliceous (orthogneiss) samples straddle the boundary of metagreywackes-derived magmas' domain. In contrast, the YS granitoids seem to come primarily from metagreywackes or orthogneisses (indistinguishable in the current projection) with only minor admixture of metapelitic (for the most siliceous and peraluminous, Ms-bearing samples) and mafic–intermediate metaigneous lithologies. Similar conclusions can be drawn based on the $Al_2O_3/(FeOt + MgO) – 3\times CaO – 5\times K_2O/Na_2O$ ternary of Laurent et al. (2014 and references therein) (Fig. 12b), where the intermediate members of all suites fall into the field of melts of K-rich mafic metaigneous rocks (see also Fig. 6c), while the acid rock types can be characterized as having metasedimentary parentage.

In order to further constrain the prospective metaigneous sources of the studied granitoids and the mechanism of their partial melting (fluid-absent vs. fluid-present), we have compared compositions of the AFMC rocks with contoured compositions of experimental melts from Amp- and Amp–Bt-bearing metaigneous sources. These data come from a compilation of Gao et al. (2016 and references therein). Both fluid-absent and fluid-present experiments, conducted at 7–15 kbar, were selected. The protoliths ranged from basaltic to rhyolitic (plus plutonic equivalents); the K-rich (shoshonitic) protoliths were disregarded. Two examples of such comparisons are shown in Fig. 12c–f. In the CIPW-normative Ab–An–Or diagram of O'Connor (1965) (Fig. 12c–d), the fluid-absent experiments cluster mostly in the domains of granite, quartz monzonite and granodiorite, while the fluid-present experiments are characterized by lower Or contents, i.e. mainly by tonalitic composition. The overall tendency to lower total alkali contents of the fluid-present melts is shown in the TAS diagram after Cox et al. (1979) (Fig. 12e–f). Based on Fig. 12, we conclude that the basic–intermediate members of the OS fit well the experimental compositions of fluid-present melts from metabasalts to metatonalites,

while the felsic OS and the entire YS rather correspond to products of fluid-absent (dehydration) melting of intermediate/acid metaigneous and metapsammitic lithologies.

8.2.3 Radiogenic isotopic evidence

Mean crustal residence of the protoliths to the AFMC granitoids is inferred from radiogenic isotope data, both zircon Hf and the whole-rock Sr–Nd (Fig. 11). Within OS, hornblendite shows somewhat more radiogenic Hf in zircon (T_{DM}^{HfC} = 1.72–1.76 Ga) than the mutually well comparable orthogneiss and quartz diorite samples (T_{DM}^{HfC} = 1.84–1.90 Ga). Surprisingly, the YS Ms–Bt granite is less evolved, still (T_{DM}^{HfC} = 1.55–1.58 Ga).

Similarly, the whole-rock Nd isotopic compositions of (ultra-)basic–intermediate samples and the acidic orthogneisses of the OS document a long crustal residence of their sources ($T_{Nd.2stg}^{DM}$ = 1.51–1.67 Ga), not substantially different from the YS granitoids ($T_{Nd.2stg}^{DM}$ = 1.54–1.78 Ga) or granite samples of uncertain age ($T_{Nd.2stg}^{DM}$ = 1.60 and 1.77 Ga).

Taken together, the Hf–Nd isotopic data document an origin from an old, well-homogenized crustal segment with a mean crustal residence of 1.5–1.9 Ga. Therefore, they resemble the Nd isotopic compositions obtained from ~800 Ma rift-related felsic members of the Bimodal Suite in the Namibian Coastal Terrane as well as contemporaneous Uruguayan granitoids within the Punta del Este Terrane (Basei et al., 2011; Koester et al., 2021; Konopásek et al., 2018; Lenz et al., 2011).

At first glance, the Sr isotope compositions differ greatly between the (less radiogenic) OS and (more radiogenic) YS (Fig. 11b, e). However, taking into account the magmatic gap of ca. 40 Myr between intrusion of both AFMC suites, much of this difference can be attributed to *in situ* growth within, in terms of its mean crustal residence, analogous sources. This can be shown by a simple calculation. The standard radioactive decay equation of:

$$^{87}Sr/^{86}Sr_{YS} - ^{87}Sr/^{86}Sr_{OS} = \Delta^{87}Sr/^{86}Sr = ^{87}Rb/^{86}Sr_{source}\left(e^{\lambda\Delta t} - 1\right)$$

can be rearranged to:

$$^{87}Rb/^{86}Sr_{source} = \Delta^{87}Sr/^{86}Sr / \left(e^{\lambda\Delta t} - 1\right)$$

where Δt is the age difference between intrusion of both suites, OS and YS, $\Delta^{87}Sr/^{86}Sr$ is the difference in their Sr initial ratios. Using, for instance, the quartz diorite NP-012 ($^{87}Sr/^{86}Sr_{622}$ ~0.7075) and Ms–Bt granite NJ-62 ($^{87}Sr/^{86}Sr_{575}$ ~0.7127) pair leads to $^{87}Rb/^{86}Sr$ of 4.1 required for the source. Such a value is plausible for both intermediate–acid metaigneous and clastic metasedimentary sources.

According to Konopásek et al. (2016), the sample NJ-62 contained a considerable proportion of xenocrystic cores. Except for a single discordant analysis, their ages scattered between 800 Ma and the granite's crystallization constrained at of 575 ± 6 Ma. Such a variability argues rather for remelting of a youthful, clastic metasedimentary material, perhaps in a developing intracontinental rift (Konopásek et al., 2018).

8.2.4 Magmatic evolution

For the Older Suite, the documented occurrence of a modally layered sequence – together with whole-rock geochemical variation – underline an important petrogenetic role for the fractionation of Amp- and/or Pl-rich crystal assemblages from quartz dioritic/tonalitic parental magma. Theoretically, garnet could have been involved during fractional crystallization and/or deep crustal anatexis as well (Alonso-Perez et al., 2009). As shown by Davidson et al. (2013), the key fractionating ferromagnesian phase (amphibole vs. garnet) can be deciphered using the shape of the chondrite-normalized REE patterns. This can be quantified by the La_N/Yb_N and Dy/Dy* ratios; of particular interest is the change of these parameters in the course of differentiation (e.g., with increasing SiO_2). A moderate increase in La_N/Yb_N and a sharp decrease in Dy/Dy* below unity (increasingly convex down patterns) should indicate

amphibole, whereas a rapid increase in La_N/Yb_N and Dy/Dy* rising quickly above 1 (increasingly convex up patterns) could document the garnet control.

Examining both plots for the AFMC data (Fig. 13a–b), we conclude that the variation in the intermediate–acid members of the OS points to the principal role of Amp crystallization, while the acid samples of the YS show an evolution compatible with deep crustal anatexis leaving garnet in the residue. Moreover, the mafic members of the OS are confirmed as Amp ± Pl cumulates, in accordance with the whole-rock geochemical variation and field relations.

These results are taken as especially significant for less siliceous compositions, keeping in mind that the REE patterns of granites s.s. are commonly compromised by the fractionation of accessory minerals, including allanite or monazite (LREE), apatite and/or titanite (MREE), as well as zircon and/or xenotime (HREE) (Bea, 1996; Evans and Hanson, 1993; Hoskin et al., 2000; Janoušek et al., 2016; Miller and Mittlefehldt, 1984).

8.3 Comparison with the Florianópolis Batholith

8.3.1 Age, whole-rock geochemical and Sr–Nd isotopic signatures

In many respects, the whole-rock major- and trace-element compositions of the AFMC granitoids are closely comparable to the selected granitoid types in the south Brazilian Florianópolis Batholith – especially those of the northerly Porto Belo and southerly Garopaba regions (Figs 6a–b, e–f, 7–9).

Temporally, the *Older Suite* (~625–620 Ma) of the AFMC could be correlated with early-phase granitic magmatism in the Porto Belo area (Quatro Ilhas and Mariscal intrusions, ca. 625–610 Ma – Chemale Jr. et al., 2012; Florisbal et al., 2012a) and in the southern part of the Florianópolis Batholith (Paulo Lopes and Garopaba plutons, ca. 626 Ma – Silva et al., 2003; Florisbal et al., 2009) (ESM 1).

Similarly to the Namibian OS, heterogeneous crustal magma sources can be proposed for the examined granitoid types of the Florianópolis Batholith (Fig. 6c, Fig. 12a–b), ranging from intermediate (tonalitic) K-rich metaigneous (for the Quatro Ilhas Pluton) to felsic quartzo–feldspathic sources (for the Mariscal, Paulo Lopes, or Garopaba intrusions). The latter, quartz–feldspathic protoliths could have corresponded to metagreywackes or – in terms of major-element composition hardly distinguishable – orthogneisses. However, field and whole-rock geochemical and Sr–Nd–Pb isotopic data have led Bitencourt and Nardi (2000) and Florisbal et al. (2009, 2012b), among others, to interpret those granitoids as enriched mantle-derived magmas with variable crustal contribution introduced by Assimilation and Fractional Crystallization processes (AFC; DePaolo, 1981).

Even though the whole-rock geochemistry of the contemporaneous granitic rocks in the Florianópolis Batholith closely resembles that of the Namibian OS (Figs 6–9), there are several important differences. First, compared to the Namibian OS data, the basic–intermediate Quatro Ilhas members are richer in K (Fig. 6c) and thus form a dark-coloured subalkaline (i.e. monzonitic) association in the P–Q diagram of Debon and Le Fort (1988) (Fig. 6d). Second, the acid samples of the Quatro Ilhas, Garopaba, Paulo Lopes, and Mariscal granites are richer in both K and Fe, which is best seen in the binary plot of SiO_2 vs. Fe# of Frost et al. (2001) (Fig. 6c, Fig. 7a).

The Sr–Nd isotopic data for the mafic rock types in the AFMC's *Older Suite* and those coeval with the Quatro Ilhas Granitoids are indistinguishable (Fig. 11b–f). In contrast, the felsic (orthogneiss) lithologies in OS are somewhat more primitive (ε_{Nd}^{i} = –3.0 to –4.8, $T_{Nd.2stg}^{DM}$ = 1.51–1.65 Ga) (Fig. 11c) than the felsic Quatro Ilhas (ε_{Nd}^{i} = –5.1 to –7.6, $T_{Nd.2stg}^{DM}$ = 1.67–1.86 Ga), Mariscal (ε_{Nd}^{i} = –6.0 to –8.0, $T_{Nd.2stg}^{DM}$ = 1.73–1.89 Ga), Paulo Lopes (ε_{Nd}^{i} = –5.5 to –5.9, $T_{Nd.2stg}^{DM}$ = 1.70–1.74 Ga) and Garopaba (ε_{Nd}^{i} = –4.3 to –4.5, $T_{Nd.2stg}^{DM}$ = 1.61–1.63 Ga) types (Fig.

11d) (Chemale Jr. et al., 2012; Florisbal et al., 2009, 2012a). Florisbal et al. (2009, 2012a) interpreted these Sr–Nd signatures as a product of increasing crustal contribution in more evolved rocks by AFC processes. Apart from Sr–Nd isotopic signatures, some whole-rock geochemical parameters, such as the high LILE (including K) contents and La/Yb_N ratios in the Quatro Ilhas mafic rocks, suggest their origin from an enriched mantle, possibly metasomatized by previous subduction.

In contrast, the time period corresponding to the intrusion of the AFMC's *Younger Suite* (~585–575 Ma) was characterized in the Florianópolis Batholith (~590 Ma) mainly by A-type magmatism, with voluminous, high-Si, shallow-level plutono-volcanic systems (including ignimbrites), locally also amphibole-bearing intermediate to acidic granitoids and associated bimodal dykes. Regarding the voluminous high-Si associations, the Ilha, Serra do Tabuleiro and Vila da Penha granites and Cambirela ignimbrites show a clear A-type affinity, high K, and conspicuous Fe enrichment, while the Hbl–Bt granitoids of the São Pedro de Alcântara Suite are high-K calc-alkaline in character (Janasi et al., 2015; Santos et al., 2019). Neither of these two igneous associations has a known counterpart in the AFMC. As no associated volcanic rocks have been described to date in the AFMC, this Complex intruded most likely relatively deep. This is in line with high inferred H_2O contents of the AFMC magmas, likely to reach the volatile saturation relatively early during ascent, and thus to solidify already at considerable depth (Müntener et al., 2021 and references therein).

The only known possible Brazilian temporal and compositional equivalent of the Namibian YS seems to be the shallow-level Zimbros Intrusive Suite in the Porto Belo region, emplaced at ~590 Ma (Chemale Jr. et al., 2012). Apart from the Zimbros and Morro dos Macacos granites, this intrusive suite is formed by a regional swarm of felsic, mafic and composite dykes. Evidence for thermal disequilibrium and transfer of xenocrysts between mafic and felsic magmas is best preserved in composite dykes, but mingling features are also found

in the granitic rocks (Bitencourt et al., 2015; Tomé et al., 2020). Although detailed comparison of Namibian YS with acid Zimbros rocks is currently hampered by the lack of published modern, high-precision trace-element and Sr–Nd isotopic data from the latter, the basic–intermediate types correspond well to the most mafic AFMC rocks both in terms of their major- (Figs 6–8) and available trace-element (Figs 8–10) compositions.

The emplacement of the Zimbros dyke swarm was largely controlled by the already waning tectonic activity of the Major Gercino Shear Zone (Tomé et al., 2020). This deep-seated, lithospheric-scale structure is thought to have played a key role in focusing both the mantle- and crust-derived magmas and facilitating open-system (mingling, mixing, and AFC) processes (Bitencourt, 1996; Bitencourt and Nardi, 2000; Bitencourt et al., 2015; Florisbal et al., 2012a; Peruchi et al., 2021; Tomé et al., 2020), probably mainly during their ascent through narrow conduits (Collins et al., 2000).

Very similar may also have been the situation in the Younger Suite of the AFMC, where the intimate association of mafic and felsic magmas and evidence for their mutual interaction is frequently observed. Also here, the mantle-derived magmas may have contributed some of the heat needed for crustal anatexis, as well as for focused thermal softening and strain localization into the zone of hybridization (Kiss et al., 2019).

8.3.2 Geochemical constraints on the geodynamic setting of the AFMC/FB magmatism

The whole-rock geochemical compositions of magmatic rocks are often used for fingerprinting their geodynamic setting (Bonin et al., 2020 and references therein), but this can be problematic in late- to post-collisional granitic suites where variable crustal and/or mantle sources may be involved (Pearce, 1996). Furthermore, the original chemistry of the parental magma is often obscured by processes such as peritectic phase entrainment, crystal accumulation, country-rock assimilation or hybridization of mantle- and crustally-derived magmas (e.g., Clemens and

Stevens, 2012; Deering and Bachmann, 2010; Didier and Barbarin, 1991). Keeping these limitations in mind, analyses from Angra Fria Magmatic Complex and Florianópolis Batholith could be plotted into some well-established geotectonic diagrams, as these often represent projections useful for geotectonic and petrogenetic considerations (Janoušek et al. 2016).

In the triangular plot Th–Hf/3–Nb/16 of Wood (1980) (Fig. 14a), most of the AFMC and FB basic–intermediate analyses fall into the continental arc-related (CAB) field. Within the AFMC, only the samples NP-012 and NP-007 plot at the boundary between the island-arc tholeiites (IAT) and MORB fields, while the hornblendites NP-013 and NJ-58 classify as EMORB or within-plate tholeiites (WPT). However, this spurious signature of both amphibole cumulates should, at least partly, reflect the preference of the amphibole lattice for Nb, compared with mildly to strongly incompatible Th and Hf (Tiepolo et al., 2007). Still, similar, albeit weaker, EMORB/WPT affinity is also shown by the Zimbros mafic dykes. All acid samples fall next to the Th apex, close to the average upper-crustal composition (UCC– Taylor and McLennan, 1995), indicative of important mature crustal contribution.

In the La/10–Y/15–Nb/8 plot of Cabanis and Lecolle (1989) (Fig. 14b), most of the OS analyses fall into the calc-alkaline part of domain I (destructive plate boundaries); only the mafic cumulates (NP-013 and NJ-58) straddle the boundary of adjacent domain II, corresponding to the late- to post-orogenic (compressive or distensive) intra-continental domains. The YS analyses are more variable, but their distribution is centred in domain II, where the average compositions of the lower and upper crust (LCC and UCC, respectively) also project.

The Hf–Rb/30–3×Ta ternary diagram (Harris et al., 1986) (Fig. 14c) serves for detailed subdivision of collision-related (and, in particular, post-collisional) granitoid suites. According to this projection, all OS and the least siliceous YS analyses correspond to volcanic-arc related (Group 1), while the acid YS samples show an affinity to syn-collisional peraluminous

intrusions (Group 2). Also, almost all the plotted Brazilian data fall into the volcanic-arc-related domain, but many of the analyses lack Ta determinations and thus cannot be discriminated.

In the binary diagram Nb/Yb vs. Th/Yb (Pearce, 2014) (Fig. 14d), all but the most mafic OS samples fall above the 'MORB–OIB array', into the region occupied by compositions with a strong crustal imprint. This includes rocks crystallized from crustally derived magmas (viz. the projection of the average upper crustal composition, UCC, of Taylor and McLennan, 1995), as well as strongly crustally contaminated mantle melts such as variously fractionated arc-related magmas. Granitic analyses from the Florianópolis Batholith are generally well comparable to the variation observed in the AFMC, with the Zimbros Suite mafic rocks spreading widely from the 'MORB–OIB array' to the 'Volcanic arc array'.

The OS Suite follows a linear trend, in which the Th/Yb ratio is positively correlated with the SiO_2 content (the most basic samples fall close to the EMORB projection point, while the more siliceous samples plot farthest from the MORB–OIB array). The OS trend is accentuated by the data points for the Zimbros mafic/composite dykes and MME, confirming the overwhelming field evidence for interaction between the EMORB-like mafic and crustally derived, felsic magmas. The YS data points indicate mostly a crustal anatectic origin; the NJ-05 dyke can be interpreted as a mantle–crust hybrid. For instance, it may represent a mantle-derived magma strongly contaminated by the crust or, more likely, a melt of an ancient, crustally contaminated metabasic source. The position of the mafic dykes NK-28 and NP-017 of unknown age in the Nb/Yb vs. Th/Yb diagram possibly corresponds to a crustally contaminated OIB-like component.

8.4 Towards a plausible geotectonic model

8.4.1 Tectonic setting

The Tonian evolution of the units that formed the future hinterland of the Kaoko–Dom Feliciano–Gariep orogenic system (Punta del Este–Coastal Terrane) has been interpreted as an axial part of a Neoproterozoic 'Adamastor Rift' that developed in a back-arc to intracontinental position, close to the edge of the Rodinia supercontinent (Konopásek et al., 2018). This interpretation is based on several lines of evidence suggesting an almost immediate transition from rifting to orogenic evolution in the northern Kaoko–Dom Feliciano–Gariep Belt, precluding the formation of large amounts of oceanic crust (Konopásek et al., 2020). The pre-orogenic connection of the African and South American forelands is evident from nearly identical detrital zircon record of the Neoproterozoic rifting-related (now metamorphosed) sedimentary rocks covering the respective basement units (Percival et al., 2021). Although the exact temporal extent of the Neoproterozoic pre-orogenic sedimentation on the South American side of the rift system remains unknown, the African foreland contains undisturbed Tonian–Cryogenian sedimentary sequences, which provide clues for interpretation that active crustal stretching ceased between the Sturtian and Marinoan global glaciation periods, i.e. at ca. 660–650 Ma (Hoffman et al., 2021).

The beginning of convergent evolution has been constrained on both sides of the northern Kaoko–Dom Feliciano–Gariep orogenic system. The onset of orogenic thickening of the northern Dom Feliciano Belt foreland was dated by Percival et al. (2022) at ca. 660–650 Ma, and similar evolution was also recognized in more southerly parts of the South American foreland (Battisti et al., 2018). On the African side of the orogen, in the Kaoko Belt, the ongoing orogenic activity is evident from the deposition of flysch sediments, which first appear between glaciogenic sedimentary rocks of the Sturtian and Marinoan global glaciation events, i.e. again

at ca. 660–650 Ma (Konopásek et al., 2017). All these findings represent a robust set of arguments for the interpretation that convergence leading to the formation of the Kaoko–Dom Feliciano–Gariep orogenic system began immediately after the cessation of crustal stretching (Konopásek et al., 2020).

Data from the northern Dom Feliciano Belt suggest that thrusting-related thickening ended at ca. 635–625 Ma, and since then, the evolution of the NW edge of the orogenic system was governed by transcurrent movements along the foreland–hinterland interface (De Toni et al., 2020a; Percival et al., 2022). Then, orogenic thrusting resumed on the African side of the orogenic system, in the Kaoko Belt, where the onset of thrusting of the orogenic hinterland onto the foreland started at ca. 580 Ma and continued until ca. 550 Ma (Goscombe and Gray, 2007; Ulrich et al., 2011). This two-stage evolution of the orogenic system is also reflected in the distribution of igneous rocks in its hinterland domain, where the ca. 630–590 Ma granitoid rocks are concentrated on its South American side, whereas those with ages of ca. 580–550 Ma appear on the African side (Fig. 1b). The only so far known exception is the Older Suite of the Angra Fria Magmatic Complex, which was interpreted as a continuation of the Florianópolis Batholith isolated on the African side of the orogen after the opening of the Atlantic Ocean (Konopásek et al., 2016).

The timing of tectonic processes preceding and accompanying the massive production of Ediacaran granitoid rocks in the hinterland domain provides clues for possible source(s) of heat necessary for such an extensive crustal and, in part, also mantle melting: a) The pre-orogenic “Adamastor Rift” was inverted almost immediately after it reached its maximum stretching accompanied by upwelling of the asthenospheric mantle and establishment of a high geothermal gradient. b) Underthrusting of fertile sediments both along the foreland–hinterland interface and during internal thrusting within the hinterland domain likely provided additional heat due

to deep burial and increasingly important *in-situ* decay of radioactive elements, but also a large amount of fluids due to ongoing prograde metamorphic reactions.

The proposed geotectonic model for associated Ediacaran magmatism, products of which are preserved on both sides of the Southern Atlantic (Angra Fria and Florianópolis magmatic complexes), is presented in Fig. 15, and its particular aspects are summarized below.

8.4.2 Ediacaran magmatic activity

The available geochronological data document that the magmatic activity in the Angra Fria Magmatic Complex showed two flare-ups, at ~625–620 Ma (Older Suite) and at ~585–575 Ma (Younger Suite). The previously published Hf-in-Zrn isotopic data (Konopásek et al., 2016), together with the newly acquired whole-rock geochemical and Sr–Nd isotopic signatures, underline an important role of intracrustal melting, with only a relatively minor contribution from juvenile, mantle-derived melts.

In terms of petrology and whole-rock geochemical composition, the older Namibian granitoids can be correlated with the contemporaneous plutons in the Florianópolis Batholith (most notably Quatro Ilhas Pluton). However, enriched-mantle-derived melts' involvement via AFC-type processes has been considered much more important for the genesis of these Brazilian intrusions (Bitencourt and Nardi, 2000; Florisbal et al., 2009, 2012b). In contrast, the Namibian Younger Suite seems to have had no contemporary equivalent in the Florianópolis Batholith, apart from the Zimbros Intrusive Suite related to the lithospheric-scale Major Gercino Shear Zone. In Zimbros, mafic members and, in particular, composite dykes require a mixed mantle–crustal parentage (Bitencourt et al., 2015; Chemale Jr. et al., 2012; Tomé et al., 2020). At this time, magmatism in the FB was characterized mainly by shallow-level volcanic sequences, often with A-type affinity (Janasi et al., 2015; Santos et al., 2019).

The AFMC whole-rock geochemical data point to partial melting of mature continental crust with late Palaeoproterozoic to early Mesoproterozoic crustal residence ages (1.9–1.5 Ga). These Nd crustal residence ages resemble the contemporaneous Uruguayan granitoids forming the basement of the Punta del Este Terrane, as well as some of the published data for felsic members of the ~800 Ma rift-related Bimodal Suite in the Namibian Coastal Terrane (Konopásek et al., 2018). Geochemical data imply that the protoliths were dominated by K-rich mafic metaigneous rocks (metabasalts and metatonalites) for the Older Suite and quartz-feldspathic (metasedimentary and/or intermediate–acid metaigneous) ones for the Younger Suite.

However, fluid-absent melting of rather refractory metabasic rocks – the assumed source of the OS – would require high temperatures. These would be difficult to achieve in the previously thinned crust of the former 'Adamastor Rift', even if the elevated rift-related heat flow persisted into the early stages of the collision. Moreover, based on amphibole chemistry, the magmas from which the studied granitoids crystallized were water-rich (ca. 10 wt. % H_2O or more). This, together with generally tonalitic, alkali-poor compositions (Fig. 12c–d), points to water-fluxed melting, substantially depressing the solidus temperature of metabasic protoliths (Sisson and Grove, 1993; Xiong et al., 2005). Indeed, Castro (2020) argued that, in order to generate sufficiently high amounts of such 'secondary' I-type magmas from granulite-grade metaigneous sources, water-fluxed melting is required.

Nevertheless, the source of hydrous fluids remains unclear. One can only speculate about the dehydration of relatively fertile upper crustal material (Weinberg and Hasalová, 2015, and references therein) of the rift shoulders or its internal parts, underthrust/buried in the course of rift inversion. Part of the water could also have been contributed by water-bearing mantle-derived magmas crystallizing at lower crustal levels (Annen et al., 2006, 2015; Collins et al., 2016, 2020).

In contrast, felsic older granitoids and the entire younger suite are most likely products of fluid-absent, probably (Ms–)Bt-dehydration melting of relatively felsic, subaluminous to (minor) peraluminous crustal sources (metagreywackes or intermediate–acid orthogneisses prevailing over metapelites). This may reflect the lower availability of free water at later stages of the orogeny, and increased increased *in-situ* heat production in the thickened crust.

The only unequivocal mantle contributions to the AFMC magmatism have been identified in the YS mingling zones and in mafic–intermediate dykes of uncertain age (cutting both the AFMC and the Amspoort magmatic suite). The elemental and isotopic compositions suggest an origin of these dykes from asthenosphere-influenced but strongly crustally contaminated magmas. However, an ultimate proof for the involvement of mantle-derived (enriched MORB-like) melts comes from the Brazilian Major Gercino Shear Zone, especially the Zimbros composite dykes.

Apart from the cumulates, the trace-element composition of the OS and YS share common features. In particular, HFSE depletion and LILE enrichment, demonstrated in many geotectonic plots as well as by the presence of a negative TNT (Ta–Nb–Ti) anomaly in NMORB-normalized spider plots (Fig. 9a–c). Such a fingerprint is often taken as a hallmark of oceanic plate subduction-related magmatism (e.g., Pearce and Peate, 1995; Pearce et al., 1984; Tatsumi and Eggins, 1995).

However, especially for felsic granitoids, it may equally well reflect remelting of pre-existing Nb–Ta-poor continental crustal sources, directly arc-related or not. It is worth keeping in mind that negative TNT anomalies are an intrinsic feature of the average continental crust (Arculus, 1987; Janoušek et al., 2010; Konopásek et al., 2020; Roberts and Clemens, 1993). A similar scenario of geotectonic “inheritance” of the TNT anomalies may also apply to some basic, mantle-derived magmatic rocks. Several cases documented in the literature reported subcontinental lithospheric mantle domains that have retained an ancient subduction signature

until a later, unrelated tectonic event triggered a new magma generation. These include rift settings, both oceanic and continental, e.g. in the Basin and Range Province, SW United States (Hawkesworth et al. 1995), Gardar Province, southern Greenland (Goodenough et al. 2002), Eastern Ghats Belt, SE India (Vijaya Kumar et al. 2015), Gakkel Ridge, Arctic Ocean (Richter et al., 2020) and northern Yangtze Block, South China (Zhang et al. 2020). The Tonian bimodal magmatism of the Punta del Este–Coastal Terrane in N Namibia and S Brazil (Konopásek et al. 2018) could be a similar case.

Moreover, in analogy with the current paradigm for the generation of magmas at active continental margins, we propose that such an apparent, arc-like geochemical signature could be (at least in part) caused by the water-fluxed melting mechanism itself. In this model, the deeply underplated/buried crustal lithologies, the presumed main source of water for partial melting of the overlying crust, released the hydrous fluid-mobile LILE but retained the immobile HFSE.

If true, this fluid-present partial melting model provides yet another mechanism for hydrous fluids-mediated LILE/HFSE fractionation that could account for, or at least contribute to, the origin of negative TNT anomalies observed in the NMORB-normalized spider plots. The mere presence of this anomaly is thus not sufficient as unequivocal evidence for magmatic arc-related origin of granitic magmas. Therefore, a reliable interpretation of geodynamic setting of granitic magmatism should rely not only on whole-rock geochemical data but also on all available geological evidence, including thorough knowledge of the units involved, mechanism of their mutual interaction (geodynamic/palaeogeographic data), as well as geochronological and structural information.

9. Conclusions

Ediacaran syn-tectonic plutonic rocks of the Angra Fria Magmatic Complex (AFMC; Kaoko Belt, NW Namibia) have their counterparts in the broadly contemporaneous Florianópolis

Batholith (FB; Santa Catarina, southern Brazil). Until the breakup of Western Gondwana and the opening of the southern Atlantic Ocean, they both belonged to a single Kaoko–Dom Feliciano–Gariep orogenic system. The newly acquired field, mineral chemistry, as well as whole-rock geochemical major-, trace- and Sr–Nd isotopic data for the AFMC provide fresh insight into the nature, prospective sources, evolution and geodynamic causes of this Pan-African plutonic activity.

1) The AFMC is subdivided into the Older Suite (OS; ~625–620 Ma: biotite augen gneisses, hornblendites, amphibole-bearing gabbros and quartz diorites–tonalites) and the Younger Suite (YS; ~585–575 Ma: amphibole–biotite tonalites to muscovite–biotite leucogranites, quartz dioritic dykes and enclave-rich mingled zones). In the Florianópolis Batholith, granitoids contemporaneous with the OS occur both along high-strain zones (Major Gercino Shear Zone: Quatro Ilhas Pluton) and in low-strain zones of the hinterland (Paulo Lopes and Garopaba plutons). The only possible temporal and compositional equivalent of the Namibian YS seems to be the Zimbros Intrusive Suite, emplaced at the final stages of the Major Gercino Shear Zone development.
2) Both AMFC suites and the comparable Brazilian intrusions in the Florianópolis Batholith (FB) are magnesian, transitional between tholeiitic and calc-alkaline. Most lithologies are metaluminous, except for the most felsic types. Apart from the cumulates, the Normal Mid-Ocean Ridge Basalt (NMORB) normalized spider plots display strong enrichments in Large Ion Lithophile Elements (LILE) (Cs, Rb, Ba and K), Th, U and Pb and deep troughs in High Field Strength Elements (HFSE: Nb, Ta and Ti).
3) The Older Suite likely originated mainly by fluid-present partial melting of metabasalts and metatonalites, followed by (near) closed-system fractional crystallization (with, or without accumulation) of amphibole ± plagioclase. For the Younger Suite, the main

process was lower crustal fluid-absent (dehydration) melting of relatively felsic protoliths (metagreywackes or intermediate–acid orthogneisses >> metapelites), leaving garnet in the residue. In the AFMC, mantle-derived, strongly crustally contaminated basic rocks are relatively rare and mostly limited to the YS and dykes of uncertain age.

4) The whole-rock geochemistry, zircon Hf and whole-rock Nd isotopic signatures suggest partial melting of a mature continental crust with a late Palaeoproterozoic to early Mesoproterozoic mean crustal residence age (1.5–1.9 Ga). By crustal residence, the studied AFMC resembles previously published data for Tonian (~800 Ma) rift-related granitoids in the Namibian Coastal and the Uruguayan Punta del Este terranes.
5) The older granitoids (in both OS and Florianópolis Batholith) are mutually comparable in composition and genesis. The YS still records communication with the mantle (deeper source), whereas in the FB, this period was characterized mainly by siliceous shallow-level, A-type plutono–volcanic systems. As an exception, the Zimbros Intrusive Suite originated by hybridization between mafic, mantle-derived (enriched MORB-like) and felsic, crustal magmas. Lithospheric-scale shear zones likely played a key role in focusing mantle- and crust-derived magmas and facilitating hybridization (mingling, mixing, and assimilation–fractional crystallization) processes.
6) In general, subduction-like LILE over HFSE enrichment in granitic rocks does not need to reflect classic oceanic subduction with attendant slab dehydration ± partial melting triggering water-fluxed melting in the metasomatized mantle wedge. Instead, such a geochemical signature may be inherited from the source, both in the continental crust and lithospheric mantle. Or it can even be shaped by high-grade metamorphism and dehydration of deeply buried continental crust and resulting water-flux melting of the overlying crustal lithologies. This scenario may occur, for instance, during intracrustal processes connected with the inversion of continental rifts.

Declaration of Competing Interest

The authors declare that they have no known competing financial interests or personal relationships that could have appeared to influence the work reported in this paper.

Acknowledgements

The manuscript was improved significantly by detailed reviews of three anonymous reviewers, and further benefited from the careful editorial work of editor-in-chief Irina M. Artemieva. We are indebted to Y. Kochergina and Z. Rodovská for technical help in the Sr–Nd isotopic laboratory. J. Haifler and R. Škoda assisted with electron-microprobe analyses. Finally, we appreciate the companionship of our late colleague and friend J. Košler during the early stage of research in the Angra Fria Complex, as well as of R. Anczkiewicz during our 2016 field campaign.

Funding: This work was supported by the Czech Grant Agency (GACR) [grant number 18-24281S to JK].

References

Alonso-Perez, R., Müntener, O., Ulmer, P., 2009. Igneous garnet and amphibole fractionation in the roots of island arcs: experimental constraints on andesitic liquids. Contributions to Mineralogy and Petrology 157, 541-558. https://doi.org/10.1007/s00410-008-0351-8.

Anderson, J.L., 1996. Status of thermobarometry in granitic batholiths. Transactions of the Royal Society of Edinburgh, Earth Sciences 87, 125-138. https://doi.org/10.1017/S0263593300006544.

Anderson, J.L., Barth, A.P., Wooden, J.L., Mazdab, F., 2008. Thermometers and Thermobarometers in Granitic Systems. In: Putirka, K.D., Tepley III, F.J. (Eds.), Minerals, Inclusions and Volcanic Processes. Mineralogical Society of America and Geochemical Society Reviews in Mineralogy and Geochemistry 69, Washington, pp. 121-142. https://doi.org/10.2138/rmg.2008.69.4.

Annen, C., Blundy, J.D., Sparks, R.S.J., 2006. The genesis of intermediate and silicic magmas in deep crustal hot zones. Journal of Petrology 47, 505-539. https://doi.org/10.1093/petrology/egi084.

Annen, C.J., Blundy, J.D., Leuthold, J., Sparks, R.S.J., 2015. Construction and evolution of igneous bodies: towards an integrated perspective of crustal magmatism. Lithos 230, 206-221. https://doi.org/10.1016/j.lithos.2015.05.008.

Arculus, R.J., 1987. The significance of source versus process in the tectonic controls of magma genesis. Journal of Volcanology and Geothermal Research 32, 1-12. https://doi.org/10.1016/0377-0273(87)90033-3.

Basei, M.A.S., Siga Jr., O., Masquelin, H., Harara, O.M., Reis Neto, J.M., Preciozzi, F., 2000. The Dom Feliciano Belt of Brazil and Uruguay and its foreland domain, the Rio de la Plata Craton, framework, tectonic evolution and correlation with similar provinces of southwest Africa. In: Cordani, U.G., Milani, E.J., Thomaz Filho, A., Campos, D.A. (Eds.), Tectonic Evolution of South America. IGC, Rio de Janeiro, 311-334.

Basei, M.A.S., Peel, E., Sánchez Bettucci, L., Preciozzi, F., Nutman, A.P., 2011. The basement of the Punta del Este Terrane (Uruguay): an African Mesoproterozoic fragment at the eastern border of the South American Río de La Plata Craton. International Journal of Earth Sciences 100, 289-304. https://doi.org/10.1007/s00531-010-0623-1.

Basei, M.A.S., Frimmel, H.E., Campos Neto, M.C., de Araujo, C.E.G., de Castro, N.A., Passarelli, C.R., 2018. The tectonic history of the southern Adamastor Ocean based on a correlation of the Kaoko and Dom Feliciano belts. In: Siegesmund, S., Basei, M.A.S., Oyhantçabal, P., Oriolo, S. (Eds.), Geology of Southwest Gondwana. Springer, Cham, pp. 63-85. 10.1007/978-3-319-68920-3_3.

Battisti, M.A., Bitencourt, M.F., De Toni, G.B., Nardi, L.V.S., Konopásek, J., 2018. Metavolcanic rocks and orthogneisses from Porongos and Várzea do Capivarita complexes: a case for identification of tectonic interleaving at different crustal levels from structural and geochemical data in southernmost Brazil. Journal of South American Earth Sciences 88, 253-274. https://doi.org/10.1016/j.jsames.2018.08.009.

Bea, F., 1996. Residence of REE, Y, Th and U in granites and crustal protoliths; implications for the chemistry of crustal melts. Journal of Petrology 37, 521-552. https://doi.org/10.1093/petrology/37.3.521.

Belousova, E.A., Kostitsyn, Y.A., Griffin, W.L., Begg, G.C., O'Reilly, S.Y., Pearson, N.J., 2010. The growth of the continental crust: constraints from zircon Hf-isotope data. Lithos 119, 457-466. https://doi.org/10.1016/j.lithos.2010.07.024.

Bitencourt, M.F., 1996. Granitóides sintectônicos da região de Porto Belo, SC: uma aboradagem petrológica e estrutural do magmatismo em zonas de cisalhamento. Unpublished Ph.D. thesis, Universidade Federal do Rio Grande do Sul, Porto Alegre.

Bitencourt, M.F., Nardi, L.V.S., 1993. Late- to post-collisional Brasiliano magmatism in southernmost Brazil. Anais da Academia Brasileira de Ciências 65, 13-16.

Bitencourt, M.F., Nardi, L.V.S., 2000. Tectonic setting and sources of magmatism related to the Southern Brazilian Shear Belt. Revista Brasileira de Geociências 30, 186-189. https://doi.org/10.25249/0375-7536.2000301186189.

Bitencourt, M.F., Florisbal, L.M., De Toni, G.B., Martini, A., Weinberg, R., 2015. Neoproterozoic syntectonic granitic magmatism in Santa Catarina, South Brazilian coast – crust and mantle contributions to granite generation within a transpressive orogen. Excursion Guide, 8th Hutton Symposium on Granites and Related Rocks, Florianópolis.

Bonin, B., Janoušek, V., Moyen, J.F., 2020. Chemical variation, modal composition and classification of granitoids. In: Janoušek, V., Bonin, B., Collins, W.J., Farina, F., Bowden, P. (Eds.), Post-Archean Granitic Rocks: Contrasting Petrogenetic Processes and Tectonic Environments. Geological Society of London Special Publications 491, 9-51. https://doi.org/10.1144/SP491-2019-138.

Bouvier, A., Vervoort, J.D., Patchett, P.J., 2008. The Lu–Hf and Sm–Nd isotopic composition of CHUR: constraints from unequilibrated chondrites and implications for the bulk composition of terrestrial planets. Earth and Planetary Science Letters 273, 48-57. https://doi.org/10.1016/j.epsl.2008.06.010.

Boynton, W.V., 1984. Cosmochemistry of the rare earth elements: meteorite studies. In: Henderson, P. (Ed.), Rare Earth Element Geochemistry. Elsevier, Amsterdam, 63-114. https://doi.org/10.1016/B978-0-444-42148-7.50008-3.

Brown, M., 2013. Granite: from genesis to emplacement. Geological Society of America Bulletin 125, 1079-1113. https://doi.org/10.1130/B30877.1.

Brown, M., Rushmer, T., 2006. Evolution and Differentiation of the Continental Crust. Cambridge University Press, Cambridge.

Cabanis, B., Lecolle, M., 1989. Le diagramme La/10-Y/15-Nb/8: un outil pour la discrimination des séries volcaniques et la mise en évidence des processus de mélange et/ou de contamination crustale. Comptes Rendus de l'Académie des Sciences. Série 2, Mécanique, Physique, Chimie, Sciences de l'univers, Sciences de la Terre 309, 2023-2029.

Castro, A., 2020. The dual origin of I-type granites: the contribution from experiments. In: Janoušek, V., Bonin, B., Collins, W.J., Farina, F., Bowden, P. (Eds.), Post-Archean Granitic Rocks: Contrasting Petrogenetic Processes and Tectonic Environments. Geological Society of London Special Publications 491, 101-145. https://doi.org/10.1144/SP491-2018-110.

Caxito, F.A., Heilbron, M., Valeriano, C.M., Bruno, H., Pedrosa-Soares, A., Alkmim, F.F., Chemale, F., Hartmann, L.A., Dantas, E., Basei, M.A.S., 2021. Integration of elemental and isotope data supports a Neoproterozoic Adamastor Ocean realm. Geochemical Perspectives Letters 17, 6–10. https://doi.org/10.7185/geochemlet.2106.

Chemale Jr, F., Mallmann, G., Bitencourt, M.F., Kawashita, K., 2012. Time constraints on magmatism along the Major Gercino Shear Zone, southern Brazil: implications for West Gondwana reconstruction. Gondwana Research 22, 184-199. https://doi.org/10.1016/j.gr.2011.08.018.

Clemens, J.D., 2003. S-type granitic magmas – petrogenetic issues, models and evidence. Earth-Science Reviews 61, 1-18. https://doi.org/10.1016/S0012-8252(02)00107-1.

Clemens, J.D., Stevens, G., 2012. What controls chemical variation in granitic magmas? Lithos 134-135, 317-329. https://doi.org/10.1016/j.lithos.2012.01.001.

Collins, W.J., Richards, S.R., Healy, B.E., Ellison, P.I., 2000. Origin of heterogeneous mafic enclaves by two-stage hybridisation in magma conduits (dykes) below and in granitic magma chambers. Transactions of the Royal Society of Edinburgh, Earth Sciences 91, 27-45. https://doi.org/10.1017/S0263593300007276.

Collins, W.J., Huang, H.Q., Jiang, X.Y., 2016. Water-fluxed crustal melting produces Cordilleran batholiths. Geology 44, 143-146. https://doi.org/10.1130/G37398.1.

Collins, W.J., Murphy, J.B., Johnson, T.E., Huang, H.Q., 2020. Critical role of water in the formation of continental crust. Nature Geoscience 13, 331-338. https://doi.org/10.1038/s41561-020-0573-6.

Cox, K.G., Bell, J.D., Pankhurst, R.J., 1979. The Interpretation of Igneous Rocks. George Allen & Unwin, London.

Davidson, J., Turner, S., Plank, T., 2013. Dy/Dy*: variations arising from mantle sources and petrogenetic processes. Journal of Petrology 54, 525-537. https://doi.org/10.1093/petrology/egs076.

De Toni, G.B., Bitencourt, M.F., Konopásek, J., Martini, A., Andrade, P.H.S., Florisbal, L.M., Campos, R.S., 2020a. Transpressive strain partitioning between the Major Gercino Shear Zone and the Tijucas Fold Belt, Dom Feliciano Belt, Santa Catarina, southern Brazil. Journal of Structural Geology 136, 104058. https://doi.org/10.1016/j.jsg.2020.104058.

De Toni, G.B., Bitencourt, M.F., Nardi, L.V.S., Florisbal, L.M., Almeida, B.S., Geraldes, M., 2020b. Dom Feliciano Belt orogenic cycle tracked by its pre-collisional magmatism: the Tonian (ca. 800 Ma) Porto Belo Complex and its correlations in southern Brazil and Uruguay. Precambrian Research 342, 105702. https://doi.org/10.1016/j.precamres.2020.105702.

de Wit, M.J., Stankiewicz, J., Reeves, C., 2008. Restoring Pan-African-Brasiliano connections: more Gondwana control, less Trans-Atlantic corruption. In: Pankhurst, R.J., Trouw, R.A.J., de Brito Neves, B.B., de Wit, M.J. (Eds.), West Gondwana: Pre-Cenozoic Correlations Across the South Atlantic Region. Geological Society of London Special Publications 294, 399-412. https://doi.org/10.1144/SP294.20.

Debon, F., Le Fort, P., 1983. A chemical–mineralogical classification of common plutonic rocks and associations. Transactions of the Royal Society of Edinburgh, Earth Sciences, 73: 135-149. https://doi.org/10.1017/S0263593300010117

Debon, F., Le Fort, P., 1988. A cationic classification of common plutonic rocks and their magmatic associations: principles, method, applications. Bulletin de Minéralogie 111, 493-510. https://doi.org/10.3406/bulmi.1988.8096.

Deering, C.D., Bachmann, O., 2010. Trace element indicators of crystal accumulation in silicic igneous rocks. Earth and Planetary Science Letters 297, 324-331. https://doi.org/10.1016/j.epsl.2010.06.034.

DePaolo, D.J., 1981. Trace element and isotopic effects of combined wallrock assimilation and fractional crystallization. Earth and Planetary Science Letters 53, 189-202.

Didier J., Barbarin, B. (Editors) 1991. Enclaves and Granite Petrology. Developments in Petrology 13. Elsevier, Amsterdam.

Elburg, M.A., 1996. Evidence of isotopic equilibration between microgranitoid enclaves and host granodiorite, Warburton Granodiorite, Lachlan Fold Belt, Australia. Lithos 38, 1-22. https://doi.org/10.1016/0024-4937(96)00003-5.

Erdmann, S., Martel, C., Pichavant, M., Kushnir, A., 2014. Amphibole as an archivist of magmatic crystallization conditions: problems, potential, and implications for inferring magma storage prior to the paroxysmal 2010 eruption of Mount Merapi, Indonesia. Contributions to Mineralogy and Petrology 167, 1016. https://doi.org/10.1007/s00410-014-1016-4.

Evans, O.C., Hanson, G.N., 1993. Accessory-mineral fractionation of rare-earth element (REE) abundances in granitoid rocks. Chemical Geology 110, 69-93. https://doi.org/10.1016/0009-2541(93)90248-H.

Fernandes, L.A.D., Tommasi, A., Porcher, C.C., 1992. Deformation patterns in the southern Brazilian branch of the Dom Feliciano Belt: a reappraisal. Journal of South American Earth Sciences 5, 77-96. https://doi.org/10.1016/0895-9811(92)90061-3.

Florisbal, L.M., Bitencourt, M.F., Nardi, L.V.S., Conceição, R.V., 2009. Early post-collisional granitic and coeval mafic magmatism of medium- to high-K tholeiitic affinity within the Neoproterozoic Southern Brazilian Shear Belt. Precambrian Research 175, 135-148. https://doi.org/10.1016/j.precamres.2009.09.003.

Florisbal, L.M., Bitencourt, M.F., Janasi, V.A., Nardi, L.V.S., Heaman, L.M., 2012a. Petrogenesis of syntectonic granites emplaced at the transition from thrusting to transcurrent tectonics in post-collisional setting: whole-rock and Sr–Nd–Pb isotope geochemistry in the Neoproterozoic Quatro Ilhas and Mariscal granites, southern Brazil. Lithos 153, 53-71. https://doi.org/10.1016/j.lithos.2012.04.031.

Florisbal, L.M., Janasi, V.A., Bitencourt, M.F., Heaman, L.M., 2012b. Space–time relation of post-collisional granitic magmatism in Santa Catarina, southern Brazil: U–Pb LA-MC-ICP-MS zircon geochronology of coeval mafic–felsic magmatism related to the Major Gercino Shear Zone. Precambrian Research 216-219, 132-151. https://doi.org/10.1016/j.precamres.2012.06.015.

Frost, B.R., 1991. Introduction to oxygen fugacity and its petrologic importance. In: Lindsay, D.H. (Ed.), Oxide Minerals: Petrologic and Magnetic Significance. Reviews in Mineralogy and Geochemistry 25, 1-9. https://doi.org/10.1515/9781501508684-004.

Frost, B.R., Barnes, C.G., Collins, W.J., Arculus, R.J., Ellis, D.J., Frost, C.D., 2001. A geochemical classification for granitic rocks. Journal of Petrology 42, 2033-2048. https://doi.org/10.1093/petrology/42.11.2033.

Gao, P., Zheng, Y.F., Zhao, Z.F., 2016. Experimental melts from crustal rocks: a lithochemical constraint on granite petrogenesis. Lithos 266-267, 133-157. https://doi.org/10.1016/j.lithos.2016.10.005.

García-Arias, M., Stevens, G., 2017. Phase equilibrium modelling of granite magma petrogenesis: A. An evaluation of the magma compositions produced by crystal entrainment in the source. Lithos 277, 131-153. https://doi.org/10.1016/j.lithos.2016.09.028.

Gerdes, A., Wörner, G., Henk, A., 2000. Post-collisional granite generation and HT–LP metamorphism by radiogenic heating: the Variscan South Bohemian Batholith. Journal of the Geological Society (London) 157, 577-587. https://doi.org/10.1144/jgs.157.3.577.

Goldstein, S.L., O'Nions, R.K., Hamilton, P.J., 1984. A Sm–Nd isotopic study of atmospheric dusts and particulates from major river systems. Earth and Planetary Science Letters 70, 221-236. https://doi.org/10.1016/0012-821X(84)90007-4.

Goodenough, K.M., Upton, B.G.J., Ellam, R.M., 2002. Long-term memory of subduction processes in the lithospheric mantle: evidence from the geochemistry of basic dykes in the Gardar Province of South Greenland. Journal of the Geological Society (London) 159, 705-714. https://doi.org/10.1144/0016-764901-154.

Goscombe, B., Gray, D.R., 2007. The Coastal Terrane of the Kaoko Belt, Namibia: outboard arc-terrane and tectonic significance. Precambrian Research 155, 139-158. https://doi.org/10.1016/j.precamres.2007.01.008.

Goscombe, B.D., Gray, D.R., 2008. Structure and strain variation at mid-crustal levels in a transpressional orogen: a review of Kaoko Belt structure and the character of West Gondwana amalgamation and dispersal. Gondwana Research 13, 45-85. https://doi.org/10.1016/j.gr.2007.07.002.

Harris, N.B.W., Pearce, J.A., Tindle, A.G., 1986. Geochemical characteristics of collision-zone magmatism. In: Coward, M.P., Ries, A.C. (Eds.), Collision Tectonics. Geological Society of London Special Publications 19, 67-81. https://doi.org/10.1144/GSL.SP.1986.019.01.04.

Hawkesworth, C., Turner, S., Gallagher, K., Hunter, A., Bradshaw, T., Rogers, N., 1995. Calc-alkaline magmatism, lithospheric thinning and extension in the Basin and Range. Journal of Geophysical Research: Solid Earth 100, 10271-10286. https://doi.org/10.1029/94JB02508.

Heine, C., Zoethout, J., Müller, R.D., 2013. Kinematics of the South Atlantic rift. Solid Earth 4, 215-253. https://doi.org/10.5194/se-4-215-2013.

Hoffman, P.F., Halverson, G.P., Schrag, D.P., Higgins, J.A., Domack, E.W., Macdonald, F.A., Pruss, S.B., Blättler, C.E., Crockford, P.W., Hodgin, E.B., Bellefroid, E.J., Johnson, B.W., Hodgskiss, M.S.W., Lamothe, K.G., LoBianco, S.J.C., Busch, J.F., Howes, B.J., Greenman, J.W., Nelson, L.L., 2021. Snowballs in Africa: sectioning a long-lived Neoproterozoic carbonate platform and its bathyal foreslope (NW Namibia). Earth-Science Reviews 219, 103616. https://doi.org/10.1016/j.earscirev.2021.103616.

Hoskin, P.W.O., Kinny, P.D., Wyborn, D., Chappell, B.W., 2000. Identifying accessory mineral saturation during differentiation in granitoid magmas: an integral approach. Journal of Petrology 41, 1365-1396. https://doi.org/10.1093/petrology/41.9.1365.

Irvine, T.N., Baragar, W.R.A., 1971. A guide to the chemical classification of the common volcanic rocks. Canadian Journal of Earth Sciences 8, 523-548. https://doi.org/10.1139/e71-055.

Jacob, J.B., Moyen, J.F., Fiannacca, P., Laurent, O., Bachmann, O., Janoušek, V., Farina, F., Villaros, A., 2021. Crustal melting vs. fractionation of basaltic magmas: Part 2, Attempting to quantify mantle and crustal contributions in granitoids. Lithos 402–403, 106292. https://doi.org/10.1016/j.lithos.2021.106292.

Janasi, V.A., Heaman, L.M., Shaulis, B., Stern, R., Bitencourt, M.F., Martins, L., 2015. Low-$\delta^{18}O$ shallow-level Neoproterozoic A-type granites from the Florianópolis Batholith, south Brazil. In: The 8th Hutton Symposium on Granites and Related Rocks. Florianópolis, Brazil, September 20–25th, 2015.

Janoušek, V., Konopásek, J., Ulrich, S., Erban, V., Tajčmanová, L., Jeřábek, P., 2010. Geochemical character and petrogenesis of Pan-African Amspoort suite of the Boundary Igneous Complex in the Kaoko Belt (NW Namibia). Gondwana Research 18, 688-707. https://doi.org/10.1016/j.gr.2010.02.014.

Janoušek, V., Moyen, J.F., Martin, H., Erban, V., Farrow, C., 2016. Geochemical Modelling of Igneous Processes – Principles and Recipes in R Language. Bringing the Power of R to a Geochemical Community. Springer-Verlag, Berlin, Heidelberg. https://doi.org/ 10.1007/978-3-662-46792-3.

Janoušek, V., Jiang, Y.D., Buriánek, D., Schulmann, K., Hanžl, P., Soejono, I., Kröner, A., Altanbaatar, B., Erban, V., Lexa, O., Ganchuluun, T., Košler, J., 2018. Cambrian–Ordovician magmatism of the Ikh-Mongol Arc System exemplified by the Khantaishir Magmatic Complex (Lake Zone, south-central Mongolia). Gondwana Research 54, 122-149. https://doi.org/10.1016/j.gr.2017.10.003.

Kemp, A.I.S., Hawkesworth, C.J., 2003. Granitic perspectives on the generation and secular evolution of the continental crust. In: Holland, H.D., Turekian, K.K. (Eds.), Treatise on Geochemistry vol. 3, The Crust (ed. R.L. Rudnick). Elsevier-Pergamon, Oxford, 349-410.

Kiss, D., Podladchikov, Y., Duretz, T., Schmalholz, S.M., 2019. Spontaneous generation of ductile shear zones by thermal softening: localization criterion, 1D to 3D modelling and application to the lithosphere. Earth and Planetary Science Letters 519, 284-296. https://doi.org/10.1016/j.epsl.2019.05.026.

Koester, E., Porcher, C.C., Pimentel, M.M., Fernandes, L.A.D., Vignol-Lelarge, M.L., Oliveira, L.D., Ramos, R.C., 2016. Further evidence of 777 Ma subduction-related continental arc magmatism in Eastern Dom Feliciano Belt, southern Brazil: the Chácara das Pedras Orthogneiss. Journal of South American Earth Sciences 68, 155-166. https://doi.org/10.1016/j.jsames.2015.12.006.

Koester, E., Bertotti, A.L., Porcher, C., Lenz, C., Triboli Vieira, D., Dal Olmo-Barbosa, L., Ramos, R., Andrade Bastos, V., Pinto, V., 2021. A evoluçao crustal do Escudo Sul–Rio-Grandense sob a perspectiva dos sistemas isotópicos Sr–Nd. In: Jelinek, A.R., Sommer, C.A. (Eds.), Contribuiçoes a Geologia do Rio Grande do Sul e de Santa Catarina. Sociedade Brasileira de Geologia, Porto Alegre, 13-27.

Konopásek, J., Košler, J., Tajčmanová, L., Ulrich, S., Kitt, S.L., 2008. Neoproterozoic igneous complex emplaced along major tectonic boundary in the Kaoko Belt (NW Namibia): ion probe and LA-ICP-MS dating of magmatic and metamorphic zircons. Journal of the Geological Society (London) 165, 153-165. https://doi.org/10.1144/0016-76492006-192.

Konopásek, J., Sláma, J., Košler, J., 2016. Linking the basement geology along the Africa–South America coasts in the South Atlantic. Precambrian Research 280, 221-230. https://doi.org/10.1016/j.precamres.2016.05.011.

Konopásek, J., Hoffmann, K. H., Sláma, J., Košler, J., 2017. The onset of flysch sedimentation in the Kaoko Belt (NW Namibia) – implications for the pre-collisional evolution of the Kaoko–Dom Feliciano–Gariep Orogen. Precambrian Research 298, 220-234. https://doi.org/ 10.1016/j.precamres.2017.06.017.

Konopásek, J., Janoušek, V., Oyhantçabal, P., Sláma, J., Ulrich, S., 2018. Did the circum-Rodinia subduction trigger the Neoproterozoic rifting along the Congo–Kalahari Craton margin? International Journal of Earth Sciences 107, 1859-1894. https://doi.org/10.1007/s00531-017-1576-4.

Konopásek, J., Cavalcante, C., Fossen, H., Janoušek, V., 2020. Adamastor – an ocean that never existed? Earth-Science Reviews 205, 103201. https://doi.org/10.1016/j.earscirev.2020.103201.

Kröner, S., Konopásek, J., Kröner, A., Passchier, C.W., Poller, U., Wingate, M.T.D., Hofmann, K.H., 2004. U–Pb and Pb–Pb zircon ages for metamorphic rocks in the Kaoko Belt of northwestern Namibia: a Palaeo- to Mesoproterozoic basement reworked during the Pan-African Orogeny. South African Journal of Geology 107, 455-476. https://doi.org/10.2113/107.3.455.

Lara, P., Oyhantçabal, P., Belousova, E., 2020. Two distinct crustal sources for Late Neoproterozoic granitic magmatism across the Sierra Ballena Shear Zone, Dom Feliciano Belt, Uruguay: whole-rock geochemistry, zircon geochronology and Sr–Nd–Hf isotope evidences. Precambrian Research 341, 105625. https://doi.org/10.1016/j.precamres.2020.105625.

Laurent, O., Martin, H., Moyen, J.F., Doucelance, R., 2014. The diversity and evolution of late-Archean granitoids: evidence for the onset of 'modern-style' plate tectonics between 3.0 and 2.5 Ga. Lithos 205, 208-235. https://doi.org/10.1016/j.lithos.2014.06.012.

Leake, B.E., Woolley, A.R., Arps, C.E.S., Birch, W.D., Gilbert, M.C., Grice, J.D., Hawthorne, F.C., Kato, A., Kisch, H.J., Krivovichev, V.G., Linthout, K., Laird, J., Mandarino, J., Maresch, W.V., Nickel, E.H., Rock, N.M.S., Schumacher, J.C., Smith, J.C., Stephenson, N.C.N., Whittaker, E.J.W., Youzhi, G., 1997. Nomenclature of amphiboles: report of the Subcommittee on Amphiboles of the International Mineralogical Association Commission on New Minerals and Mineral Names. Mineralogical Magazine 61, 295-321. https://doi.org/10.1180/minmag.1997.061.405.13.

Lenz, C., Fernandes, L.A.D., McNaughton, N.J., Porcher, C.C., Masquelin, H., 2011. U–Pb SHRIMP ages for the Cerro Bori orthogneisses, Dom Feliciano Belt in Uruguay: evidences of a ~800 Ma magmatic and ~650 Ma metamorphic event. Precambrian Research 185, 149-163. https://doi.org/10.1016/j.precamres.2011.01.007.

Liew, T.C., Hofmann, A.W., 1988. Precambrian crustal components, plutonic associations, plate environment of the Hercynian Fold Belt of Central Europe: indications from a Nd and Sr isotopic study. Contributions to Mineralogy and Petrology 98, 129-138. https://doi.org/10.1007/BF00402106.

Martil, M.M.D., Bitencourt, M.F., Nardi, L.V.S., Koester, E., Pimentel, M.M., 2017. Pre-collisional, Neoproterozoic (ca. 790 Ma) continental arc magmatism in southern Mantiqueira Province, Brazil: geochemical and isotopic constraints from the Várzea do Capivarita Complex. Lithos 274-275, 39-52. https://doi.org/10.1016/j.lithos.2016.11.011.

Masberg, P., Mihm, D., Jung, S., 2005. Major and trace element and isotopic (Sr, Nd, O) constraints for Pan-African crustally contaminated grey granite gneisses from the southern Kaoko Belt, Namibia. Lithos 84, 25-50. https://doi.org/10.1016/j.lithos.2005.02.001.

Masquelin, H., D'Avila Fernandes, L.A., Lenz, C., Porcher, C.C., McNaughton, N.J., 2012. The Cerro Olivo Complex: a pre-collisional Neoproterozoic magmatic arc in Eastern Uruguay. International Geology Review 54, 1161-1183. https://doi.org/doi: 10.1080/00206814.2011.626597.

Miller, C.F., Mittlefehldt, D.W., 1984. Extreme fractionation in felsic magma chambers; a product of liquid-state diffusion or fractional crystallization? Earth and Planetary Science Letters 68, 151-158. https://doi.org/10.1016/0012-821X(84)90147-X.

Moyen, J.F., Janoušek, V., Laurent, O., Bachmann, O., Jacob, J.B., Farina, F., Fiannacca, P., Villaros, A. 2021. Crustal melting vs. fractionation of basaltic magmas: Part 1, Granites and paradigms. Lithos 402–403, 106291. https://doi.org/10.1016/j.lithos.2021.106291.

Müntener, O., Ulmer, P., Blundy, J.D., 2021. Superhydrous arc magmas in the Alpine context. Elements 17, 35-40. https://doi.org/10.2138/gselements.17.1.35.

Nardi, L.V.S., Bitencourt, M.F., 1993. Tholeiitic, late-orogenic basic magmatism in the region of Porto Belo, southern Brazil. In: Noronha, F., Marques, M., Nogueira, P. (Eds.), IX Semana de Geoquímica e II

Congresso de Geoquímica dos Países de Língua Portuguesa, 14–20 de Novembro de 1993. Universidade do Porto, Porto, 131-135.

O'Connor, J.T., 1965. A classification for quartz-rich igneous rocks based on feldspar ratios. In: US Geological Survey Professional Paper B525. USGS, 79–84. https://doi.org/10.3133/pp525B.

Ohta, T., Arai, H., 2007. Statistical empirical index of chemical weathering in igneous rocks: a new tool for evaluating the degree of weathering. Chemical Geology 240, 280-297. https://doi.org/10.1016/j.chemgeo.2007.02.017.

Oyhantçabal, P., Siegesmund, S., Wemmer, K., Frei, R., Layer, P., 2007. Post-collisional transition from calc-alkaline to alkaline magmatism during transcurrent deformation in the southernmost Dom Feliciano Belt (Braziliano–Pan-African, Uruguay). Lithos 98, 141-159. https://doi.org/10.1016/j.lithos.2007.03.001.

Oyhantçabal, P., Siegesmund, S., Wemmer, K., Presnyakov, S., Layer, P., 2009. Geochronological constraints on the evolution of the southern Dom Feliciano Belt (Uruguay). Journal of the Geological Society (London) 166, 1075-1084. https://doi.org/10.1016/j.lithos.2007.03.001.

Pearce, J.A., 1996. Sources and settings of granitic rocks. Episodes 19, 120-125. https://doi.org/10.18814/epiiugs/1996/v19i4/005.

Pearce, J.A., 2014. Immobile element fingerprinting of ophiolites. Elements 10, 101-108. https://doi.org/10.2113/gselements.10.2.101.

Pearce, J.A, Peate, D.W., 1995. Tectonic implications of the composition of volcanic arc magmas. Annual Review of Earth and Planetary Sciences 23, 251-285. https://doi.org/ 10.1146/annurev.ea.23.050195.001343.

Pearce, J.A., Harris, N.B.W., Tindle, A.G., 1984. Trace element discrimination diagrams for the tectonic interpretation of granitic rocks. Journal of Petrology 25, 956–983. https://doi.org/10.1093/petrology/25.4.956.

Peccerillo, A., Taylor, S.R., 1976. Geochemistry of Eocene calc-alkaline volcanic rocks from the Kastamonu area, Northern Turkey. Contributions to Mineralogy and Petrology 58, 63-81. https://doi.org/ 10.1007/BF00384745.

Percival, J.J., Konopásek, J., Eiesland, R., Sláma, J., De Campos, R.S., Battisti, M.A., Bitencourt, M.F., 2021. Pre-orogenic connection of the foreland domains of the Kaoko–Dom Feliciano–Gariep orogenic system. Precambrian Research 354, 106060. https://doi.org/10.1016/j.precamres.2020.106060.

Percival, J.J., Konopásek, J., Anczkiewicz, R., Ganerød, M., Sláma, J., De Campos, R.S., Bitencourt, M.F., 2022. Tectono-metamorphic evolution of the northern Dom Feliciano Belt foreland, Santa Catarina, Brazil: implications for models of subduction-driven orogenesis. Tectonics 41, e2021TC007014. https://doi.org/10.1029/2021TC007014.

Peruchi, F.M., Florisbal, L.M., Bitencourt, M.F., Padilha, D.F., Nardi, L.V.S. 2021. Ediacaran post-collisional K-rich granitic magmatism within the Major Gercino Shear Zone, southern Brazil: an example of prolonged magmatism and differentiation under active transcurrent tectonism. Lithos 402–403, 106341. https://doi.org/10.1016/j.lithos.2021.106341.

Philipp, R.P., Machado, R., 2005. The Late Neoproterozoic granitoid magmatism of the Pelotas Batholith, southern Brazil. Journal of South American Earth Sciences 19, 461-478. https://doi.org/10.1016/j.jsames.2005.06.010.

Pin, C., Binon, M., Belin, J.M., Barbarin, B., Clemens, J.D., 1990. Origin of microgranular enclaves in granitoids – equivocal Sr–Nd evidence from Hercynian rocks in the Massif Central (France). Journal of Geophysical Research 95, 17821-17828. https://doi.org/10.1029/JB095iB11p17821.

Porada, H., 1979. The Damara–Ribeira Orogen of the Pan-African/Brasiliano Cycle in Namibia (South-West Africa) and Brazil as interpreted in terms of continental collision. Tectonophysics 57, 237-265. https://doi.org/10.1016/0040-1951(79)90150-1.

Putirka, K., 2016. Amphibole thermometers and barometers for igneous systems and some implications for eruption mechanisms of felsic magmas at arc volcanoes. American Mineralogist 101, 841-858. https://doi.org/10.2138/am-2016-5506.

Rapp, R.P., Watson, E.B., 1995. Dehydration melting of metabasalt at 8–32 kbar: implications for continental growth and crust–mantle recycling. Journal of Petrology 36, 891-931. https://doi.org/10.1093/petrology/36.4.891.

Rapp, R.P., Watson, E.B., Miller, C.F., 1991. Partial melting of amphibolite/eclogite and the origin of Archean trondhjemites and tonalites. Precambrian Research 51, 1-25. https://doi.org/10.1016/0301-9268(91)90092-O.

Richter, M., Nebel, O., Maas, R., Mather, B., Nebel-Jacobsen, Y., Capitanio, F.A., Dick, H.J.B., Cawood, P.A., 2020. An Early Cretaceous subduction-modified mantle underneath the ultraslow spreading Gakkel Ridge, Arctic Ocean. Science Advances 6, eabb4340. https://doi.org/10.1126/sciadv.abb4340.

Ridolfi, F., Renzulli, A., 2012. Calcic amphiboles in calc-alkaline and alkaline magmas: thermobarometric and chemometric empirical equations valid up to 1,130 °C and 2.2 GPa. Contributions to Mineralogy and Petrology 163, 877-895. https://doi.org/10.1007/s00410-011-0704-6.

Roberts, M.P., Clemens, J.D., 1993. Origin of high-potassium, calc-alkaline, I-type granitoids. Geology 21, 825-828. https://doi.org/10.1130/0091-7613(1993)021<0825:OOHPTA>2.3.CO;2.

Robinson, J.A., Wood, B.J., 1998. The depth of the spinel to garnet transition at the peridotite solidus. Earth and Planetary Science Letters 164, 277-284. https://doi.org/10.1016/S0012-821X(98)00213-1.

Rudnick, R.L., Gao, S., 2003. The composition of the continental crust. In: Holland, H.D., Turekian, K.K. (Eds.), Treatise on Geochemistry vol. 3, The Crust (ed. R.L. Rudnick). Elsevier-Pergamon, Oxford, 1-64.

Santos, E.A., Sommer, C.A., Waichel, B.L., Haag, M.B., 2019. Ediacaran post-collisional high-silica volcanism associated to the Florianópolis Batholith, Dom Feliciano Belt, southernmost Brazil: lithofacies analysis and petrology. Journal of South American Earth Sciences 96, 102299. https://doi.org/10.1016/j.jsames.2019.102299.

Seth, B., Kröner, A., Mezger, K., Nemchin, A.A., Pidgeon, R.T., Okrusch, M., 1998. Archaean to Neoproterozoic magmatic events in the Kaoko Belt of NW Namibia and their geodynamic significance. Precambrian Research 92, 341-363. https://doi.org/10.1016/S0301-9268(98)00086-2.

Silva, L.C., McNaughton, N.J., Hartmann, L.A., Fletcher, I.R., 2003. Contrasting zircon growth patterns in Neoproterozoic granites of southern Brazil revealed by SHRIMP U–Pb analyses and SEM imaging: consequences for the discrimination of emplacement and inheritance ages. In: IV South American Symposium on Isotope Geology, Salvador. Short Papers, CBPM 2, pp. 687–690.

Sisson, T.W., Grove, T.L., 1993. Temperatures and H_2O contents of low-MgO high-alumina basalts. Contributions to Mineralogy and Petrology 113, 167-184. https://doi.org/10.1007/BF00283226.

Sun, S.S., McDonough, W.F., 1989. Chemical and isotopic systematics of oceanic basalts: implications for mantle composition and processes. In: Saunders, A.D., Norry, M. (Eds.), Magmatism in the Ocean Basins. Geological Society of London Special Publications 42, 313-345. https://doi.org/10.1144/GSL.SP.1989.042.01.19.

Tatsumi, Y., Eggins, S., 1995. Subduction Zone Magmatism. Frontiers in Earth Sciences, Blackwell, Cambridge, Mass.

Taylor, S.R., McLennan, S.M., 1995. The geochemical evolution of the continental crust. Reviews in Geophysics 33, 241-265. https://doi.org/10.1029/95RG00262.

Taylor, S.R., McLennan, S.M., 2009. Planetary Crusts: Their Composition, Origin and Evolution. Cambridge University Press, Cambridge.

Tiepolo, M., Oberti, R., Zanetti, A., Vannucci, R., Foley, S.F., 2007. Trace-element partitioning between amphibole and silicate melt. In: Hawthorne, F.C., Oberti, R., Della Ventura, G., Mottana, A. (Eds.), Amphiboles. Crystal chemistry, Occurrence and Health Issues. Reviews in Mineralogy and Geochemistry 67, 417-452. https://doi.org/10.2138/rmg.2007.67.11.

Tomé, C.R., Bitencourt, M.F., Raposo, M.I.B., Savian, J.F., 2020. Magnetic fabric data on interactive syntectonic magmas of contrasting composition in composite dikes from south Brazil. Journal of Geodynamics 138, 101754. https://doi.org/10.1016/j.jog.2020.101754.

Ulrich, S., Konopásek, J., Jeřábek, P., Tajčmanová, L., 2011. Transposition of structures in the Neoproterozoic Kaoko Belt (NW Namibia) and their absolute timing. International Journal of Earth Sciences 100, 415-429. https://doi.org/10.1007/s00531-010-0573-7.

Urann, B.M., Le Roux, V., Jagoutz, O., Müntener, O., Behn, M.D. Chin, E.J., in print. High water content of arc magmas recorded in cumulates from subduction zone lower crust. Nature Geoscience15, 501-508. https://doi.org/10.1038/s41561-022-00947-w..

Vijaya Kumar, K., Rathna, K., Leelanandam, C., 2015. Proterozoic subduction-related and continental rift-zone mafic magmas from the Eastern Ghats Belt, SE India: geochemical characteristics and mantle sources. Current Science 108, 184-197. http://www.jstor.org/stable/24218157.

Villaseca, C., Barbero, L., Herreros, V., 1998. A re-examination of the typology of peraluminous granite types in intracontinental orogenic belts. Transactions of the Royal Society of Edinburgh, Earth Sciences 89, 113-119. https://doi.org/10.1017/S0263593300007045.

Weinberg, R.F., Hasalová, P., 2015. Water-fluxed melting of the continental crust: a review. Lithos, 212–215: 158-188. https://doi.org/ 10.1016/j.lithos.2014.08.021.

Whitney, D.L., Evans, B.W., 2010. Abbreviations for names of rock-forming minerals. American Mineralogist 95, 185-187. https://doi.org/10.2138/am.2010.3371.

Will, T.M., Gaucher, C., Ling, X.X., Li, X.H., Li, Q.L., Frimmel, H.E., 2019. Neoproterozoic magmatic and metamorphic events in the Cuchilla Dionisio Terrane, Uruguay, and possible correlations across the South Atlantic. Precambrian Research 320, 303-322. https://doi.org/10.1016/j.precamres.2018.11.004.

Wilson, M., 1989. Igneous Petrogenesis. Unwin Hyman, London.

Wolf, M.B., Wyllie, P.J., 1994. Dehydratation-melting of amphibolite at 10 kbar: the effects of temperature and time. Contributions to Mineralogy and Petrology 115, 369-383. https://doi.org/10.1007/BF00320972.

Wood, D.A., 1980. The application of a Th–Hf–Ta diagram to problems of tectonomagmatic classification and to establishing the nature of crustal contamination of basaltic lavas of the British Tertiary volcanic province. Earth and Planetary Science Letters 50, 11-30. https://doi.org/10.1016/0012-821X(80)90116-8.

Xiong, X.L., Adam, J., Green, T.H., 2005. Rutile stability and rutile/melt HFSE partitioning during partial melting of hydrous basalt: implications for TTG genesis. Chemical Geology 218, 339-359. https://doi.org/10.1016/j.chemgeo.2005.01.014.

Yavuz, F., Döner, Z., 2017. WinAmptb: a Windows program for calcic amphibole thermobarometry. Periodico di Mineralogia, 86: 135-167. https://doi.org/10.2451/2017PM710.

Zhang, X.Q., Zhang, H.F., Zou, H., 2020. Rift-related Neoproterozoic tholeiitic layered mafic intrusions at northern Yangtze Block, South China: mineral chemistry evidence. Lithos 356–357, 105376. https://doi.org/10.1016/j.lithos.2020.105376.

Figure captions

Fig. 1a) Simplified geological map of the Kaoko–Dom Feliciano–Gariep orogenic system. The mutual position of the African and South American continents is shown at 140 Ma (after Heine et al., 2013), i.e., at the time of maximum pre-Atlantic crustal stretching and before the formation of first oceanic crust. The position and extent of the map relative to the present-day shape of the African and South American continents is shown in the inset. Abbreviations: AFMC – Angra Fria Magmatic Complex; MV – Montevideo; PA – Porto Alegre; FL – Florianópolis; LÜ – Lüderitz; SW – Swakopmund. (Meta)cratonic domains: 1 – Congo Craton; 2 – Rehoboth Inlier; 3 – Namaqua Metamorphic Complex; 4 – Río de la Plata Craton–Piedra Alta Terrane; 5 – Río de la Plata Craton–Nico Pérez Terrane; 6 – Luis Alves Terrane. **b)** Distribution of U–Pb zircon ages for pre- and syn-/post-orogenic (meta)igneous rocks in the hinterland parts of the Kaoko and Dom Feliciano belts (see ESM 1 for the underlying dataset).

Fig. 2 Left: Satellite image of the Angra Fria Bay in NW Namibia with outlines of geological units presented in the geological map. Right: Geological map of the best accessible part of the Angra Fria Magmatic Complex with locations of studied samples. Note the north point, i.e. that both panels are rotated by ca. 45°. Satellite image: Sentinel-2 data (acquired: 17/02/2020), B8/B4/B3 as RGB.

Fig. 3a) Felsic orthogneiss of the Older Suite with steep fabric and upright folds (left hand side of the photograph). **b)** A close-up of an augen orthogneiss of the Older Suite (sample NP-014). **c)** Enclaves of hornblendite (samples NJ-58, NP-013) in Bt–Amp quartz diorite (samples NJ-59, NP-011) of the Older Suite. **d)** A close-up of a contact between quartz diorite of the Older Suite with strong magmatic/subsolidus fabric (left) and apparently fabric-free granite of the Younger Suite (right). **e)** A close-up of a contact between orthogneiss of the Older Suite (right) and apparently undeformed

granite of the Younger Suite (left). **f)** Swarm of mafic microgranular enclaves in medium-grained amphibole–biotite tonalite (sample NP-009) of the Younger Suite. **g)** Coarse-grained and sparsely porphyritic biotite granite (samples NK-16, NP-021) of the Younger Suite. **h)** Fine-grained mafic dyke (samples NK-26, NP-017) cutting quartz diorite of the Older Suite.

Fig. 4 Back-scattered electron (BSE) images showing textures of the magmatic rocks belonging to the Older (a–d) and Younger (e–h) suites of the Angra Fria Magmatic Complex. **a)** Biotite–titanite–magnetite clot in augengneiss NP-018. **b)** Large amphibole crystals of two generations (Amp1, Amp2) and a secondary assemblage of albite–K-feldspar–chlorite–calcite in hornblendite NP-013. **c)** Two amphibole generations within a single euhedral crystal, quartz diorite NP-012. **d)** Association of epidote with allanite in quartz diorite NP-011. **e)** Subhedral texture of the Amp–Bt tonalite NP-009. **f)** Large, partly altered (biotitized and chloritized) amphibole grain associated with Zrn and Ttn in Amp–Bt granodiorite NP-007. **g)** Muscovite–biotite intergrowth in the granodiorite NP-021. **h)** Large muscovite crystal surrounded by tiny biotite flakes in the leucogranite NP-010. Abbreviations for mineral names are after Whitney and Evans (2010) except for Tiox – Ti-oxide, In b–c are distinguished the two generations of amphibole, older, Si-poor Amp1 and younger, Si-rich Amp2.

Fig. 5 Binary classification diagram Si (apfu) vs. atomic Mg/(Mg + Fe^{2+}) for amphiboles (Leake et al., 1997). **a)** Calcic amphiboles, $(Na + K)_A < 0.5$ apfu. **b)** Calcic amphiboles, $(Na + K)_A \geq 0.5$ apfu. Constraints on magma temperature, oxygen fugacity (fO_2) and H_2O contents based on compositions of primary AFMC amphiboles and empirical model of Ridolfi and Renzulli (2012). **c)** Binary plot of temperature (°C) vs. fO_2. Selected oxygen buffers were plotted using the database of Frost (1991). **d)** Binary plot of temperature (°C) vs. inferred H_2O contents in the magma (wt. %).

Fig. 6 Classification diagrams for plutonic rocks of the Angra Fria Magmatic Complex and Florianópolis Batholith, part 1. **a)** Total alkali–silica (TAS) diagram after Cox et al. (1979) with the alkaline/subalkaline boundary of Irvine and Baragar (1971). **b)** Ternary AFM (A = Na_2O + K_2O, F = FeOt, M = MgO in wt. %) plot after Irvine and Baragar (1971) to distinguish between tholeiitic and calc-alkaline series. **c)** SiO_2 vs. K_2O diagram (Peccerillo and Taylor, 1976) discriminating between the low-K, normal-K, high-K calc-alkaline and shoshonitic rocks. **d)** Multicationic P–Q ('nomenclature') diagram of Debon and Le Fort (1988), where *P* represents the proportion of K-feldspar to plagioclase and *Q* the quartz content. The reference compositions of the twelve petrographic types are also shown as follows: to – tonalite, trondhjemite; gd – granodiorite; ad – adamellite (= monzogranite); gr – granite (= syenogranite); dq – quartz diorite, quartz gabbro, quartz anorthosite; mzdq – quartz monzodiorite, quartz monzogabbro; mzq – quartz monzonite; sq – quartz syenite; go – gabbro, diorite, anorthosite; mzgo – monzogabbro, monzodiorite; mz – monzonite; s – syenite. **e)** Multicationic B–A ('characteristic minerals') plot of the same authors; *B* represents the content of mafic minerals and *A* the balance of aluminium vs. calcium and alkalis (aluminosity). Typical of each of the sectors is a characteristic mineral assemblage; the I, II and III fields are for decreasingly peraluminous rocks [I – muscovite > biotite, II – biotite > muscovite, III – biotite (± minor amphibole)], the IV, V and VI fields for increasingly Al-deficient (metaluminous) rocks (IV – biotite, amphibole, ± clinopyroxene, V – clinopyroxene ± amphibole ± biotite, VI – unusual mineral associations, such as carbonatites]. **f)** Multicationic K/(K + Na) vs. B plot of Debon and Le Fort (1988) to distinguish the sodic/potassic and the mesocratic/subleucocratic/leucocratic associations. Note that the plotting colours for the AFMC reflect silica contents in each of the samples.

Fig. 7 Classification diagrams for plutonic rocks of the Angra Fria Magmatic Complex and Florianópolis Batholith, part 2. **a)** SiO_2 vs. FeOt/(FeOt + MgO). **b)** SiO_2 vs. Modified Alkali–Lime Index (MALI, $Na_2O + K_2O - CaO$). Both diagrams are from Frost et al. (2001) using major-element oxides expressed in wt. %.

Fig. 8 Binary plots of SiO_2 vs. selected major-element oxides (wt. %) and trace elements (ppm). See **Fig. 6** for legend.

Fig. 9 Normal Mid-Ocean Ridge Basalt (NMORB) normalized (Sun and McDonough, 1989) spider plots for the individual plutonic suites from the Angra Fria Magmatic Complex (**a–c**) and Florianópolis Batholith (**d–f**).The grey field in the background shows the total variation in the whole AFMC dataset. The patterns are colour-coded by SiO_2 contents.

Fig. 10a–c Chondrite-normalized (Boynton, 1984) REE spider plots for three age groups of plutonic rocks from the AFMC. The grey field in the background shows the total variation. The patterns for individual samples are colour-coded by SiO_2 contents.

Fig. 11 In-zircon Hf (a) and whole-rock Sr–Nd (b–e) isotopic compositions of the AFMC. **a)** Two-stage Hf evolution diagram for zircons dated and analysed by Konopásek et al. (2016). The crustal Hf model age (T_{DM}^{HfC}) was calculated separately for each zircon grain, assuming a mean crustal $^{176}Lu/^{177}Hf$ ratio of 0.015 for the 2nd stage of the model (Rudnick and Gao, 2003). The Depleted Mantle line is after Belousova et al. (2010), the composition of CHUR from Bouvier et ε_{Nd}^{i} al. (2008). **b)** – Whole-rock $^{87}Sr/^{86}Sr_i$ vs. plot for the AFMC. **c)** Two-stage Nd evolution diagram. DM = Depleted Mantle evolution lines after Goldstein et al. (1984) and Liew and Hofmann (1988). The extra tick marks on the ordinate denote ε_{Nd}^{i} values, on the abscissa two-stage Depleted Mantle model ages, $T_{Nd.2stg}^{DM}$ (Liew and Hofmann, 1988). **d)** Binary plot of SiO_2 (wt. %) vs. $^{87}Sr/^{86}Sr_i$. **(e)** Binary plot of SiO_2 vs. ε_{Nd}^{i}. The whole-rock Sr–Nd isotopic analyses

from the Florianópolis Batholith in (b–e) are from Florisbal et al. (2009) (Paulo Lopes and Garopaba), Florisbal et al. (2012a) (Quatro Ilhas and Mariscal) and Chemale Jr. et al. (2012) (Zimbros, Quatro Ilhas and Mariscal).

Fig. 12 Diagrams to distinguish granitic melts derived from various crustal sources. In a–b, only acid–intermediate samples (SiO_2 > 52 wt. %) from AFMC and FB are plotted. **a**) Binary plot (CaO/(MgO + FeOt) vs. Al_2O_3/(MgO + FeOt) in mol. % after Gerdes et al. (2000). **b**) Ternary plot Al_2O_3/(FeOt + MgO) – 3×CaO – 5×K_2O/Na_2O (wt. %) of Laurent et al. (2014 and references therein) based on compilation of the available experimental data.

Comparison of the AFMC data with experimental melts from Amp- (filled grey symbols) and Amp–Bt-bearing (hollow grey symbols) metaigneous rocks, both fluid-absent (circles) and fluid-present (squares) as compiled by Gao et al. (2016 and references therein). The contours correspond to 25, 50 and 75% of the each experimental dataset. **c–d)** CIPW-normative Ab–An–Or diagram of O'Connor (1965). **e–f)** Total alkali–silica (TAS) diagram after Cox et al. (1979).

Fig. 13 Binary plots underlining the important petrogenetic role played by amphibole or garnet. (**a)** – SiO_2 (wt. %) vs. the La_N/Yb_N ratio. (**b**) – SiO_2 (wt. %) vs. the Dy/Dy* parameter (Davidson et al., 2013); Also shown are trends of fractional crystallization (diamonds) and batch partial melting (triangles) (5% tick interval in both cases) for single mineral phases: amphibole, garnet, and plagioclase. The partition coefficients are the same as used by Janoušek et al. (2018 and references therein).

Fig. 14 Geotectonic diagrams based on whole-rock geochemical compositions of the Angra Fria Magmatic Complex and Florianópolis Batholith. **a**) Triangular plot Th–Hf/3–Nb/16 of Wood (1980). IAT – Island-Arc Tholeiites, CAB – Calc-Alkaline Basalts, N-MORB

– Normal Mid-Ocean Ridge Basalts, E-MORB – Enriched Mid-Ocean Ridge Basalts, WPT – Within-Plate Tholeiites, WPA – Within-Plate Alkali Basalts. **b**) La/10–Y/15–Nb/8 plot of Cabanis and Lecolle (1989), where the Y/Nb serves as the "alkalinity index" and La/Y as the "calc-alkaline index". I – Orogenic, compressive, destructive plate boundaries; II – Late- to post-orogenic (compressive or distensive) intra-continental domains; III – Anorogenic (distensive) inter-plate domains. **c**) Hf–Rb/30–3×Ta ternary diagram (Harris et al., 1986).VA – (Group 1) Pre-collision calc-alkaline (volcanic-arc) intrusions, Group 2 – Syn-collision peraluminous intrusions (leucogranites), Group 3 – Late or post-collision calc-alkaline intrusions, WP – (Group 4) Post-collision alkaline intrusions (within-plate intrusions). **d**) Binary diagram Nb/Yb vs. Th/Yb (Pearce, 2014). The 'MORB–OIB array' is formed by average NMORB, EMORB and OIB compositions are taken from Sun and McDonough (1989); UCC and LCC are average compositions of the upper and lower continental crust (Taylor and McLennan, 1995).

Fig. 15 Schematic cross-sections illustrating the inferred tectonic setting of the Angra Fria and Florianópolis magmatic complexes at the time of intrusion of the Older (ca. 625 Ma) and Younger (ca. 580 Ma) suites of the former (AFMC). **a)** Situation at ca. 625 Ma featuring fully developed fold-and-thrust belt on the South American side and first intrusions of the Florianópolis Batholith along the foreland–hinterland boundary. This time slice also shows the coeval intrusions in the internal parts of the developing hinterland domain, one of them being the Older Suite of the AFMC. **b)** Situation at ca. 580 Ma, during transition to partitioned transpression on the South American side and intrusion of voluminous young magmatic rocks of the Florianópolis Batholith. African side of the orogenic system shows beginning of thrusting of the hinterland over the foreland accompanied by early intrusions along the thrust interface, as well as

continuing magmatic activity in the AFMC represented by the Younger Suite. Syn-orogenic sediments covering the orogenic hinterland and the Kaoko foreland, as well as the ca. 650–630 Ma early intrusions into the hinterland domain are omitted to maintain clarity of the figures.

Abbreviations: IPSZ – Itajaí–Perimbó Shear Zone, MGSZ – Major Gercino Shear Zone, FB – Florianópolis Batholith, AFMC – Angra Fria Magmatic Complex, VSZ – Village Shear Zone, PSZ – Purros Shear Zone.

Table captions

Table 1 Summary of the amphibole-derived melt parameters

Table 2 Sr–Nd isotopic data for the Angra Fria Magmatic Complex

Electronic supplementary material

ESM 1 Overview of the geochronological data from the Florianópolis Batholith and Porto Belo Complex (S Brazil) and Kaoko Belt (NW Namibia)

ESM 2 Sample locations and their GPS coordinates

ESM 3 Analytical techniques

ESM 4 Selected electron-microprobe analyses of the main rock-forming minerals and selected accessories in the rocks of the AFMC

ESM 5 Whole-rock major-element analyses from the AFMC (wt. %)

ESM 6 Whole-rock trace-element analyses from the AFMC (ppm)

ESM 7 Supplementary major-element diagrams. **a)** Ternary plot F–M–W (fresh felsic igneous rocks, fresh mafic igneous rocks and chemical weathering components) of Ohta and Arai (2007). All the AFMC seem reasonably fresh, as they all plot onto the (dashed) igneous rocks trend. **b)** A–B ('characteristic minerals') diagram of Debon and Le Fort (1983, 1988) with a more detailed subdivision of the peraluminous domain proposed by Villaseca

et al. (1998) – l-P: low peraluminous, m-P: moderately peraluminous, h-P: highly peraluminous and f-P: felsic peraluminous. **c)** Multicationic B vs. Mg/(Fe + Mg) diagram (maficity vs. mg#) (Debon and Le Fort 1988).

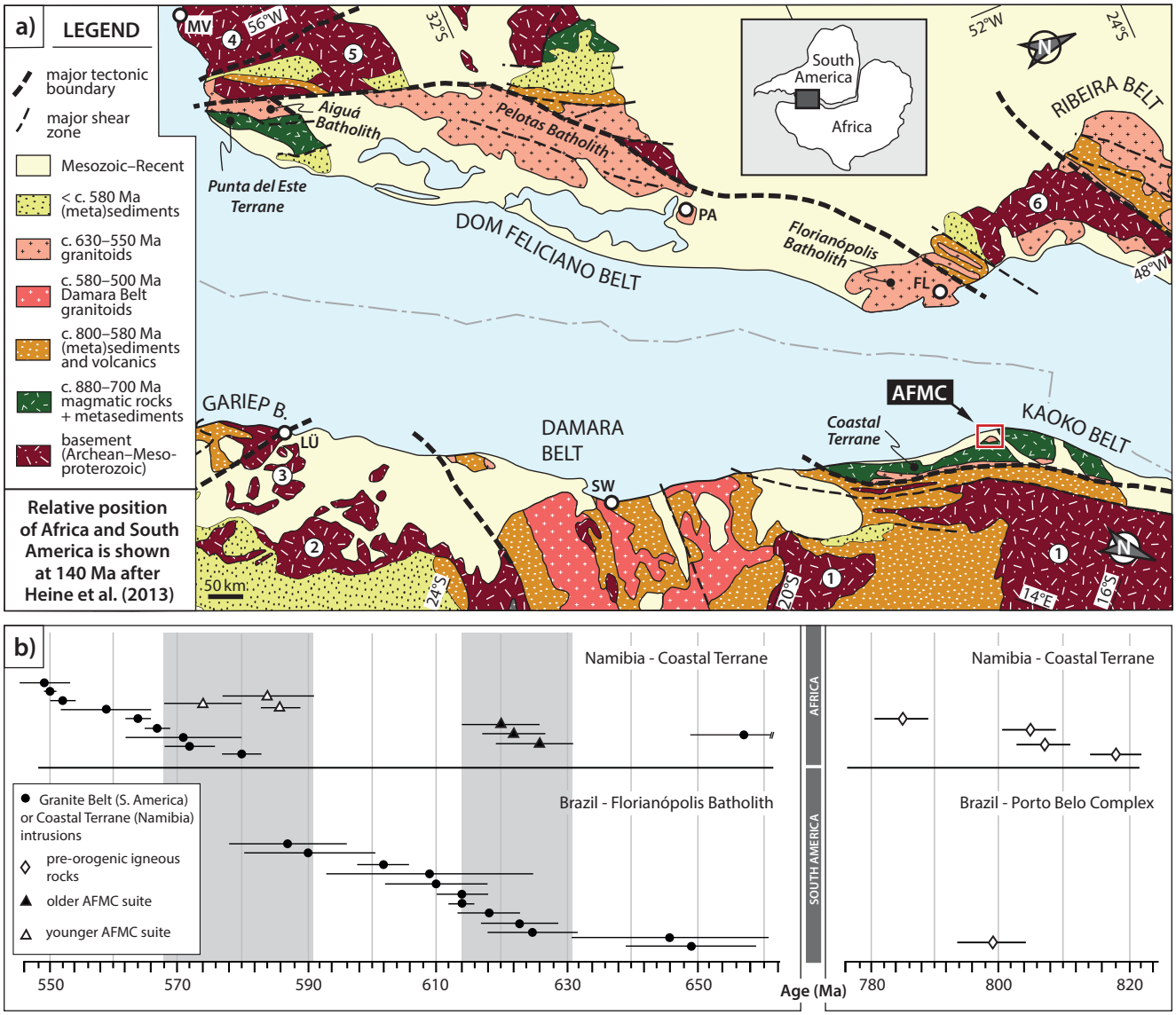

Janoušek et al., Fig. 1
Double column width

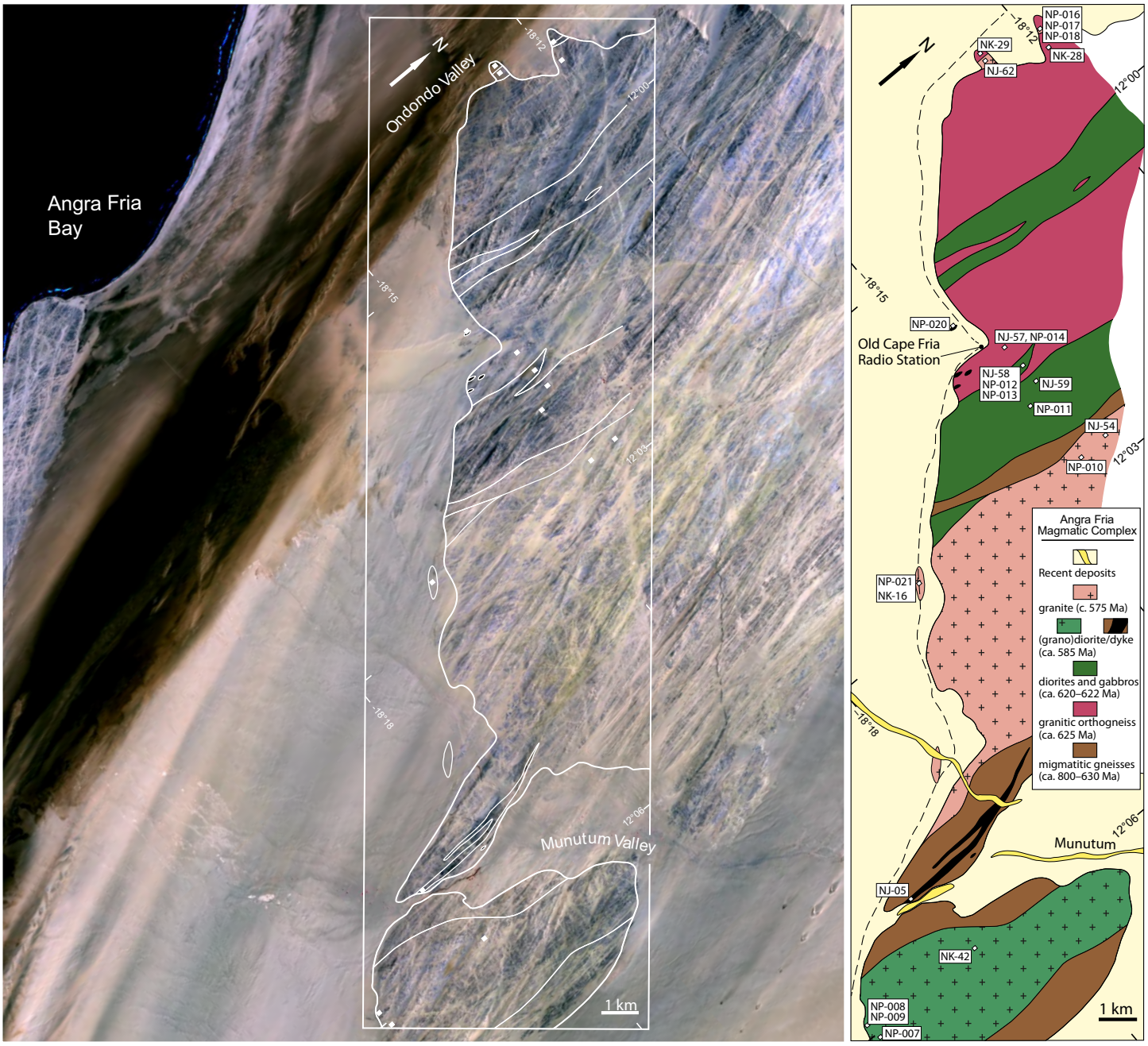

Janoušek et al., Fig. 2
Double column width

Janoušek et al., Fig. 3
Double column width

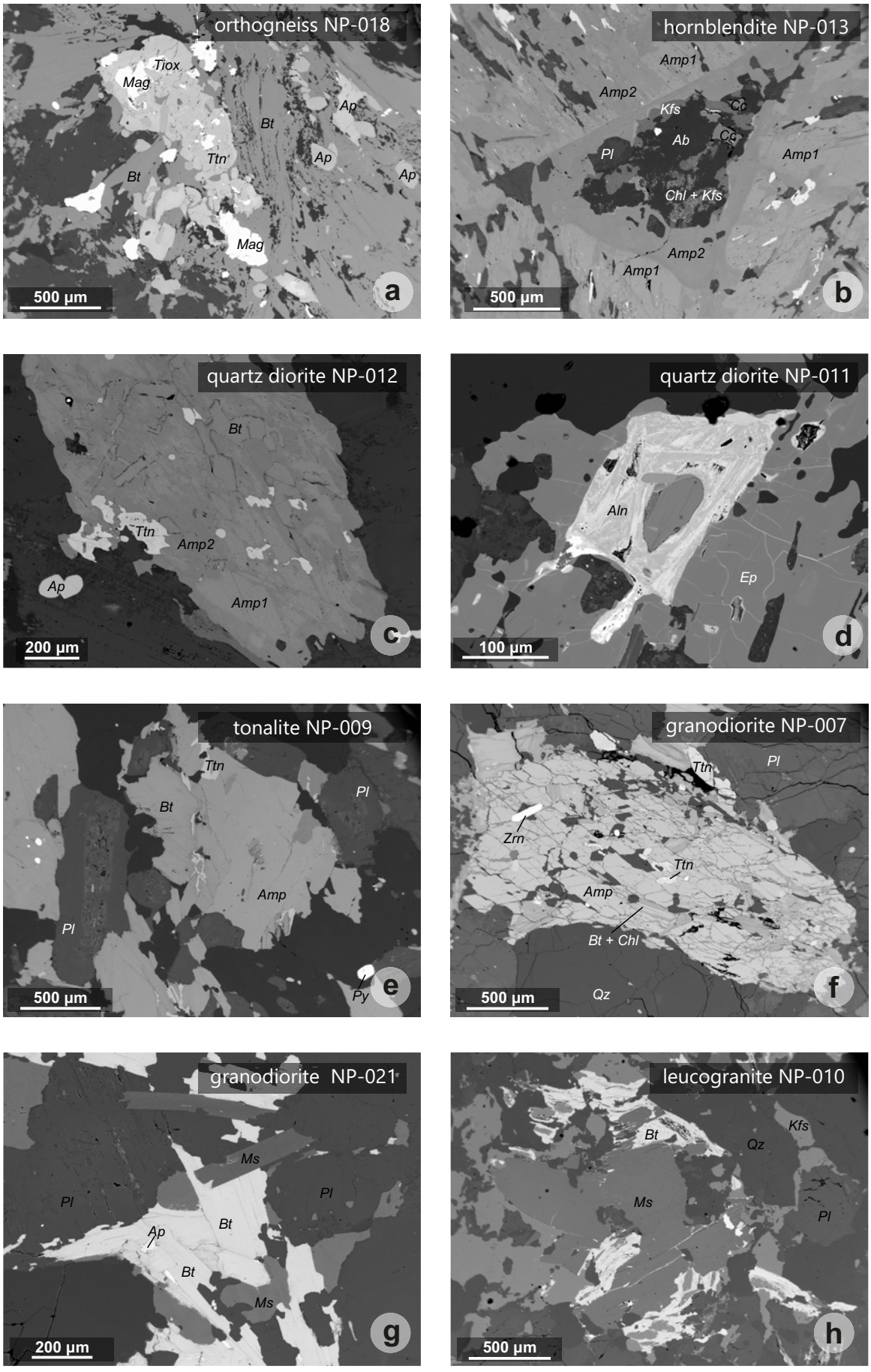

Janoušek et al., Fig. 4
Double column width

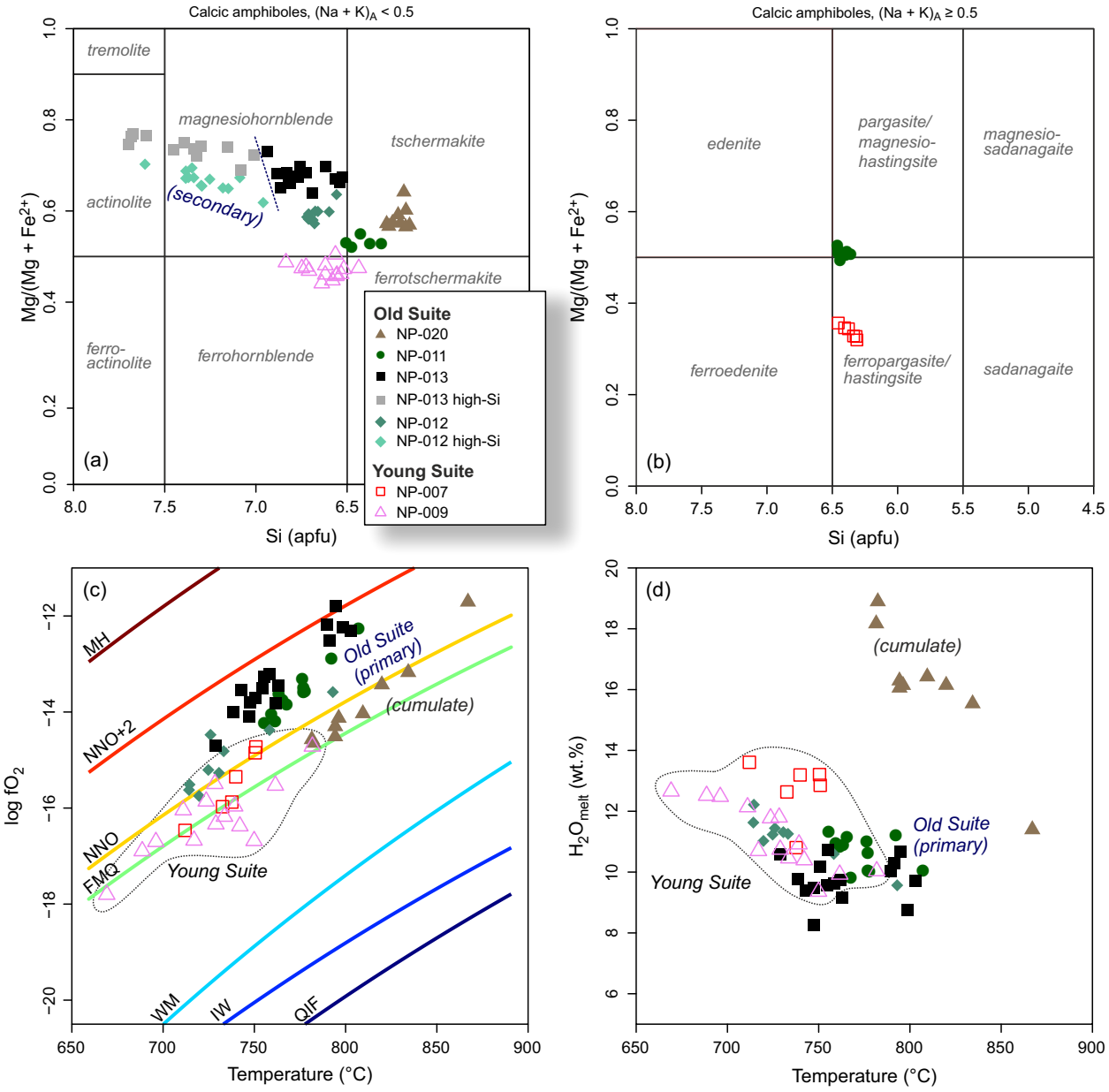

Janoušek et al., Fig. 5
Double column width

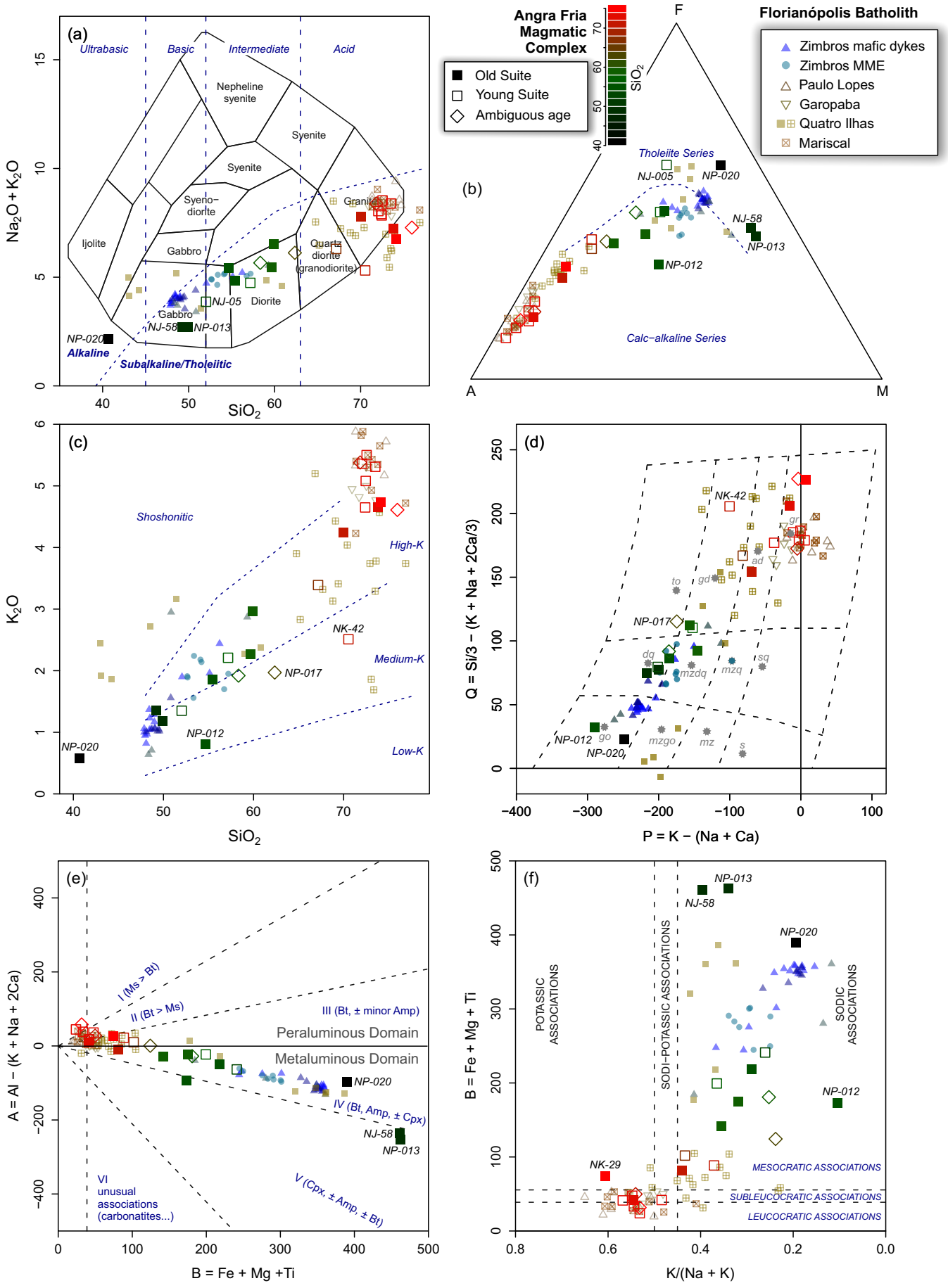

Janoušek et al., Fig. 6
Double column width

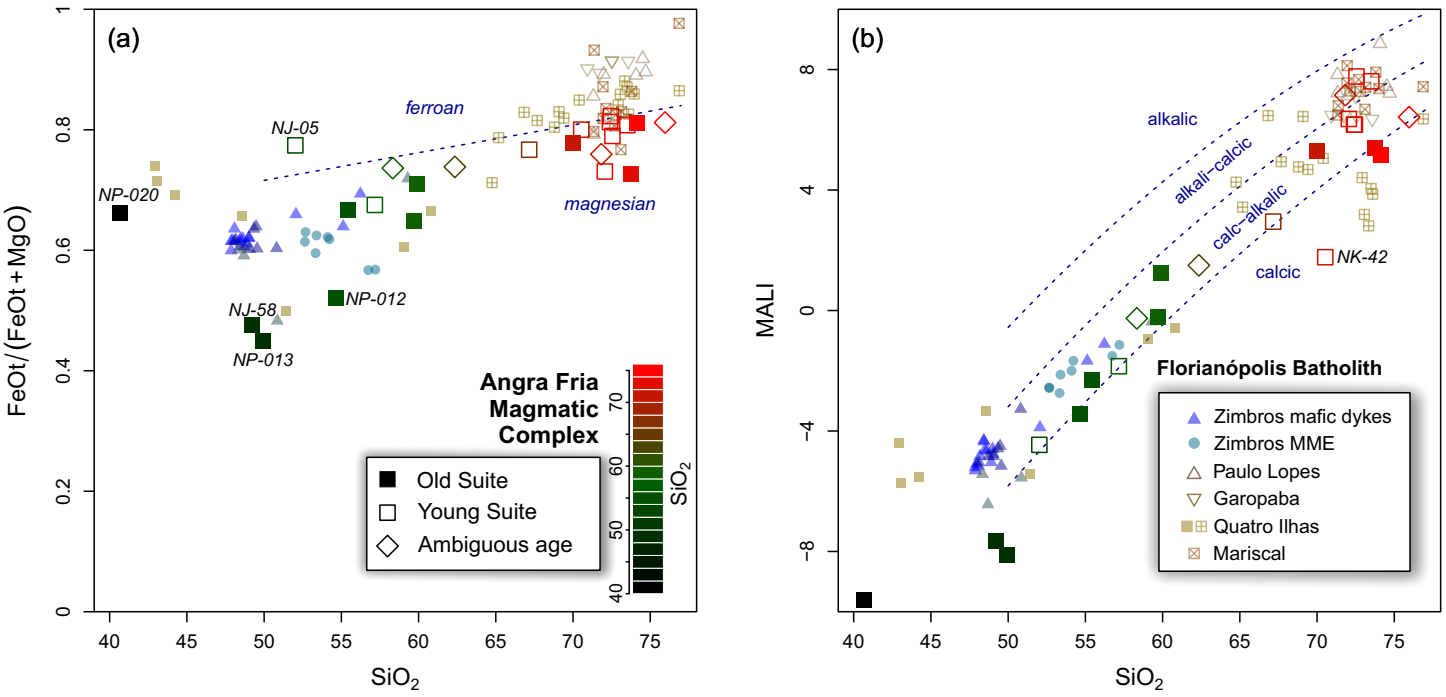

Janoušek et al., Fig. 7
Double column width

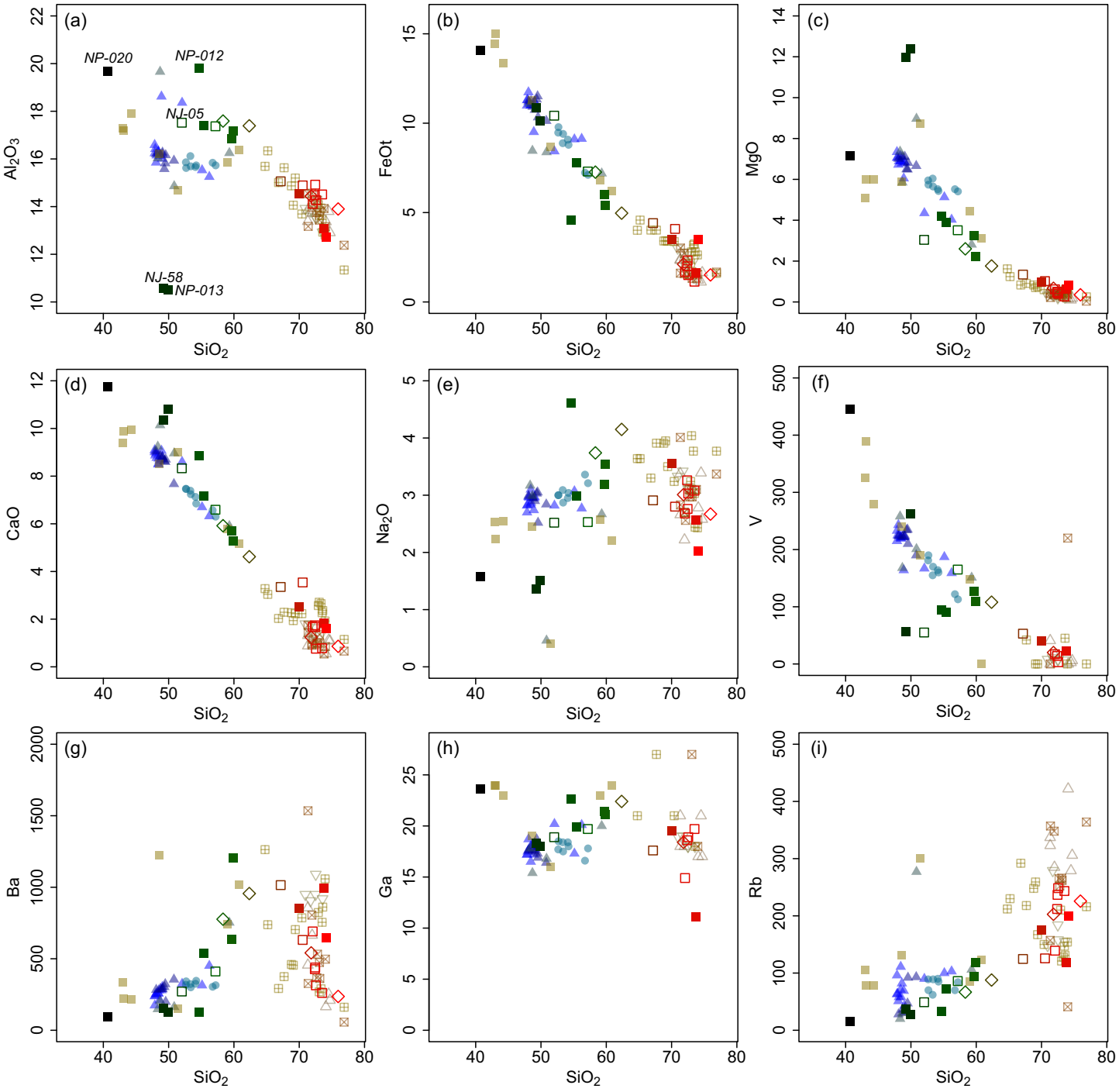

Janoušek et al., Fig. 8
Double column width

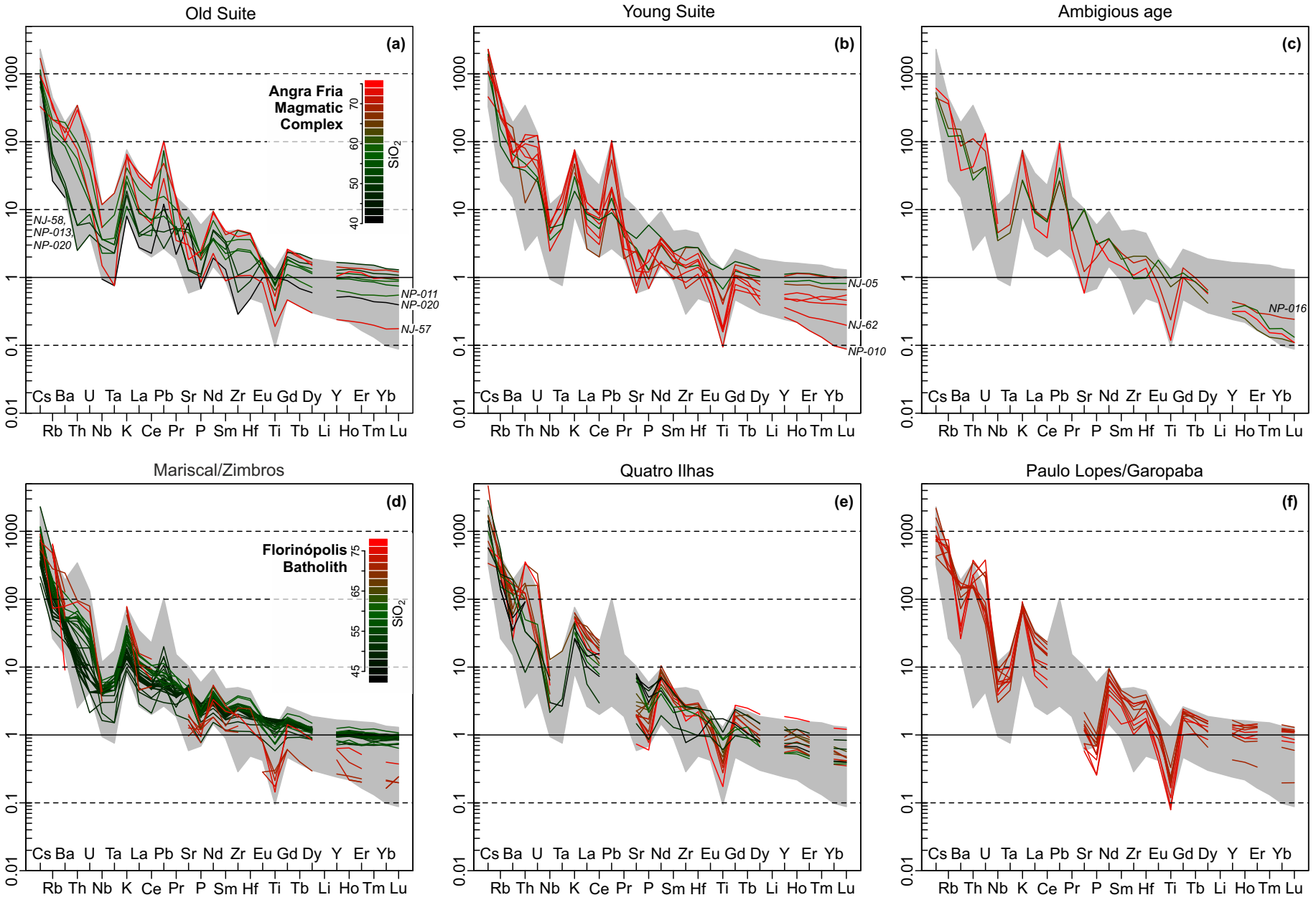

Janoušek et al., Fig. 9
Double column width
Landscape

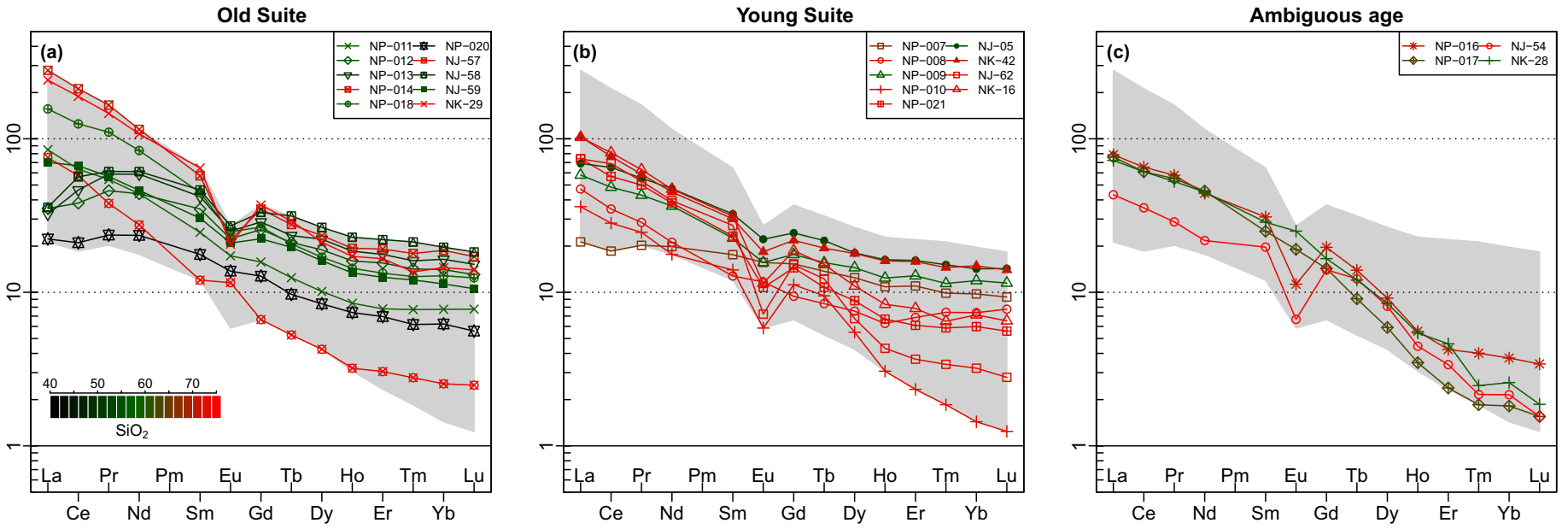

Janoušek et al., Fig. 10
Double column width
Landscape

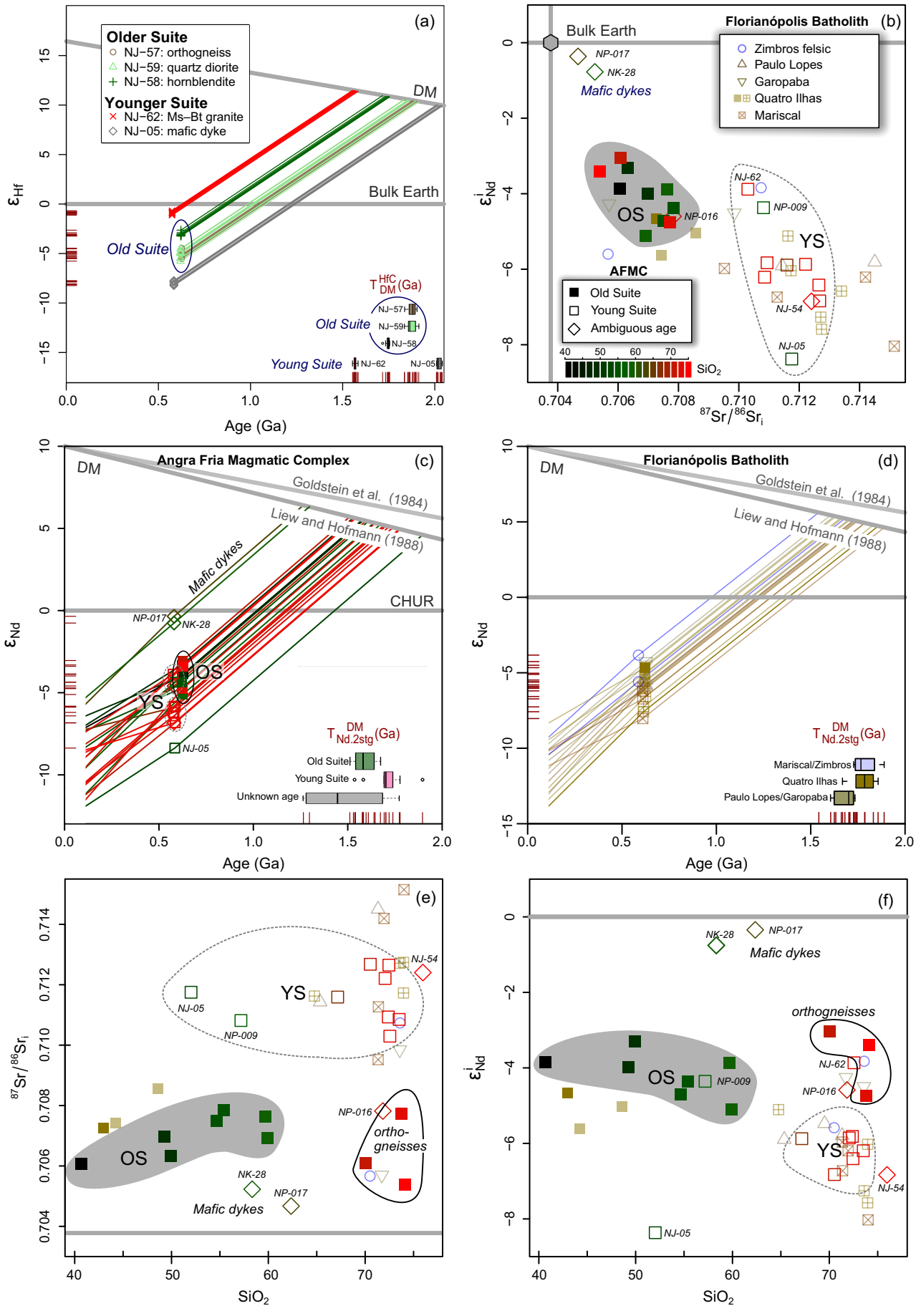

Janoušek et al., Fig. 11
Full page

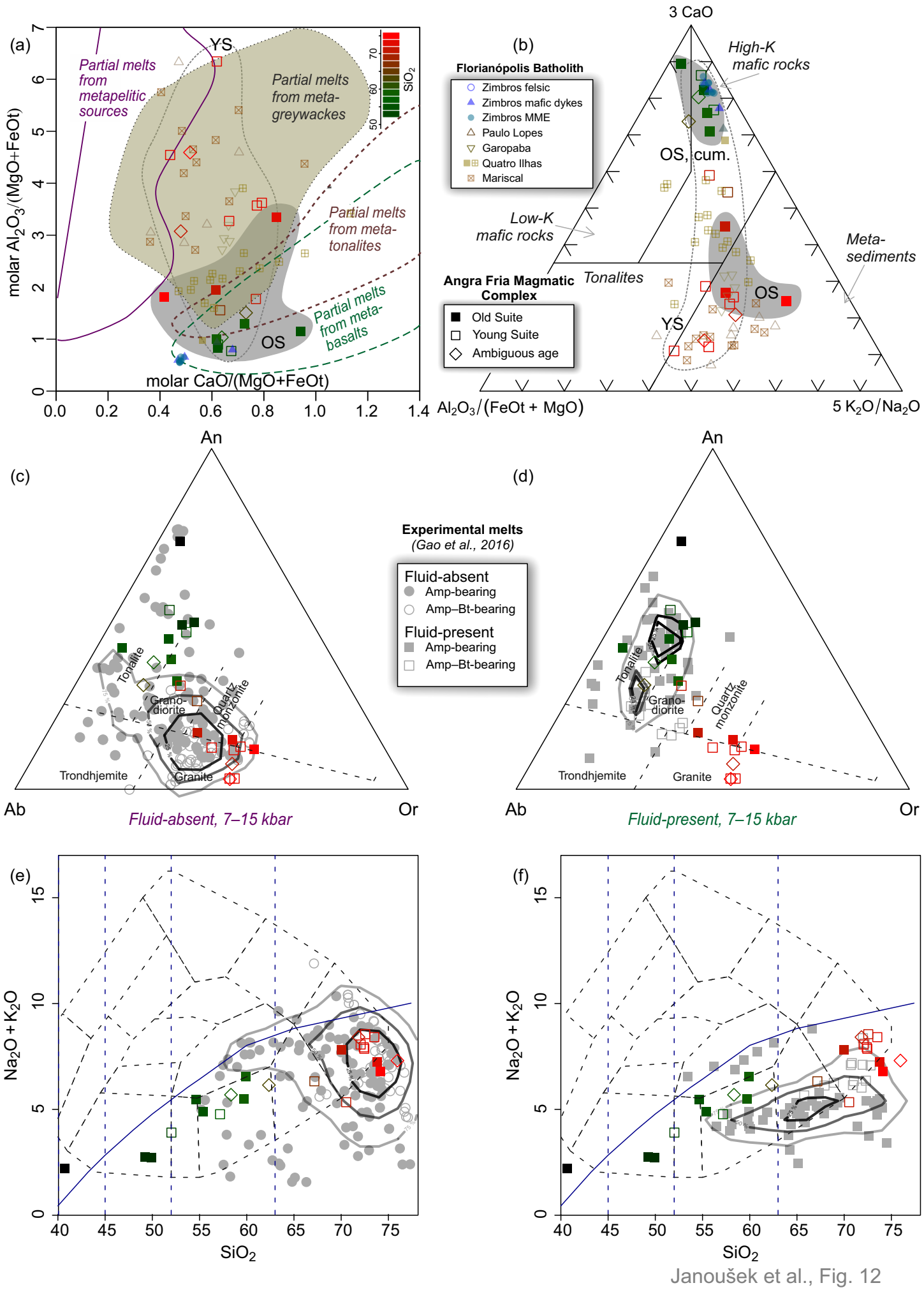

Janoušek et al., Fig. 12
Double column width

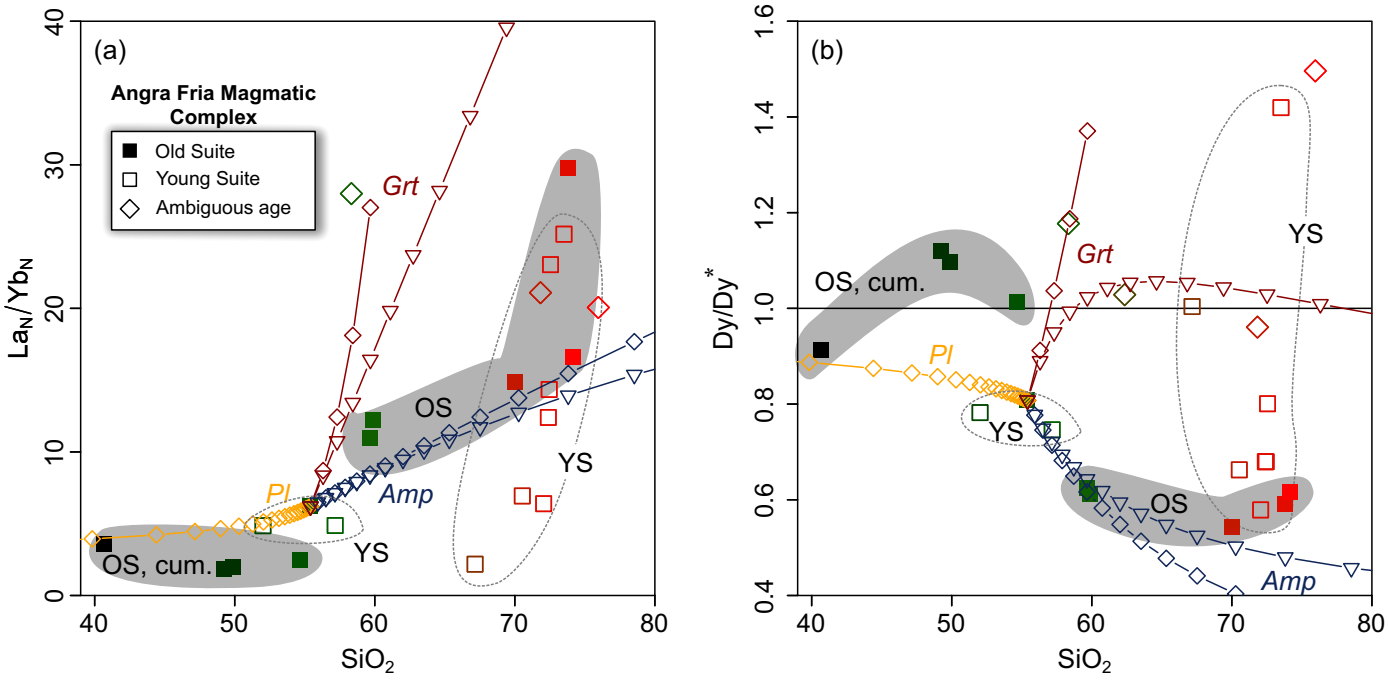

Janoušek et al., Fig. 13
Double column width

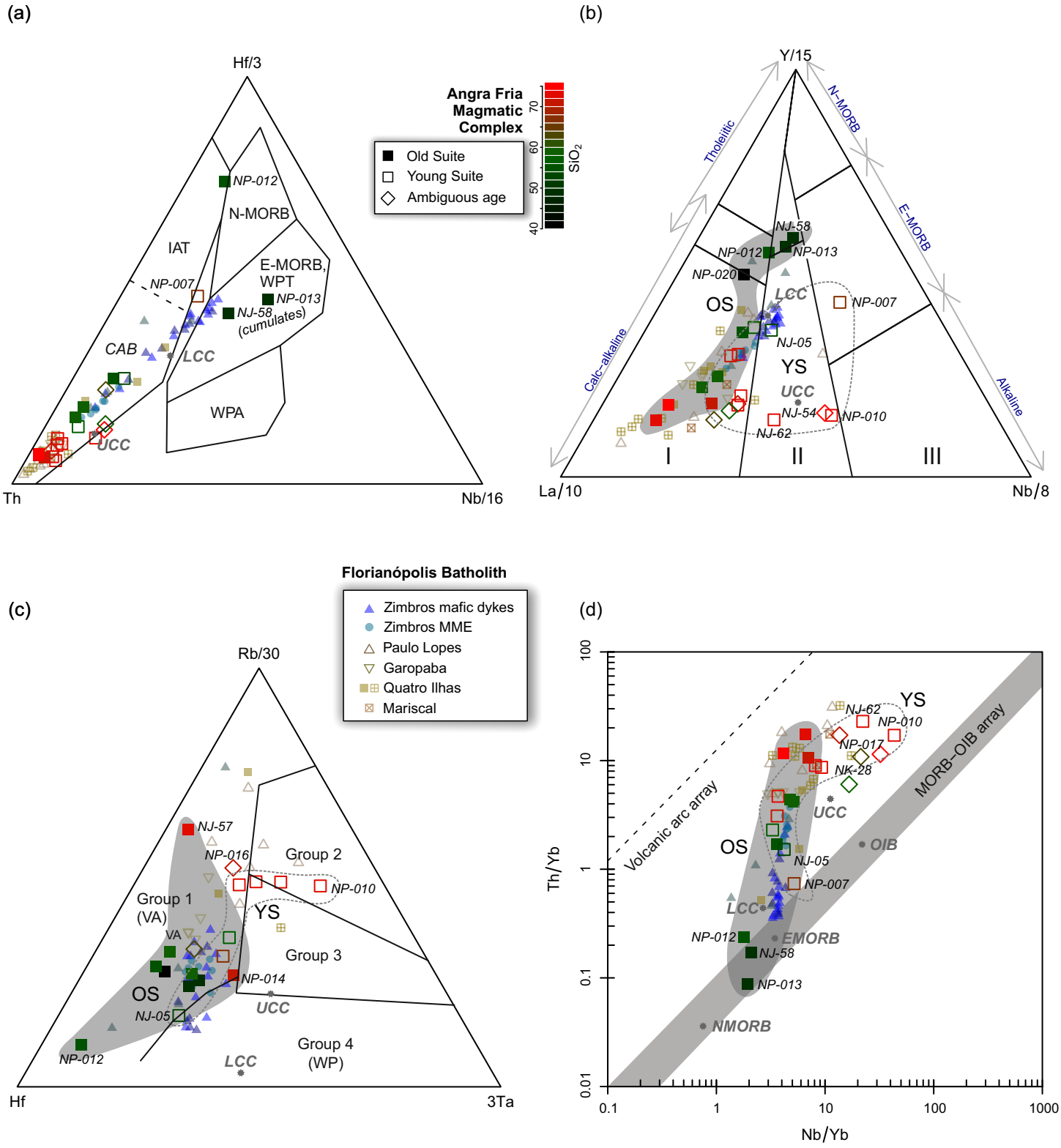

Janoušek et al., Fig. 14
Double column width

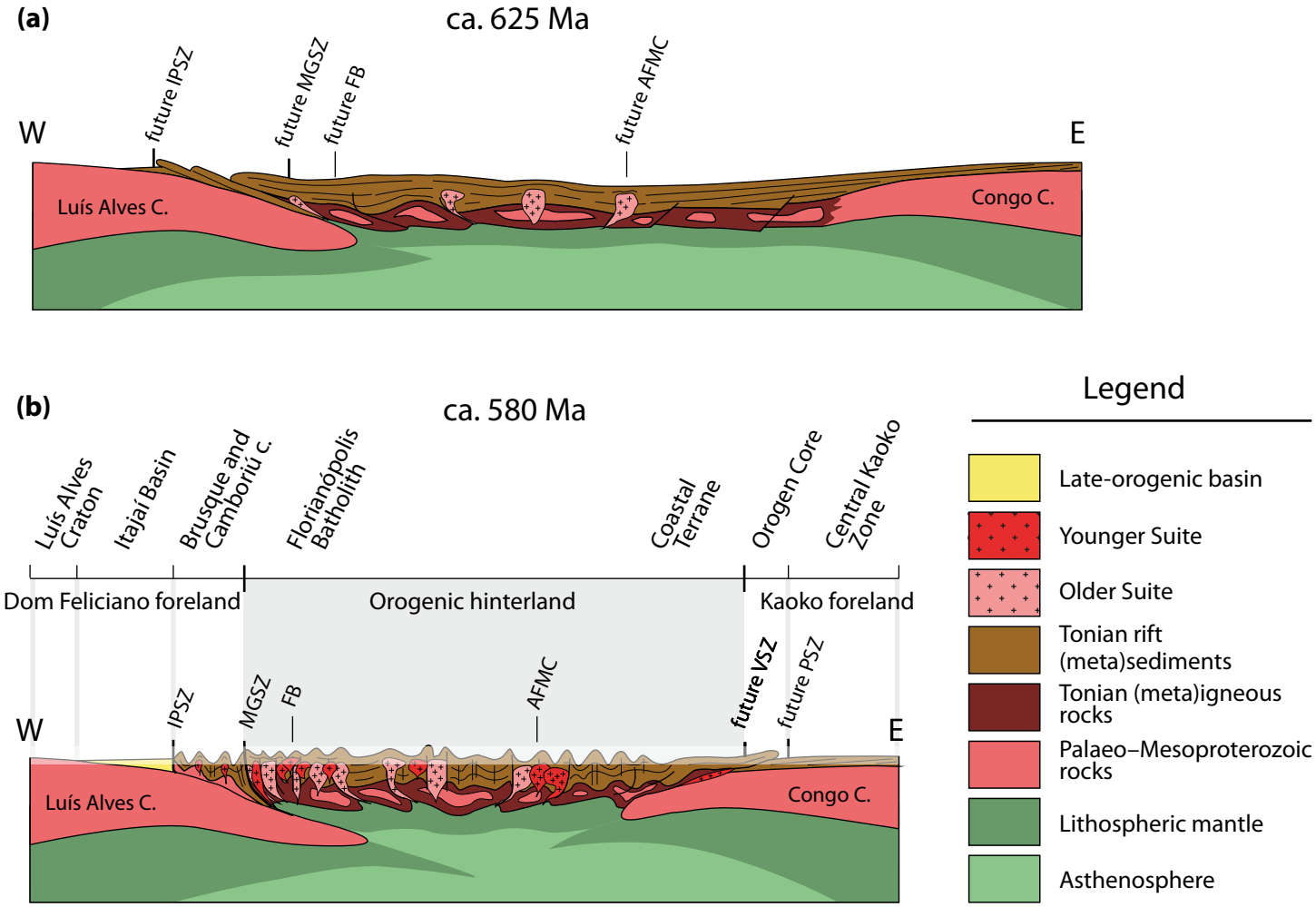

Janoušek et al., Fig. 15
Double column width

DOM FELICIANO BELT								
Sample	Lithotype	Method	Age (Ma)	Error (Ma)	Geological Unit	Tectonic Unit	Geological Province	Reference
PBF-8E	metatonalite	U–Pb ID–TIMS zircon	649	10	xenolith	Florianópolis Batholith	Dom Feliciano Belt	Chemale et al. (2012)
PBF-4G	tonalitic gneiss	U–Pb LA–MS–ICPMS zircon	646	15	megaxenolith	Florianópolis Batholith	Dom Feliciano Belt	Chemale et al. (2012)
PMP-26C	granite	U–Pb LA–MS–ICPMS zircon	625	7	Quatro Ilhas Granite	Florianópolis Batholith	Dom Feliciano Belt	Florisbal et al. (2012)
PBF-285	metagranite	U–Pb LA–MS–ICPMS zircon	623	6	Quatro Ilhas Granite	Florianópolis Batholith	Dom Feliciano Belt	Chemale et al. (2012)
PBF-33E	granitic dyke	U–Pb LA–MS–ICPMS zircon	618	5	Quatro Ilhas Granite dyke	Florianópolis Batholith	Dom Feliciano Belt	Chemale et al. (2012)
PMP-27B	Bt monzogranite	U–Pb LA–MS–ICPMS zircon	614	4	Quatro Ilhas Granite	Florianópolis Batholith	Dom Feliciano Belt	Florisbal et al. (2012)
MG-362	Amp–Bt syenogranite	U–Pb ID–TIMS zircon	614	2	Syenogranite	Florianópolis Batholith	Dom Feliciano Belt	Passarelli et al. (2010)
PMP-25D	granite	U–Pb LA–MS–ICPMS zircon	610	8	Mariscal Granite	Florianópolis Batholith	Dom Feliciano Belt	Florisbal et al. (2012)
MG-220	monzogranite	U–Pb ID–TIMS zircon	609	16	Monzogranite	Florianópolis Batholith	Dom Feliciano Belt	Passarelli et al. (2010)
PBF-29B	granite	U–Pb ID–TIMS zircon	602	4	Estalheiro Granite	Florianópolis Batholith	Dom Feliciano Belt	Chemale et al. (2012)
PBF-649	granite	U–Pb ID–TIMS zircon	590	10	Morro dos Macacos Granite	Florianópolis Batholith	Dom Feliciano Belt	Chemale et al. (2012)
PBF-94A	granite	U–Pb SHRIMP zircon	587	9	Zimbros Granite	Florianópolis Batholith	Dom Feliciano Belt	Chemale et al. (2012)
PB-57G	granitic orthogneiss	U–Pb LA–MS–ICPMS zircon	799	4	xenolith	Porto Belo Complex	Dom Feliciano Belt	De Toni et al. (2020)
KAOKO BELT								
Sample	Lithotype	Method	Age (Ma)	Error (Ma)	Geological Unit	Tectonic Unit	Geological Province	Reference
NO-13	orthogneiss	U–Pb SIMS zircon	818	3	Coastal Terrane	Coastal Terrane	Kaoko Belt	Konopásek et al. (2018)
NI-061	orthogneiss	U–Pb SIMS zircon	807	4	Coastal Terrane	Coastal Terrane	Kaoko Belt	Konopásek et al. (2018)
WZ-118	orthogneiss	U–Pb SIMS zircon	805	4	Coastal Terrane	Coastal Terrane	Kaoko Belt	Konopásek et al. (2008)
NO-19A	orthogneiss	U–Pb SIMS zircon	785	4	Coastal Terrane	Coastal Terrane	Kaoko Belt	Konopásek et al. (2018)
BK 27	monzogranitic augengneiss	U–Pb Zrn evaporation	656	8	Coastal Terrane	Coastal Terrane	Kaoko Belt	Seth et al. (1998)
NJ-57	granitic orthogneiss	U–Pb LA–MS–ICPMS zircon	626	5	Angra Fria Complex	Coastal Terrane	Kaoko Belt	Konopásek et al. (2016)
NJ-58	Hbl gabbro	U–Pb LA–MS–ICPMS zircon	622	5	Angra Fria Complex	Coastal Terrane	Kaoko Belt	Konopásek et al. (2016)
NJ-59	diorite	U–Pb LA–MS–ICPMS zircon	620	6	Angra Fria Complex	Coastal Terrane	Kaoko Belt	Konopásek et al. (2016)
NK-42	granodiorite–tonalite	U–Pb SIMS zircon	586	3	Angra Fria Complex	Coastal Terrane	Kaoko Belt	Konopásek et al. (2016)
NJ-05	diorite	U–Pb LA–MS–ICPMS zircon	584	7	Angra Fria Complex	Coastal Terrane	Kaoko Belt	Konopásek et al. (2016)
BK 426	granodioritic augengneiss	U–Pb SHRIMP zircon	580	3	Boundary Igneous Complex	Coastal Terrane	Kaoko Belt	Seth et al. (1998)
NJ-62	Ms–Bt granite	U–Pb LA–MS–ICPMS zircon	574	6	Angra Fria Complex	Coastal Terrane	Kaoko Belt	Konopásek et al. (2016)
WZ-186	granite	U–Pb LA–MS–ICPMS zircon	572	4	Boundary Igneous Complex	Coastal Terrane	Kaoko Belt	Konopásek et al. (2008)
WZ-022	Grt granite	U–Pb LA–MS–ICPMS zircon	571	9	Boundary Igneous Complex	Coastal Terrane	Kaoko Belt	Konopásek et al. (2008)
BK 24	granodioritic gneiss	U–Pb Zrn evaporation	567	2	Coastal Terrane	Coastal Terrane	Kaoko Belt	Seth et al. (1998)
BK 43	granite	U–Pb Zrn evaporation	564	2	Coastal Terrane	Coastal Terrane	Kaoko Belt	Seth et al. (1998)
DK 344	orthogneiss	U–Pb ID–TIMS zircon	559	7	Coastal Terrane	Coastal Terrane	Kaoko Belt	Franz et al. (1999)
BK 19	metagranite	U–Pb Zrn evaporation	552	2	Boundary Igneous Complex	Coastal Terrane	Kaoko Belt	Seth et al. (1998)
Na 00/14	granite	U–Pb Zrn evaporation	550	1	Boundary Igneous Complex	Coastal Terrane	Kaoko Belt	Kröner et al. (2004)
Na 118/2	granite	U–Pb Zrn evaporation	549	4	Boundary Igneous Complex	Coastal Terrane	Kaoko Belt	Kröner et al. (2004)

Chemale Jr, F., Mallmann, G., Bitencourt, M.F. and Kawashita, K., 2012. Time constraints on magmatism along the Major Gercino Shear Zone, southern Brazil: implications for West Gondwana reconstruction. Gondwana Research, 22: 184-199.

De Toni, G.B., Bitencourt, M.F., Nardi, L.V.S., Florisbal, L.M., Almeida, B.S. and Geraldes, M., 2020. Dom Feliciano Belt orogenic cycle tracked by its pre-collisional magmatism: the Tonian (ca. 800 Ma) Porto Belo Complex and its correlations in southern Brazil and Uruguay. Precambrian Research, 342: 105702.

Florisbal, L.M., Janasi, V.A., Bitencourt, M.F. and Heaman, L.M., 2012. Space-time relation of post-collisional granitic magmatism in Santa Catarina, southern Brazil: U-Pb LA-MC-ICP-MS zircon geochronology of coeval mafic-felsic magmatism related to the Major Gercino Shear Zone. Precambrian Research, 216-219: 132-151.

Franz, L., Romer, R.L. and Dingeldey, D.P., 1999. Diachronous Pan-African granulite-facies metamorphism (650 Ma and 550 Ma) in the Kaoko Belt, NW Namibia. European Journal of Mineralogy, 11: 167-180.

Konopásek, J., Janoušek, V., Oyhantçabal, P., Sláma, J. and Ulrich, S., 2018. Did the circum-Rodinia subduction trigger the Neoproterozoic rifting along the Congo-Kalahari Craton margin? Int. J. Earth Sci. (Geol. Rundsch.), 107: 1859-1894.

Konopásek, J., Košler, J., Tajčmanová, L., Ulrich, S. and Kitt, S.L., 2008. Neoproterozoic igneous complex emplaced along major tectonic boundary in the Kaoko Belt (NW Namibia): ion probe and LA-ICP-MS dating of magmatic and metamorphic zircons. Journal of the Geological Society (London), 165: 153-165.

Konopásek, J., Sláma, J. and Košler, J., 2016. Linking the basement geology along the Africa-South America coasts in the South Atlantic. Precambrian Research, 280: 221-230.

Kröner, S., Konopásek, J., Kröner, A., Passchier, C.W., Poller, U., Wingate, M.T.D. and Hofmann, K.H., 2004. U-Pb and Pb-Pb zircon ages for metamorphic rocks in the Kaoko Belt of northwestern Namibia: a Palaeo- to Mesoproterozoic basement reworked during the Pan-African orogeny. South African Journal of Geology, 107: 455-476.

Passarelli, C.R., Basei, M.A.S., Siga, O., McReath, I. and Campos Neto, M.C., 2010. Deformation and geochronology of syntectonic granitoids emplaced in the Major Gercino Shear Zone, southeastern South America. Gondwana Research, 17: 688-703.

Seth, B., Kröner, A., Mezger, K., Nemchin, A.A., Pidgeon, R.T. and Okrusch, M., 1998. Archaean to Neoproterozoic magmatic events in the Kaoko Belt of NW Namibia and their geodynamic significance. Precambrian Research, 92: 341-363.

ESM 2: Sample locations and their GPS coordinates

Sample	Lab	Groups	Age	Rock type	SiO_2 (wt. %)	GPS [WGS 84]
NP-011	CGS	Old	626	Bt–Amp quartz diorite	59.69	S 18°14.504', E 12°01.951'
NJ-59	*UB* †	*Old*	*620*	*equivalent of NP11*	*55.41*	*S 18°14.399', E 12°01.717'*
NP-012	CGS	Old	622	Bt–Amp quartz diorite	54.65	S 18°14.344', E 12°01.614'
NP-013	CGS	Old	622	very coarse-grained honblendite	49.90	S 18°14.325', E 12°01.616'
NJ-58	UB†	Old	622	*equivalent of NP013*	49.23	S 18°14.311', E 12°01.605'
NP-020	CGS	Old	630	medium-grained Amp gabbro	40.69	S 18°14.581', E 12°00.897'
NP-014	CGS	Old	626	v. coarse-grained Bt augengneiss	70.01	S 18°14.317', E 12°01.201'
NP-018	CGS	Old	626	Bt augengneiss	59.89	S 18°11.861', E 11°58.981'
NJ-57	*UB* †	*Old*	*626*	*equivalent of NP014*	*73.78*	*S 18°14.328', E 12°01.321'*
NK-29	UB	Old	630	Bt orthogneiss with red Kfs, intruded by NJ-62	74.12	S 18°12.476', E 11°58.815'
NP-007	CGS	Young	586	medium-grained Amp–Bt granodiorite	67.16	S 18°20.066', E 12°06.023'
NK-42	*UB* †	*Young*	*586*	*equivalent of NP007*	*70.53*	*S 18°18.707', E 12°05.961'*
NP-009	CGS	Young	586	medium-grained Amp–Bt tonalite	57.17	S 18°20.111', E 12°05.853'
NP-008	CGS	Young	586	coarse-grained leucocratic granite	72.06	S 18°20.123', E 12°05.812'
NJ-05	*UB* †	*Young*	*584*	*(quartz) dioritic dyke*	*52.02*	*S 18°18.888', E 12°05.117'*
NP-021	CGS	Young	580	coarse-grained Ms–Bt granite	72.39	S 18°16.601', E 12°02.638'
NK-16	UB	Young	580	equivalent of NP-021	72.45	S 18°16.618', E 12°12.652'
NJ-62	*UB* †	*Young*	*575*	*Ms–Bt granite*	*72.55*	*S 18°12.494', E 11°58.873'*
NP-010	CGS	Young	575	fine-grained Ms-Bt leucogranite, gray	73.51	S 18°14.457', E 12°02.763'
NJ-54	UB	Unclear	580	pink Ms granite	75.96	S 18°14.105', E 12°02.739'
NP-016	CGS	Unclear	580	medium-grained gray granite, intrudes OG of	71.83	S 18°11.875', E 11°59.049'
NP-017	CGS	Unclear	580	fine-grained mafic dyke	62.35	S 18°11.877', E 11°59.007'
NK-28	UB	Unclear	580	quartz diorite dyke	58.33	S 18°11.874', E 11°59.253'

† *(italics) published by Konopásek et al. (2016)*

ESM 3: Analytical techniques

1.1 Electron microprobe

The chemical compositions of rock-forming minerals were determined using a CAMECA SX100 electron-microprobe analyser (EMPA) at the Joint Laboratory of Electron Microscopy and Microanalysis, Department of Geological Sciences, Masaryk University, Brno and Czech Geological Survey (operators P. Gadas, J. Haifler, and R. Škoda). Operating conditions for analyses were as follows: an accelerating voltage of 15 kV, a beam current of 10 nA for silicates (feldspars, amphibole, mica) and apatite, 20 nA for accessory minerals (rutile, ilmenite, chromite, zircon, monazite), a beam diameter of 5 μm for silicates, 10 μm for apatite and 2 μm for other accessory minerals.

The element concentrations in silicate minerals and phosphates were analysed using the following standards and X-ray lines: K_α lines – sanidine (Si, Al, K), albite (Na), pyrope (Mg), wollastonite (Ca), almandine (Fe), spessartine (Mn), titanite (Ti), chromite (Cr), fluorapatite (P), $ScVO_4$ (Sc, V), gahnite (Zn), $SrSO_4$ (S), topaz (F), vanadinite (Cl); L_α lines – $SrSO_4$ (Sr), baryte (Ba), Rb-leucite (Rb), columbite "Ivigtut" (Nb), zircon (Zr), synthetic Y-, La-, Ce-anhydrous phosphates (Y, La, Ce); L_β lines – Pr- , Nd- , Sm- , Gd-, Yb-synthetic anhydrous phosphates (Pr, Nd, Sm, Gd, Yb); M_α lines – brabantite (Th), native hafnium (Hf). For oxides the following standards and X-ray lines were used: K_α lines – TiO (Ti), $MgAl_2O_4$ (Mg, Al), hematite, columbite (Fe), chromite (Cr), wollastonite (Ca), Ni_2SiO_4 (Ni), $ScVO_4$ (V), titanite (Si), Mn_2SiO_4 (Mn), gahnite (Zn), native Co (Co); L_α line – zircon (Zr), gahnite (Zn), columbite "Ivigtut" (Nb), Sn (Sn), W (W). Analytical conditions and standards used for zircon and monazite were similar to those described by Breiter et al. (2009) and Čopjaková et al. (2011). The peak counting time was 10–20 s for major and 20–120 s for minor to trace elements. The raw data were processed using the X–φ or PAP matrix correction routine (Merlet, 1994; Pouchou and Pichoir, 1985). Based on the counting statistics, the measurement error expressed as 2σ is approximately <1 rel. % for concentrations around 20 wt. % and <5 rel. % for concentrations around 5 wt. % and <15 rel. % for concentrations around 1 wt. %.

The mineral analyses were recast to mineral formulae (atoms per formula unit, apfu) and end-members using the R-language package *GCDkit-Mineral* (Janoušek et al., 2006a) as follows: feldspars on basis of 8 O equivalents, biotite on the basis of 22 charges. Amphibole formulae were calculated assuming 15 cations without Na and K (15–NK: Schumacher, 1997) and classified based on the IMA scheme (Leake et al., 1997). The formulae of apatite were

recalculated on the basis of 12.5 O equivalents, zircon 16 O, ilmenite 3 O and titanite 20 O with Fe^{II}/Fe^{III} allocated assuming 12 cations per formula unit (Droop, 1987). The mineral abbreviations are from Whitney and Evans (2010).

1.2 Whole-rock geochemistry

For the samples whose names start with 'NP' and selected samples of the 'NJ' series, 20 whole-rock samples, each 5–10 kg in weight, were obtained in the field (see **ESM 3** for their list and locations). After conventional crushing and homogenization, the powders produced using an agate mill were analyzed at ACME Labs/Bureau Veritas Commodities Canada Ltd. (Vancouver, Canada; (*http://acmelab.com*). The major and minor elements were determined by Inductively-Coupled Plasma Emission Spectrometry (ICP-ES; procedure LF 302) and most trace elements (Rb, Cs, Ba, Sr, Be, Ga, Th, U, Zr, Hf, Nb, Ta, Sc, Co, V, Sn, W, Y, and REE) by Inductively-Coupled Plasma Mass Spectrometry (ICP-MS; procedure LF 100). The dissolution of the rock powders in both cases followed fusion with a $LiBO_2/Li_2B_4O_7$ flux. This approach ensures that the entire sample is digested, including refractory phases such as zircon and sphene. The analyses of remaining trace elements, and transition metals in particular (Ni, Pb, Zn, Cu, Sb and Mo), were carried out by ICP-MS following modified aqua regia digestion (1:1:1 HNO_3:HCl:H_2O mixture – procedure AQ200).

The major- and trace-element analyses for samples NK-42, NK-16, and NK-29 were acquired at University Bergen. The major elements were analysed using a X-ray fluorescence (XRF) spectrometer Philips PW 1404 from glass discs fused with lithium tetraborate flux. Also selected metals (Co, V, Zn and Cu) were measured by the same XRF device but on pressed pellets. The remaining trace elements were determined by ICP-MS (Thermo Element2 HR-ICP-MS) using a microwave digestion system and a HNO_3 + HCl + HF mixture.

For plotting, statistical calculations, recalculations of the isotopic data as well as numerical modelling of the whole-rock geochemical data served a freeware R package *GCDkit* (Janoušek et al., 2006b; 2016). In this work, the Mg number (mg#) is defined as:

$$100\frac{MgO}{FeOt + MgO}[mol.\%]$$

and the A/CNK index (Shand, 1927) as:

$$\frac{Al_2O_3}{CaO + Na_2O + K_2O}[mol.\%].$$

For description of chondrite-normalized REE patterns serves the conventional Eu/Eu* ratio, reflecting the magnitude of the Eu anomaly:

$$\frac{Eu}{Eu*} = Eu_N \Big/ \sqrt{Sm_N Gd_N}$$

where *N* refers to concentrations normalized to chondritic abundances (Boynton, 1984). Moreover, their curvature is expressed using the Dy/Dy* parameter (Davidson et al., 2013) defined as:

$$\frac{Dy}{Dy*} = \frac{Dy_N}{La_N^{4/13} Yb_N^{9/13}}.$$

1.3 Whole-rock Sr–Nd isotopes

The first batch of 13 whole-rock Sr–Nd isotopic analyses was performed on Triton Plus (Thermo Fisher Scientific) Thermal-Ionization Mass Spectrometer (TIMS) at the Czech Geological Survey, Prague–Barrandov (V. Erban, J. Kochergina, Z. Rodovská). Samples were dissolved using a combined HF–HNO_3 + HCl—$HClO_4$ digestion. Strontium and Rare Earth Elements (REE) fractions were isolated from the bulk matrix via an ion-exchange chromatography technique using AG 50W-X8 resin (Bio-Rad Laboratories, Inc.). Subsequently, Sr spec resin (Triskem Intl.) was used for purification of the Sr fraction (Pin et al., 1994); the Nd and Sm cut was purified using Ln spec resin (Triskem Intl.) (Pin and Zalduegui, 1997). Complete analytical details were reported by Míková and Denková (2007). The measurements were carried out in static mode using a single Ta filament assembly for Sr, double Re filament assembly for Nd. The $^{143}Nd/^{144}Nd$ ratios were corrected for mass fractionation to $^{146}Nd/^{144}Nd = 0.7219$ and $^{87}Sr/^{86}Sr$ ratios were corrected assuming $^{88}Sr/^{86}Sr = 8.375209$. External reproducibility and measurement accuracy was demonstrated by repeated analyses of the NBS 987 ($^{87}Sr/^{86}Sr = 0.710253 \pm 44$ (2σ, n = 50) and JNdi-1 ($^{143}Nd/^{144}Nd = 0.512099 \pm 20$ (2σ, n = 31) reference materials (Jochum et al., 2005; see Tanaka et al., 2000). The Rb, Sr, Sm and Nd concentrations were obtained by ICP-MS (see above).

The second batch of Sr–Nd analyses (series NJ and NK, 4 previously unpublished and 6 from Konopásek et al. (2016)) was acquired using the Finnigan MAT 262 TIMS at the University of Bergen. Samples were dissolved using a combined HF–HCl–HNO_3 acid attack and pure elements were isolated by exchange chromatography techniques as detailed in Le Roex and Lanyon (1998). The TIMS Rb–Sr and Sm–Nd isotopic analyses were performed in dynamic ($^{143}Nd/^{144}Nd$ and $^{87}Sr/^{86}Sr$) and static ($^{84}Sr/^{86}Sr$, $^{87}Rb/^{85}Rb$, $^{148}Nd/^{144}Nd$ and $^{149}Sm/^{152}Sm$) mode using a double Re filament assembly. Concentrations of Sr, Rb, Nd and Sm were quantified by isotopic dilution with $^{84}Sr/^{87}Rb$ and $^{148}Nd/^{149}Sm$ mixed spikes. The $^{143}Nd/^{144}Nd$ ratios were corrected for mass fractionation to $^{146}Nd/^{144}Nd = 0.7219$ (Wasserburg

et al., 1981). External reproducibility is estimated from repeat analyses of the La Jolla ($^{143}Nd/^{144}Nd = 0.511850 \pm 0.000006$, 2σ) and NIST SRM 987 ($^{87}Sr/^{86}Sr = 0.71024 \pm 0.00002$, 2σ) isotopic standards. For further analytical details, see Konopásek et al. (2016).

In both cases, the decay constants applied to age-correct the isotopic ratios are from Steiger and Jäger (1977 – Sr) and Lugmair and Marti (1978 – Nd). The (ε^{i}_{Nd} values and single-stage CHUR Nd model ages were obtained using Bulk Earth parameters of Jacobsen and Wasserburg (1980), the two-stage Depleted Mantle Nd model ages (T^{DM}_{Nd} .2stg) were calculated after Liew and Hofmann (1988).

References

Boynton, W.V., 1984. Cosmochemistry of the rare earth elements: meteorite studies. In: P. Henderson (Editor), Rare Earth Element Geochemistry. Elsevier, Amsterdam, pp. 63-114.

Breiter, K., Čopjaková, R. and Škoda, R., 2009. The involvement of F, CO_2, and As in the alteration of Zr-Th-REE-bearing accessory minerals in the Hora Svaté Kateřiny A-type granite, Czech Republic. Canadian Mineralogist, 47: 1375-1398.

Davidson, J., Turner, S. and Plank, T., 2013. Dy/Dy*: variations arising from mantle sources and petrogenetic processes. Journal of Petrology, 54: 525-537.

Droop, G.T.R., 1987. A general equation for estimating Fe^{3+} concentrations in ferromagnesian silicates using stoichiometric criteria. Mineralogical Magazine, 51: 431-435.

Čopjaková, R., Novák, M. and Franců, E., 2011. Formation of authigenic monazite-(Ce) to monazite-(Nd) from Upper Carboniferous graywackes of the Drahany Upland: Roles of the chemical composition of host rock and burial temperature. Lithos, 127: 373-385.

Jacobsen, S.B. and Wasserburg, G.J., 1980. Sm–Nd isotopic evolution of chondrites. Earth and Planetary Science Letters, 50: 139-155.

Janoušek, V., Erban, V. and Farrow, C.M., 2006a. Using the R language for graphical presentation and interpretation of compositional data in mineralogy: introducing the package GCDkit-Mineral. useR! 2006 Book of Abstracts. Austrian Association for Statistical Computing (AASC) and Wirtschaftsuniversität Wien, Vienna.

Janoušek, V., Farrow, C.M. and Erban, V., 2006b. Interpretation of whole-rock geochemical data in igneous geochemistry: introducing Geochemical Data Toolkit (GCDkit). Journal of Petrology, 47: 1255-1259.

Janoušek, V., Moyen, J.F., Martin, H., Erban, V. and Farrow, C., 2016. Geochemical Modelling of Igneous Processes – Principles and Recipes in R Language. Bringing the Power of R to a Geochemical Community. Springer, Berlin.

Jochum, K.P., Nohl, U., Herwig, K., Lammel, E., Stoll, B. and Hofmann, A.W., 2005. GeoReM: a new geochemical database for reference materials and isotopic standards. Geostandards and Geoanalytical Research, 29: 333-338.

Konopásek, J., Sláma, J. and Košler, J., 2016. Linking the basement geology along the Africa-South

America coasts in the South Atlantic. Precambrian Research, 280: 221-230.

le Roex, A.P. and Lanyon, R., 1998. Isotope and trace element geochemistry of Cretaceous Damaraland lamprophyres and carbonatites, northwestern Namibia: evidence for plume-lithosphere interactions. Journal of Petrology, 39: 1117-1146.

Leake, B.E., Woolley, A.R., Arps, C.E.S., Birch, W.D., Gilbert, M.C., Grice, J.D., Hawthorne, F.C., Kato, A., Kisch, H.J., Krivovichev, V.G., Linthout, K., Laird, J., Mandarino, J., Maresch, W.V., Nickel, E.H., Rock, N.M.S., Schumacher, J.C., Smith, J.C., Stephenson, N.C.N., Whittaker, E.J.W. and Youzhi, G., 1997. Nomenclature of amphiboles: report of the Subcommittee on Amphiboles of the International Mineralogical Association Commission on New Minerals and Mineral Names. Mineralogical Magazine, 61: 295-321.

Liew, T.C. and Hofmann, A.W., 1988. Precambrian crustal components, plutonic associations, plate environment of the Hercynian Fold Belt of Central Europe: indications from a Nd and Sr isotopic study. Contributions to Mineralogy and Petrology, 98: 129-138.

Lugmair, G.W. and Marti, K., 1978. Lunar initial $^{143}Nd/^{144}Nd$: differential evolution line of the lunar crust and mantle. Earth and Planetary Science Letters, 39: 349-357.

Merlet, C., 1994. An accurate computer correction program for quantitative electron probe microanalysis. Mikrochim Acta, 114-115: 363-376.

Míková, J. and Denková, P., 2007. Modified chromatographic separation scheme for Sr and Nd isotope analysis in geological silicate samples. Journal of Geosciences, 52: 221-226.

Pin, C., Briot, D., Bassin, C. and Poitrasson, F., 1994. Concomitant separation of strontium and samarium-neodymium for isotopic analysis in silicate samples, based on specific extraction chromatography. Analytica Chimica Acta, 298: 209-217.

Pin, C. and Zalduegui, J.F.S., 1997. Sequential separation of light rare-earth elements, thorium and uranium by miniaturized extraction chromatography: application to isotopic analyses of silicate rocks. Analytica Chimica Acta, 339: 79-89.

Pouchou, J.L. and Pichoir, F., 1985. "PAP" (frZ) procedure for improved quantitative microanalysis. In: J.T. Armstrong (Editor), Microbeam Analysis. San Francisco Press, San Francisco, pp. 104-106.

Schumacher, J.C., 1997. Appendix 2. The estimation of the proportion of ferric iron in the electron-microprobe analysis of amphiboles. Canadian Mineralogist, 35: 238-246.

Shand, S.J., 1927. Eruptive Rocks. Thomas Murby, London.

Steiger, R.H. and Jäger, E., 1977. Subcommission on Geochronology; convention on the use of decay constants in geo- and cosmochronology. Earth and Planetary Science Letters, 36: 359-362.

Tanaka, T., Togashi, S., Kamioka, H., Amakawa, H., Kagami, H., Hamamoto, T., Yuhara, M., Orihashi, Y., Yoneda, S., Shimizu, H., Kunimaru, T., Takahashi, K., Yanagi, T., Nakano, T., Fujimaki, H., Shinjo, R., Asahara, Y., Tanimizu, M. and Dragusanu, C., 2000. JNdi-1: a neodymium isotopic reference in consistency with LaJolla neodymium. Chemical Geology, 168: 279-281.

Wasserburg, G.J., Jacobsen, S.B., DePaolo, D.J., McCulloch, M.T. and Wen, T., 1981. Precise determination of Sm/Nd ratios, Sm and Nd isotopic abundances in standard solutions. Geochimica et Cosmochimica Acta, 45: 2311-2324.

Whitney, D.L. and Evans, B.W., 2010. Abbreviations for names of rock-forming minerals. American Mineralogist, 95: 185-187.

ESM 5: Whole-rock major-element analyses from the AFMC (wt. %)

	NP-020	*NJ-58*	NP-013	NP-012	*NJ-59*	NP-011	NP-018	NP-014	*NJ-57*	NK-29
Groups	Old	*Old*	Old	Old	*Old*	Old	Old	Old	*Old*	Old
Rock type	medium-grained gabbro	*v. coarse-grained honblendite*	v. coarse-grained honblendite	Amp-Bt tonalite	*Amp-bearing QtzD*	Amp-bearing QtzD	Bt augengneiss	v. coarse-grained Bt augengneiss	*v. coarse-grained Bt augengneiss*	orthogneiss with red Kfs, intruded by NJ-62
Lab	ACME	*ACME†*	ACME	ACME	*ACME†*	ACME	ACME	ACME	*ACME†*	UB
SiO_2	40.69	*49.23*	49.90	54.65	*55.41*	59.69	59.89	70.01	*73.78*	74.12
TiO_2	1.27	*0.99*	1.16	0.41	*1.05*	0.82	0.94	0.67	*0.24*	0.45
Al_2O_3	19.68	*10.57*	10.50	19.82	*17.40*	16.86	17.17	14.54	*13.07*	12.71
Fe_2O_3	15.63	*12.07*	11.24	5.07	*8.67*	6.67	5.99	3.86	*1.83*	3.87
MnO	0.16	*0.25*	0.21	0.11	*0.14*	0.11	0.11	0.07	*0.04*	0.03
MgO	7.17	*11.98*	12.38	4.21	*3.89*	3.26	2.21	0.99	*0.62*	0.81
CaO	11.76	*10.36*	10.82	8.85	*7.15*	5.69	5.27	2.51	*1.82*	1.60
Na_2O	1.58	*1.36*	1.51	4.61	*2.99*	3.19	3.54	3.55	*2.56*	2.02
K_2O	0.58	*1.36*	1.18	0.81	*1.86*	2.27	2.97	4.24	*4.66*	4.73
P_2O_5	0.08	*0.13*	0.12	0.24	*0.26*	0.21	0.26	0.22	*0.10*	0.29
LOI	1.1	*1.2*	0.5	1.0	*0.9*	1.0	1.3	-0.9	*1.1*	0.8
Σ	99.70	99.50	99.52	99.78	99.72	99.77	99.65	99.76	99.82	101.45
K_2O/Na_2O	0.37	*1.00*	0.78	0.18	*0.62*	0.71	0.84	1.19	*1.82*	2.34
A/CNK	0.80	*0.47*	0.45	0.81	*0.87*	0.93	0.92	0.97	*1.04*	1.12
mg#	47.61	*66.29*	68.57	62.19	*47.06*	49.19	42.23	33.69	*40.16*	29.31

	NJ-05	**NP-009**	**NP-007**	***NK-42***	**NP-008**	**NP-021**	**NK-16**	***NJ-62***	**NP-010**
Groups	*Young*	Young	Young	*Young*	Young	Young	Young	*Young*	Young
Rock type	*(quartz) dioritic dyke*	medium-grained Amp-bearing tonalite	medium-grained Bt-Amp granodiorite	*medium-grained Bt-Amp granodiorite*	coarse-grained leucogranite	coarse-grained Bt granite	coarse-grained Bt granite	*Ms-Bt granite*	fine-grained Ms-Bt leucogranite
Lab	*ACME†*	ACME	ACME	*UB†*	ACME	ACME	UB	*ACME†*	ACME
SiO_2	*52.02*	57.17	67.16	*70.53*	72.06	72.39	72.45	*72.55*	73.51
TiO_2	*1.65*	0.85	0.58	*0.51*	0.20	0.21	0.23	*0.20*	0.12
Al_2O_3	*17.52*	17.37	15.06	*14.89*	14.12	14.48	14.92	*14.27*	14.51
Fe_2O_3	*11.58*	8.11	4.90	*4.54*	1.87	2.22	2.58	*1.67*	1.26
MnO	*0.17*	0.13	0.08	*0.08*	0.03	0.05	0.06	*0.04*	0.03
MgO	*3.04*	3.51	1.34	*1.02*	0.62	0.46	0.50	*0.40*	0.27
CaO	*8.33*	6.59	3.35	*3.54*	1.68	1.74	1.67	*0.76*	0.78
Na_2O	*2.52*	2.53	2.91	*2.80*	2.68	3.26	2.76	*3.03*	3.08
K_2O	*1.35*	2.21	3.39	*2.51*	5.36	4.65	5.08	*5.50*	5.31
P_2O_5	*0.69*	0.15	0.15	*0.11*	0.08	0.14	0.20	*0.28*	0.30
LOI	*0.9*	1.2	0.9	*0.8*	1.2	0.3	0.7	*1.2*	0.8
Σ	99.77	99.82	99.82	101.32	99.90	99.90	101.15	99.90	99.97
K_2O/Na_2O	*0.54*	0.87	1.16	*0.90*	2.00	1.43	1.84	*1.82*	1.72
A/CNK	*0.84*	0.94	1.04	*1.08*	1.06	1.07	1.14	*1.16*	1.19
mg#	*34.21*	46.16	35.14	*30.80*	39.64	29.10	27.74	*32.18*	29.80

	NK-28	NP-017	NP-016	NJ-54
Groups	Ambiguous	Ambiguous	Ambiguous	Ambiguous
Rock type	quartz diorite dyke	fine-grained quartz diorite dyke	medium-grained gray granite, intrudes OS orthogneisse	pink Ms granite
Lab	ACME	ACME	ACME	ACME
SiO_2	58.33	62.35	71.83	75.96
TiO_2	1.22	0.92	0.30	0.15
Al_2O_3	17.59	17.39	14.44	13.90
Fe_2O_3	8.07	5.52	2.35	1.68
MnO	0.09	0.06	0.03	0.03
MgO	2.60	1.76	0.67	0.35
CaO	5.92	4.62	1.24	0.86
Na_2O	3.74	4.15	3.01	2.67
K_2O	1.92	1.97	5.38	4.61
P_2O_5	0.36	0.35	0.23	0.41
LOI	0.8	0.6	0.4	0.8
Σ	100.63	99.69	99.88	101.41
K_2O/Na_2O	0.51	0.47	1.79	1.73
A/CNK	0.93	1.00	1.11	1.27
mg#	38.96	38.71	36.10	29.22

Laboratories: ACME: ACME Labs/Bureau Veritas Commodities (Vancouver, Canada) ;UB: University of Bergen

†, italics: data for samples discussed by Konopásek et al. (2016)

AMPHIBOLE formulae recalculated on the basis of 23 oxygen equivalents
Fe^{II}/Fe^{III} allocated assuming 13-CNK: 13 cations without Ca, Na and K

	1	2	3	4	5	6	7	8	9	10	11	12	13
Sample	NP-011	NP-011	NP-011	NP-011	NP-011	NP-011	NP-011	NP-011	NP-011	NP-011	NP-011	NP-011	NP-012 high Si
Suite	Old	Old	Old	Old	Old	Old	Old	Old	Old	Old	Old	Old	Old
Petrology	Amp-bearing QtzD	Amp-bearing QtzD	Amp-bearing QtzD	Amp-bearing QtzD	Amp-bearing QtzD	Amp-bearing QtzD	Amp-bearing QtzD	Amp-bearing QtzD	Amp-bearing QtzD	Amp-bearing QtzD	Amp-bearing QtzD	Amp-bearing QtzD	Amp-Bt tonalite
SiO_2	42.415	43.097	42.548	42.718	41.909	41.696	42.155	41.927	42.105	42.667	42.721	42.761	47.606
TiO_2	1.270	0.616	1.108	1.086	0.975	1.192	1.285	1.152	1.114	1.256	1.234	1.091	0.357
Al_2O_3	10.514	10.897	11.163	11.140	11.815	11.438	11.036	11.087	11.301	10.909	10.903	10.939	8.596
V_2O_3	b.d.l.	b.d.l.	b.d.l.	b.d.l.	b.d.l.	0.096	b.d.l.	b.d.l.	b.d.l.	b.d.l.	0.097	b.d.l.	b.d.l.
Cr_2O_3	b.d.l.	0.217	b.d.l.	b.d.l.	0.051	0.053	b.d.l.	0.053	b.d.l.	b.d.l.	b.d.l.	b.d.l.	b.d.l.
Fe_2O_3	4.053	4.441	3.087	3.732	5.883	4.436	3.344	5.060	4.690	5.021	3.616	4.048	1.046
MgO	9.228	9.188	8.843	8.944	8.810	8.582	9.033	9.006	8.778	9.473	9.157	9.070	12.359
CaO	11.785	11.904	12.105	11.867	11.750	11.688	12.185	11.809	11.754	11.760	11.929	11.807	12.976
MnO	0.449	0.429	0.414	0.455	0.477	0.519	0.421	0.436	0.430	0.460	0.415	0.445	0.388
FeO	14.811	14.523	16.124	15.368	14.048	14.903	15.761	14.345	14.878	13.821	15.230	14.856	13.598
ZnO	b.d.l.	b.d.l.	b.d.l.	b.d.l.	b.d.l.	b.d.l.	b.d.l.	b.d.l.	b.d.l.	b.d.l.	b.d.l.	b.d.l.	b.d.l.
Na_2O	1.109	1.105	1.195	1.100	1.124	1.037	1.082	1.042	1.060	1.062	1.132	1.102	0.855
K_2O	1.326	1.076	1.270	1.419	1.380	1.514	1.398	1.350	1.447	1.321	1.310	1.207	0.529
F	0.156	0.126	0.147	0.146	0.161	0.152	0.134	0.148	0.132	0.150	0.168	0.147	0.347
Cl	0.021	0.035	0.040	0.030	0.027	0.037	b.d.l.	0.030	0.026	0.034	0.021	0.025	b.d.l.
H_2O	1.870	1.897	1.886	1.890	1.880	1.863	1.896	1.871	1.885	1.888	1.883	1.885	1.882
O=F	-0.066	-0.053	-0.062	-0.061	-0.068	-0.064	-0.056	-0.062	-0.056	-0.063	-0.071	-0.062	-0.146
O=Cl	-0.005	-0.008	-0.009	-0.007	-0.006	-0.008	–	-0.007	-0.006	-0.008	-0.005	-0.006	–
Σ	98.937	99.490	99.859	99.827	100.217	99.134	99.674	99.247	99.538	99.751	99.740	99.316	100.392
Si	6.462	6.505	6.441	6.454	6.312	6.360	6.399	6.375	6.388	6.426	6.455	6.476	6.960
Ti	0.146	0.070	0.126	0.123	0.110	0.137	0.147	0.132	0.127	0.142	0.140	0.124	0.039
Al	1.888	1.938	1.991	1.983	2.097	2.056	1.974	1.986	2.021	1.936	1.941	1.952	1.481
V	0.000	0.000	0.000	0.000	0.000	0.012	0.000	0.000	0.000	0.000	0.012	0.000	0.000
Cr	0.000	0.026	0.000	0.000	0.006	0.006	0.000	0.006	0.000	0.000	0.000	0.000	0.000
Fe^{III}	0.465	0.504	0.352	0.424	0.667	0.509	0.382	0.579	0.535	0.569	0.411	0.461	0.115
Mg	2.096	2.068	1.996	2.015	1.978	1.952	2.044	2.041	1.985	2.127	2.063	2.048	2.694
Ca	1.924	1.925	1.963	1.921	1.896	1.910	1.982	1.924	1.911	1.897	1.931	1.916	2.032
Mn	0.058	0.055	0.053	0.058	0.061	0.067	0.054	0.056	0.055	0.059	0.053	0.057	0.048
Fe^{II}	1.887	1.833	2.041	1.942	1.769	1.901	2.001	1.824	1.888	1.741	1.924	1.881	1.663
Zn	0.000	0.000	0.000	0.000	0.000	0.000	0.000	0.000	0.000	0.000	0.000	0.000	0.000
Na	0.328	0.323	0.351	0.322	0.328	0.307	0.318	0.307	0.312	0.310	0.332	0.324	0.242
K	0.258	0.207	0.245	0.273	0.265	0.295	0.271	0.262	0.280	0.254	0.252	0.233	0.099
F	0.075	0.060	0.070	0.070	0.077	0.073	0.064	0.071	0.063	0.071	0.080	0.070	0.160
Cl	0.005	0.009	0.010	0.008	0.007	0.010	0.000	0.008	0.007	0.009	0.005	0.006	0.000
Σ.atoms	15.590	15.525	15.640	15.594	15.573	15.595	15.635	15.571	15.572	15.541	15.600	15.549	15.534
Si_T	6.462	6.505	6.441	6.454	6.312	6.360	6.399	6.375	6.388	6.426	6.455	6.476	6.960
Al_T	1.538	1.495	1.559	1.546	1.688	1.640	1.601	1.625	1.612	1.574	1.545	1.524	1.040
Σ_T	8.000	8.000	8.000	8.000	8.000	8.000	8.000	8.000	8.000	8.000	8.000	8.000	8.000
Al_C	0.349	0.444	0.432	0.438	0.409	0.417	0.373	0.361	0.409	0.362	0.396	0.428	0.441
Ti_C	0.146	0.070	0.126	0.123	0.110	0.137	0.147	0.132	0.127	0.142	0.140	0.124	0.039
Fe^{III}_C	0.465	0.504	0.352	0.424	0.667	0.509	0.382	0.579	0.535	0.569	0.411	0.461	0.115
V_C	0.000	0.000	0.000	0.000	0.000	0.012	0.000	0.000	0.000	0.000	0.012	0.000	0.000
Cr_C	0.000	0.026	0.000	0.000	0.006	0.006	0.000	0.006	0.000	0.000	0.000	0.000	0.000
Mg_C	2.096	2.068	1.996	2.015	1.978	1.952	2.044	2.041	1.985	2.127	2.063	2.048	2.694
Zn_C	0.000	0.000	0.000	0.000	0.000	0.000	0.000	0.000	0.000	0.000	0.000	0.000	0.000
Fe^{II}_C	1.887	1.833	2.041	1.942	1.769	1.901	2.001	1.824	1.888	1.741	1.924	1.881	1.663
Mn_C	0.058	0.055	0.053	0.058	0.061	0.067	0.054	0.056	0.055	0.059	0.053	0.057	0.048
Σ_C	5.000	5.000	5.000	5.000	5.000	5.000	5.000	5.000	5.000	5.000	5.000	5.000	5.000
Mn_B	0.000	0.000	0.000	0.000	0.000	0.000	0.000	0.000	0.000	0.000	0.000	0.000	0.000
Fe^{II} B	0.000	0.000	0.000	0.000	0.000	0.000	0.000	0.000	0.000	0.000	0.000	0.000	0.000
Zn_B	0.000	0.000	0.000	0.000	0.000	0.000	0.000	0.000	0.000	0.000	0.000	0.000	0.000
Mg_B	0.000	0.000	0.000	0.000	0.000	0.000	0.000	0.000	0.000	0.000	0.000	0.000	0.000
Cr_B	0.000	0.000	0.000	0.000	0.000	0.000	0.000	0.000	0.000	0.000	0.000	0.000	0.000
V_B	0.000	0.000	0.000	0.000	0.000	0.000	0.000	0.000	0.000	0.000	0.000	0.000	0.000
Fe^{III}_B	0.000	0.000	0.000	0.000	0.000	0.000	0.000	0.000	0.000	0.000	0.000	0.000	0.000
Ti_B	0.000	0.000	0.000	0.000	0.000	0.000	0.000	0.000	0.000	0.000	0.000	0.000	0.000
Al_B	0.000	0.000	0.000	0.000	0.000	0.000	0.000	0.000	0.000	0.000	0.000	0.000	0.000
Ca_B	1.924	1.925	1.963	1.921	1.896	1.910	1.982	1.924	1.911	1.897	1.931	1.916	2.000
Na_B	0.076	0.075	0.037	0.079	0.104	0.090	0.018	0.076	0.089	0.103	0.069	0.084	0.000
Σ_B	2.000	2.000	2.000	2.000	2.000	2.000	2.000	2.000	2.000	2.000	2.000	2.000	2.000
Na_A	0.251	0.248	0.314	0.243	0.224	0.217	0.300	0.231	0.222	0.208	0.263	0.239	0.242
Ca_A	0.000	0.000	0.000	0.000	0.000	0.000	0.000	0.000	0.000	0.000	0.000	0.000	0.032
Al_A	0.000	0.000	0.000	0.000	0.000	0.000	0.000	0.000	0.000	0.000	0.000	0.000	0.000
Ti_A	0.000	0.000	0.000	0.000	0.000	0.000	0.000	0.000	0.000	0.000	0.000	0.000	0.000
Fe^{III}_A	0.000	0.000	0.000	0.000	0.000	0.000	0.000	0.000	0.000	0.000	0.000	0.000	0.000
V_A	0.000	0.000	0.000	0.000	0.000	0.000	0.000	0.000	0.000	0.000	0.000	0.000	0.000
Cr_A	0.000	0.000	0.000	0.000	0.000	0.000	0.000	0.000	0.000	0.000	0.000	0.000	0.000
Mn_A	0.000	0.000	0.000	0.000	0.000	0.000	0.000	0.000	0.000	0.000	0.000	0.000	0.000
Mg_A	0.000	0.000	0.000	0.000	0.000	0.000	0.000	0.000	0.000	0.000	0.000	0.000	0.000
Zn_A	0.000	0.000	0.000	0.000	0.000	0.000	0.000	0.000	0.000	0.000	0.000	0.000	0.000
Fe^{II}_A	0.000	0.000	0.000	0.000	0.000	0.000	0.000	0.000	0.000	0.000	0.000	0.000	0.000
K_A	0.258	0.207	0.245	0.273	0.265	0.295	0.271	0.262	0.280	0.254	0.252	0.233	0.099
Vc_A	0.491	0.544	0.441	0.483	0.510	0.488	0.429	0.507	0.498	0.539	0.485	0.528	0.627
Σ_A	1.000	1.000	1.000	1.000	1.000	1.000	1.000	1.000	1.000	1.000	1.000	1.000	1.000
Σ_cations	15.509	15.456	15.559	15.516	15.490	15.512	15.571	15.492	15.502	15.461	15.515	15.472	15.373
F_OH	0.075	0.060	0.070	0.070	0.077	0.073	0.064	0.071	0.063	0.071	0.080	0.070	0.160
Cl_OH	0.005	0.009	0.010	0.008	0.007	0.010	0.000	0.008	0.007	0.009	0.005	0.006	0.000
OH_OH	1.919	1.931	1.919	1.923	1.916	1.917	1.936	1.921	1.930	1.920	1.914	1.923	1.840
Σ_OH	2.000	2.000	2.000	2.000	2.000	2.000	2.000	2.000	2.000	2.000	2.000	2.000	2.000
Si apfu	6.462	6.505	6.441	6.454	6.312	6.360	6.399	6.375	6.388	6.426	6.455	6.476	6.960
$Mg/(Mg + Fe^{II})$	0.526	0.530	0.494	0.509	0.528	0.507	0.505	0.528	0.513	0.550	0.517	0.521	0.618

14	15	16	17	18	19	20	21	22	23	24	25	26	27	28
NP-012 high Si Old	NP-012 high Si Old	NP-012 Old	NP-012 high Si Old	NP-012 Old	NP-012 high Si Old	NP-012 Old	NP-012 high Si Old	NP-012 Old	NP-012 high Si Old	NP-012 Old	NP-012 Old	NP-012 high Si Old	NP-012 high Si Old	NP-012 Old
Amp-Bt tonalite	Amp-Bt tonalite	Amp-Bt tonalite	Amp-Bt tonalite	Amp-Bt tonalite	Amp-Bt tonalite	Amp-Bt tonalite	Amp-Bt tonalite	Amp-Bt tonalite	Amp-Bt tonalite	Amp-Bt tonalite	Amp-Bt tonalite	Amp-Bt tonalite	Amp-Bt tonalite	Amp-Bt tonalite
50.522	49.424	45.273	49.827	44.866	50.852	44.832	51.192	45.207	49.597	45.498	45.908	49.757	53.551	45.484
0.211	0.453	0.948	0.354	0.899	0.288	0.985	0.239	0.867	0.531	1.035	1.045	0.483	0.163	1.138
5.671	6.676	10.228	6.092	10.371	5.330	10.178	5.194	10.401	7.247	10.482	10.335	7.234	3.394	10.822
b.d.l.	b.d.l.	b.d.l.	b.d.l.	b.d.l.	b.d.l.	0.159	b.d.l.	b.d.l.	b.d.l.	b.d.l.	b.d.l.	b.d.l.	b.d.l.	b.d.l.
b.d.l.	b.d.l.	b.d.l.	b.d.l.	b.d.l.	b.d.l.	b.d.l.	b.d.l.	b.d.l.	b.d.l.	0.055	b.d.l.	b.d.l.	b.d.l.	0.069
0.726	1.808	2.281	1.051	2.219	1.461	1.364	1.324	1.990	3.007	3.147	1.600	1.748	1.005	3.462
14.118	13.177	10.843	13.343	11.142	14.003	10.850	14.086	10.885	13.462	11.046	11.133	13.148	15.437	11.048
12.839	12.519	12.159	12.513	12.199	12.579	12.629	12.807	12.535	12.717	12.342	12.614	12.702	12.961	12.431
0.344	0.334	0.310	0.391	0.284	0.294	0.319	0.433	0.348	0.407	0.326	0.376	0.346	0.371	0.388
12.227	12.620	13.622	12.547	13.269	12.112	14.468	12.274	14.048	11.656	13.186	14.263	12.665	11.650	13.225
b.d.l.	b.d.l.	b.d.l.	b.d.l.	b.d.l.	b.d.l.	b.d.l.	b.d.l.	b.d.l.	b.d.l.	b.d.l.	b.d.l.	b.d.l.	b.d.l.	b.d.l.
0.612	0.762	0.899	0.573	0.989	0.574	0.875	0.483	0.882	0.656	0.868	0.943	0.681	0.347	1.006
0.279	0.463	0.929	0.396	1.099	0.324	0.943	0.310	0.917	0.490	0.924	0.927	0.423	0.178	0.927
0.325	0.309	0.313	0.318	0.340	0.284	0.331	0.309	0.339	0.304	0.294	0.251	0.266	0.308	0.352
b.d.l.	b.d.l.	b.d.l.	b.d.l.	b.d.l.	b.d.l.	b.d.l.	b.d.l.	b.d.l.	b.d.l.	b.d.l.	b.d.l.	b.d.l.	b.d.l.	b.d.l.
1.906	1.909	1.861	1.892	1.844	1.928	1.850	1.926	1.857	1.940	1.895	1.925	1.952	1.960	1.884
-0.137	-0.130	-0.132	-0.134	-0.143	-0.120	-0.139	-0.130	-0.143	-0.128	-0.124	-0.106	-0.112	-0.130	-0.148
–	–	–	–	–	–	–	–	–	–	–	–	–	–	–
99.644	100.324	99.534	99.163	99.378	99.908	99.643	100.447	100.134	101.887	100.974	101.214	101.293	101.195	102.088
7.341	7.181	6.721	7.296	6.675	7.370	6.679	7.385	6.687	7.088	6.660	6.711	7.151	7.608	6.598
0.023	0.050	0.106	0.039	0.101	0.031	0.110	0.026	0.096	0.057	0.114	0.115	0.052	0.017	0.124
0.971	1.143	1.789	1.051	1.818	0.910	1.787	0.883	1.813	1.221	1.808	1.781	1.225	0.568	1.850
0.000	0.000	0.000	0.000	0.000	0.000	0.019	0.000	0.000	0.000	0.000	0.000	0.000	0.000	0.000
0.000	0.000	0.000	0.000	0.000	0.000	0.000	0.000	0.000	0.000	0.006	0.000	0.000	0.000	0.008
0.079	0.198	0.255	0.116	0.248	0.159	0.153	0.144	0.222	0.323	0.347	0.176	0.189	0.107	0.378
3.058	2.854	2.400	2.913	2.471	3.025	2.410	3.029	2.400	2.868	2.411	2.426	2.817	3.270	2.389
1.999	1.949	1.934	1.963	1.944	1.953	2.016	1.979	1.986	1.947	1.936	1.976	1.956	1.973	1.932
0.042	0.041	0.039	0.048	0.036	0.036	0.040	0.053	0.044	0.049	0.040	0.047	0.042	0.045	0.048
1.486	1.533	1.691	1.536	1.651	1.468	1.802	1.481	1.738	1.393	1.614	1.744	1.522	1.384	1.604
0.000	0.000	0.000	0.000	0.000	0.000	0.000	0.000	0.000	0.000	0.000	0.000	0.000	0.000	0.000
0.172	0.215	0.259	0.163	0.285	0.161	0.253	0.135	0.253	0.182	0.246	0.267	0.190	0.096	0.283
0.052	0.086	0.176	0.074	0.209	0.060	0.179	0.057	0.173	0.089	0.173	0.173	0.078	0.032	0.172
0.149	0.142	0.147	0.147	0.160	0.130	0.156	0.141	0.159	0.137	0.136	0.116	0.121	0.138	0.161
0.000	0.000	0.000	0.000	0.000	0.000	0.000	0.000	0.000	0.000	0.000	0.000	0.000	0.000	0.000
15.372	15.391	15.516	15.347	15.598	15.305	15.603	15.313	15.571	15.356	15.491	15.531	15.344	15.239	15.548
7.341	7.181	6.721	7.296	6.675	7.370	6.679	7.385	6.687	7.088	6.660	6.711	7.151	7.608	6.598
0.659	0.819	1.279	0.704	1.325	0.630	1.321	0.615	1.313	0.912	1.340	1.289	0.849	0.392	1.402
8.000	8.000	8.000	8.000	8.000	8.000	8.000	8.000	8.000	8.000	8.000	8.000	8.000	8.000	8.000
0.312	0.324	0.510	0.347	0.493	0.280	0.465	0.268	0.500	0.309	0.468	0.492	0.377	0.176	0.449
0.023	0.050	0.106	0.039	0.101	0.031	0.110	0.026	0.096	0.057	0.114	0.115	0.052	0.017	0.124
0.079	0.198	0.255	0.116	0.248	0.159	0.153	0.144	0.222	0.323	0.347	0.176	0.189	0.107	0.378
0.000	0.000	0.000	0.000	0.000	0.000	0.019	0.000	0.000	0.000	0.000	0.000	0.000	0.000	0.000
0.000	0.000	0.000	0.000	0.000	0.000	0.000	0.000	0.000	0.000	0.006	0.000	0.000	0.000	0.008
3.058	2.854	2.400	2.913	2.471	3.025	2.410	3.029	2.400	2.868	2.411	2.426	2.817	3.270	2.389
0.000	0.000	0.000	0.000	0.000	0.000	0.000	0.000	0.000	0.000	0.000	0.000	0.000	0.000	0.000
1.486	1.533	1.691	1.536	1.651	1.468	1.802	1.481	1.738	1.393	1.614	1.744	1.522	1.384	1.604
0.042	0.041	0.039	0.048	0.036	0.036	0.040	0.052	0.044	0.049	0.040	0.047	0.042	0.045	0.048
5.000	5.000	5.000	5.000	5.000	5.000	5.000	5.000	5.000	5.000	5.000	5.000	5.000	5.000	5.000
0.000	0.000	0.000	0.000	0.000	0.000	0.000	0.000	0.000	0.000	0.000	0.000	0.000	0.000	0.000
0.000	0.000	0.000	0.000	0.000	0.000	0.000	0.000	0.000	0.000	0.000	0.000	0.000	0.000	0.000
0.000	0.000	0.000	0.000	0.000	0.000	0.000	0.000	0.000	0.000	0.000	0.000	0.000	0.000	0.000
0.000	0.000	0.000	0.000	0.000	0.000	0.000	0.000	0.000	0.000	0.000	0.000	0.000	0.000	0.000
0.000	0.000	0.000	0.000	0.000	0.000	0.000	0.000	0.000	0.000	0.000	0.000	0.000	0.000	0.000
0.000	0.000	0.000	0.000	0.000	0.000	0.000	0.000	0.000	0.000	0.000	0.000	0.000	0.000	0.000
0.000	0.000	0.000	0.000	0.000	0.000	0.000	0.000	0.000	0.000	0.000	0.000	0.000	0.000	0.000
0.000	0.000	0.000	0.000	0.000	0.000	0.000	0.000	0.000	0.000	0.000	0.000	0.000	0.000	0.000
0.000	0.000	0.000	0.000	0.000	0.000	0.000	0.000	0.000	0.000	0.000	0.000	0.000	0.000	0.000
1.999	1.949	1.934	1.963	1.944	1.953	2.000	1.979	1.986	1.947	1.936	1.976	1.956	1.973	1.932
0.001	0.051	0.066	0.037	0.056	0.047	0.000	0.020	0.014	0.053	0.064	0.024	0.044	0.027	0.068
2.000	2.000	2.000	2.000	2.000	2.000	2.000	2.000	2.000	2.000	2.000	2.000	2.000	2.000	2.000
0.171	0.163	0.193	0.126	0.230	0.115	0.253	0.115	0.239	0.129	0.182	0.243	0.146	0.068	0.215
0.000	0.000	0.000	0.000	0.000	0.000	0.016	0.000	0.000	0.000	0.000	0.000	0.000	0.000	0.000
0.000	0.000	0.000	0.000	0.000	0.000	0.000	0.000	0.000	0.000	0.000	0.000	0.000	0.000	0.000
0.000	0.000	0.000	0.000	0.000	0.000	0.000	0.000	0.000	0.000	0.000	0.000	0.000	0.000	0.000
0.000	0.000	0.000	0.000	0.000	0.000	0.000	0.000	0.000	0.000	0.000	0.000	0.000	0.000	0.000
0.000	0.000	0.000	0.000	0.000	0.000	0.000	0.000	0.000	0.000	0.000	0.000	0.000	0.000	0.000
0.000	0.000	0.000	0.000	0.000	0.000	0.000	0.000	0.000	0.000	0.000	0.000	0.000	0.000	0.000
0.000	0.000	0.000	0.000	0.000	0.000	0.000	0.000	0.000	0.000	0.000	0.000	0.000	0.000	0.000
0.000	0.000	0.000	0.000	0.000	0.000	0.000	0.000	0.000	0.000	0.000	0.000	0.000	0.000	0.000
0.000	0.000	0.000	0.000	0.000	0.000	0.000	0.000	0.000	0.000	0.000	0.000	0.000	0.000	0.000
0.000	0.000	0.000	0.000	0.000	0.000	0.000	0.000	0.000	0.000	0.000	0.000	0.000	0.000	0.000
0.052	0.086	0.176	0.074	0.209	0.060	0.179	0.057	0.173	0.089	0.173	0.173	0.078	0.032	0.172
0.777	0.751	0.631	0.800	0.562	0.825	0.552	0.828	0.588	0.782	0.645	0.584	0.777	0.899	0.613
1.000	1.000	1.000	1.000	1.000	1.000	1.000	1.000	1.000	1.000	1.000	1.000	1.000	1.000	1.000
15.223	15.249	15.369	15.200	15.438	15.175	15.448	15.172	15.412	15.218	15.355	15.415	15.223	15.100	15.387
0.149	0.142	0.147	0.147	0.160	0.130	0.156	0.141	0.159	0.137	0.136	0.116	0.121	0.138	0.161
0.000	0.000	0.000	0.000	0.000	0.000	0.000	0.000	0.000	0.000	0.000	0.000	0.000	0.000	0.000
1.851	1.858	1.853	1.853	1.840	1.870	1.844	1.859	1.841	1.863	1.864	1.884	1.879	1.862	1.839
2.000	2.000	2.000	2.000	2.000	2.000	2.000	2.000	2.000	2.000	2.000	2.000	2.000	2.000	2.000
7.341	7.181	6.721	7.296	6.675	7.370	6.679	7.385	6.687	7.088	6.660	6.711	7.151	7.608	6.598
0.673	0.651	0.587	0.655	0.600	0.673	0.572	0.672	0.580	0.673	0.599	0.582	0.649	0.703	0.598

29	30	31	32	33	34	35	36	37	38	39	40	41	42	43
NP-012 high Si Old	NP-012 Old	NP-012 high Si Old	NP-012 high Si Old	NP-012 Old	NP-012 high Si Old	NP-013 Old	NP-013 high Si Old	NP-013 Old	NP-013 high Si Old	NP-013 Old	NP-013 high Si Old	NP-013 high Si Old	NP-013 Old	NP-013 Old
Amp-Bt tonalite	Amp-Bt tonalite	Amp-Bt tonalite	Amp-Bt tonalite	Amp-Bt tonalite	Amp-Bt tonalite	Horn-blendite	Horn-blendite	Horn-blendite	Horn-blendite	Horn-blendite	Horn-blendite	Horn-blendite	Horn-blendite	Horn-blendite
51.879	45.021	50.285	51.681	46.179	50.651	47.449	50.814	45.479	53.834	46.753	49.199	51.273	46.712	46.812
0.271	1.248	0.450	0.206	1.132	0.385	1.026	0.391	1.013	0.164	0.912	0.513	0.308	0.953	0.796
5.452	10.705	6.260	5.247	10.203	5.877	9.492	5.798	10.361	3.702	9.293	7.909	5.958	9.671	9.672
b.d.l.	b.d.l.	b.d.l.	b.d.l.	b.d.l.	b.d.l.	b.d.l.	b.d.l.	b.d.l.	b.d.l.	b.d.l.	b.d.l.	b.d.l.	b.d.l.	b.d.l.
b.d.l.	0.057	b.d.l.	0.065	b.d.l.	b.d.l.	0.120	0.163	0.186	b.d.l.	0.157	0.105	0.147	0.216	0.206
2.880	5.153	1.728	2.058	2.634	1.640	2.015	0.462	0.704	1.489	0.413	1.012	1.966	0.838	1.175
14.322	11.197	13.729	14.318	11.197	13.579	13.325	15.209	12.436	16.589	12.890	14.009	15.390	13.035	12.955
12.599	12.194	12.624	12.723	12.481	12.565	12.610	12.884	12.818	12.760	12.653	12.765	12.740	12.625	12.855
0.401	0.342	0.310	0.376	0.360	0.289	0.301	0.316	0.245	0.318	0.274	0.282	0.291	0.288	0.329
11.228	11.421	12.072	11.595	13.660	12.685	10.971	10.547	12.541	9.103	12.268	11.245	9.528	11.621	11.825
b.d.l.	0.292	b.d.l.	b.d.l.	b.d.l.	b.d.l.	b.d.l.	b.d.l.	b.d.l.	b.d.l.	b.d.l.	b.d.l.	b.d.l.	b.d.l.	b.d.l.
0.505	0.809	0.647	0.427	0.843	0.704	0.947	0.634	0.990	0.383	0.999	0.874	0.579	0.954	0.928
0.328	0.901	0.343	0.340	0.920	0.349	0.670	0.290	0.927	0.103	0.704	0.404	0.300	0.783	0.646
0.266	0.312	0.280	0.258	0.259	0.288	0.247	0.239	0.253	0.214	0.219	0.239	0.205	0.237	0.245
b.d.l.	b.d.l.	b.d.l.	b.d.l.	b.d.l.	b.d.l.	b.d.l.	b.d.l.	b.d.l.	b.d.l.	b.d.l.	b.d.l.	b.d.l.	b.d.l.	b.d.l.
1.977	1.887	1.938	1.967	1.928	1.937	1.957	1.965	1.915	2.015	1.936	1.964	1.999	1.937	1.939
-0.112	-0.131	-0.118	-0.109	-0.109	-0.121	-0.104	-0.101	-0.107	-0.090	-0.092	-0.101	-0.086	-0.100	-0.103
–	–	–	–	–	–	–	–	–	–	–	–	–	–	–
101.997	101.407	100.547	101.152	101.687	100.827	101.026	99.611	99.762	100.584	99.380	100.420	100.598	99.770	100.280
7.350	6.558	7.253	7.384	6.711	7.300	6.830	7.325	6.691	7.603	6.865	7.084	7.302	6.821	6.812
0.029	0.137	0.049	0.022	0.124	0.042	0.111	0.042	0.112	0.017	0.101	0.056	0.033	0.105	0.087
0.910	1.838	1.064	0.884	1.747	0.998	1.610	0.985	1.796	0.616	1.608	1.342	1.000	1.664	1.659
0.000	0.000	0.000	0.000	0.000	0.000	0.000	0.000	0.000	0.000	0.000	0.000	0.000	0.000	0.000
0.000	0.007	0.000	0.007	0.000	0.000	0.014	0.019	0.022	0.000	0.018	0.012	0.017	0.025	0.024
0.307	0.565	0.188	0.221	0.288	0.178	0.218	0.050	0.078	0.158	0.046	0.110	0.211	0.092	0.129
3.025	2.432	2.952	3.050	2.426	2.918	2.859	3.269	2.728	3.493	2.822	3.007	3.268	2.838	2.810
1.912	1.903	1.951	1.948	1.943	1.940	1.945	1.990	2.020	1.931	1.990	1.969	1.944	1.975	2.004
0.048	0.042	0.038	0.046	0.044	0.035	0.037	0.039	0.031	0.038	0.034	0.034	0.035	0.036	0.041
1.330	1.391	1.456	1.386	1.660	1.529	1.321	1.272	1.543	1.075	1.506	1.354	1.135	1.419	1.439
0.000	0.031	0.000	0.000	0.000	0.000	0.000	0.000	0.000	0.000	0.000	0.000	0.000	0.000	0.000
0.139	0.228	0.181	0.118	0.238	0.197	0.264	0.177	0.282	0.105	0.284	0.244	0.160	0.270	0.262
0.059	0.167	0.063	0.062	0.171	0.064	0.123	0.053	0.174	0.019	0.132	0.074	0.055	0.146	0.120
0.119	0.144	0.128	0.117	0.119	0.131	0.112	0.109	0.118	0.096	0.102	0.109	0.092	0.109	0.113
0.000	0.000	0.000	0.000	0.000	0.000	0.000	0.000	0.000	0.000	0.000	0.000	0.000	0.000	0.000
15.230	15.442	15.322	15.244	15.471	15.332	15.444	15.330	15.595	15.150	15.508	15.396	15.251	15.501	15.499
7.350	6.558	7.253	7.384	6.711	7.300	6.830	7.325	6.691	7.603	6.865	7.084	7.302	6.821	6.812
0.650	1.442	0.747	0.616	1.289	0.700	1.170	0.675	1.309	0.397	1.135	0.916	0.698	1.179	1.188
8.000	8.000	8.000	8.000	8.000	8.000	8.000	8.000	8.000	8.000	8.000	8.000	8.000	8.000	8.000
0.261	0.396	0.317	0.268	0.458	0.298	0.440	0.310	0.487	0.219	0.473	0.427	0.302	0.486	0.471
0.029	0.137	0.049	0.022	0.124	0.042	0.111	0.042	0.112	0.017	0.101	0.056	0.033	0.105	0.087
0.307	0.565	0.188	0.221	0.288	0.178	0.218	0.050	0.078	0.158	0.046	0.110	0.211	0.092	0.129
0.000	0.000	0.000	0.000	0.000	0.000	0.000	0.000	0.000	0.000	0.000	0.000	0.000	0.000	0.000
0.000	0.007	0.000	0.007	0.000	0.000	0.014	0.019	0.022	0.000	0.018	0.012	0.017	0.025	0.024
3.025	2.432	2.952	3.050	2.426	2.918	2.859	3.269	2.728	3.493	2.822	3.007	3.268	2.838	2.810
0.000	0.031	0.000	0.000	0.000	0.000	0.000	0.000	0.000	0.000	0.000	0.000	0.000	0.000	0.000
1.330	1.391	1.456	1.386	1.660	1.529	1.321	1.272	1.543	1.075	1.506	1.354	1.135	1.419	1.439
0.048	0.042	0.038	0.046	0.044	0.035	0.037	0.038	0.030	0.038	0.034	0.034	0.035	0.036	0.040
5.000	5.000	5.000	5.000	5.000	5.000	5.000	5.000	5.000	5.000	5.000	5.000	5.000	5.000	5.000
0.000	0.000	0.000	0.000	0.000	0.000	0.000	0.000	0.000	0.000	0.000	0.000	0.000	0.000	0.000
0.000	0.000	0.000	0.000	0.000	0.000	0.000	0.000	0.000	0.000	0.000	0.000	0.000	0.000	0.000
0.000	0.000	0.000	0.000	0.000	0.000	0.000	0.000	0.000	0.000	0.000	0.000	0.000	0.000	0.000
0.000	0.000	0.000	0.000	0.000	0.000	0.000	0.000	0.000	0.000	0.000	0.000	0.000	0.000	0.000
0.000	0.000	0.000	0.000	0.000	0.000	0.000	0.000	0.000	0.000	0.000	0.000	0.000	0.000	0.000
0.000	0.000	0.000	0.000	0.000	0.000	0.000	0.000	0.000	0.000	0.000	0.000	0.000	0.000	0.000
0.000	0.000	0.000	0.000	0.000	0.000	0.000	0.000	0.000	0.000	0.000	0.000	0.000	0.000	0.000
0.000	0.000	0.000	0.000	0.000	0.000	0.000	0.000	0.000	0.000	0.000	0.000	0.000	0.000	0.000
1.912	1.903	1.951	1.948	1.943	1.940	1.945	1.990	2.000	1.931	1.990	1.969	1.944	1.975	2.000
0.087	0.097	0.049	0.052	0.056	0.060	0.055	0.010	0.000	0.069	0.010	0.031	0.056	0.025	0.000
2.000	2.000	2.000	2.000	2.000	2.000	2.000	2.000	2.000	2.000	2.000	2.000	2.000	2.000	2.000
0.052	0.131	0.132	0.066	0.181	0.137	0.209	0.167	0.282	0.036	0.275	0.213	0.104	0.245	0.262
0.000	0.000	0.000	0.000	0.000	0.000	0.000	0.000	0.021	0.000	0.000	0.000	0.000	0.000	0.004
0.000	0.000	0.000	0.000	0.000	0.000	0.000	0.000	0.000	0.000	0.000	0.000	0.000	0.000	0.000
0.000	0.000	0.000	0.000	0.000	0.000	0.000	0.000	0.000	0.000	0.000	0.000	0.000	0.000	0.000
0.000	0.000	0.000	0.000	0.000	0.000	0.000	0.000	0.000	0.000	0.000	0.000	0.000	0.000	0.000
0.000	0.000	0.000	0.000	0.000	0.000	0.000	0.000	0.000	0.000	0.000	0.000	0.000	0.000	0.000
0.000	0.000	0.000	0.000	0.000	0.000	0.000	0.000	0.000	0.000	0.000	0.000	0.000	0.000	0.000
0.000	0.000	0.000	0.000	0.000	0.000	0.000	0.000	0.000	0.000	0.000	0.000	0.000	0.000	0.000
0.000	0.000	0.000	0.000	0.000	0.000	0.000	0.000	0.000	0.000	0.000	0.000	0.000	0.000	0.000
0.000	0.000	0.000	0.000	0.000	0.000	0.000	0.000	0.000	0.000	0.000	0.000	0.000	0.000	0.000
0.059	0.167	0.063	0.062	0.171	0.064	0.123	0.053	0.174	0.019	0.132	0.074	0.055	0.146	0.120
0.889	0.701	0.805	0.872	0.648	0.799	0.668	0.779	0.523	0.946	0.593	0.713	0.842	0.609	0.614
1.000	1.000	1.000	1.000	1.000	1.000	1.000	1.000	1.000	1.000	1.000	1.000	1.000	1.000	1.000
15.111	15.299	15.194	15.128	15.352	15.201	15.332	15.221	15.477	15.054	15.406	15.287	15.158	15.391	15.386
0.119	0.144	0.128	0.117	0.119	0.131	0.112	0.109	0.118	0.096	0.102	0.109	0.092	0.109	0.113
0.000	0.000	0.000	0.000	0.000	0.000	0.000	0.000	0.000	0.000	0.000	0.000	0.000	0.000	0.000
1.881	1.856	1.872	1.883	1.881	1.869	1.888	1.891	1.882	1.904	1.898	1.891	1.908	1.891	1.887
2.000	2.000	2.000	2.000	2.000	2.000	2.000	2.000	2.000	2.000	2.000	2.000	2.000	2.000	2.000
7.350	6.558	7.253	7.384	6.711	7.300	6.830	7.325	6.691	7.603	6.865	7.084	7.302	6.821	6.812
0.695	0.636	0.670	0.688	0.594	0.656	0.684	0.720	0.639	0.765	0.652	0.690	0.742	0.667	0.661

44	45	46	47	48	49	50	51	52	53	54	55	56	57	59
NP-013	NP-013 high Si	NP-013	NP-013	NP-013 high Si	NP-013 high Si	NP-013 high Si	NP-013	NP-013	NP-013 high Si	NP-013 high Si	NP-013	NP-013 high Si	NP-013	NP-013
Old	Old	Old	Old	Old	Old	Old	Old	Old	Old	Old	Old	Old	Old	Old
Horn-blendite	Horn-blendite	Horn-blendite	Horn-blendite	Horn-blendite	Horn-blendite	Horn-blendite	Horn-blendite	Horn-blendite	Horn-blendite	Horn-blendite	Horn-blendite	Horn-blendite	Horn-blendite	Horn-blendite
47.312	52.259	46.942	47.231	54.835	50.850	49.391	45.385	47.134	52.568	52.154	47.321	54.918	47.123	45.649
0.979	0.207	1.115	1.157	0.177	0.343	0.556	1.214	0.879	0.325	0.286	1.154	0.130	1.144	1.160
9.201	5.111	9.861	10.035	3.176	7.006	8.084	11.842	9.647	4.819	5.660	9.753	2.819	10.215	11.044
b.d.l.	b.d.l.	b.d.l.	b.d.l.	b.d.l.	b.d.l.	b.d.l.	b.d.l.	b.d.l.	b.d.l.	b.d.l.	b.d.l.	b.d.l.	0.147	b.d.l.
0.126	0.129	0.128	0.163	b.d.l.	0.151	0.159	0.161	0.097	0.125	0.247	0.225	0.049	0.221	0.170
0.845	0.293	1.916	2.268	0.579	2.814	2.593	3.376	2.526	2.318	2.148	1.442	0.575	2.265	3.509
13.488	15.845	13.098	13.476	17.067	15.167	14.512	12.328	13.103	15.999	15.448	13.008	16.864	13.200	12.699
12.637	12.948	12.620	12.746	12.906	12.778	12.848	12.310	12.809	12.869	12.870	12.593	13.167	12.686	12.164
0.321	0.286	0.299	0.286	0.322	0.289	0.303	0.275	0.296	0.330	0.293	0.303	0.317	0.294	0.298
11.190	10.235	11.296	10.448	9.426	9.464	9.926	10.596	11.191	9.516	9.883	11.616	10.209	10.915	9.804
b.d.l.	b.d.l.	b.d.l.	b.d.l.	b.d.l.	b.d.l.	b.d.l.	b.d.l.	b.d.l.	b.d.l.	b.d.l.	b.d.l.	b.d.l.	b.d.l.	b.d.l.
0.859	0.554	0.922	0.896	0.394	0.798	0.765	0.930	0.807	0.593	0.582	0.914	0.288	0.986	0.862
0.837	0.230	0.909	0.659	0.128	0.376	0.551	1.307	0.740	0.244	0.173	0.814	0.077	0.799	1.116
0.273	0.216	0.241	0.242	0.196	0.225	0.182	0.245	0.228	0.223	0.213	0.220	0.173	0.271	0.290
b.d.l.	b.d.l.	b.d.l.	b.d.l.	b.d.l.	b.d.l.	b.d.l.	0.025	b.d.l.	b.d.l.	b.d.l.	b.d.l.	b.d.l.	b.d.l.	b.d.l.
1.928	2.000	1.957	1.970	2.044	2.011	2.015	1.947	1.963	2.015	2.020	1.972	2.055	1.962	1.915
-0.115	-0.091	-0.101	-0.102	-0.083	-0.095	-0.077	-0.103	-0.096	-0.094	-0.090	-0.093	-0.073	-0.114	-0.122
–	–	–	–	–	–	–	-0.006	–	–	–	–	–	–	–
99.881	100.221	101.202	101.475	101.167	102.177	101.808	101.832	101.324	101.850	101.888	101.242	101.568	102.115	100.558
6.883	7.450	6.768	6.760	7.686	7.156	7.009	6.527	6.787	7.394	7.338	6.812	7.697	6.726	6.616
0.107	0.022	0.121	0.125	0.019	0.036	0.059	0.131	0.095	0.034	0.030	0.125	0.014	0.123	0.126
1.577	0.859	1.675	1.692	0.525	1.162	1.352	2.007	1.637	0.799	0.938	1.655	0.466	1.718	1.886
0.000	0.000	0.000	0.000	0.000	0.000	0.000	0.000	0.000	0.000	0.000	0.000	0.000	0.017	0.000
0.014	0.015	0.015	0.018	0.000	0.017	0.018	0.018	0.011	0.014	0.027	0.026	0.005	0.025	0.019
0.092	0.031	0.208	0.244	0.061	0.298	0.277	0.365	0.274	0.245	0.227	0.156	0.061	0.243	0.383
2.925	3.368	2.815	2.875	3.566	3.182	3.070	2.643	2.813	3.355	3.240	2.792	3.524	2.809	2.744
1.969	1.978	1.949	1.954	1.938	1.927	1.953	1.897	1.976	1.939	1.940	1.942	1.977	1.940	1.889
0.040	0.035	0.037	0.035	0.038	0.034	0.036	0.033	0.036	0.039	0.035	0.037	0.038	0.036	0.037
1.361	1.220	1.362	1.251	1.105	1.114	1.178	1.274	1.348	1.119	1.163	1.398	1.197	1.303	1.188
0.000	0.000	0.000	0.000	0.000	0.000	0.000	0.000	0.000	0.000	0.000	0.000	0.000	0.000	0.000
0.242	0.153	0.258	0.249	0.107	0.218	0.210	0.259	0.225	0.162	0.159	0.255	0.078	0.273	0.242
0.155	0.042	0.167	0.120	0.023	0.068	0.100	0.240	0.136	0.044	0.031	0.149	0.014	0.145	0.206
0.126	0.097	0.110	0.110	0.087	0.100	0.082	0.111	0.104	0.099	0.095	0.100	0.077	0.122	0.133
0.000	0.000	0.000	0.000	0.000	0.000	0.000	0.006	0.000	0.000	0.000	0.000	0.000	0.000	0.000
15.493	15.270	15.485	15.432	15.154	15.312	15.345	15.513	15.441	15.244	15.225	15.447	15.146	15.481	15.470
6.883	7.450	6.768	6.760	7.686	7.156	7.009	6.527	6.787	7.394	7.338	6.812	7.697	6.726	6.616
1.117	0.550	1.232	1.240	0.314	0.844	0.991	1.473	1.213	0.606	0.662	1.188	0.303	1.274	1.384
8.000	8.000	8.000	8.000	8.000	8.000	8.000	8.000	8.000	8.000	8.000	8.000	8.000	8.000	8.000
0.460	0.309	0.443	0.452	0.210	0.318	0.361	0.534	0.424	0.193	0.277	0.467	0.163	0.445	0.503
0.107	0.022	0.121	0.125	0.019	0.036	0.059	0.131	0.095	0.034	0.030	0.125	0.014	0.123	0.126
0.092	0.031	0.208	0.244	0.061	0.298	0.277	0.365	0.274	0.245	0.227	0.156	0.061	0.243	0.383
0.000	0.000	0.000	0.000	0.000	0.000	0.000	0.000	0.000	0.000	0.000	0.000	0.000	0.017	0.000
0.014	0.015	0.015	0.018	0.000	0.017	0.018	0.018	0.011	0.014	0.027	0.026	0.005	0.025	0.019
2.925	3.368	2.815	2.875	3.566	3.182	3.070	2.643	2.813	3.355	3.240	2.792	3.524	2.809	2.744
0.000	0.000	0.000	0.000	0.000	0.000	0.000	0.000	0.000	0.000	0.000	0.000	0.000	0.000	0.000
1.361	1.220	1.362	1.251	1.105	1.114	1.178	1.274	1.348	1.119	1.163	1.398	1.197	1.303	1.188
0.040	0.035	0.036	0.035	0.038	0.034	0.036	0.033	0.036	0.039	0.035	0.037	0.037	0.036	0.037
5.000	5.000	5.000	5.000	5.000	5.000	5.000	5.000	5.000	5.000	5.000	5.000	5.000	5.000	5.000
0.000	0.000	0.000	0.000	0.000	0.000	0.000	0.000	0.000	0.000	0.000	0.000	0.000	0.000	0.000
0.000	0.000	0.000	0.000	0.000	0.000	0.000	0.000	0.000	0.000	0.000	0.000	0.000	0.000	0.000
0.000	0.000	0.000	0.000	0.000	0.000	0.000	0.000	0.000	0.000	0.000	0.000	0.000	0.000	0.000
0.000	0.000	0.000	0.000	0.000	0.000	0.000	0.000	0.000	0.000	0.000	0.000	0.000	0.000	0.000
0.000	0.000	0.000	0.000	0.000	0.000	0.000	0.000	0.000	0.000	0.000	0.000	0.000	0.000	0.000
0.000	0.000	0.000	0.000	0.000	0.000	0.000	0.000	0.000	0.000	0.000	0.000	0.000	0.000	0.000
0.000	0.000	0.000	0.000	0.000	0.000	0.000	0.000	0.000	0.000	0.000	0.000	0.000	0.000	0.000
0.000	0.000	0.000	0.000	0.000	0.000	0.000	0.000	0.000	0.000	0.000	0.000	0.000	0.000	0.000
0.000	0.000	0.000	0.000	0.000	0.000	0.000	0.000	0.000	0.000	0.000	0.000	0.000	0.000	0.000
1.969	1.978	1.949	1.954	1.938	1.927	1.953	1.897	1.976	1.939	1.940	1.942	1.977	1.940	1.889
0.031	0.022	0.050	0.046	0.062	0.073	0.047	0.103	0.024	0.060	0.060	0.057	0.023	0.060	0.111
2.000	2.000	2.000	2.000	2.000	2.000	2.000	2.000	2.000	2.000	2.000	2.000	2.000	2.000	2.000
0.212	0.131	0.207	0.203	0.045	0.144	0.164	0.156	0.202	0.101	0.099	0.198	0.056	0.213	0.131
0.000	0.000	0.000	0.000	0.000	0.000	0.000	0.000	0.000	0.000	0.000	0.000	0.000	0.000	0.000
0.000	0.000	0.000	0.000	0.000	0.000	0.000	0.000	0.000	0.000	0.000	0.000	0.000	0.000	0.000
0.000	0.000	0.000	0.000	0.000	0.000	0.000	0.000	0.000	0.000	0.000	0.000	0.000	0.000	0.000
0.000	0.000	0.000	0.000	0.000	0.000	0.000	0.000	0.000	0.000	0.000	0.000	0.000	0.000	0.000
0.000	0.000	0.000	0.000	0.000	0.000	0.000	0.000	0.000	0.000	0.000	0.000	0.000	0.000	0.000
0.000	0.000	0.000	0.000	0.000	0.000	0.000	0.000	0.000	0.000	0.000	0.000	0.000	0.000	0.000
0.000	0.000	0.000	0.000	0.000	0.000	0.000	0.000	0.000	0.000	0.000	0.000	0.000	0.000	0.000
0.000	0.000	0.000	0.000	0.000	0.000	0.000	0.000	0.000	0.000	0.000	0.000	0.000	0.000	0.000
0.000	0.000	0.000	0.000	0.000	0.000	0.000	0.000	0.000	0.000	0.000	0.000	0.000	0.000	0.000
0.000	0.000	0.000	0.000	0.000	0.000	0.000	0.000	0.000	0.000	0.000	0.000	0.000	0.000	0.000
0.155	0.042	0.167	0.120	0.023	0.068	0.100	0.240	0.136	0.044	0.031	0.149	0.014	0.145	0.206
0.633	0.827	0.625	0.677	0.932	0.788	0.736	0.604	0.662	0.855	0.870	0.653	0.931	0.642	0.663
1.000	1.000	1.000	1.000	1.000	1.000	1.000	1.000	1.000	1.000	1.000	1.000	1.000	1.000	1.000
15.367	15.172	15.375	15.323	15.068	15.212	15.263	15.396	15.338	15.145	15.130	15.347	15.069	15.358	15.337
0.126	0.097	0.110	0.110	0.087	0.100	0.082	0.111	0.104	0.099	0.095	0.100	0.077	0.122	0.133
0.000	0.000	0.000	0.000	0.000	0.000	0.000	0.006	0.000	0.000	0.000	0.000	0.000	0.000	0.000
1.874	1.903	1.890	1.890	1.913	1.900	1.918	1.882	1.896	1.901	1.905	1.900	1.923	1.878	1.867
2.000	2.000	2.000	2.000	2.000	2.000	2.000	2.000	2.000	2.000	2.000	2.000	2.000	2.000	2.000
6.883	7.450	6.768	6.760	7.686	7.156	7.009	6.527	6.787	7.394	7.338	6.812	7.697	6.726	6.616
0.682	0.734	0.674	0.697	0.763	0.741	0.723	0.675	0.676	0.750	0.736	0.666	0.746	0.683	0.698

60	61	62	64	65	66	67	68	69	70	72	73	74	75	76
NP-013	NP-013 high Si	NP-013	NP-013	NP-020	NP-020	NP-020	NP-020	NP-020	NP-020	NP-020	NP-020	NP-020	NP-007	NP-007
Old	Old	Old	Old	Old	Old	Old	Old	Old	Old	Old	Old	Old	Young	Young
Horn-blendite	Horn-blendite	Horn-blendite	Horn-blendite	medium-grained gabbro	medium-grained gabbro	medium-grained gabbro	medium-grained gabbro	medium-grained gabbro	medium-grained gabbro	medium-grained gabbro	medium-grained gabbro	medium-grained gabbro	medium-grained Amp-Bt granodiorite	medium-grained Amp-Bt granodiorite
45.147	54.758	44.723	48.495	42.405	42.015	42.149	41.822	42.707	42.477	42.141	41.732	42.262	41.625	42.152
1.373	0.168	1.311	1.155	0.467	0.428	0.557	0.541	0.511	0.485	0.889	0.542	0.507	0.836	1.108
11.277	2.843	11.310	8.523	14.931	16.135	15.312	15.774	15.450	15.984	14.472	16.221	16.125	11.408	10.694
b.d.l.	b.d.l.	b.d.l.	b.d.l.	b.d.l.	b.d.l.	b.d.l.	0.129	b.d.l.	b.d.l.	0.141	0.128	b.d.l.	b.d.l.	b.d.l.
0.171	b.d.l.	0.157	0.198	b.d.l.	b.d.l.	b.d.l.	b.d.l.	b.d.l.	b.d.l.	b.d.l.	b.d.l.	b.d.l.	b.d.l.	b.d.l.
3.081	1.146	2.890	1.771	4.789	4.529	5.879	4.861	4.638	3.523	7.898	5.580	6.351	3.524	3.503
12.256	17.292	12.151	14.586	9.054	8.870	9.095	8.817	9.211	8.952	9.636	8.537	9.017	5.968	6.258
12.216	13.068	12.329	12.656	11.533	11.703	11.403	11.618	11.636	11.656	10.850	11.257	11.317	11.899	11.847
0.302	0.233	0.257	0.251	0.227	0.187	0.167	0.190	0.159	0.186	0.250	0.213	0.206	0.495	0.593
10.738	9.228	11.067	9.603	12.067	11.772	11.187	12.092	12.154	12.226	9.596	11.526	10.638	20.097	20.137
b.d.l.	b.d.l.	b.d.l.	b.d.l.	b.d.l.	b.d.l.	0.000	b.d.l.	b.d.l.	b.d.l.	b.d.l.	b.d.l.	b.d.l.	b.d.l.	b.d.l.
1.049	0.311	1.036	0.818	1.724	1.486	1.658	1.726	1.850	1.554	1.814	1.779	1.683	1.037	1.178
0.994	0.125	1.046	0.669	0.173	0.251	0.214	0.260	0.191	0.239	0.545	0.225	0.194	1.444	1.362
0.292	0.221	0.214	0.259	0.159	0.143	0.134	0.104	0.109	0.119	0.163	0.130	0.130	0.236	0.207
b.d.l.	b.d.l.	b.d.l.	b.d.l.	b.d.l.	b.d.l.	b.d.l.	0.021	b.d.l.	b.d.l.	b.d.l.	b.d.l.	b.d.l.	0.025	0.028
1.910	2.030	1.936	1.965	1.926	1.940	1.940	1.952	1.975	1.958	1.927	1.944	1.960	1.814	1.837
-0.123	-0.093	-0.090	-0.109	-0.067	-0.060	-0.056	-0.044	-0.046	-0.050	-0.069	-0.055	-0.055	-0.099	-0.087
–	–	–	–	–	–	–	-0.005	–	–	–	–	–	-0.006	-0.006
100.683	101.330	100.338	100.840	99.388	99.399	99.639	99.858	100.545	99.309	100.253	99.759	100.335	100.303	100.810
6.563	7.672	6.538	6.937	6.283	6.208	6.220	6.178	6.251	6.271	6.189	6.158	6.177	6.406	6.455
0.150	0.018	0.144	0.124	0.052	0.048	0.062	0.060	0.056	0.054	0.098	0.060	0.056	0.097	0.128
1.932	0.469	1.948	1.437	2.607	2.809	2.663	2.746	2.665	2.781	2.505	2.821	2.778	2.069	1.930
0.000	0.000	0.000	0.000	0.000	0.000	0.000	0.015	0.000	0.000	0.017	0.015	0.000	0.000	0.000
0.020	0.000	0.018	0.022	0.000	0.000	0.000	0.000	0.000	0.000	0.000	0.000	0.000	0.000	0.000
0.337	0.121	0.318	0.191	0.534	0.504	0.653	0.540	0.511	0.391	0.873	0.620	0.699	0.408	0.404
2.656	3.612	2.648	3.110	2.000	1.954	2.001	1.942	2.010	1.970	2.110	1.878	1.965	1.369	1.429
1.903	1.962	1.931	1.939	1.831	1.852	1.803	1.839	1.825	1.844	1.707	1.779	1.772	1.962	1.944
0.037	0.028	0.032	0.030	0.028	0.023	0.021	0.024	0.020	0.023	0.031	0.027	0.026	0.065	0.077
1.305	1.081	1.353	1.149	1.495	1.454	1.381	1.494	1.488	1.509	1.178	1.422	1.300	2.587	2.579
0.000	0.000	0.000	0.000	0.000	0.000	0.000	0.000	0.000	0.000	0.000	0.000	0.000	0.000	0.000
0.296	0.084	0.294	0.227	0.495	0.426	0.474	0.494	0.525	0.445	0.516	0.509	0.477	0.309	0.350
0.184	0.022	0.195	0.122	0.033	0.047	0.040	0.049	0.036	0.045	0.102	0.042	0.036	0.283	0.266
0.134	0.098	0.099	0.117	0.075	0.067	0.063	0.049	0.050	0.056	0.076	0.061	0.060	0.115	0.100
0.000	0.000	0.000	0.000	0.000	0.000	0.000	0.005	0.000	0.000	0.000	0.000	0.000	0.007	0.007
15.517	15.167	15.519	15.406	15.433	15.392	15.380	15.436	15.436	15.389	15.401	15.391	15.345	15.676	15.666
6.563	7.672	6.538	6.937	6.283	6.208	6.220	6.178	6.251	6.271	6.189	6.158	6.177	6.406	6.455
1.437	0.328	1.462	1.063	1.717	1.792	1.780	1.822	1.749	1.729	1.811	1.842	1.823	1.594	1.545
8.000	8.000	8.000	8.000	8.000	8.000	8.000	8.000	8.000	8.000	8.000	8.000	8.000	8.000	8.000
0.495	0.141	0.487	0.373	0.890	1.017	0.883	0.925	0.916	1.052	0.693	0.978	0.955	0.475	0.384
0.150	0.018	0.144	0.124	0.052	0.048	0.062	0.060	0.056	0.054	0.098	0.060	0.056	0.097	0.128
0.337	0.121	0.318	0.191	0.534	0.504	0.653	0.540	0.511	0.391	0.873	0.620	0.699	0.408	0.404
0.000	0.000	0.000	0.000	0.000	0.000	0.000	0.015	0.000	0.000	0.017	0.015	0.000	0.000	0.000
0.020	0.000	0.018	0.022	0.000	0.000	0.000	0.000	0.000	0.000	0.000	0.000	0.000	0.000	0.000
2.656	3.612	2.648	3.110	2.000	1.954	2.001	1.942	2.010	1.970	2.110	1.878	1.965	1.369	1.429
0.000	0.000	0.000	0.000	0.000	0.000	0.000	0.000	0.000	0.000	0.000	0.000	0.000	0.000	0.000
1.305	1.081	1.353	1.149	1.495	1.454	1.381	1.494	1.488	1.509	1.178	1.422	1.300	2.587	2.579
0.037	0.027	0.032	0.030	0.028	0.023	0.021	0.024	0.020	0.023	0.031	0.027	0.025	0.064	0.077
5.000	5.000	5.000	5.000	5.000	5.000	5.000	5.000	5.000	5.000	5.000	5.000	5.000	5.000	5.000
0.000	0.000	0.000	0.000	0.000	0.000	0.000	0.000	0.000	0.000	0.000	0.000	0.000	0.000	0.000
0.000	0.000	0.000	0.000	0.000	0.000	0.000	0.000	0.000	0.000	0.000	0.000	0.000	0.000	0.000
0.000	0.000	0.000	0.000	0.000	0.000	0.000	0.000	0.000	0.000	0.000	0.000	0.000	0.000	0.000
0.000	0.000	0.000	0.000	0.000	0.000	0.000	0.000	0.000	0.000	0.000	0.000	0.000	0.000	0.000
0.000	0.000	0.000	0.000	0.000	0.000	0.000	0.000	0.000	0.000	0.000	0.000	0.000	0.000	0.000
0.000	0.000	0.000	0.000	0.000	0.000	0.000	0.000	0.000	0.000	0.000	0.000	0.000	0.000	0.000
0.000	0.000	0.000	0.000	0.000	0.000	0.000	0.000	0.000	0.000	0.000	0.000	0.000	0.000	0.000
0.000	0.000	0.000	0.000	0.000	0.000	0.000	0.000	0.000	0.000	0.000	0.000	0.000	0.000	0.000
0.000	0.000	0.000	0.000	0.000	0.000	0.000	0.000	0.000	0.000	0.000	0.000	0.000	0.000	0.000
1.903	1.962	1.931	1.939	1.831	1.852	1.803	1.839	1.825	1.844	1.707	1.779	1.772	1.962	1.944
0.097	0.038	0.069	0.060	0.169	0.148	0.197	0.161	0.175	0.156	0.293	0.221	0.228	0.038	0.056
2.000	2.000	2.000	2.000	2.000	2.000	2.000	2.000	2.000	2.000	2.000	2.000	2.000	2.000	2.000
0.198	0.046	0.225	0.167	0.326	0.278	0.277	0.333	0.350	0.289	0.224	0.288	0.249	0.272	0.293
0.000	0.000	0.000	0.000	0.000	0.000	0.000	0.000	0.000	0.000	0.000	0.000	0.000	0.000	0.000
0.000	0.000	0.000	0.000	0.000	0.000	0.000	0.000	0.000	0.000	0.000	0.000	0.000	0.000	0.000
0.000	0.000	0.000	0.000	0.000	0.000	0.000	0.000	0.000	0.000	0.000	0.000	0.000	0.000	0.000
0.000	0.000	0.000	0.000	0.000	0.000	0.000	0.000	0.000	0.000	0.000	0.000	0.000	0.000	0.000
0.000	0.000	0.000	0.000	0.000	0.000	0.000	0.000	0.000	0.000	0.000	0.000	0.000	0.000	0.000
0.000	0.000	0.000	0.000	0.000	0.000	0.000	0.000	0.000	0.000	0.000	0.000	0.000	0.000	0.000
0.000	0.000	0.000	0.000	0.000	0.000	0.000	0.000	0.000	0.000	0.000	0.000	0.000	0.000	0.000
0.000	0.000	0.000	0.000	0.000	0.000	0.000	0.000	0.000	0.000	0.000	0.000	0.000	0.000	0.000
0.000	0.000	0.000	0.000	0.000	0.000	0.000	0.000	0.000	0.000	0.000	0.000	0.000	0.000	0.000
0.000	0.000	0.000	0.000	0.000	0.000	0.000	0.000	0.000	0.000	0.000	0.000	0.000	0.000	0.000
0.184	0.022	0.195	0.122	0.033	0.047	0.040	0.049	0.036	0.045	0.102	0.042	0.036	0.283	0.266
0.617	0.931	0.580	0.711	0.641	0.675	0.682	0.618	0.615	0.666	0.674	0.669	0.715	0.445	0.441
1.000	1.000	1.000	1.000	1.000	1.000	1.000	1.000	1.000	1.000	1.000	1.000	1.000	1.000	1.000
15.383	15.069	15.420	15.289	15.358	15.325	15.318	15.382	15.385	15.334	15.326	15.330	15.285	15.555	15.559
0.134	0.098	0.099	0.117	0.075	0.067	0.063	0.049	0.050	0.056	0.076	0.061	0.060	0.115	0.100
0.000	0.000	0.000	0.000	0.000	0.000	0.000	0.005	0.000	0.000	0.000	0.000	0.000	0.007	0.007
1.866	1.902	1.901	1.883	1.925	1.933	1.937	1.946	1.950	1.944	1.924	1.939	1.940	1.879	1.892
2.000	2.000	2.000	2.000	2.000	2.000	2.000	2.000	2.000	2.000	2.000	2.000	2.000	2.000	2.000
6.563	7.672	6.538	6.937	6.283	6.208	6.220	6.178	6.251	6.271	6.189	6.158	6.177	6.406	6.455
0.670	0.770	0.662	0.730	0.572	0.573	0.592	0.565	0.575	0.566	0.642	0.569	0.602	0.346	0.357

77	78	79	80	81	82	83	84	85	86	87	88	89	90	91
NP-007	NP-007	NP-007	NP-007	NP-009	NP-009	NP-009	NP-009	NP-009	NP-009	NP-009	NP-009	NP-009	NP-009	NP-009
Young medium-grained Amp-Bt granodiorite	Young medium-grained Amp-Bt granodiorite	Young medium-grained Amp-Bt granodiorite	Young medium-grained Amp-Bt granodiorite	Young medium-grained Amp-Bt tonalite	Young medium-grained Amp-Bt tonalite	Young medium-grained Amp-Bt tonalite	Young medium-grained Amp-Bt tonalite	Young medium-grained Amp-Bt tonalite	Young medium-grained Amp-Bt tonalite	Young medium-grained Amp-Bt tonalite	Young medium-grained Amp-Bt tonalite	Young medium-grained Amp-Bt tonalite	Young medium-grained Amp-Bt tonalite	Young medium-grained Amp-Bt tonalite
40.797	40.994	40.850	41.313	43.904	43.781	43.892	44.649	44.261	45.763	44.112	44.823	43.548	44.465	43.378
0.948	0.876	0.890	0.899	1.611	1.558	1.301	0.619	0.782	0.519	1.531	0.684	1.505	0.719	1.502
11.954	12.022	12.023	11.371	10.756	10.737	10.058	9.899	10.585	9.612	10.264	10.242	10.552	10.154	11.248
b.d.l.	0.111	b.d.l.	b.d.l.	0.101	0.136	0.106	b.d.l.	0.124	b.d.l.	b.d.l.	0.097	b.d.l.	b.d.l.	0.179
b.d.l.	b.d.l.	b.d.l.	b.d.l.	b.d.l.	b.d.l.	b.d.l.	b.d.l.	b.d.l.	b.d.l.	b.d.l.	b.d.l.	b.d.l.	b.d.l.	b.d.l.
3.408	2.991	2.898	4.272	2.520	2.246	1.964	1.771	2.677	2.202	1.015	1.557	1.706	1.827	3.738
5.444	5.609	5.646	5.799	8.249	8.331	8.484	8.750	8.747	9.001	8.235	8.837	8.179	8.618	8.438
11.808	11.878	11.836	11.718	12.026	12.097	12.365	12.224	12.252	12.124	12.285	12.313	12.095	12.233	12.193
0.543	0.541	0.536	0.580	0.416	0.490	0.532	0.475	0.444	0.435	0.507	0.482	0.471	0.481	0.477
20.666	20.459	20.698	19.713	17.451	17.430	17.715	17.279	16.839	16.874	18.593	17.223	17.986	17.407	16.641
b.d.l.	b.d.l.	b.d.l.	b.d.l.	b.d.l.	b.d.l.	b.d.l.	b.d.l.	b.d.l.	b.d.l.	b.d.l.	b.d.l.	b.d.l.	b.d.l.	b.d.l.
1.182	1.106	1.365	1.059	0.957	1.012	0.848	0.868	0.960	0.783	0.842	0.870	0.969	0.881	1.049
1.572	1.538	1.504	1.422	1.062	1.032	1.029	0.962	1.054	0.878	1.218	0.975	1.160	1.008	1.108
0.185	0.209	0.183	0.200	0.100	0.114	0.134	0.103	0.107	0.107	0.111	0.108	0.096	0.068	0.095
0.046	0.033	0.047	0.042	0.035	0.027	b.d.l.	b.d.l.	0.039	b.d.l.	0.039	b.d.l.	0.033	b.d.l.	b.d.l.
1.823	1.818	1.827	1.817	1.939	1.931	1.915	1.927	1.932	1.946	1.925	1.940	1.922	1.946	1.958
-0.078	-0.088	-0.077	-0.084	-0.042	-0.048	-0.056	-0.043	-0.045	-0.045	-0.047	-0.045	-0.040	-0.029	-0.040
-0.010	-0.007	-0.011	-0.009	-0.008	-0.006	–	–	-0.009	–	-0.009	–	-0.007	–	–
100.287	100.089	100.214	100.112	101.076	100.868	100.287	99.482	100.749	100.199	100.622	100.105	100.174	99.779	101.964
6.312	6.338	6.318	6.377	6.560	6.556	6.620	6.748	6.619	6.835	6.639	6.725	6.580	6.709	6.436
0.110	0.102	0.104	0.104	0.181	0.176	0.148	0.070	0.088	0.058	0.173	0.077	0.171	0.082	0.168
2.180	2.190	2.191	2.068	1.894	1.895	1.788	1.763	1.865	1.692	1.820	1.811	1.879	1.805	1.967
0.000	0.014	0.000	0.000	0.012	0.016	0.013	0.000	0.015	0.000	0.000	0.012	0.000	0.000	0.021
0.000	0.000	0.000	0.000	0.000	0.000	0.000	0.000	0.000	0.000	0.000	0.000	0.000	0.000	0.000
0.397	0.348	0.337	0.496	0.283	0.253	0.223	0.201	0.301	0.247	0.115	0.176	0.194	0.207	0.417
1.256	1.293	1.302	1.334	1.837	1.860	1.908	1.972	1.950	2.004	1.848	1.977	1.843	1.938	1.866
1.957	1.967	1.961	1.938	1.925	1.941	1.998	1.979	1.963	1.940	1.981	1.979	1.958	1.977	1.938
0.071	0.071	0.070	0.076	0.053	0.062	0.068	0.061	0.056	0.055	0.065	0.061	0.060	0.061	0.060
2.674	2.645	2.677	2.545	2.180	2.183	2.234	2.184	2.106	2.108	2.340	2.161	2.273	2.196	2.065
0.000	0.000	0.000	0.000	0.000	0.000	0.000	0.000	0.000	0.000	0.000	0.000	0.000	0.000	0.000
0.355	0.331	0.409	0.317	0.277	0.294	0.248	0.254	0.278	0.227	0.246	0.253	0.284	0.258	0.302
0.310	0.303	0.297	0.280	0.202	0.197	0.198	0.185	0.201	0.167	0.234	0.187	0.224	0.194	0.210
0.091	0.102	0.090	0.098	0.047	0.054	0.064	0.049	0.051	0.051	0.053	0.051	0.046	0.032	0.045
0.012	0.009	0.012	0.011	0.009	0.007	0.000	0.000	0.010	0.000	0.010	0.000	0.008	0.000	0.000
15.724	15.713	15.769	15.644	15.461	15.493	15.508	15.468	15.503	15.384	15.523	15.470	15.520	15.461	15.494
6.312	6.338	6.318	6.377	6.560	6.556	6.620	6.748	6.619	6.835	6.639	6.725	6.580	6.709	6.436
1.688	1.662	1.682	1.623	1.440	1.444	1.380	1.252	1.381	1.165	1.361	1.275	1.420	1.291	1.564
8.000	8.000	8.000	8.000	8.000	8.000	8.000	8.000	8.000	8.000	8.000	8.000	8.000	8.000	8.000
0.492	0.528	0.510	0.445	0.453	0.451	0.407	0.512	0.484	0.527	0.459	0.536	0.459	0.514	0.403
0.110	0.102	0.104	0.104	0.181	0.176	0.148	0.070	0.088	0.058	0.173	0.077	0.171	0.082	0.168
0.397	0.348	0.337	0.496	0.283	0.253	0.223	0.201	0.301	0.247	0.115	0.176	0.194	0.207	0.417
0.000	0.014	0.000	0.000	0.012	0.016	0.013	0.000	0.015	0.000	0.000	0.012	0.000	0.000	0.021
0.000	0.000	0.000	0.000	0.000	0.000	0.000	0.000	0.000	0.000	0.000	0.000	0.000	0.000	0.000
1.256	1.293	1.302	1.334	1.837	1.860	1.908	1.972	1.950	2.004	1.848	1.977	1.843	1.938	1.866
0.000	0.000	0.000	0.000	0.000	0.000	0.000	0.000	0.000	0.000	0.000	0.000	0.000	0.000	0.000
2.674	2.645	2.677	2.545	2.180	2.183	2.234	2.184	2.106	2.108	2.340	2.161	2.273	2.196	2.065
0.071	0.071	0.070	0.075	0.053	0.062	0.068	0.061	0.056	0.055	0.065	0.061	0.060	0.061	0.060
5.000	5.000	5.000	5.000	5.000	5.000	5.000	5.000	5.000	5.000	5.000	5.000	5.000	5.000	5.000
0.000	0.000	0.000	0.000	0.000	0.000	0.000	0.000	0.000	0.000	0.000	0.000	0.000	0.000	0.000
0.000	0.000	0.000	0.000	0.000	0.000	0.000	0.000	0.000	0.000	0.000	0.000	0.000	0.000	0.000
0.000	0.000	0.000	0.000	0.000	0.000	0.000	0.000	0.000	0.000	0.000	0.000	0.000	0.000	0.000
0.000	0.000	0.000	0.000	0.000	0.000	0.000	0.000	0.000	0.000	0.000	0.000	0.000	0.000	0.000
0.000	0.000	0.000	0.000	0.000	0.000	0.000	0.000	0.000	0.000	0.000	0.000	0.000	0.000	0.000
0.000	0.000	0.000	0.000	0.000	0.000	0.000	0.000	0.000	0.000	0.000	0.000	0.000	0.000	0.000
0.000	0.000	0.000	0.000	0.000	0.000	0.000	0.000	0.000	0.000	0.000	0.000	0.000	0.000	0.000
0.000	0.000	0.000	0.000	0.000	0.000	0.000	0.000	0.000	0.000	0.000	0.000	0.000	0.000	0.000
1.957	1.967	1.961	1.938	1.925	1.941	1.998	1.979	1.963	1.940	1.981	1.979	1.958	1.977	1.938
0.043	0.033	0.039	0.062	0.075	0.059	0.002	0.021	0.037	0.060	0.019	0.021	0.042	0.023	0.062
2.000	2.000	2.000	2.000	2.000	2.000	2.000	2.000	2.000	2.000	2.000	2.000	2.000	2.000	2.000
0.312	0.299	0.371	0.255	0.202	0.235	0.246	0.234	0.241	0.167	0.226	0.232	0.242	0.235	0.240
0.000	0.000	0.000	0.000	0.000	0.000	0.000	0.000	0.000	0.000	0.000	0.000	0.000	0.000	0.000
0.000	0.000	0.000	0.000	0.000	0.000	0.000	0.000	0.000	0.000	0.000	0.000	0.000	0.000	0.000
0.000	0.000	0.000	0.000	0.000	0.000	0.000	0.000	0.000	0.000	0.000	0.000	0.000	0.000	0.000
0.000	0.000	0.000	0.000	0.000	0.000	0.000	0.000	0.000	0.000	0.000	0.000	0.000	0.000	0.000
0.000	0.000	0.000	0.000	0.000	0.000	0.000	0.000	0.000	0.000	0.000	0.000	0.000	0.000	0.000
0.000	0.000	0.000	0.000	0.000	0.000	0.000	0.000	0.000	0.000	0.000	0.000	0.000	0.000	0.000
0.000	0.000	0.000	0.000	0.000	0.000	0.000	0.000	0.000	0.000	0.000	0.000	0.000	0.000	0.000
0.000	0.000	0.000	0.000	0.000	0.000	0.000	0.000	0.000	0.000	0.000	0.000	0.000	0.000	0.000
0.000	0.000	0.000	0.000	0.000	0.000	0.000	0.000	0.000	0.000	0.000	0.000	0.000	0.000	0.000
0.000	0.000	0.000	0.000	0.000	0.000	0.000	0.000	0.000	0.000	0.000	0.000	0.000	0.000	0.000
0.310	0.303	0.297	0.280	0.202	0.197	0.198	0.185	0.201	0.167	0.234	0.187	0.224	0.194	0.210
0.378	0.398	0.333	0.465	0.595	0.568	0.556	0.581	0.558	0.666	0.540	0.581	0.534	0.571	0.550
1.000	1.000	1.000	1.000	1.000	1.000	1.000	1.000	1.000	1.000	1.000	1.000	1.000	1.000	1.000
15.622	15.602	15.667	15.535	15.405	15.432	15.444	15.419	15.442	15.334	15.460	15.418	15.466	15.429	15.450
0.091	0.102	0.090	0.098	0.047	0.054	0.064	0.049	0.051	0.051	0.053	0.051	0.046	0.032	0.045
0.012	0.009	0.012	0.011	0.009	0.007	0.000	0.000	0.010	0.000	0.010	0.000	0.008	0.000	0.000
1.897	1.889	1.898	1.891	1.944	1.939	1.936	1.951	1.940	1.949	1.937	1.949	1.946	1.968	1.955
2.000	2.000	2.000	2.000	2.000	2.000	2.000	2.000	2.000	2.000	2.000	2.000	2.000	2.000	2.000
6.312	6.338	6.318	6.377	6.560	6.556	6.620	6.748	6.619	6.835	6.639	6.725	6.580	6.709	6.436
0.320	0.328	0.327	0.344	0.457	0.460	0.461	0.474	0.481	0.487	0.441	0.478	0.448	0.469	0.475

92	93	94
NP-009	NP-009	NP-009
Young	Young	Young
medium-grained Amp-Bt tonalite	medium-grained Amp-Bt tonalite	medium-grained Amp-Bt tonalite
44.777	44.277	43.752
0.778	1.956	1.481
10.673	10.584	10.890
b.d.l.	b.d.l.	b.d.l.
b.d.l.	b.d.l.	b.d.l.
4.899	2.989	3.398
9.013	8.433	8.422
12.249	12.144	12.120
0.497	0.481	0.519
15.782	17.532	16.747
b.d.l.	b.d.l.	b.d.l.
0.922	1.053	0.802
1.103	1.006	1.259
0.113	0.092	b.d.l.
b.d.l.	b.d.l.	b.d.l.
1.969	1.974	1.996
-0.048	-0.039	–
–	–	–
102.728	102.482	101.387
6.564	6.532	6.518
0.086	0.217	0.166
1.844	1.840	1.912
0.000	0.000	0.000
0.000	0.000	0.000
0.540	0.332	0.381
1.970	1.855	1.871
1.924	1.920	1.934
0.062	0.060	0.065
1.935	2.163	2.087
0.000	0.000	0.000
0.262	0.301	0.232
0.206	0.189	0.239
0.052	0.043	0.000
0.000	0.000	0.000
15.445	15.453	15.405
6.564	6.532	6.518
1.436	1.468	1.482
8.000	8.000	8.000
0.408	0.373	0.430
0.086	0.217	0.166
0.540	0.332	0.381
0.000	0.000	0.000
0.000	0.000	0.000
1.970	1.855	1.871
0.000	0.000	0.000
1.935	2.163	2.087
0.061	0.060	0.065
5.000	5.000	5.000
0.000	0.000	0.000
0.000	0.000	0.000
0.000	0.000	0.000
0.000	0.000	0.000
0.000	0.000	0.000
0.000	0.000	0.000
0.000	0.000	0.000
0.000	0.000	0.000
0.000	0.000	0.000
1.924	1.920	1.934
0.076	0.080	0.066
2.000	2.000	2.000
0.186	0.221	0.166
0.000	0.000	0.000
0.000	0.000	0.000
0.000	0.000	0.000
0.000	0.000	0.000
0.000	0.000	0.000
0.000	0.000	0.000
0.000	0.000	0.000
0.000	0.000	0.000
0.000	0.000	0.000
0.000	0.000	0.000
0.206	0.189	0.239
0.608	0.590	0.595
1.000	1.000	1.000
15.392	15.410	15.405
0.052	0.043	0.000
0.000	0.000	0.000
1.948	1.957	2.000
2.000	2.000	2.000
6.564	6.532	6.518
0.504	0.462	0.473

CLINOPYROXENE formulae recalculated on the basis of 6 oxygen equivalents
Fe^{II}/Fe^{III} allocated assuming Papike (et al. 1974 in Putirka 2008)

	67	XX
Comment	NP-013	NP-013
Suite	Old	Old
Rock	Horn-blendite	Horn-blendite
SiO_2	53.067	53.110
TiO_2	0.140	0.165
Al_2O_3	1.348	1.368
Cr_2O_3	0.241	0.113
Fe_2O_3	0.817	1.031
MgO	14.334	14.077
CaO	24.212	24.480
MnO	0.323	0.290
FeO	5.077	5.085
Na_2O	0.426	0.493
F	0.110	b.d.l.
Σ	100.095	100.212
Si	1.967	1.967
Ti	0.004	0.005
Al	0.059	0.060
Cr	0.007	0.003
Fe^{III}	0.023	0.029
Mg	0.792	0.777
Ca	0.961	0.971
Mn	0.010	0.009
Fe^{II}	0.157	0.158
Na	0.031	0.035
Σ.atoms	4.011	4.014
Si_T	1.967	1.967
Al_T	0.033	0.033
Σ_T	2.000	2.000
Al_M_1	0.026	0.027
$Fe^{III}\_M_1$	0.023	0.029
Ti_M_1	0.004	0.005
Cr_M_1	0.007	0.003
Mg_M_1	0.792	0.777
$Fe^{II}\_M_1$	0.148	0.158
Mn_M_1	0.000	0.002
Σ_M_1	1.000	1.000
Mg_M_2	0.000	0.000
$Fe^{II}\_M_2$	0.009	0.000
Mn_M_2	0.010	0.008
Ca_M_2	0.961	0.971
Na_M_2	0.031	0.035
Σ_M_2	1.011	1.014
Σ_cations	4.011	4.014
Fe	0.180	0.186
Fe^{III}/Fe_{tot}	0.126	0.154
X_{Mg}	0.815	0.807
Al^{IV}/Al^{VI}	1.272	1.217
Al^{IV}	0.033	0.033
Al^{VI}	0.026	0.027
aDi	0.651	0.655
Jd	0.026	0.027
CaTs	0.000	0.000
CaTi	0.016	0.016
CrCaTs	0.004	0.002
DiHd	0.941	0.953
EnFs	0.015	0.005
Σ.end	1.003	1.003
En	0.012	0.004
Di	0.759	0.762

BIOTITE formulae recalculated on the basis of 22 charges

	1	2	3	4	5	6	7	8	9	10
Comment	NP-011	NP-011	NP-011	NP-011	NP-011	NP-011	NP-011	NP-011	NP-012	NP-012
Suite	Old	Old	Old	Old	Old	Old	Old	Old	Old	Old
Petrology	Amp-bearing QtzD	Amp-bearing QtzD	Amp-bearing QtzD	Amp-bearing QtzD	Amp-bearing QtzD	Amp-bearing QtzD	Amp-bearing QtzD	Amp-bearing QtzD	Amp-Bt tonalite	Amp-Bt tonalite
SiO_2	36.735	36.801	37.037	36.992	36.557	37.065	36.292	36.232	38.111	38.178
TiO_2	1.698	1.638	1.719	1.880	2.307	1.913	2.622	2.261	2.084	1.826
Al_2O_3	16.005	15.586	15.987	16.013	16.435	16.857	16.670	15.986	15.799	16.117
V_2O_3	b.d.l.	b.d.l.	b.d.l.	b.d.l.	0.098	b.d.l.	0.192	b.d.l.	b.d.l.	b.d.l.
Cr_2O_3	0.100	b.d.l.	0.068	0.049	b.d.l.	b.d.l.	b.d.l.	b.d.l.	b.d.l.	b.d.l.
MgO	12.066	12.350	11.899	12.013	9.714	9.740	9.651	9.220	13.420	13.279
CaO	b.d.l.	b.d.l.	b.d.l.	b.d.l.	b.d.l.	b.d.l.	b.d.l.	b.d.l.	b.d.l.	b.d.l.
MnO	0.325	0.256	0.306	0.335	0.207	0.280	0.268	0.206	0.240	0.241
FeO	17.592	18.479	18.204	17.579	20.049	20.246	19.226	20.875	17.243	17.053
BaO	0.312	0.218	0.294	0.359	0.437	0.360	0.652	0.415	0.189	0.213
Na_2O	0.088	b.d.l.	0.099	0.106	b.d.l.	0.124	b.d.l.	b.d.l.	0.075	0.093
K_2O	9.597	9.270	9.553	9.369	9.405	9.283	9.495	9.163	9.844	9.484
F	0.289	0.280	0.288	0.278	0.393	0.409	0.407	0.447	0.740	0.780
Cl	0.027	0.027	0.032	0.027	0.019	b.d.l.	b.d.l.	b.d.l.	b.d.l.	b.d.l.
H_2O	3.774	3.778	3.795	3.795	3.717	3.750	3.712	3.646	3.693	3.667
O=F	-0.122	-0.118	-0.121	-0.117	-0.165	-0.172	-0.171	-0.188	-0.312	-0.328
O=Cl	-0.006	-0.006	-0.007	-0.006	-0.004	–	–	–	–	–
Σ	98.481	98.559	99.153	98.672	99.168	99.855	99.015	98.262	101.126	100.602
Si	2.811	2.817	2.819	2.820	2.805	2.818	2.787	2.816	2.826	2.836
Ti	0.098	0.094	0.098	0.108	0.133	0.109	0.151	0.132	0.116	0.102
Al	1.443	1.406	1.434	1.439	1.486	1.510	1.509	1.464	1.381	1.411
V	0.000	0.000	0.000	0.000	0.006	0.000	0.012	0.000	0.000	0.000
Cr	0.006	0.000	0.004	0.003	0.000	0.000	0.000	0.000	0.000	0.000
Mg	1.377	1.409	1.350	1.365	1.111	1.104	1.105	1.068	1.484	1.471
Ca	0.000	0.000	0.000	0.000	0.000	0.000	0.000	0.000	0.000	0.000
Mn	0.021	0.017	0.020	0.022	0.013	0.018	0.017	0.014	0.015	0.015
Fe^{II}	1.126	1.183	1.159	1.121	1.287	1.287	1.235	1.357	1.069	1.059
Ba	0.009	0.007	0.009	0.011	0.013	0.011	0.020	0.013	0.005	0.006
Na	0.013	0.000	0.015	0.016	0.000	0.018	0.000	0.000	0.011	0.013
K	0.937	0.905	0.927	0.911	0.921	0.900	0.930	0.909	0.931	0.899
F	0.070	0.068	0.069	0.067	0.095	0.098	0.099	0.110	0.174	0.183
Cl	0.004	0.004	0.004	0.003	0.002	0.000	0.000	0.000	0.000	0.000
Σ.atoms	7.915	7.909	7.908	7.885	7.874	7.875	7.865	7.883	8.012	7.996
Si_T	2.811	2.817	2.819	2.820	2.805	2.818	2.787	2.816	2.826	2.836
Al_T	1.189	1.183	1.181	1.180	1.195	1.182	1.213	1.184	1.174	1.164
Σ_T	4.000	4.000	4.000	4.000	4.000	4.000	4.000	4.000	4.000	4.000
Al_M	0.255	0.223	0.253	0.259	0.291	0.328	0.296	0.281	0.207	0.247
Mg_M	1.377	1.409	1.350	1.365	1.111	1.104	1.105	1.068	1.484	1.471
Fe^{II}_M	1.126	1.183	1.159	1.121	1.287	1.287	1.235	1.357	1.069	1.059
Mn_M	0.021	0.017	0.020	0.022	0.013	0.018	0.017	0.014	0.015	0.015
Cr_M	0.006	0.000	0.004	0.003	0.000	0.000	0.000	0.000	0.000	0.000
Ti_M	0.098	0.094	0.098	0.108	0.133	0.109	0.151	0.132	0.116	0.102
V_M	0.000	0.000	0.000	0.000	0.006	0.000	0.012	0.000	0.000	0.000
Vc_M	0.118	0.074	0.116	0.123	0.158	0.153	0.184	0.148	0.109	0.106
Σ_M	3.000	3.000	3.000	3.000	3.000	3.000	3.000	3.000	3.000	3.000
K_I	0.937	0.905	0.927	0.911	0.921	0.900	0.930	0.909	0.931	0.899
Na_I	0.013	0.000	0.015	0.016	0.000	0.018	0.000	0.000	0.011	0.013
Ba_I	0.009	0.007	0.009	0.011	0.013	0.011	0.020	0.013	0.005	0.006
Ca_I	0.000	0.000	0.000	0.000	0.000	0.000	0.000	0.000	0.000	0.000
Σ_I	0.959	0.912	0.951	0.937	0.934	0.929	0.950	0.921	0.947	0.918
Σ_cations	7.841	7.838	7.835	7.815	7.776	7.777	7.766	7.773	7.838	7.812
F_OH	0.070	0.068	0.069	0.067	0.095	0.098	0.099	0.110	0.174	0.183
Cl_OH	0.004	0.004	0.004	0.003	0.002	0.000	0.000	0.000	0.000	0.000
OH_OH	1.927	1.929	1.927	1.929	1.902	1.902	1.901	1.890	1.826	1.817
Σ_OH	2.000	2.000	2.000	2.000	2.000	2.000	2.000	2.000	2.000	2.000
X_{Fe}	0.450	0.456	0.462	0.451	0.537	0.538	0.528	0.560	0.419	0.419

11	12	13	14	15	16	17	18	19	20	21
NP-012	NP-012	NP-013	NP-013	NP-013	NP-018	NP-018	NP-018	NP-018	NP-020	NP-020
Old	Old	Old	Old	Old	Old	Old	Old	Old	Old	Old
Amp-Bt tonalite	Amp-Bt tonalite	Horn-blendite	Horn-blendite	Horn-blendite	Bt augen-gneiss	Bt augen-gneiss	Bt augen-gneiss	Bt augen-gneiss	medium-grained gabbro	medium-grained gabbro
37.678	37.687	38.372	38.264	38.176	36.645	37.305	36.790	37.169	37.292	37.824
2.242	2.103	1.271	1.548	1.425	1.867	1.864	1.841	1.866	1.376	1.314
15.719	15.665	16.239	16.489	16.395	16.265	16.042	16.270	16.343	17.197	17.186
b.d.l.	b.d.l.	b.d.l.	b.d.l.	b.d.l.	b.d.l.	0.105	b.d.l.	b.d.l.	0.102	b.d.l.
b.d.l.	0.060	0.161	0.210	0.145	b.d.l.	b.d.l.	b.d.l.	b.d.l.	b.d.l.	b.d.l.
13.085	12.746	14.793	14.731	14.946	11.189	11.628	11.712	11.590	13.728	14.325
0.307	b.d.l.	0.080	b.d.l.	b.d.l.	b.d.l.	b.d.l.	b.d.l.	b.d.l.	b.d.l.	b.d.l.
0.196	0.210	0.154	0.133	0.179	0.392	0.445	0.378	0.297	b.d.l.	b.d.l.
17.437	17.654	14.452	14.893	14.708	19.014	18.379	17.924	18.388	15.899	16.181
0.129	0.168	b.d.l.	0.114	0.133	0.240	0.188	0.245	0.237	0.305	0.205
0.151	0.163	0.143	b.d.l.	0.135	0.086	0.068	0.079	b.d.l.	0.274	0.302
9.488	9.524	9.785	10.165	9.631	9.947	9.636	9.665	9.493	8.843	8.765
0.783	0.729	0.565	0.576	0.556	0.446	0.476	0.454	0.489	0.246	0.254
0.026	b.d.l.	b.d.l.	b.d.l.	b.d.l.	0.033	0.024	0.025	0.020	b.d.l.	b.d.l.
3.639	3.649	3.774	3.797	3.790	3.713	3.728	3.710	3.718	3.890	3.937
-0.330	-0.307	-0.238	-0.243	-0.234	-0.188	-0.200	-0.191	-0.206	-0.104	-0.107
-0.006	–	–	–	–	-0.007	-0.005	-0.006	-0.005	–	–
100.544	100.051	99.552	100.678	99.985	99.642	99.682	98.896	99.400	99.048	100.186
2.813	2.829	2.846	2.819	2.824	2.794	2.825	2.806	2.818	2.791	2.795
0.126	0.119	0.071	0.086	0.079	0.107	0.106	0.106	0.106	0.077	0.073
1.383	1.386	1.420	1.432	1.429	1.461	1.432	1.462	1.460	1.517	1.497
0.000	0.000	0.000	0.000	0.000	0.000	0.006	0.000	0.000	0.006	0.000
0.000	0.004	0.009	0.012	0.008	0.000	0.000	0.000	0.000	0.000	0.000
1.456	1.426	1.636	1.618	1.648	1.272	1.313	1.332	1.310	1.532	1.578
0.025	0.000	0.006	0.000	0.000	0.000	0.000	0.000	0.000	0.000	0.000
0.012	0.013	0.010	0.008	0.011	0.025	0.029	0.024	0.019	0.000	0.000
1.089	1.108	0.897	0.918	0.910	1.212	1.164	1.143	1.166	0.995	1.000
0.004	0.005	0.000	0.003	0.004	0.007	0.006	0.007	0.007	0.009	0.006
0.022	0.024	0.021	0.000	0.019	0.013	0.010	0.012	0.000	0.040	0.043
0.904	0.912	0.926	0.955	0.909	0.967	0.931	0.940	0.918	0.844	0.826
0.185	0.173	0.133	0.134	0.130	0.108	0.114	0.110	0.117	0.058	0.059
0.003	0.000	0.000	0.000	0.000	0.004	0.003	0.003	0.003	0.000	0.000
8.021	7.999	7.974	7.985	7.972	7.970	7.937	7.946	7.924	7.870	7.878
2.813	2.829	2.846	2.819	2.824	2.794	2.825	2.806	2.818	2.791	2.795
1.187	1.171	1.154	1.181	1.176	1.206	1.175	1.194	1.182	1.209	1.205
4.000	4.000	4.000	4.000	4.000	4.000	4.000	4.000	4.000	4.000	4.000
0.196	0.215	0.266	0.251	0.253	0.255	0.256	0.269	0.278	0.308	0.292
1.456	1.426	1.636	1.618	1.648	1.272	1.313	1.332	1.310	1.532	1.578
1.089	1.108	0.897	0.918	0.910	1.212	1.164	1.143	1.166	0.995	1.000
0.012	0.013	0.010	0.008	0.011	0.025	0.029	0.024	0.019	0.000	0.000
0.000	0.004	0.009	0.012	0.008	0.000	0.000	0.000	0.000	0.000	0.000
0.126	0.119	0.071	0.086	0.079	0.107	0.106	0.106	0.106	0.077	0.073
0.000	0.000	0.000	0.000	0.000	0.000	0.006	0.000	0.000	0.006	0.000
0.121	0.115	0.111	0.108	0.090	0.129	0.126	0.126	0.121	0.081	0.057
3.000	3.000	3.000	3.000	3.000	3.000	3.000	3.000	3.000	3.000	3.000
0.904	0.912	0.926	0.955	0.909	0.967	0.931	0.940	0.918	0.844	0.826
0.022	0.024	0.021	0.000	0.019	0.013	0.010	0.012	0.000	0.040	0.043
0.004	0.005	0.000	0.003	0.004	0.007	0.006	0.007	0.007	0.009	0.006
0.025	0.000	0.006	0.000	0.000	0.000	0.000	0.000	0.000	0.000	0.000
0.954	0.941	0.953	0.959	0.932	0.987	0.946	0.959	0.925	0.893	0.875
7.833	7.826	7.841	7.851	7.842	7.859	7.820	7.833	7.805	7.812	7.818
0.185	0.173	0.133	0.134	0.130	0.108	0.114	0.110	0.117	0.058	0.059
0.003	0.000	0.000	0.000	0.000	0.004	0.003	0.003	0.003	0.000	0.000
1.812	1.827	1.867	1.866	1.870	1.888	1.883	1.887	1.880	1.942	1.941
2.000	2.000	2.000	2.000	2.000	2.000	2.000	2.000	2.000	2.000	2.000
0.428	0.437	0.354	0.362	0.356	0.488	0.470	0.462	0.471	0.394	0.388

22	23	24	25	26	27	28	29	30	31	32
NP-020	NP-020	NP-007	NP-007	NP-007	NP-007	NP-007	NP-007	NP-009	NP-009	NP-009
Old	Old	Young	Young	Young	Young	Young	Young	Young	Young	Young
medium-grained gabbro	medium-grained gabbro	medium-grained Amp-Bt granodiorite	medium-grained Amp-Bt granodiorite	medium-grained Amp-Bt granodiorite	medium-grained Amp-Bt granodiorite	medium-grained Amp-Bt granodiorite	medium-grained Amp-Bt granodiorite	medium-grained Amp-Bt tonalite	medium-grained Amp-Bt tonalite	medium-grained Amp-Bt tonalite
37.351	37.263	35.353	35.849	35.513	35.498	35.188	35.562	36.887	36.578	36.772
1.596	1.944	2.907	2.401	2.412	2.217	2.140	2.363	2.084	2.027	2.466
17.297	17.028	15.933	16.096	16.074	16.460	16.093	16.423	16.919	16.864	16.609
0.120	b.d.l.	b.d.l.	b.d.l.	b.d.l.	b.d.l.	b.d.l.	b.d.l.	b.d.l.	b.d.l.	b.d.l.
b.d.l.	b.d.l.	b.d.l.	b.d.l.	b.d.l.	b.d.l.	b.d.l.	b.d.l.	b.d.l.	b.d.l.	b.d.l.
13.620	13.926	6.769	6.976	6.991	7.282	7.208	6.812	9.793	9.604	9.382
b.d.l.	b.d.l.	b.d.l.	b.d.l.	b.d.l.	b.d.l.	b.d.l.	b.d.l.	b.d.l.	b.d.l.	b.d.l.
b.d.l.	b.d.l.	0.383	0.397	0.319	0.365	0.361	0.371	0.324	0.289	0.303
15.465	15.490	24.934	24.234	24.596	24.140	24.353	24.498	22.177	21.452	21.593
0.282	0.250	0.118	0.131	0.117	0.120	0.152	0.163	0.116	0.315	0.295
0.225	0.211	b.d.l.	b.d.l.	b.d.l.	0.123	0.076	b.d.l.	b.d.l.	0.080	0.242
8.799	8.828	9.619	9.381	9.806	9.304	9.525	9.612	9.447	9.559	9.371
0.245	0.226	0.340	0.352	0.342	0.353	0.384	0.350	0.166	0.215	0.204
b.d.l.	b.d.l.	b.d.l.	0.034	0.035	0.031	0.027	b.d.l.	0.031	0.029	0.037
3.891	3.906	3.674	3.663	3.663	3.665	3.618	3.674	3.909	3.844	3.853
-0.103	-0.095	-0.143	-0.148	-0.144	-0.149	-0.162	-0.147	-0.070	-0.091	-0.086
–	–	–	-0.008	-0.008	-0.007	-0.006	–	-0.007	-0.007	-0.008
98.788	98.976	99.887	99.358	99.716	99.403	98.958	99.681	102.110	101.061	101.033
2.795	2.785	2.764	2.801	2.778	2.772	2.771	2.777	2.769	2.774	2.785
0.090	0.109	0.171	0.141	0.142	0.130	0.127	0.139	0.118	0.116	0.140
1.525	1.500	1.468	1.482	1.482	1.515	1.494	1.511	1.497	1.507	1.482
0.007	0.000	0.000	0.000	0.000	0.000	0.000	0.000	0.000	0.000	0.000
0.000	0.000	0.000	0.000	0.000	0.000	0.000	0.000	0.000	0.000	0.000
1.519	1.551	0.789	0.812	0.815	0.848	0.846	0.793	1.096	1.086	1.059
0.000	0.000	0.000	0.000	0.000	0.000	0.000	0.000	0.000	0.000	0.000
0.000	0.000	0.025	0.026	0.021	0.024	0.024	0.025	0.021	0.019	0.019
0.968	0.968	1.630	1.583	1.609	1.576	1.604	1.600	1.392	1.361	1.368
0.008	0.007	0.004	0.004	0.004	0.004	0.005	0.005	0.003	0.009	0.009
0.033	0.031	0.000	0.000	0.000	0.019	0.012	0.000	0.000	0.012	0.036
0.840	0.842	0.959	0.935	0.978	0.927	0.957	0.957	0.904	0.925	0.905
0.058	0.053	0.084	0.087	0.085	0.087	0.096	0.086	0.039	0.052	0.049
0.000	0.000	0.000	0.005	0.005	0.004	0.004	0.000	0.004	0.004	0.005
7.843	7.846	7.895	7.876	7.918	7.905	7.939	7.894	7.861	7.880	7.857
2.795	2.785	2.764	2.801	2.778	2.772	2.771	2.777	2.769	2.774	2.785
1.205	1.215	1.236	1.199	1.222	1.228	1.229	1.223	1.231	1.226	1.215
4.000	4.000	4.000	4.000	4.000	4.000	4.000	4.000	4.000	4.000	4.000
0.320	0.284	0.232	0.283	0.259	0.286	0.265	0.288	0.265	0.281	0.267
1.519	1.551	0.789	0.812	0.815	0.848	0.846	0.793	1.096	1.086	1.059
0.968	0.968	1.630	1.583	1.609	1.576	1.604	1.600	1.392	1.361	1.368
0.000	0.000	0.025	0.026	0.021	0.024	0.024	0.025	0.021	0.019	0.019
0.000	0.000	0.000	0.000	0.000	0.000	0.000	0.000	0.000	0.000	0.000
0.090	0.109	0.171	0.141	0.142	0.130	0.127	0.139	0.118	0.116	0.140
0.007	0.000	0.000	0.000	0.000	0.000	0.000	0.000	0.000	0.000	0.000
0.096	0.087	0.152	0.154	0.153	0.135	0.134	0.155	0.090	0.121	0.146
3.000	3.000	3.000	3.000	3.000	3.000	3.000	3.000	3.000	3.000	3.000
0.840	0.842	0.959	0.935	0.978	0.927	0.957	0.957	0.904	0.925	0.905
0.033	0.031	0.000	0.000	0.000	0.019	0.012	0.000	0.000	0.012	0.036
0.008	0.007	0.004	0.004	0.004	0.004	0.005	0.005	0.003	0.009	0.009
0.000	0.000	0.000	0.000	0.000	0.000	0.000	0.000	0.000	0.000	0.000
0.881	0.879	0.963	0.939	0.982	0.949	0.973	0.962	0.908	0.946	0.950
7.785	7.792	7.811	7.785	7.829	7.813	7.839	7.807	7.818	7.825	7.804
0.058	0.053	0.084	0.087	0.085	0.087	0.096	0.086	0.039	0.052	0.049
0.000	0.000	0.000	0.005	0.005	0.004	0.004	0.000	0.004	0.004	0.005
1.942	1.947	1.916	1.909	1.911	1.909	1.901	1.914	1.957	1.945	1.946
2.000	2.000	2.000	2.000	2.000	2.000	2.000	2.000	2.000	2.000	2.000
0.389	0.384	0.674	0.661	0.664	0.650	0.655	0.669	0.559	0.556	0.564

33	34	35	36	37	38	39	40	41	42
NP-009	NP-010	NP-010	NP-010	NP-010	NP-010	NP-021	NP-021	NP-021	NP-021
Young	Young	Young	Young	Young	Young	Young	Young	Young	Young
medium-grained Amp-Bt tonalite	gray (Ms?) Bt granite	gray (Ms?) Bt granite	gray (Ms?) Bt granite	gray (Ms?) Bt granite	gray (Ms?) Bt granite	coarse-grained Bt granite	coarse-grained Bt granite	coarse-grained Bt granite	coarse-grained Bt granite
36.843	33.876	32.147	34.436	34.515	34.698	34.879	34.683	34.961	35.115
2.390	2.190	2.264	2.288	2.173	2.333	2.400	2.652	2.837	2.668
16.597	19.902	19.034	20.026	19.733	19.653	17.905	18.035	17.440	17.580
b.d.l.	b.d.l.	b.d.l.	b.d.l.	b.d.l.	b.d.l.	b.d.l.	b.d.l.	b.d.l.	b.d.l.
b.d.l.	b.d.l.	b.d.l.	b.d.l.	b.d.l.	b.d.l.	b.d.l.	b.d.l.	b.d.l.	b.d.l.
9.465	5.974	6.483	5.684	5.739	5.837	5.320	5.179	4.993	5.257
b.d.l.	b.d.l.	b.d.l.	b.d.l.	b.d.l.	b.d.l.	b.d.l.	0.079	b.d.l.	0.058
0.294	0.462	0.485	0.402	0.512	0.383	0.636	0.525	0.565	0.580
21.594	24.797	26.944	24.618	24.687	23.889	24.478	24.677	24.900	24.702
0.244	b.d.l.	b.d.l.	b.d.l.	b.d.l.	b.d.l.	b.d.l.	b.d.l.	b.d.l.	0.106
0.094	0.089	b.d.l.	0.088	0.074	b.d.l.	b.d.l.	b.d.l.	b.d.l.	b.d.l.
9.496	8.945	6.737	9.376	9.403	9.310	9.515	9.173	9.380	9.455
0.230	0.620	0.451	0.569	0.551	0.663	0.732	0.648	0.712	0.714
b.d.l.	b.d.l.	b.d.l.	b.d.l.	b.d.l.	b.d.l.	0.025	b.d.l.	b.d.l.	0.022
3.851	3.578	3.555	3.633	3.634	3.573	3.464	3.508	3.472	3.484
-0.097	-0.261	-0.190	-0.240	-0.232	-0.279	-0.308	-0.273	-0.300	-0.301
–	–	–	–	–	–	-0.006	–	–	-0.005
101.002	100.172	97.910	100.881	100.789	100.059	99.040	98.887	98.960	99.436
2.790	2.623	2.558	2.646	2.657	2.677	2.740	2.726	2.752	2.750
0.136	0.128	0.136	0.132	0.126	0.135	0.142	0.157	0.168	0.157
1.481	1.816	1.785	1.813	1.790	1.787	1.658	1.670	1.618	1.623
0.000	0.000	0.000	0.000	0.000	0.000	0.000	0.000	0.000	0.000
0.000	0.000	0.000	0.000	0.000	0.000	0.000	0.000	0.000	0.000
1.068	0.690	0.769	0.651	0.659	0.671	0.623	0.607	0.586	0.614
0.000	0.000	0.000	0.000	0.000	0.000	0.000	0.007	0.000	0.005
0.019	0.030	0.033	0.026	0.033	0.025	0.042	0.035	0.038	0.038
1.367	1.606	1.793	1.582	1.589	1.541	1.608	1.622	1.639	1.618
0.007	0.000	0.000	0.000	0.000	0.000	0.000	0.000	0.000	0.003
0.014	0.013	0.000	0.013	0.011	0.000	0.000	0.000	0.000	0.000
0.917	0.884	0.684	0.919	0.923	0.916	0.953	0.920	0.942	0.945
0.055	0.152	0.113	0.138	0.134	0.162	0.182	0.161	0.177	0.177
0.000	0.000	0.000	0.000	0.000	0.000	0.003	0.000	0.000	0.003
7.854	7.941	7.870	7.920	7.923	7.914	7.951	7.903	7.919	7.933
2.790	2.623	2.558	2.646	2.657	2.677	2.740	2.726	2.752	2.750
1.210	1.377	1.442	1.354	1.343	1.323	1.260	1.274	1.248	1.250
4.000	4.000	4.000	4.000	4.000	4.000	4.000	4.000	4.000	4.000
0.270	0.439	0.342	0.459	0.447	0.463	0.397	0.396	0.370	0.373
1.068	0.690	0.769	0.651	0.659	0.671	0.623	0.607	0.586	0.614
1.367	1.606	1.793	1.582	1.589	1.541	1.608	1.622	1.639	1.618
0.019	0.030	0.033	0.026	0.033	0.025	0.042	0.035	0.038	0.038
0.000	0.000	0.000	0.000	0.000	0.000	0.000	0.000	0.000	0.000
0.136	0.128	0.136	0.132	0.126	0.135	0.142	0.157	0.168	0.157
0.000	0.000	0.000	0.000	0.000	0.000	0.000	0.000	0.000	0.000
0.139	0.107	0.000	0.150	0.145	0.164	0.187	0.184	0.200	0.199
3.000	3.000	3.072	3.000	3.000	3.000	3.000	3.000	3.000	3.000
0.917	0.884	0.684	0.919	0.923	0.916	0.953	0.920	0.942	0.945
0.014	0.013	0.000	0.013	0.011	0.000	0.000	0.000	0.000	0.000
0.007	0.000	0.000	0.000	0.000	0.000	0.000	0.000	0.000	0.003
0.000	0.000	0.000	0.000	0.000	0.000	0.000	0.007	0.000	0.005
0.938	0.897	0.684	0.932	0.934	0.916	0.953	0.926	0.942	0.953
7.799	7.790	7.756	7.782	7.789	7.753	7.766	7.742	7.742	7.753
0.055	0.152	0.113	0.138	0.134	0.162	0.182	0.161	0.177	0.177
0.000	0.000	0.000	0.000	0.000	0.000	0.003	0.000	0.000	0.003
1.945	1.848	1.887	1.862	1.866	1.838	1.815	1.839	1.823	1.820
2.000	2.000	2.000	2.000	2.000	2.000	2.000	2.000	2.000	2.000
0.561	0.699	0.700	0.708	0.707	0.697	0.721	0.728	0.737	0.725

K-FELDSPAR formulae recalculated on the basis of 8 oxygen equivalents

	90	91	39	49	122	123	124	125	126	75	76	88
Comment	NP-011	NP-011	NP-013	NP-013	NP-018	NP-018	NP-018	NP-018	NP-018	NP-007	NP-007	NP-007
Suite	Old	Old	Old	Old	Old	Old	Old	Old	Old	Young	Young	Young
Petrology	Amp-bearing QtzD	Amp-bearing QtzD	Horn-blendite	Horn-blendite	Bt augen-gneiss	Bt augen-gneiss	Bt augen-gneiss	Bt augen-gneiss	Bt augen-gneiss	medium-grained Amp-Bt granodiorite	medium-grained Amp-Bt granodiorite	medium-grained Amp-Bt granodiorite
P_2O_5	b.d.l.	b.d.l.	b.d.l.	b.d.l.	b.d.l.	b.d.l.	b.d.l.	b.d.l.	b.d.l.	b.d.l.	b.d.l.	b.d.l.
SiO_2	64.421	64.338	65.362	64.586	64.352	64.435	63.964	63.830	61.441	64.582	64.461	63.882
Al_2O_3	17.984	17.903	18.013	18.140	18.809	18.573	18.353	18.430	19.188	18.619	18.390	18.362
Fe_2O_3	0.174	0.079	0.338	0.000	0.000	0.000	0.000	0.079	0.000	0.000	0.109	0.000
CaO	b.d.l.	b.d.l.	b.d.l.	b.d.l.	b.d.l.	b.d.l.	b.d.l.	b.d.l.	b.d.l.	b.d.l.	b.d.l.	b.d.l.
BaO	0.258	0.116	b.d.l.	b.d.l.	0.634	1.511	1.146	1.513	4.659	0.800	0.865	0.745
Na_2O	0.117	0.289	0.106	0.175	0.727	0.785	0.880	0.639	0.714	0.643	0.643	0.588
K_2O	16.348	16.666	16.753	16.509	15.971	15.517	15.383	15.579	13.989	15.544	15.867	16.058
F	b.d.l.	b.d.l.	0.084	0.080	b.d.l.	b.d.l.	b.d.l.	b.d.l.	b.d.l.	b.d.l.	b.d.l.	b.d.l.
Σ	99.302	99.391	100.656	99.490	100.493	100.821	99.726	100.070	99.991	100.188	100.335	99.635
P	0.000	0.000	0.000	0.000	0.000	0.000	0.000	0.000	0.000	0.000	0.000	0.000
Si	3.006	3.004	3.010	3.005	2.974	2.981	2.984	2.978	2.922	2.988	2.987	2.983
Al	0.989	0.985	0.977	0.995	1.024	1.012	1.009	1.013	1.075	1.015	1.004	1.010
Fe^{III}	0.006	0.003	0.012	0.000	0.000	0.000	0.000	0.003	0.000	0.000	0.004	0.000
Ca	0.000	0.000	0.000	0.000	0.000	0.000	0.000	0.000	0.000	0.000	0.000	0.000
Ba	0.005	0.002	0.000	0.000	0.011	0.027	0.021	0.028	0.087	0.015	0.016	0.014
Na	0.011	0.026	0.009	0.016	0.065	0.070	0.080	0.058	0.066	0.058	0.058	0.053
K	0.973	0.992	0.984	0.980	0.942	0.916	0.915	0.927	0.849	0.917	0.938	0.956
Σ.atoms	4.989	5.012	4.992	4.995	5.017	5.006	5.009	5.007	4.998	4.992	5.007	5.017
Si_Si	2.000	2.000	2.000	2.000	2.000	2.000	2.000	2.000	2.000	2.000	2.000	2.000
Σ_Si	2.000	2.000	2.000	2.000	2.000	2.000	2.000	2.000	2.000	2.000	2.000	2.000
P_T	0.000	0.000	0.000	0.000	0.000	0.000	0.000	0.000	0.000	0.000	0.000	0.000
Si_T	1.006	1.004	1.010	1.005	0.974	0.981	0.984	0.978	0.922	0.988	0.987	0.983
Al_T	0.989	0.985	0.977	0.995	1.024	1.012	1.009	1.013	1.075	1.015	1.004	1.010
Fe^{III}_T	0.006	0.003	0.012	0.000	0.000	0.000	0.000	0.003	0.000	0.000	0.004	0.000
Σ_T	2.000	1.991	1.999	2.000	1.999	1.993	1.993	1.994	1.997	2.003	1.995	1.993
Na_A	0.011	0.026	0.009	0.016	0.065	0.070	0.080	0.058	0.066	0.058	0.058	0.053
K_A	0.973	0.992	0.984	0.980	0.942	0.916	0.915	0.927	0.849	0.917	0.938	0.956
Ca_A	0.000	0.000	0.000	0.000	0.000	0.000	0.000	0.000	0.000	0.000	0.000	0.000
Fe^{III}_A	0.000	0.000	0.000	0.000	0.000	0.000	0.000	0.000	0.000	0.000	0.000	0.000
Ba_A	0.005	0.002	0.000	0.000	0.011	0.027	0.021	0.028	0.087	0.015	0.016	0.014
Σ_A	0.989	1.021	0.994	0.996	1.018	1.013	1.016	1.013	1.001	0.989	1.011	1.023
Ab	0.011	0.026	0.010	0.016	0.064	0.069	0.078	0.057	0.066	0.058	0.057	0.052
An	0.000	0.000	0.000	0.000	0.000	0.000	0.000	0.000	0.000	0.000	0.000	0.000
Or	0.985	0.972	0.990	0.984	0.925	0.904	0.901	0.916	0.848	0.927	0.927	0.935
Cln	0.005	0.002	0.000	0.000	0.011	0.027	0.021	0.027	0.087	0.015	0.016	0.013
Sl	0.000	0.000	0.000	0.000	0.000	0.000	0.000	0.000	0.000	0.000	0.000	0.000

92	93	23	28	33	36	41	57	63	64	18	29
NP-007 Young medium-grained Amp Bt granodiorite	NP-007 Young medium-grained Amp Bt granodiorite	NP-010 Young gray (Ms?) Bt granite	NP-010 Young gray (Ms?) Bt granite	NP-010 Young gray (Ms?) Bt granite	NP-010 Young gray (Ms?) Bt granite	NP-010 Young gray (Ms?) Bt granite	NP-021 Young coarse-grained Bt granite	NP-021 Young coarse-grained Bt granite	NP-021 Young coarse-grained Bt granite	NP-017 Unknown fine-grained mafic dyke	NP-017 Unknown fine-grained mafic dyke
b.d.l.	b.d.l.	0.266	0.200	0.312	0.247	b.d.l.	b.d.l.	b.d.l.	b.d.l.	b.d.l.	b.d.l.
63.973	64.957	65.956	65.778	65.043	64.869	65.417	64.894	64.831	64.658	65.189	62.862
18.278	18.475	18.562	19.128	18.540	18.477	18.619	18.093	18.548	18.597	18.063	18.986
0.000	0.000	0.000	0.000	0.000	0.000	0.000	0.000	0.000	0.000	0.079	0.086
b.d.l.	b.d.l.	b.d.l.	b.d.l.	b.d.l.	b.d.l.	b.d.l.	b.d.l.	b.d.l.	b.d.l.	b.d.l.	b.d.l.
0.748	0.773	0.201	b.d.l.	0.197	b.d.l.	b.d.l.	0.140	0.171	0.125	b.d.l.	2.858
0.650	0.712	0.869	1.222	0.970	1.206	0.831	0.724	0.944	0.707	b.d.l.	1.655
15.702	15.767	15.711	15.032	15.133	15.219	15.661	16.036	15.851	16.102	16.730	13.576
b.d.l.	b.d.l.	b.d.l.	b.d.l.	b.d.l.	0.095	b.d.l.	b.d.l.	b.d.l.	b.d.l.	b.d.l.	b.d.l.
99.351	100.684	101.565	101.360	100.195	100.113	100.528	99.887	100.345	100.189	100.061	100.023
0.000	0.000	0.010	0.008	0.012	0.010	0.000	0.000	0.000	0.000	0.000	0.000
2.990	2.993	2.994	2.980	2.987	2.986	2.998	3.005	2.989	2.987	3.013	2.945
1.007	1.003	0.993	1.021	1.003	1.002	1.006	0.987	1.008	1.012	0.984	1.048
0.000	0.000	0.000	0.000	0.000	0.000	0.000	0.000	0.000	0.000	0.003	0.003
0.000	0.000	0.000	0.000	0.000	0.000	0.000	0.000	0.000	0.000	0.000	0.000
0.014	0.014	0.004	0.000	0.004	0.000	0.000	0.003	0.003	0.002	0.000	0.052
0.059	0.064	0.076	0.107	0.086	0.108	0.074	0.065	0.084	0.063	0.000	0.150
0.936	0.927	0.910	0.869	0.887	0.894	0.916	0.947	0.932	0.949	0.986	0.811
5.005	5.001	4.987	4.986	4.979	4.999	4.994	5.007	5.016	5.013	4.987	5.010
2.000	2.000	2.000	2.000	2.000	2.000	2.000	2.000	2.000	2.000	2.000	2.000
2.000	2.000	2.000	2.000	2.000	2.000	2.000	2.000	2.000	2.000	2.000	2.000
0.000	0.000	0.010	0.008	0.012	0.010	0.000	0.000	0.000	0.000	0.000	0.000
0.990	0.993	0.994	0.980	0.987	0.986	0.998	1.005	0.989	0.987	1.013	0.945
1.007	1.003	0.993	1.021	1.003	1.002	1.006	0.987	1.008	1.012	0.984	1.048
0.000	0.000	0.000	0.000	0.000	0.000	0.000	0.000	0.000	0.000	0.003	0.003
1.996	1.996	1.997	2.009	2.003	1.998	2.004	1.993	1.996	1.999	2.000	1.996
0.059	0.064	0.076	0.107	0.086	0.108	0.074	0.065	0.084	0.063	0.000	0.150
0.936	0.927	0.910	0.869	0.887	0.894	0.916	0.947	0.932	0.949	0.986	0.811
0.000	0.000	0.000	0.000	0.000	0.000	0.000	0.000	0.000	0.000	0.000	0.000
0.000	0.000	0.000	0.000	0.000	0.000	0.000	0.000	0.000	0.000	0.000	0.000
0.014	0.014	0.004	0.000	0.004	0.000	0.000	0.003	0.003	0.002	0.000	0.052
1.009	1.004	0.990	0.976	0.976	1.001	0.989	1.015	1.020	1.014	0.987	1.014
0.058	0.063	0.077	0.110	0.088	0.107	0.075	0.064	0.083	0.062	0.000	0.148
0.000	0.000	0.000	0.000	0.000	0.000	0.000	0.000	0.000	0.000	0.000	0.000
0.928	0.923	0.919	0.890	0.908	0.893	0.925	0.933	0.914	0.935	1.000	0.800
0.014	0.014	0.004	0.000	0.004	0.000	0.000	0.003	0.003	0.002	0.000	0.052
0.000	0.000	0.000	0.000	0.000	0.000	0.000	0.000	0.000	0.000	0.000	0.000

PLAGIOCLASE formulae recalculated on the basis of 8 oxygen equivalents

	1	2	3	4	5	6	7	8	9	10	11
Comment	NP-011	NP-011	NP-011	NP-011	NP-011	NP-011	NP-011	NP-012	NP-012	NP-012	NP-012
Suite	Old	Old	Old	Old	Old	Old	Old	Old	Old	Old	Old
Petrology	Amp-bearing QtzD	Amp-bearing QtzD	Amp-bearing QtzD	Amp-bearing QtzD	Amp-bearing QtzD	Amp-bearing QtzD	Amp-bearing QtzD	Amp-Bt tonalite	Amp-Bt tonalite	Amp-Bt tonalite	Amp-Bt tonalite
P_2O_5	b.d.l.	b.d.l.	b.d.l.	b.d.l.	b.d.l.	b.d.l.	b.d.l.	b.d.l.	b.d.l.	b.d.l.	b.d.l.
SiO_2	57.080	58.266	58.917	57.729	58.399	57.888	58.524	58.279	58.419	58.972	57.870
Al_2O_3	27.428	26.134	26.406	27.070	26.065	26.346	25.797	25.703	25.239	25.699	26.643
Fe_2O_3	0.082	0.000	0.000	0.000	0.000	0.000	0.000	0.000	0.000	0.000	0.118
CaO	9.631	8.824	8.442	9.280	8.470	8.729	8.386	8.660	8.169	8.091	9.059
SrO	b.d.l.	b.d.l.	b.d.l.	b.d.l.	b.d.l.	b.d.l.	b.d.l.	b.d.l.	b.d.l.	b.d.l.	b.d.l.
Na_2O	6.566	6.782	7.009	6.194	6.557	6.473	7.034	6.798	6.672	6.499	6.418
K_2O	0.128	0.118	0.065	0.064	0.086	0.093	0.085	0.141	0.066	0.099	0.058
Rb_2O	b.d.l.	b.d.l.	b.d.l.	b.d.l.	b.d.l.	b.d.l.	b.d.l.	b.d.l.	b.d.l.	b.d.l.	b.d.l.
F	b.d.l.	b.d.l.	b.d.l.	b.d.l.	b.d.l.	b.d.l.	b.d.l.	b.d.l.	b.d.l.	b.d.l.	b.d.l.
Σ	100.915	100.124	100.839	100.337	99.577	99.529	99.826	99.581	98.565	99.360	100.166
P	0.000	0.000	0.000	0.000	0.000	0.000	0.000	0.000	0.000	0.000	0.000
Si	2.544	2.607	2.613	2.576	2.619	2.601	2.623	2.620	2.645	2.644	2.587
Al	1.441	1.378	1.380	1.423	1.378	1.395	1.362	1.362	1.346	1.358	1.404
Fe^{III}	0.003	0.000	0.000	0.000	0.000	0.000	0.000	0.000	0.000	0.000	0.004
Ca	0.460	0.423	0.401	0.444	0.407	0.420	0.403	0.417	0.396	0.389	0.434
Sr	0.000	0.000	0.000	0.000	0.000	0.000	0.000	0.000	0.000	0.000	0.000
Na	0.567	0.588	0.603	0.536	0.570	0.564	0.611	0.592	0.586	0.565	0.556
K	0.007	0.007	0.004	0.004	0.005	0.005	0.005	0.008	0.004	0.006	0.003
Rb	0.000	0.000	0.000	0.000	0.000	0.000	0.000	0.000	0.000	0.000	0.000
Σ.atoms	5.022	5.002	5.000	4.982	4.979	4.986	5.004	4.999	4.977	4.962	4.989
Si_Si	2.000	2.000	2.000	2.000	2.000	2.000	2.000	2.000	2.000	2.000	2.000
Σ_Si	2.000	2.000	2.000	2.000	2.000	2.000	2.000	2.000	2.000	2.000	2.000
P_T	0.000	0.000	0.000	0.000	0.000	0.000	0.000	0.000	0.000	0.000	0.000
Si_T	0.544	0.607	0.613	0.576	0.619	0.601	0.623	0.620	0.645	0.644	0.587
Al_T	1.441	1.378	1.380	1.423	1.378	1.395	1.362	1.362	1.346	1.358	1.404
Fe^{III} T	0.003	0.000	0.000	0.000	0.000	0.000	0.000	0.000	0.000	0.000	0.004
Σ_T	1.987	1.984	1.993	1.999	1.997	1.996	1.985	1.982	1.991	2.002	1.995
Na_A	0.567	0.588	0.603	0.536	0.570	0.564	0.611	0.592	0.586	0.565	0.556
K_A	0.007	0.007	0.004	0.004	0.005	0.005	0.005	0.008	0.004	0.006	0.003
Ca_A	0.460	0.423	0.401	0.444	0.407	0.420	0.403	0.417	0.396	0.389	0.434
Fe^{III}_A	0.000	0.000	0.000	0.000	0.000	0.000	0.000	0.000	0.000	0.000	0.000
Sr_A	0.000	0.000	0.000	0.000	0.000	0.000	0.000	0.000	0.000	0.000	0.000
Rb_A	0.000	0.000	0.000	0.000	0.000	0.000	0.000	0.000	0.000	0.000	0.000
Σ_A	1.034	1.018	1.007	0.983	0.982	0.989	1.019	1.018	0.986	0.959	0.994
Ab	0.548	0.578	0.598	0.545	0.581	0.570	0.600	0.582	0.594	0.589	0.560
An	0.445	0.416	0.398	0.451	0.414	0.425	0.395	0.410	0.402	0.405	0.437
Or	0.007	0.007	0.004	0.004	0.005	0.005	0.005	0.008	0.004	0.006	0.003
Cln	0.000	0.000	0.000	0.000	0.000	0.000	0.000	0.000	0.000	0.000	0.000
Sl	0.000	0.000	0.000	0.000	0.000	0.000	0.000	0.000	0.000	0.000	0.000

12	13	14	15	16	17	18	19	20	21	22	23
NP-012 Old	NP-012 Old	NP-012 Old	NP-012 Old	NP-012 Old	NP-013 Old	NP-013 Old	NP-013 Old	NP-013 Old	NP-013 Old	NP-013 Old	NP-013 Old
Amp-Bt tonalite	Amp-Bt tonalite	Amp-Bt tonalite	Amp-Bt tonalite	Amp-Bt tonalite	Horn-blendite	Horn-blendite	Horn-blendite	Horn-blendite	Horn-blendite	Horn-blendite	Horn-blendite
b.d.l.	b.d.l.	b.d.l.	b.d.l.	b.d.l.	b.d.l.	b.d.l.	b.d.l.	b.d.l.	b.d.l.	b.d.l.	b.d.l.
57.549	58.834	58.708	57.712	58.158	59.854	57.561	60.046	57.065	58.416	59.278	59.163
26.589	25.570	26.147	26.478	26.573	25.021	26.739	24.895	26.617	25.642	25.602	25.756
0.000	0.071	0.000	0.000	0.000	0.000	0.000	0.000	0.194	0.000	0.000	0.000
9.059	8.090	8.526	8.873	8.638	7.359	9.270	7.005	9.396	8.396	7.934	7.859
b.d.l.	b.d.l.	b.d.l.	b.d.l.	b.d.l.	b.d.l.	b.d.l.	b.d.l.	b.d.l.	b.d.l.	b.d.l.	b.d.l.
6.318	6.664	6.794	6.268	6.746	7.064	5.960	7.635	6.150	6.461	6.990	7.450
0.053	0.053	b.d.l.	b.d.l.	b.d.l.	0.111	b.d.l.	0.078	b.d.l.	b.d.l.	0.105	b.d.l.
b.d.l.	b.d.l.	b.d.l.	b.d.l.	b.d.l.	b.d.l.	b.d.l.	b.d.l.	b.d.l.	b.d.l.	b.d.l.	b.d.l.
b.d.l.	b.d.l.	b.d.l.	0.091	b.d.l.	b.d.l.	b.d.l.	b.d.l.	b.d.l.	b.d.l.	b.d.l.	b.d.l.
99.568	99.282	100.175	99.422	100.115	99.409	99.530	99.659	99.422	98.915	99.909	100.228
0.000	0.000	0.000	0.000	0.000	0.000	0.000	0.000	0.000	0.000	0.000	0.000
2.587	2.643	2.619	2.597	2.598	2.679	2.586	2.683	2.573	2.634	2.647	2.637
1.409	1.353	1.374	1.404	1.399	1.320	1.415	1.311	1.414	1.363	1.347	1.353
0.000	0.002	0.000	0.000	0.000	0.000	0.000	0.000	0.007	0.000	0.000	0.000
0.436	0.389	0.407	0.428	0.413	0.353	0.446	0.335	0.454	0.406	0.380	0.375
0.000	0.000	0.000	0.000	0.000	0.000	0.000	0.000	0.000	0.000	0.000	0.000
0.551	0.580	0.587	0.547	0.584	0.613	0.519	0.661	0.538	0.565	0.605	0.644
0.003	0.003	0.000	0.000	0.000	0.006	0.000	0.004	0.000	0.000	0.006	0.000
0.000	0.000	0.000	0.000	0.000	0.000	0.000	0.000	0.000	0.000	0.000	0.000
4.986	4.971	4.988	4.975	4.995	4.971	4.966	4.995	4.985	4.967	4.985	5.009
2.000	2.000	2.000	2.000	2.000	2.000	2.000	2.000	2.000	2.000	2.000	2.000
2.000	2.000	2.000	2.000	2.000	2.000	2.000	2.000	2.000	2.000	2.000	2.000
0.000	0.000	0.000	0.000	0.000	0.000	0.000	0.000	0.000	0.000	0.000	0.000
0.587	0.643	0.619	0.597	0.598	0.679	0.586	0.683	0.573	0.634	0.647	0.637
1.409	1.353	1.374	1.404	1.399	1.320	1.415	1.311	1.414	1.363	1.347	1.353
0.000	0.002	0.000	0.000	0.000	0.000	0.000	0.000	0.007	0.000	0.000	0.000
1.996	1.998	1.993	2.000	1.997	1.999	2.001	1.994	1.994	1.997	1.994	1.990
0.551	0.580	0.587	0.547	0.584	0.613	0.519	0.661	0.538	0.565	0.605	0.644
0.003	0.003	0.000	0.000	0.000	0.006	0.000	0.004	0.000	0.000	0.006	0.000
0.436	0.389	0.407	0.428	0.413	0.353	0.446	0.335	0.454	0.406	0.380	0.375
0.000	0.000	0.000	0.000	0.000	0.000	0.000	0.000	0.000	0.000	0.000	0.000
0.000	0.000	0.000	0.000	0.000	0.000	0.000	0.000	0.000	0.000	0.000	0.000
0.000	0.000	0.000	0.000	0.000	0.000	0.000	0.000	0.000	0.000	0.000	0.000
0.990	0.973	0.995	0.974	0.998	0.972	0.965	1.001	0.991	0.970	0.991	1.019
0.556	0.597	0.590	0.561	0.586	0.631	0.538	0.661	0.542	0.582	0.611	0.632
0.441	0.400	0.410	0.439	0.414	0.363	0.462	0.335	0.458	0.418	0.383	0.368
0.003	0.003	0.000	0.000	0.000	0.007	0.000	0.004	0.000	0.000	0.006	0.000
0.000	0.000	0.000	0.000	0.000	0.000	0.000	0.000	0.000	0.000	0.000	0.000
0.000	0.000	0.000	0.000	0.000	0.000	0.000	0.000	0.000	0.000	0.000	0.000

25	26	27	28	29	30	31	32	33	34	35	36
NP-013 Old	NP-013 Old	NP-013 Old	NP-013 Old	NP-018 Old	NP-018 Old	NP-018 Old	NP-018 Old	NP-018 Old	NP-018 Old	NP-018 Old	NP-020 Old
Horn-blendite	Horn-blendite	Horn-blendite	Horn-blendite	Bt augen-gneiss	Bt augen-gneiss	Bt augen-gneiss	Bt augen-gneiss	Bt augen-gneiss	Bt augen-gneiss	Bt augen-gneiss	medium-grained gabbro
b.d.l.	b.d.l.	b.d.l.	b.d.l.	b.d.l.	b.d.l.	b.d.l.	b.d.l.	b.d.l.	b.d.l.	b.d.l.	b.d.l.
61.303	58.587	57.538	59.570	60.172	60.165	59.544	58.643	62.577	60.420	63.199	46.509
24.452	26.108	26.997	25.538	25.310	25.320	24.907	26.644	23.609	25.531	23.622	34.076
0.000	0.000	0.000	0.000	0.000	0.113	0.077	0.099	0.000	0.000	0.000	0.000
6.470	8.630	9.304	7.858	7.265	7.443	7.181	8.632	5.165	7.080	5.053	17.923
b.d.l.	b.d.l.	b.d.l.	b.d.l.	b.d.l.	b.d.l.	b.d.l.	b.d.l.	b.d.l.	b.d.l.	b.d.l.	0.200
7.866	7.186	6.269	6.451	7.516	7.174	8.036	7.171	8.962	7.626	8.820	1.382
b.d.l.	b.d.l.	b.d.l.	b.d.l.	0.147	0.073	0.153	0.103	0.086	0.100	0.207	b.d.l.
b.d.l.	b.d.l.	b.d.l.	b.d.l.	b.d.l.	b.d.l.	b.d.l.	b.d.l.	b.d.l.	b.d.l.	b.d.l.	b.d.l.
b.d.l.	b.d.l.	b.d.l.	b.d.l.	b.d.l.	b.d.l.	b.d.l.	b.d.l.	b.d.l.	b.d.l.	b.d.l.	b.d.l.
100.091	100.511	100.108	99.417	100.410	100.288	99.898	101.292	100.399	100.757	100.901	100.090
0.000	0.000	0.000	0.000	0.000	0.000	0.000	0.000	0.000	0.000	0.000	0.000
2.719	2.611	2.574	2.663	2.671	2.671	2.664	2.595	2.763	2.670	2.774	2.139
1.278	1.371	1.423	1.345	1.324	1.325	1.313	1.390	1.229	1.330	1.222	1.847
0.000	0.000	0.000	0.000	0.000	0.004	0.003	0.003	0.000	0.000	0.000	0.000
0.307	0.412	0.446	0.376	0.345	0.354	0.344	0.409	0.244	0.335	0.238	0.883
0.000	0.000	0.000	0.000	0.000	0.000	0.000	0.000	0.000	0.000	0.000	0.005
0.676	0.621	0.544	0.559	0.647	0.617	0.697	0.615	0.767	0.653	0.751	0.123
0.000	0.000	0.000	0.000	0.008	0.004	0.009	0.006	0.005	0.006	0.012	0.000
0.000	0.000	0.000	0.000	0.000	0.000	0.000	0.000	0.000	0.000	0.000	0.000
4.980	5.014	4.986	4.944	4.995	4.975	5.031	5.019	5.008	4.994	4.996	4.999
2.000	2.000	2.000	2.000	2.000	2.000	2.000	2.000	2.000	2.000	2.000	2.000
2.000	2.000	2.000	2.000	2.000	2.000	2.000	2.000	2.000	2.000	2.000	2.000
0.000	0.000	0.000	0.000	0.000	0.000	0.000	0.000	0.000	0.000	0.000	0.000
0.719	0.611	0.574	0.663	0.671	0.671	0.664	0.595	0.763	0.670	0.774	0.139
1.278	1.371	1.423	1.345	1.324	1.325	1.313	1.390	1.229	1.330	1.222	1.847
0.000	0.000	0.000	0.000	0.000	0.004	0.003	0.003	0.000	0.000	0.000	0.000
1.997	1.982	1.997	2.008	1.994	2.000	1.980	1.988	1.992	2.000	1.996	1.987
0.676	0.621	0.544	0.559	0.647	0.617	0.697	0.615	0.767	0.653	0.751	0.123
0.000	0.000	0.000	0.000	0.008	0.004	0.009	0.006	0.005	0.006	0.012	0.000
0.307	0.412	0.446	0.376	0.345	0.354	0.344	0.409	0.244	0.335	0.238	0.883
0.000	0.000	0.000	0.000	0.000	0.000	0.000	0.000	0.000	0.000	0.000	0.000
0.000	0.000	0.000	0.000	0.000	0.000	0.000	0.000	0.000	0.000	0.000	0.005
0.000	0.000	0.000	0.000	0.000	0.000	0.000	0.000	0.000	0.000	0.000	0.000
0.984	1.033	0.990	0.935	1.000	0.976	1.050	1.030	1.016	0.994	1.000	1.012
0.687	0.601	0.549	0.598	0.646	0.633	0.664	0.597	0.755	0.657	0.751	0.122
0.313	0.399	0.451	0.402	0.345	0.363	0.328	0.397	0.240	0.337	0.238	0.873
0.000	0.000	0.000	0.000	0.008	0.004	0.008	0.006	0.005	0.006	0.012	0.000
0.000	0.000	0.000	0.000	0.000	0.000	0.000	0.000	0.000	0.000	0.000	0.000
0.000	0.000	0.000	0.000	0.000	0.000	0.000	0.000	0.000	0.000	0.000	0.005

37	38	39	40	41	42	43	44	45	46	47	48
NP-020 Old	NP-020 Old	NP-020 Old	NP-020 Old	NP-020 Old	NP-020 Old	NP-020 Old	NP-020 Old	NP-020 Old	NP-007 Young	NP-007 Young	NP-007 Young
medium-grained gabbro	medium-grained gabbro	medium-grained gabbro	medium-grained gabbro	medium-grained gabbro	medium-grained gabbro	medium-grained gabbro	medium-grained gabbro	medium-grained gabbro	medium-grained Amp-Bt granodiorite	medium-grained Amp-Bt granodiorite	medium-grained Amp-Bt granodiorite
b.d.l.	b.d.l.	b.d.l.	b.d.l.	b.d.l.	b.d.l.	b.d.l.	b.d.l.	b.d.l.	b.d.l.	b.d.l.	b.d.l.
46.187	48.546	48.378	47.943	49.325	48.111	47.862	47.873	47.515	57.040	69.434	58.040
34.557	32.987	32.910	32.662	32.234	33.167	33.272	32.845	33.351	26.957	20.242	26.577
0.131	0.178	0.000	0.176	0.154	0.000	0.092	0.089	0.121	0.084	0.260	0.000
18.103	16.566	16.846	16.841	15.816	17.027	17.112	16.996	17.223	9.460	0.179	8.925
0.162	0.131	0.126	0.218	0.197	0.145	0.179	0.132	0.177	b.d.l.	b.d.l.	b.d.l.
1.369	2.270	2.107	2.171	2.681	2.212	2.206	2.145	2.003	6.056	11.157	6.876
b.d.l.	b.d.l.	b.d.l.	b.d.l.	b.d.l.	b.d.l.	b.d.l.	b.d.l.	b.d.l.	0.129	0.091	0.146
b.d.l.	b.d.l.	b.d.l.	b.d.l.	b.d.l.	b.d.l.	b.d.l.	b.d.l.	b.d.l.	b.d.l.	b.d.l.	b.d.l.
b.d.l.	b.d.l.	b.d.l.	b.d.l.	b.d.l.	b.d.l.	b.d.l.	b.d.l.	b.d.l.	b.d.l.	b.d.l.	b.d.l.
100.509	100.678	100.367	100.011	100.407	100.662	100.723	100.080	100.390	99.726	101.363	100.564
0.000	0.000	0.000	0.000	0.000	0.000	0.000	0.000	0.000	0.000	0.000	0.000
2.118	2.211	2.210	2.203	2.249	2.195	2.185	2.198	2.177	2.565	2.986	2.588
1.868	1.771	1.772	1.769	1.732	1.784	1.790	1.777	1.801	1.428	1.026	1.397
0.005	0.006	0.000	0.006	0.005	0.000	0.003	0.003	0.004	0.003	0.008	0.000
0.890	0.808	0.825	0.829	0.773	0.832	0.837	0.836	0.845	0.456	0.008	0.426
0.004	0.003	0.003	0.006	0.005	0.004	0.005	0.004	0.005	0.000	0.000	0.000
0.122	0.200	0.187	0.193	0.237	0.196	0.195	0.191	0.178	0.528	0.930	0.595
0.000	0.000	0.000	0.000	0.000	0.000	0.000	0.000	0.000	0.007	0.005	0.008
0.000	0.000	0.000	0.000	0.000	0.000	0.000	0.000	0.000	0.000	0.000	0.000
5.006	5.000	4.997	5.006	5.001	5.011	5.016	5.008	5.010	4.987	4.964	5.015
2.000	2.000	2.000	2.000	2.000	2.000	2.000	2.000	2.000	2.000	2.000	2.000
2.000	2.000	2.000	2.000	2.000	2.000	2.000	2.000	2.000	2.000	2.000	2.000
0.000	0.000	0.000	0.000	0.000	0.000	0.000	0.000	0.000	0.000	0.000	0.000
0.118	0.211	0.210	0.203	0.249	0.195	0.185	0.198	0.177	0.565	0.986	0.588
1.868	1.771	1.772	1.769	1.732	1.784	1.790	1.777	1.801	1.428	1.026	1.397
0.005	0.006	0.000	0.006	0.005	0.000	0.003	0.003	0.004	0.003	0.000	0.000
1.991	1.988	1.982	1.978	1.986	1.979	1.979	1.978	1.982	1.996	2.012	1.985
0.122	0.200	0.187	0.193	0.237	0.196	0.195	0.191	0.178	0.528	0.930	0.595
0.000	0.000	0.000	0.000	0.000	0.000	0.000	0.000	0.000	0.007	0.005	0.008
0.890	0.808	0.825	0.829	0.773	0.832	0.837	0.836	0.845	0.456	0.008	0.426
0.000	0.000	0.000	0.000	0.000	0.000	0.000	0.000	0.000	0.000	0.008	0.000
0.004	0.003	0.003	0.006	0.005	0.004	0.005	0.004	0.005	0.000	0.000	0.000
0.000	0.000	0.000	0.000	0.000	0.000	0.000	0.000	0.000	0.000	0.000	0.000
1.016	1.012	1.015	1.028	1.015	1.032	1.037	1.030	1.028	0.991	0.952	1.029
0.120	0.198	0.184	0.188	0.234	0.190	0.188	0.185	0.173	0.533	0.986	0.578
0.876	0.799	0.813	0.806	0.761	0.807	0.807	0.811	0.822	0.460	0.009	0.414
0.000	0.000	0.000	0.000	0.000	0.000	0.000	0.000	0.000	0.007	0.005	0.008
0.000	0.000	0.000	0.000	0.000	0.000	0.000	0.000	0.000	0.000	0.000	0.000
0.004	0.003	0.003	0.006	0.005	0.004	0.005	0.003	0.005	0.000	0.000	0.000

49	50	51	52	53	54	55	56	57	58	59	60
NP-007 Young medium-grained Amp-Bt granodiorite	NP-007 Young medium-grained Amp-Bt granodiorite	NP-007 Young medium-grained Amp-Bt granodiorite	NP-009 Young medium-grained Amp-Bt tonalite	NP-009 Young medium-grained Amp-Bt tonalite	NP-009 Young medium-grained Amp-Bt tonalite	NP-009 Young medium-grained Amp-Bt tonalite	NP-009 Young medium-grained Amp-Bt tonalite	NP-009 Young medium-grained Amp-Bt tonalite	NP-009 Young medium-grained Amp-Bt tonalite	NP-009 Young medium-grained Amp-Bt tonalite	NP-009 Young medium-grained Amp-Bt tonalite
b.d.l.	b.d.l.	b.d.l.	b.d.l.	b.d.l.	b.d.l.	b.d.l.	b.d.l.	b.d.l.	b.d.l.	b.d.l.	b.d.l.
57.740	64.606	59.035	56.573	56.554	56.295	55.986	47.755	59.468	48.619	56.619	56.442
26.545	22.314	25.696	27.454	27.469	27.376	27.265	32.689	25.167	32.331	27.049	28.012
0.000	0.000	0.000	0.000	0.071	0.000	0.000	0.098	0.060	0.113	0.000	0.081
8.652	3.456	7.784	10.072	9.989	10.337	10.146	16.950	10.073	16.413	9.759	10.738
b.d.l.	b.d.l.	b.d.l.	b.d.l.	b.d.l.	b.d.l.	b.d.l.	b.d.l.	b.d.l.	b.d.l.	b.d.l.	b.d.l.
6.555	9.086	7.094	5.397	6.085	5.677	5.821	1.904	4.781	2.350	5.451	5.562
0.133	0.096	0.095	0.065	0.119	0.080	0.099	b.d.l.	0.092	0.065	0.102	0.098
b.d.l.	b.d.l.	b.d.l.	b.d.l.	b.d.l.	b.d.l.	b.d.l.	b.d.l.	b.d.l.	b.d.l.	b.d.l.	0.233
b.d.l.	b.d.l.	b.d.l.	b.d.l.	b.d.l.	b.d.l.	b.d.l.	b.d.l.	b.d.l.	b.d.l.	b.d.l.	b.d.l.
99.625	99.558	99.704	99.561	100.287	99.765	99.317	99.396	99.641	99.891	98.980	101.166
0.000	0.000	0.000	0.000	0.000	0.000	0.000	0.000	0.000	0.000	0.000	0.000
2.593	2.852	2.642	2.546	2.536	2.536	2.534	2.203	2.658	2.230	2.561	2.515
1.405	1.161	1.355	1.456	1.451	1.453	1.454	1.777	1.326	1.748	1.442	1.471
0.000	0.000	0.000	0.000	0.002	0.000	0.000	0.003	0.002	0.004	0.000	0.003
0.416	0.163	0.373	0.486	0.480	0.499	0.492	0.838	0.482	0.807	0.473	0.513
0.000	0.000	0.000	0.000	0.000	0.000	0.000	0.000	0.000	0.000	0.000	0.000
0.571	0.778	0.615	0.471	0.529	0.496	0.511	0.170	0.414	0.209	0.478	0.481
0.008	0.005	0.005	0.004	0.007	0.005	0.006	0.000	0.005	0.004	0.006	0.006
0.000	0.000	0.000	0.000	0.000	0.000	0.000	0.000	0.000	0.000	0.000	0.007
4.993	4.959	4.991	4.963	5.005	4.988	4.997	4.992	4.888	5.001	4.960	4.994
2.000	2.000	2.000	2.000	2.000	2.000	2.000	2.000	2.000	2.000	2.000	2.000
2.000	2.000	2.000	2.000	2.000	2.000	2.000	2.000	2.000	2.000	2.000	2.000
0.000	0.000	0.000	0.000	0.000	0.000	0.000	0.000	0.000	0.000	0.000	0.000
0.593	0.852	0.642	0.546	0.536	0.536	0.534	0.203	0.658	0.230	0.561	0.515
1.405	1.161	1.355	1.456	1.451	1.453	1.454	1.777	1.326	1.748	1.442	1.471
0.000	0.000	0.000	0.000	0.002	0.000	0.000	0.003	0.002	0.004	0.000	0.003
1.998	2.013	1.997	2.003	1.990	1.989	1.988	1.984	1.986	1.981	2.003	1.989
0.571	0.778	0.615	0.471	0.529	0.496	0.511	0.170	0.414	0.209	0.478	0.481
0.008	0.005	0.005	0.004	0.007	0.005	0.006	0.000	0.005	0.004	0.006	0.006
0.416	0.163	0.373	0.486	0.480	0.499	0.492	0.838	0.482	0.807	0.473	0.513
0.000	0.000	0.000	0.000	0.000	0.000	0.000	0.000	0.000	0.000	0.000	0.000
0.000	0.000	0.000	0.000	0.000	0.000	0.000	0.000	0.000	0.000	0.000	0.000
0.000	0.000	0.000	0.000	0.000	0.000	0.000	0.000	0.000	0.000	0.000	0.007
0.995	0.946	0.994	0.960	1.016	0.999	1.009	1.008	0.902	1.019	0.957	1.005
0.574	0.822	0.619	0.490	0.521	0.496	0.506	0.169	0.459	0.205	0.500	0.481
0.419	0.173	0.375	0.506	0.472	0.499	0.488	0.831	0.535	0.791	0.494	0.513
0.008	0.006	0.005	0.004	0.007	0.005	0.006	0.000	0.006	0.004	0.006	0.006
0.000	0.000	0.000	0.000	0.000	0.000	0.000	0.000	0.000	0.000	0.000	0.000
0.000	0.000	0.000	0.000	0.000	0.000	0.000	0.000	0.000	0.000	0.000	0.000

61	62	63	64	65	66	67	68	69	70	71	72
NP-009 Young	NP-009 Young	NP-009 Young	NP-010 Young	NP-010 Young	NP-010 Young	NP-010 Young	NP-010 Young	NP-021 Young	NP-021 Young	NP-021 Young	NP-021 Young
medium-grained Amp-Bt tonalite	medium-grained Amp-Bt tonalite	medium-grained Amp-Bt tonalite	gray (Ms?) Bt granite	gray (Ms?) Bt granite	gray (Ms?) Bt granite	gray (Ms?) Bt granite	gray (Ms?) Bt granite	coarse-grained Bt granite	coarse-grained Bt granite	coarse-grained Bt granite	coarse-grained Bt granite
b.d.l.	b.d.l.	b.d.l.	0.257	0.156	0.432	b.d.l.	0.276	b.d.l.	b.d.l.	b.d.l.	0.096
55.180	57.098	56.749	66.950	65.583	67.249	66.501	66.522	62.404	60.615	62.712	62.109
29.165	27.813	28.253	21.423	21.655	21.723	21.877	21.474	23.601	24.664	23.423	23.948
0.194	0.088	0.000	0.000	0.000	0.000	0.000	0.000	0.080	0.000	0.000	0.000
11.779	10.150	10.604	2.124	2.322	2.057	2.696	2.188	5.452	6.806	4.939	5.210
b.d.l.	b.d.l.	b.d.l.	b.d.l.	b.d.l.	b.d.l.	b.d.l.	b.d.l.	b.d.l.	b.d.l.	b.d.l.	b.d.l.
5.107	5.959	5.661	10.874	10.507	11.052	10.708	10.520	8.403	7.722	8.578	8.343
0.111	0.088	0.095	0.134	0.122	0.114	0.239	0.151	0.105	0.200	0.163	0.188
b.d.l.	b.d.l.	b.d.l.	b.d.l.	0.188	b.d.l.	b.d.l.	b.d.l.	b.d.l.	b.d.l.	b.d.l.	b.d.l.
b.d.l.	b.d.l.	0.085	b.d.l.	b.d.l.	b.d.l.	b.d.l.	b.d.l.	b.d.l.	b.d.l.	b.d.l.	b.d.l.
101.536	101.196	101.447	101.762	100.533	102.627	102.021	101.131	100.045	100.007	99.815	99.894
0.000	0.000	0.000	0.009	0.006	0.016	0.000	0.010	0.000	0.000	0.000	0.004
2.456	2.535	2.517	2.892	2.874	2.880	2.874	2.889	2.763	2.698	2.779	2.752
1.529	1.455	1.477	1.090	1.118	1.096	1.114	1.099	1.232	1.294	1.223	1.251
0.007	0.003	0.000	0.000	0.000	0.000	0.000	0.000	0.003	0.000	0.000	0.000
0.562	0.483	0.504	0.098	0.109	0.094	0.125	0.102	0.259	0.325	0.234	0.247
0.000	0.000	0.000	0.000	0.000	0.000	0.000	0.000	0.000	0.000	0.000	0.000
0.441	0.513	0.487	0.911	0.892	0.918	0.897	0.886	0.721	0.666	0.737	0.717
0.006	0.005	0.005	0.007	0.007	0.006	0.013	0.008	0.006	0.011	0.009	0.011
0.000	0.000	0.000	0.000	0.005	0.000	0.000	0.000	0.000	0.000	0.000	0.000
5.000	4.994	4.990	5.008	5.011	5.010	5.024	4.994	4.983	4.994	4.983	4.981
2.000	2.000	2.000	2.000	2.000	2.000	2.000	2.000	2.000	2.000	2.000	2.000
2.000	2.000	2.000	2.000	2.000	2.000	2.000	2.000	2.000	2.000	2.000	2.000
0.000	0.000	0.000	0.009	0.006	0.016	0.000	0.010	0.000	0.000	0.000	0.004
0.456	0.535	0.517	0.892	0.874	0.880	0.874	0.889	0.763	0.698	0.779	0.752
1.529	1.455	1.477	1.090	1.118	1.096	1.114	1.099	1.232	1.294	1.223	1.251
0.007	0.003	0.000	0.000	0.000	0.000	0.000	0.000	0.003	0.000	0.000	0.000
1.991	1.994	1.994	1.992	1.997	1.992	1.989	1.998	1.997	1.992	2.002	2.006
0.441	0.513	0.487	0.911	0.892	0.918	0.897	0.886	0.721	0.666	0.737	0.717
0.006	0.005	0.005	0.007	0.007	0.006	0.013	0.008	0.006	0.011	0.009	0.011
0.562	0.483	0.504	0.098	0.109	0.094	0.125	0.102	0.259	0.325	0.234	0.247
0.000	0.000	0.000	0.000	0.000	0.000	0.000	0.000	0.000	0.000	0.000	0.000
0.000	0.000	0.000	0.000	0.000	0.000	0.000	0.000	0.000	0.000	0.000	0.000
0.000	0.000	0.000	0.000	0.005	0.000	0.000	0.000	0.000	0.000	0.000	0.000
1.008	1.001	0.996	1.016	1.014	1.018	1.035	0.996	0.986	1.002	0.981	0.975
0.437	0.513	0.489	0.896	0.885	0.901	0.867	0.889	0.732	0.665	0.751	0.735
0.557	0.482	0.506	0.097	0.108	0.093	0.121	0.102	0.262	0.324	0.239	0.254
0.006	0.005	0.005	0.007	0.007	0.006	0.013	0.008	0.006	0.011	0.009	0.011
0.000	0.000	0.000	0.000	0.000	0.000	0.000	0.000	0.000	0.000	0.000	0.000
0.000	0.000	0.000	0.000	0.000	0.000	0.000	0.000	0.000	0.000	0.000	0.000

73	74	75	76	77	78	79
NP-021	NP-017	NP-017	NP-017	NP-017	NP-017	NP-017
Young	Unknown	Unknown	Unknown	Unknown	Unknown	Unknown
coarse-grained Bt granite	fine-grained mafic dyke	fine-grained mafic dyke	fine-grained mafic dyke	fine-grained mafic dyke	fine-grained mafic dyke	fine-grained mafic dyke
b.d.l.	b.d.l.	b.d.l.	b.d.l.	b.d.l.	b.d.l.	b.d.l.
68.706	60.399	59.757	60.009	59.571	60.972	59.532
20.341	24.759	25.760	25.417	25.656	25.135	25.581
0.000	0.000	0.000	0.110	0.000	0.000	0.193
0.742	6.866	7.664	7.149	7.618	6.654	7.761
b.d.l.	0.117	0.118	0.169	0.120	0.114	0.101
11.278	7.224	7.040	7.370	7.120	8.012	7.328
0.118	0.071	0.084	0.225	0.098	0.077	0.074
b.d.l.	b.d.l.	b.d.l.	b.d.l.	b.d.l.	b.d.l.	b.d.l.
b.d.l.	b.d.l.	b.d.l.	b.d.l.	b.d.l.	b.d.l.	b.d.l.
101.185	99.436	100.423	100.449	100.183	100.964	100.570
0.000	0.000	0.000	0.000	0.000	0.000	0.000
2.968	2.699	2.653	2.665	2.652	2.689	2.646
1.036	1.304	1.348	1.330	1.346	1.306	1.340
0.000	0.000	0.000	0.004	0.000	0.000	0.006
0.034	0.329	0.365	0.340	0.363	0.314	0.369
0.000	0.003	0.003	0.004	0.003	0.003	0.003
0.945	0.626	0.606	0.635	0.615	0.685	0.631
0.007	0.004	0.005	0.013	0.006	0.004	0.004
0.000	0.000	0.000	0.000	0.000	0.000	0.000
4.989	4.964	4.979	4.991	4.985	5.002	4.999
2.000	2.000	2.000	2.000	2.000	2.000	2.000
2.000	2.000	2.000	2.000	2.000	2.000	2.000
0.000	0.000	0.000	0.000	0.000	0.000	0.000
0.968	0.699	0.653	0.665	0.652	0.689	0.646
1.036	1.304	1.348	1.330	1.346	1.306	1.340
0.000	0.000	0.000	0.004	0.000	0.000	0.006
2.004	2.003	2.000	1.999	1.998	1.996	1.992
0.945	0.626	0.606	0.635	0.615	0.685	0.631
0.007	0.004	0.005	0.013	0.006	0.004	0.004
0.034	0.329	0.365	0.340	0.363	0.314	0.369
0.000	0.000	0.000	0.000	0.000	0.000	0.000
0.000	0.003	0.003	0.004	0.003	0.003	0.003
0.000	0.000	0.000	0.000	0.000	0.000	0.000
0.985	0.962	0.978	0.992	0.987	1.007	1.008
0.959	0.651	0.619	0.640	0.623	0.680	0.627
0.035	0.342	0.373	0.343	0.368	0.312	0.367
0.007	0.004	0.005	0.013	0.006	0.004	0.004
0.000	0.000	0.000	0.000	0.000	0.000	0.000
0.000	0.003	0.003	0.004	0.003	0.003	0.003

MUSCOVITE formulae recalculated on the basis of 11 O equivalents

	25	27	31	38	51	59	66	10
Comment	NP-010	NP-010	NP-010	NP-010	NP-021	NP-021	NP-021	NP-017
Suite	Young	Young	Young	Young	Young	Young	Young	Unknown
Petrology	gray (Ms?) Bt granite	gray (Ms?) Bt granite	gray (Ms?) Bt granite	gray (Ms?) Bt granite	coarse-grained Bt granite	coarse-grained Bt granite	coarse-grained Bt granite	fine-grained mafic dyke
SiO_2	46.217	46.345	46.118	46.552	47.113	47.021	45.782	46.366
TiO_2	0.453	0.575	0.388	0.554	0.505	0.782	0.709	0.743
Al_2O_3	35.215	35.433	35.721	34.995	34.934	33.964	34.583	29.602
MgO	0.552	0.511	0.401	0.561	0.804	0.812	0.700	1.514
FeO	1.364	1.299	1.172	1.382	2.513	2.812	2.446	5.154
BaO	b.d.l.	b.d.l.	b.d.l.	b.d.l.	0.090	b.d.l.	b.d.l.	1.319
Na_2O	0.415	0.423	0.376	0.445	0.285	0.281	0.428	0.222
K_2O	11.007	10.658	10.723	10.832	10.723	10.643	10.615	10.310
F	0.252	0.258	0.227	0.202	0.324	0.339	0.266	0.108
H_2O	4.372	4.382	4.383	4.406	4.404	4.361	4.346	4.312
O=F	-0.106	-0.109	-0.096	-0.085	-0.136	-0.143	-0.112	-0.045
Σ	99.741	99.776	99.414	99.844	101.559	100.872	99.763	99.604
Si	3.086	3.085	3.079	3.101	3.100	3.118	3.070	3.187
Ti	0.023	0.029	0.019	0.028	0.025	0.039	0.036	0.038
Al	2.771	2.780	2.811	2.747	2.709	2.654	2.733	2.398
Mg	0.055	0.051	0.040	0.056	0.079	0.080	0.070	0.155
Fe^{II}	0.076	0.072	0.065	0.077	0.138	0.156	0.137	0.296
Ba	0.000	0.000	0.000	0.000	0.002	0.000	0.000	0.036
Na	0.054	0.055	0.049	0.057	0.036	0.036	0.056	0.030
K	0.937	0.905	0.913	0.920	0.900	0.900	0.908	0.904
F	0.053	0.054	0.048	0.043	0.067	0.071	0.056	0.023
Σ.atoms	7.055	7.030	7.025	7.029	7.057	7.055	7.066	7.066
Si_T	3.086	3.085	3.079	3.101	3.100	3.118	3.070	3.187
Al_T	0.914	0.915	0.921	0.899	0.900	0.882	0.930	0.813
Σ_T	4.000	4.000	4.000	4.000	4.000	4.000	4.000	4.000
Al_M	1.857	1.865	1.890	1.848	1.808	1.772	1.803	1.584
Mg_M	0.055	0.051	0.040	0.056	0.079	0.080	0.070	0.155
Fe^{II}_M	0.076	0.072	0.065	0.077	0.113	0.147	0.127	0.261
Ti_M	0.023	0.029	0.019	0.028	0.000	0.000	0.000	0.000
Σ_M	2.010	2.017	2.015	2.009	2.000	2.000	2.000	2.000
K_I	0.937	0.905	0.913	0.920	0.900	0.900	0.908	0.904
Na_I	0.054	0.055	0.049	0.057	0.036	0.036	0.056	0.030
Ba_I	0.000	0.000	0.000	0.000	0.002	0.000	0.000	0.036
Σ_I	0.991	0.960	0.962	0.978	0.939	0.936	0.964	0.969
Σ_cations	7.002	6.976	6.977	6.987	6.989	6.984	7.010	7.043
F_OH	0.053	0.054	0.048	0.043	0.067	0.071	0.056	0.023
OH_OH	1.947	1.946	1.952	1.957	1.933	1.929	1.944	1.977
Σ_OH	2.000	2.000	2.000	2.000	2.000	2.000	2.000	2.000

EPIDOTE for
Fe^{II}/Fe^{III} alloc

Comment
Suite
Petrology
SiO_2
TiO_2
Al_2O_3
V_2O_3
Fe_2O_3
CaO
MnO
FeO
SrO
F
H_2O
O=F
Σ
Si
Ti
Al
V
Fe^{III}
Ca
Mn^{II}
Fe^{II}
Sr
F
Σ.atoms
Si_Z
Al_Z
Σ_Z
Ti_M
Al_M
V_M
Fe^{III}_M
Fe^{II}_M
Mn_M
Σ_M
Mn_A
Fe^{II}_A
Ca_A
Sr_A
Σ_A

ALLANITE formulae recalculated on the basis of 12.5 oxygen equivalents
Fe^{II}/Fe^{III} allocated assuming 8 cations per formula unit (Droop 1987)

	83	92	26	31	32	33	15
Comment	NP-011	NP-011	NP-012	NP-012	NP-012	NP-012	NP-009
Suite	Old	Old	Old	Old	Old	Old	Young
Petrology	Amp-bearing QtzD	Amp-bearing QtzD	Amp-Bt tonalite	Amp-Bt tonalite	Amp-Bt tonalite	Amp-Bt tonalite	medium-grained Amp-Bt tonalite
P_2O_5	b.d.l.	b.d.l.	b.d.l.	b.d.l.	0.062	b.d.l.	b.d.l.
SiO_2	33.773	33.150	35.958	34.514	34.356	33.505	34.219
TiO_2	0.323	0.510	0.187	0.236	0.344	0.476	0.532
ThO_2	0.105	0.095	b.d.l.	b.d.l.	0.379	0.733	0.332
Al_2O_3	14.209	17.719	23.656	21.233	19.674	19.213	17.147
Sc_2O_3	b.d.l.	b.d.l.	0.033	b.d.l.	b.d.l.	b.d.l.	b.d.l.
Fe_2O_3	11.289	6.943	5.564	4.621	5.609	5.048	5.466
Y_2O_3	0.095	0.161	0.400	0.378	b.d.l.	b.d.l.	0.143
La_2O_3	3.146	2.454	0.854	3.524	4.007	3.354	3.122
Ce_2O_3	6.245	5.733	3.705	7.274	7.985	6.724	7.874
Pr_2O_3	0.588	0.532	0.591	0.732	0.832	0.612	0.625
Nd_2O_3	2.027	2.123	3.133	2.722	2.345	1.938	2.461
Sm_2O_3	0.236	0.201	0.577	0.330	0.128	b.d.l.	b.d.l.
Gd_2O_3	b.d.l.	b.d.l.	0.317	0.278	b.d.l.	b.d.l.	b.d.l.
MgO	0.541	0.429	0.285	0.616	1.234	0.823	0.498
CaO	15.394	15.679	19.178	16.007	15.714	16.248	15.166
MnO	0.295	0.308	0.167	0.212	0.218	0.296	0.291
FeO	6.055	5.093	3.595	5.914	5.443	3.750	7.440
SrO	b.d.l.	b.d.l.	b.d.l.	b.d.l.	b.d.l.	0.265	0.421
Na_2O	0.152	0.214	b.d.l.	b.d.l.	b.d.l.	0.230	b.d.l.
F	0.061	0.130	0.133	0.147	0.167	0.261	0.071
Cl	0.050	0.079	b.d.l.	b.d.l.	b.d.l.	b.d.l.	b.d.l.
H_2O	1.545	1.521	1.708	1.633	1.604	1.497	1.590
O=F	-0.026	-0.055	-0.056	-0.062	-0.070	-0.110	-0.030
O=Cl	-0.011	-0.018	b.d.l.	b.d.l.	b.d.l.	b.d.l.	b.d.l.
Σ	96.092	93.003	99.985	100.310	100.031	94.864	97.367
Si	3.116	3.079	3.002	3.001	3.015	3.056	3.113
Ti	0.022	0.036	0.012	0.015	0.023	0.033	0.036
Th	0.002	0.002	0.000	0.000	0.008	0.015	0.007
Al	1.545	1.939	2.327	2.176	2.035	2.065	1.838
Fe^{III}	0.784	0.485	0.350	0.302	0.370	0.347	0.374
Y	0.005	0.008	0.018	0.017	0.000	0.000	0.007
La	0.107	0.084	0.026	0.113	0.130	0.113	0.105
Ce	0.211	0.195	0.113	0.232	0.257	0.225	0.262
Pr	0.020	0.018	0.018	0.023	0.027	0.020	0.021
Nd	0.067	0.070	0.093	0.085	0.073	0.063	0.080
Sm	0.008	0.006	0.017	0.010	0.004	0.000	0.000
Gd	0.000	0.000	0.009	0.008	0.000	0.000	0.000
Mg	0.074	0.059	0.035	0.080	0.161	0.112	0.068
Ca	1.522	1.560	1.715	1.491	1.477	1.588	1.478
Mn	0.023	0.024	0.012	0.016	0.016	0.023	0.022
Fe^{II}	0.467	0.396	0.251	0.430	0.399	0.286	0.566
Sr	0.000	0.000	0.000	0.000	0.000	0.014	0.022
Na	0.027	0.039	0.000	0.000	0.000	0.041	0.000
F	0.018	0.039	0.036	0.041	0.047	0.076	0.021
Σ.atoms	8.018	8.039	8.033	8.041	8.042	8.076	8.021
Si_Z	3.116	3.079	3.002	3.001	3.015	3.056	3.113
Σ_Z	3.116	3.079	3.002	3.001	3.015	3.056	3.113
Ti_M	0.022	0.036	0.012	0.015	0.023	0.033	0.036
Al_M	1.545	1.939	2.327	2.176	2.035	2.065	1.838
Mg_M	0.074	0.059	0.035	0.080	0.161	0.112	0.068
Fe^{III}_M	0.784	0.485	0.350	0.302	0.370	0.347	0.374
Fe^{II}_M	0.467	0.396	0.251	0.426	0.399	0.286	0.566
Mn_M	0.023	0.024	0.012	0.000	0.011	0.023	0.022
Σ_M	2.916	2.939	2.987	3.000	3.000	2.865	2.905
Mn_A	0.000	0.000	0.000	0.016	0.005	0.000	0.000
Fe^{II}_A	0.000	0.000	0.000	0.004	0.000	0.000	0.000
Ca_A	1.522	1.560	1.715	1.491	1.477	1.588	1.478
Sr_A	0.000	0.000	0.000	0.000	0.000	0.014	0.022
Na_A	0.027	0.039	0.000	0.000	0.000	0.041	0.000
La_A	0.107	0.084	0.026	0.113	0.130	0.113	0.105
Ce_A	0.211	0.195	0.113	0.232	0.257	0.225	0.262
Pr_A	0.020	0.018	0.018	0.023	0.027	0.020	0.021
Nd_A	0.067	0.070	0.093	0.085	0.073	0.000	0.080
Sm_A	0.008	0.006	0.017	0.010	0.004	0.000	0.000
Gd_A	0.000	0.000	0.009	0.008	0.000	0.000	0.000
Y_A	0.005	0.008	0.018	0.017	0.000	0.000	0.007
Th_A	0.002	0.002	0.000	0.000	0.008	0.000	0.007
Vc_A	0.032	0.018	0.000	0.001	0.020	0.000	0.018
Σ_A	2.000	2.000	2.009	2.000	2.000	2.000	2.000
Σ_cations	8.000	8.000	7.998	8.000	7.995	8.000	8.000
F_F	0.018	0.039	0.036	0.041	0.047	0.076	0.021
OH_F	0.982	0.961	0.964	0.959	0.953	0.924	0.979
Σ_F	1.000	1.000	1.000	1.000	1.000	1.000	1.000
REE	0.417	0.382	0.294	0.488	0.490	0.421	0.475
REE + Th	0.419	0.384	0.294	0.488	0.498	0.436	0.481

TITANITE formulae recalculated on the basis of 20 oxygen equivalents
Fe^{II}/Fe^{III} allocated assuming 12 cations per formula unit (Droop 1987)

	1	2	3	4	5	6	7	8	9	10
Comment	NP-012	NP-012	NP-012	NP-012	NP-013	NP-013	NP-018	NP-018	NP-018	NP-018
Suite	Old	Old	Old	Old	Old	Old	Old	Old	Old	Old
Petrology	Amp-Bt tonalite	Amp-Bt tonalite	Amp-Bt tonalite	Amp-Bt tonalite	Hornblendite	Hornblendite	Bt augengneiss	Bt augengneiss	Bt augengneiss	Bt augengneiss
Nb_2O_5	0.516	0.240	b.d.l.	0.086	b.d.l.	b.d.l.	b.d.l.	0.174	0.302	0.115
SiO_2	30.209	30.313	30.609	30.934	31.120	30.978	30.571	30.377	28.797	29.344
TiO_2	36.867	36.987	36.723	36.498	37.536	37.632	37.723	37.497	35.269	36.637
Al_2O_3	1.541	1.393	2.358	2.348	1.494	1.827	1.561	1.255	1.777	1.347
V_2O_3	b.d.l.	b.d.l.	b.d.l.	0.237	b.d.l.	0.273	b.d.l.	b.d.l.	b.d.l.	b.d.l.
Fe_2O_3	1.048	0.924	0.639	0.622	0.559	0.625	0.967	1.371	1.455	1.296
Y_2O_3	0.474	0.492	0.230	0.309	0.098	0.076	0.110	0.146	0.831	0.127
Ce_2O_3	0.558	0.510	0.135	0.172	0.161	0.187	0.261	0.300	0.518	0.210
Nd_2O_3	0.460	0.418	b.d.l.	b.d.l.	b.d.l.	b.d.l.	b.d.l.	0.215	0.717	0.282
Sm_2O_3	b.d.l.	b.d.l.	b.d.l.	b.d.l.	b.d.l.	b.d.l.	b.d.l.	b.d.l.	0.291	b.d.l.
Gd_2O_3	b.d.l.	b.d.l.	b.d.l.	b.d.l.	b.d.l.	b.d.l.	b.d.l.	b.d.l.	b.d.l.	b.d.l.
CaO	27.857	28.001	29.037	29.117	29.184	29.079	28.571	28.558	24.950	26.736
MnO	0.073	0.100	0.065	b.d.l.	0.054	b.d.l.	0.131	0.162	0.186	0.132
FeO	0.000	0.000	0.000	0.000	0.000	0.000	0.000	0.000	0.000	0.000
BaO	b.d.l.	b.d.l.	b.d.l.	b.d.l.	b.d.l.	b.d.l.	b.d.l.	b.d.l.	b.d.l.	b.d.l.
Na_2O	b.d.l.	b.d.l.	b.d.l.	b.d.l.	b.d.l.	b.d.l.	b.d.l.	b.d.l.	b.d.l.	b.d.l.
F	0.348	0.381	0.877	0.897	0.533	0.568	0.660	0.574	0.491	0.655
Σ	99.951	99.759	100.673	101.220	100.739	101.245	100.555	100.629	95.584	96.881
Nb	0.031	0.014	0.000	0.005	0.000	0.000	0.000	0.010	0.019	0.007
Si	3.970	3.986	3.957	3.980	4.017	3.980	3.971	3.955	3.994	3.978
Ti	3.645	3.658	3.571	3.532	3.645	3.637	3.686	3.672	3.679	3.736
Al	0.239	0.216	0.359	0.356	0.227	0.277	0.239	0.193	0.290	0.215
V	0.000	0.000	0.000	0.024	0.000	0.028	0.000	0.000	0.000	0.000
Fe^{III}	0.104	0.091	0.062	0.060	0.054	0.060	0.095	0.134	0.152	0.132
Y	0.033	0.034	0.016	0.021	0.007	0.005	0.008	0.010	0.061	0.009
Ce	0.027	0.025	0.006	0.008	0.008	0.009	0.012	0.014	0.026	0.010
Nd	0.022	0.020	0.000	0.000	0.000	0.000	0.000	0.010	0.036	0.014
Sm	0.000	0.000	0.000	0.000	0.000	0.000	0.000	0.000	0.014	0.000
Gd	0.000	0.000	0.000	0.000	0.000	0.000	0.000	0.000	0.000	0.000
Ca	3.922	3.945	4.021	4.013	4.036	4.003	3.976	3.983	3.707	3.883
Mn	0.008	0.011	0.007	0.000	0.006	0.000	0.014	0.018	0.022	0.015
Fe^{II}	0.000	0.000	0.000	0.000	0.000	0.000	0.000	0.000	0.000	0.000
Ba	0.000	0.000	0.000	0.000	0.000	0.000	0.000	0.000	0.000	0.000
Na	0.000	0.000	0.000	0.000	0.000	0.000	0.000	0.000	0.000	0.000
Σ.atoms	12.000	12.000	12.000	12.000	12.000	12.000	12.000	12.000	12.000	12.000
Ti_Y	3.645	3.658	3.571	3.532	3.645	3.637	3.686	3.672	3.679	3.736
Al_Y	0.239	0.216	0.359	0.356	0.227	0.277	0.239	0.193	0.290	0.215
Fe^{III}_Y	0.104	0.091	0.062	0.060	0.054	0.060	0.095	0.134	0.152	0.132
Σ_Y	3.987	3.966	3.992	3.948	3.927	3.974	4.019	3.999	4.122	4.084
Ca_X	3.922	3.945	4.021	4.013	4.036	4.003	3.976	3.983	3.707	3.883
Na_X	0.000	0.000	0.000	0.000	0.000	0.000	0.000	0.000	0.000	0.000
Ce_X	0.027	0.025	0.006	0.008	0.008	0.009	0.012	0.014	0.026	0.010
Nd_X	0.022	0.020	0.000	0.000	0.000	0.000	0.000	0.010	0.036	0.014
Sm_X	0.000	0.000	0.000	0.000	0.000	0.000	0.000	0.000	0.014	0.000
Gd_X	0.000	0.000	0.000	0.000	0.000	0.000	0.000	0.000	0.000	0.000
Mn_X	0.008	0.011	0.007	0.000	0.006	0.000	0.014	0.018	0.022	0.015
Ba_X	0.000	0.000	0.000	0.000	0.000	0.000	0.000	0.000	0.000	0.000
Fe^{II}_X	0.000	0.000	0.000	0.000	0.000	0.000	0.000	0.000	0.000	0.000
V_X	0.000	0.000	0.000	0.024	0.000	0.028	0.000	0.000	0.000	0.000
Nb_X	0.031	0.014	0.000	0.005	0.000	0.000	0.000	0.010	0.019	0.007
Y_X	0.033	0.034	0.016	0.021	0.007	0.005	0.008	0.010	0.061	0.009
Σ_X	4.043	4.049	4.051	4.072	4.056	4.045	4.010	4.046	3.885	3.938
Si_Si	3.970	3.986	3.957	3.980	4.017	3.980	3.971	3.955	3.994	3.978
Σ_Si	3.970	3.986	3.957	3.980	4.017	3.980	3.971	3.955	3.994	3.978
Σ_cations	12.000	12.000	12.000	12.000	12.000	12.000	12.000	12.000	12.000	12.000

11	12	13	14	15	16	17	18	19	20
NP-007	NP-007	NP-007	NP-007	NP-009	NP-009	NP-009	NP-009	NP-009	NP-017
Young	Young	Young	Young	Young	Young	Young	Young	Young	Unknown
medium-grained Amp-Bt granodiorite	medium-grained Amp-Bt granodiorite	medium-grained Amp-Bt granodiorite	medium-grained Amp-Bt granodiorite	medium-grained Amp-Bt tonalite	medium-grained Amp-Bt tonalite	medium-grained Amp-Bt tonalite	medium-grained Amp-Bt tonalite	medium-grained Amp-Bt tonalite	fine-grained mafic dyke
0.159	0.317	0.097	0.285	b.d.l.	0.100	0.147	0.263	0.091	b.d.l.
30.567	30.300	30.001	30.418	30.151	30.813	30.471	30.203	30.758	30.987
35.808	36.863	36.610	37.711	37.069	38.325	38.044	37.272	37.435	35.307
2.970	2.036	1.913	1.842	1.901	1.215	1.344	1.332	1.515	2.151
b.d.l.	b.d.l.	b.d.l.	b.d.l.	b.d.l.	b.d.l.	b.d.l.	b.d.l.	b.d.l.	0.344
0.401	0.814	1.156	0.731	0.819	0.433	0.392	0.491	0.468	0.830
0.089	0.579	0.458	0.176	b.d.l.	0.188	0.113	0.449	0.189	b.d.l.
b.d.l.	0.180	0.206	0.163	0.182	b.d.l.	b.d.l.	0.197	b.d.l.	b.d.l.
b.d.l.	b.d.l.	b.d.l.	b.d.l.	b.d.l.	0.157	b.d.l.	b.d.l.	b.d.l.	b.d.l.
b.d.l.	b.d.l.	b.d.l.	b.d.l.	b.d.l.	b.d.l.	b.d.l.	b.d.l.	b.d.l.	b.d.l.
b.d.l.	0.281	0.221	b.d.l.	b.d.l.	b.d.l.	b.d.l.	b.d.l.	b.d.l.	b.d.l.
27.967	28.204	27.781	28.746	28.968	29.066	29.169	28.737	29.117	29.329
b.d.l.	0.079	0.082	0.111	0.046	0.051	0.070	0.080	0.089	0.101
0.000	0.000	0.000	0.000	0.000	0.000	0.000	0.000	0.000	0.000
b.d.l.	b.d.l.	b.d.l.	b.d.l.	b.d.l.	b.d.l.	b.d.l.	b.d.l.	b.d.l.	1.067
b.d.l.	b.d.l.	0.038	0.037	b.d.l.	b.d.l.	b.d.l.	b.d.l.	b.d.l.	b.d.l.
1.274	0.602	0.855	0.704	0.433	0.398	0.413	0.380	0.468	0.768
99.235	100.255	99.418	100.924	99.569	100.746	100.163	99.404	100.130	100.884
0.009	0.019	0.006	0.017	0.000	0.006	0.009	0.016	0.005	0.000
4.014	3.955	3.956	3.935	3.931	3.985	3.957	3.963	3.992	4.002
3.537	3.620	3.631	3.670	3.636	3.729	3.716	3.678	3.655	3.430
0.460	0.313	0.297	0.281	0.292	0.185	0.206	0.206	0.232	0.327
0.000	0.000	0.000	0.000	0.000	0.000	0.000	0.000	0.000	0.036
0.040	0.080	0.115	0.071	0.080	0.042	0.038	0.048	0.046	0.081
0.006	0.040	0.032	0.012	0.000	0.013	0.008	0.031	0.013	0.000
0.000	0.009	0.010	0.008	0.009	0.000	0.000	0.009	0.000	0.000
0.000	0.000	0.000	0.000	0.000	0.007	0.000	0.000	0.000	0.000
0.000	0.000	0.000	0.000	0.000	0.000	0.000	0.000	0.000	0.000
0.000	0.012	0.010	0.000	0.000	0.000	0.000	0.000	0.000	0.000
3.934	3.944	3.924	3.984	4.047	4.027	4.058	4.039	4.048	4.058
0.000	0.009	0.009	0.012	0.005	0.006	0.008	0.009	0.010	0.011
0.000	0.000	0.000	0.000	0.000	0.000	0.000	0.000	0.000	0.000
0.000	0.000	0.000	0.000	0.000	0.000	0.000	0.000	0.000	0.054
0.000	0.000	0.010	0.009	0.000	0.000	0.000	0.000	0.000	0.000
12.000	12.000	12.000	12.000	12.000	12.000	12.000	12.000	12.000	12.000
3.537	3.620	3.631	3.670	3.636	3.729	3.716	3.678	3.655	3.430
0.460	0.313	0.297	0.281	0.292	0.185	0.206	0.206	0.232	0.327
0.040	0.080	0.115	0.071	0.080	0.042	0.038	0.048	0.046	0.081
4.036	4.013	4.043	4.022	4.008	3.956	3.961	3.933	3.932	3.839
3.934	3.944	3.924	3.984	4.047	4.027	4.058	4.039	4.048	4.058
0.000	0.000	0.010	0.009	0.000	0.000	0.000	0.000	0.000	0.000
0.000	0.009	0.010	0.008	0.009	0.000	0.000	0.009	0.000	0.000
0.000	0.000	0.000	0.000	0.000	0.007	0.000	0.000	0.000	0.000
0.000	0.000	0.000	0.000	0.000	0.000	0.000	0.000	0.000	0.000
0.000	0.012	0.010	0.000	0.000	0.000	0.000	0.000	0.000	0.000
0.000	0.009	0.009	0.012	0.005	0.006	0.008	0.009	0.010	0.011
0.000	0.000	0.000	0.000	0.000	0.000	0.000	0.000	0.000	0.054
0.000	0.000	0.000	0.000	0.000	0.000	0.000	0.000	0.000	0.000
0.000	0.000	0.000	0.000	0.000	0.000	0.000	0.000	0.000	0.036
0.009	0.019	0.006	0.017	0.000	0.006	0.009	0.016	0.005	0.000
0.006	0.040	0.032	0.012	0.000	0.013	0.008	0.031	0.013	0.000
3.950	4.032	4.001	4.042	4.060	4.059	4.082	4.105	4.076	4.159
4.014	3.955	3.956	3.935	3.931	3.985	3.957	3.963	3.992	4.002
4.014	3.955	3.956	3.935	3.931	3.985	3.957	3.963	3.992	4.002
12.000	12.000	12.000	12.000	12.000	12.000	12.000	12.000	12.000	12.000

ZIRCON formulae recalculated on the basis of 16 oxygen equivalents

	79	84	87	101	74	81	82	13	14	17	18
Comment	NP-007	NP-007	NP-007	NP-018	NP-011	NP-011	NP-011	NP-012	NP-012	NP-012	NP-012
Suite	Young	Young	Young	Old	Old	Old	Old	Old	Old	Old	Old
Petrology	medium-grained Amp-Bt granodiorite	medium-grained Amp-Bt granodiorite	medium-grained Amp-Bt granodiorite	Bt augengneiss	Amp-bearing QtzD	Amp-bearing QtzD	Amp-bearing QtzD	Amp-Bt tonalite	Amp-Bt tonalite	Amp-Bt tonalite	Amp-Bt tonalite
SiO_2	32.143	32.408	31.952	32.057	32.387	31.932	32.114	32.052	32.838	32.827	32.874
ZrO_2	64.718	64.293	64.381	65.037	65.621	65.058	65.037	65.695	66.429	65.331	66.281
HfO_2	1.280	1.316	1.506	0.995	1.233	1.239	1.247	0.957	1.461	1.538	1.245
ThO_2	b.d.l.	b.d.l.	b.d.l.	b.d.l.	b.d.l.	b.d.l.	b.d.l.	b.d.l.	b.d.l.	0.117	b.d.l.
Al_2O_3	b.d.l.	b.d.l.	b.d.l.	b.d.l.	b.d.l.	b.d.l.	b.d.l.	b.d.l.	b.d.l.	0.092	b.d.l.
Sc_2O_3	b.d.l.	b.d.l.	b.d.l.	b.d.l.	b.d.l.	0.027	b.d.l.	0.046	b.d.l.	b.d.l.	b.d.l.
Fe_2O_3	0.139	0.341	0.000	0.373	0.174	0.147	0.000	0.000	0.000	0.123	0.158
Y_2O_3	b.d.l.	0.160	b.d.l.	0.172	b.d.l.	0.269	b.d.l.	0.193	b.d.l.	b.d.l.	b.d.l.
Yb_2O_3	b.d.l.	b.d.l.	b.d.l.	b.d.l.	b.d.l.	0.170	b.d.l.	b.d.l.	b.d.l.	b.d.l.	b.d.l.
CaO	b.d.l.	b.d.l.	b.d.l.	b.d.l.	b.d.l.	b.d.l.	0.110	b.d.l.	0.026	0.124	b.d.l.
Σ	98.280	98.518	97.839	98.634	99.415	98.842	98.508	98.943	100.754	100.152	100.558
Si	4.009	4.027	4.008	3.987	3.996	3.976	3.999	3.978	4.001	4.018	4.007
Zr	3.936	3.895	3.938	3.943	3.948	3.949	3.949	3.975	3.946	3.899	3.939
Hf	0.046	0.047	0.054	0.035	0.043	0.044	0.044	0.034	0.051	0.054	0.043
Th	0.000	0.000	0.000	0.000	0.000	0.000	0.000	0.000	0.000	0.003	0.000
Al	0.000	0.000	0.000	0.000	0.000	0.000	0.000	0.000	0.000	0.013	0.000
Fe^{III}	0.013	0.032	0.000	0.035	0.016	0.014	0.000	0.000	0.000	0.011	0.014
Y	0.000	0.011	0.000	0.011	0.000	0.018	0.000	0.013	0.000	0.000	0.000
Ca	0.000	0.000	0.000	0.000	0.000	0.000	0.015	0.000	0.003	0.016	0.000
Σ.atoms	8.003	8.011	8.000	8.012	8.004	8.001	8.007	7.999	8.002	8.014	8.004
Zr_M	3.936	3.895	3.938	3.943	3.948	3.949	3.949	3.975	3.946	3.899	3.939
Al_M	0.000	0.000	0.000	0.000	0.000	0.000	0.000	0.000	0.000	0.013	0.000
Hf_M	0.046	0.047	0.054	0.035	0.043	0.044	0.044	0.034	0.051	0.054	0.043
Fe^{III} M	0.013	0.032	0.000	0.035	0.016	0.014	0.000	0.000	0.000	0.011	0.014
Th_M	0.000	0.000	0.000	0.000	0.000	0.000	0.000	0.000	0.000	0.003	0.000
Ca_M	0.000	0.000	0.000	0.000	0.000	0.000	0.015	0.000	0.003	0.016	0.000
Y_M	0.000	0.011	0.000	0.011	0.000	0.018	0.000	0.013	0.000	0.000	0.000
Σ_M	3.994	3.984	3.992	4.025	4.008	4.025	4.008	4.022	4.001	3.997	3.997
Si_Si	4.009	4.027	4.008	3.987	3.996	3.976	3.999	3.978	4.001	4.018	4.007
Σ_cations	8.003	8.011	8.000	8.012	8.004	8.001	8.007	7.999	8.002	8.014	8.004

APATITE formulae recalculated on the basis of 12.5 oxygen equivalents

	69	89	97	10	25	54	61	106	111	118
Comment	NP-011	NP-011	NP-011	NP-012	NP-012	NP-013	NP-013	NP-018	NP-018	NP-018
Suite	Old	Old	Old	Old	Old	Old	Old	Old	Old	Old
Petrology	Amp-bearing QtzD	Amp-bearing QtzD	Amp-bearing QtzD	Amp-Bt tonalite	Amp-Bt tonalite	Hornblendite	Hornblendite	Bt augengneiss	Bt augengneiss	Bt augengneiss
SO_3	0.117	0.124	b.d.l.	0.132	0.067	0.108	b.d.l.	0.260	0.295	b.d.l.
P_2O_5	40.837	40.500	40.181	41.416	41.544	42.120	41.579	42.002	41.782	42.163
SiO_2	0.185	0.305	0.274	0.286	0.280	0.180	0.127	0.316	0.257	0.152
Y_2O_3	b.d.l.	b.d.l.	0.104	b.d.l.	0.101	b.d.l.	b.d.l.	b.d.l.	b.d.l.	b.d.l.
CaO	55.470	55.282	55.038	56.518	56.747	56.468	57.038	56.340	55.852	56.133
MnO	b.d.l.	b.d.l.	b.d.l.	b.d.l.	b.d.l.	b.d.l.	b.d.l.	b.d.l.	b.d.l.	b.d.l.
FeO	0.000	0.283	0.000	0.000	0.109	0.000	0.092	0.097	0.000	0.164
Na_2O	0.051	b.d.l.	b.d.l.	b.d.l.	b.d.l.	b.d.l.	b.d.l.	0.074	b.d.l.	b.d.l.
F	2.694	3.331	2.945	3.612	3.524	3.568	3.077	3.628	3.607	4.372
Cl	0.030	0.041	0.052	b.d.l.	b.d.l.	b.d.l.	b.d.l.	b.d.l.	b.d.l.	b.d.l.
H_2O	0.473	0.162	0.325	0.075	0.123	0.110	0.333	0.086	0.082	0.000
O=F	-1.134	-1.403	-1.240	-1.521	-1.484	-1.502	-1.296	-1.528	-1.519	-1.841
O=Cl	-0.007	-0.009	-0.012	–	–	–	–	–	–	–
Σ	98.716	98.616	97.667	100.519	101.012	101.052	100.951	101.276	100.356	101.143
S	0.007	0.008	0.000	0.008	0.004	0.007	0.000	0.016	0.019	0.000
P	2.949	2.934	2.940	2.940	2.939	2.967	2.944	2.951	2.958	2.978
Si	0.016	0.026	0.024	0.024	0.023	0.015	0.011	0.026	0.021	0.013
Y	0.000	0.000	0.005	0.000	0.004	0.000	0.000	0.000	0.000	0.000
Ca	5.069	5.069	5.096	5.077	5.080	5.033	5.112	5.009	5.005	5.018
Mn	0.000	0.000	0.000	0.000	0.000	0.000	0.000	0.000	0.000	0.000
Fe^{II}	0.000	0.020	0.000	0.000	0.008	0.000	0.006	0.007	0.000	0.011
Na	0.008	0.000	0.000	0.000	0.000	0.000	0.000	0.012	0.000	0.000
F	0.727	0.901	0.805	0.958	0.931	0.939	0.814	0.952	0.954	1.154
Cl	0.004	0.006	0.008	0.000	0.000	0.000	0.000	0.000	0.000	0.000
Σ.atoms	8.781	8.964	8.877	9.007	8.989	8.960	8.887	8.973	8.958	9.174
P_Z	2.949	2.934	2.940	2.940	2.939	2.967	2.944	2.951	2.958	2.978
Si_Z	0.016	0.026	0.024	0.024	0.023	0.015	0.011	0.026	0.021	0.013
S_Z	0.007	0.008	0.000	0.008	0.004	0.007	0.000	0.016	0.019	0.000
Mn_Z	0.000	0.000	0.000	0.000	0.000	0.000	0.000	0.000	0.000	0.000
Σ_Z	2.972	2.968	2.963	2.972	2.966	2.988	2.955	2.993	2.999	2.991
Ca_M	5.069	5.069	5.096	5.077	5.080	5.033	5.112	5.009	5.005	5.018
Mn_M	0.000	0.000	0.000	0.000	0.000	0.000	0.000	0.000	0.000	0.000
Fe^{II}_M	0.000	0.020	0.000	0.000	0.008	0.000	0.006	0.007	0.000	0.011
Na_M	0.008	0.000	0.000	0.000	0.000	0.000	0.000	0.012	0.000	0.000
Y_M	0.000	0.000	0.005	0.000	0.004	0.000	0.000	0.000	0.000	0.000
Σ_M	5.078	5.089	5.101	5.077	5.092	5.033	5.118	5.028	5.005	5.029
F_X	0.727	0.901	0.805	0.958	0.931	0.939	0.814	0.952	0.954	1.154
Cl_X	0.004	0.006	0.008	0.000	0.000	0.000	0.000	0.000	0.000	0.000
OH_X	0.269	0.093	0.187	0.042	0.069	0.061	0.186	0.048	0.046	0.000
Σ_X	1.000	1.000	1.000	1.000	1.000	1.000	1.000	1.000	1.000	1.154
Σ_cations	8.050	8.057	8.064	8.050	8.058	8.022	8.073	8.021	8.004	8.020
F_Ap	0.727	0.901	0.805	0.958	0.931	0.939	0.814	0.952	0.954	1.154
Cl_Ap	0.004	0.006	0.008	0.000	0.000	0.000	0.000	0.000	0.000	0.000
OH_Ap	0.269	0.093	0.187	0.042	0.069	0.061	0.186	0.048	0.046	0.000

94	95	53	65	5	14	23
NP-007 Young medium-grained Amp-Bt granodiorite	NP-007 Young medium-grained Amp-Bt granodiorite	NP-021 Young coarse-grained Bt granite	NP-021 Young coarse-grained Bt granite	NP-017 Unknown fine-grained mafic dyke	NP-017 Unknown fine-grained mafic dyke	NP-017 Unknown fine-grained mafic dyke
b.d.l.	b.d.l.	b.d.l.	b.d.l.	0.290	0.862	0.109
41.870	41.845	41.585	41.667	40.842	39.001	41.533
0.263	0.137	0.108	0.110	0.172	0.470	0.115
0.158	b.d.l.	0.151	0.104	b.d.l.	b.d.l.	b.d.l.
56.149	56.417	55.222	56.283	54.852	54.565	55.258
b.d.l.	b.d.l.	0.247	0.153	b.d.l.	b.d.l.	b.d.l.
0.000	0.000	0.085	0.000	0.000	0.440	0.392
b.d.l.	b.d.l.	0.060	b.d.l.	0.196	0.244	b.d.l.
3.560	4.211	4.030	3.978	3.917	3.540	3.433
b.d.l.	b.d.l.	b.d.l.	b.d.l.	b.d.l.	b.d.l.	b.d.l.
0.104	0.000	0.000	0.000	0.000	0.055	0.146
-1.499	-1.773	-1.697	-1.675	-1.649	-1.491	-1.446
–	–	–	–	–	–	–
100.605	100.837	99.791	100.620	98.620	97.686	99.541
0.000	0.000	0.000	0.000	0.019	0.056	0.007
2.965	2.966	2.976	2.961	2.952	2.856	2.971
0.022	0.011	0.009	0.009	0.015	0.041	0.010
0.007	0.000	0.007	0.005	0.000	0.000	0.000
5.033	5.061	5.002	5.062	5.018	5.058	5.003
0.000	0.000	0.018	0.011	0.000	0.000	0.000
0.000	0.000	0.006	0.000	0.000	0.032	0.028
0.000	0.000	0.010	0.000	0.032	0.041	0.000
0.942	1.115	1.078	1.056	1.058	0.969	0.918
0.000	0.000	0.000	0.000	0.000	0.000	0.000
8.969	9.154	9.105	9.103	9.094	9.052	8.937
2.965	2.966	2.976	2.961	2.952	2.856	2.971
0.022	0.011	0.009	0.009	0.015	0.041	0.010
0.000	0.000	0.000	0.000	0.019	0.056	0.007
0.000	0.000	0.015	0.011	0.000	0.000	0.000
2.987	2.978	3.000	2.981	2.986	2.953	2.988
5.033	5.061	5.002	5.062	5.018	5.058	5.003
0.000	0.000	0.003	0.000	0.000	0.000	0.000
0.000	0.000	0.006	0.000	0.000	0.032	0.028
0.000	0.000	0.010	0.000	0.032	0.041	0.000
0.007	0.000	0.007	0.005	0.000	0.000	0.000
5.040	5.061	5.028	5.066	5.050	5.130	5.031
0.942	1.115	1.078	1.056	1.058	0.969	0.918
0.000	0.000	0.000	0.000	0.000	0.000	0.000
0.058	0.000	0.000	0.000	0.000	0.031	0.082
1.000	1.115	1.078	1.056	1.058	1.000	1.000
8.027	8.039	8.028	8.047	8.036	8.083	8.019
0.942	1.115	1.078	1.056	1.058	0.969	0.918
0.000	0.000	0.000	0.000	0.000	0.000	0.000
0.058	0.000	0.000	0.000	0.000	0.031	0.082

SPINEL formulae recalculated on the basis of 4 oxygen equivalents
Fe^{II}/Fe^{III} allocated assuming 3 cations per formula unit (Droop 1987)

	73	85	96	98	99	100	116	37
Comment	NP-011	NP-011	NP-011	NP-011	NP-018	NP-018	NP-018	NP-020
Suite	Old	Old	Old	Old	Old	Old	Old	Old
Petrology	Amp-bearing QtzD	Amp-bearing QtzD	Amp-bearing QtzD	Amp-bearing QtzD	Bt augengneiss	Bt augengneiss	Bt augengneiss	medium-grained gabbro
SiO_2	0.102	0.065	0.114	0.116	0.073	0.053	0.078	0.125
TiO_2	b.d.l.	b.d.l.	0.051	b.d.l.	b.d.l.	0.069	0.421	0.173
Al_2O_3	b.d.l.	b.d.l.	b.d.l.	b.d.l.	b.d.l.	0.160	b.d.l.	0.152
V_2O_3	0.065	0.052	0.054	0.055	0.167	0.341	0.085	1.055
Cr_2O_3	0.130	b.d.l.	0.066	0.031	0.056	0.070	b.d.l.	0.266
Fe_2O_3	68.119	68.640	68.324	68.560	68.550	67.972	67.600	66.673
CaO	b.d.l.	0.083	b.d.l.	b.d.l.	b.d.l.	b.d.l.	0.144	b.d.l.
MnO	0.064	b.d.l.	b.d.l.	0.055	0.067	b.d.l.	0.076	b.d.l.
FeO	30.848	30.955	31.161	31.108	31.054	31.141	31.137	31.345
CoO	0.074	b.d.l.	b.d.l.	b.d.l.	b.d.l.	b.d.l.	b.d.l.	b.d.l.
Σ	99.401	99.795	99.770	99.925	99.966	99.805	99.541	99.788
Si	0.004	0.003	0.004	0.004	0.003	0.002	0.003	0.005
Ti	0.000	0.000	0.001	0.000	0.000	0.002	0.012	0.005
Al	0.000	0.000	0.000	0.000	0.000	0.007	0.000	0.007
V	0.002	0.002	0.002	0.002	0.005	0.011	0.003	0.033
Cr	0.004	0.000	0.002	0.001	0.002	0.002	0.000	0.008
Fe^{III}	1.986	1.993	1.985	1.988	1.988	1.972	1.967	1.933
Ca	0.000	0.003	0.000	0.000	0.000	0.000	0.006	0.000
Mn	0.002	0.000	0.000	0.002	0.002	0.000	0.002	0.000
Fe^{II}	1.000	0.999	1.006	1.003	1.001	1.004	1.007	1.010
Co	0.002	0.000	0.000	0.000	0.000	0.000	0.000	0.000
Σ.atoms	3.000	3.000	3.000	3.000	3.000	3.000	3.000	3.000
Fe^{III}_B	1.986	1.993	1.985	1.988	1.988	1.972	1.967	1.933
Al_B	0.000	0.000	0.000	0.000	0.000	0.007	0.000	0.007
Cr_B	0.004	0.000	0.002	0.001	0.002	0.002	0.000	0.008
V_B	0.002	0.002	0.002	0.002	0.005	0.011	0.003	0.033
Si_B	0.004	0.003	0.004	0.004	0.003	0.002	0.003	0.005
Fe^{II} B	0.004	0.003	0.007	0.004	0.003	0.006	0.028	0.015
Σ_B	2.000	2.000	2.000	2.000	2.000	2.000	2.000	2.000
Fe^{II}_A	0.996	0.997	0.999	0.998	0.998	0.998	0.979	0.995
Co_A	0.002	0.000	0.000	0.000	0.000	0.000	0.000	0.000
Ti_A	0.000	0.000	0.001	0.000	0.000	0.002	0.012	0.005
Mn_A	0.002	0.000	0.000	0.002	0.002	0.000	0.002	0.000
Ca_A	0.000	0.003	0.000	0.000	0.000	0.000	0.006	0.000
Σ_A	1.000	1.000	1.000	1.000	1.000	1.000	1.000	1.000
Σ_cations	3.000	3.000	3.000	3.000	3.000	3.000	3.000	3.000

6	15	20	24
NP-017	NP-017	NP-017	NP-017
Unknown	Unknown	Unknown	Unknown
fine-grained mafic dyke	fine-grained mafic dyke	fine-grained mafic dyke	fine-grained mafic dyke
0.121	0.112	0.119	0.605
0.060	0.072	0.292	b.d.l.
b.d.l.	b.d.l.	b.d.l.	0.221
0.266	0.212	0.269	0.048
b.d.l.	0.037	0.028	b.d.l.
67.661	67.692	67.210	65.916
b.d.l.	b.d.l.	0.149	0.040
b.d.l.	b.d.l.	0.110	b.d.l.
30.966	30.971	30.818	31.230
b.d.l.	b.d.l.	0.073	b.d.l.
99.073	99.096	99.068	98.061
0.005	0.004	0.005	0.024
0.002	0.002	0.009	0.000
0.000	0.000	0.000	0.010
0.008	0.007	0.008	0.002
0.000	0.001	0.001	0.000
1.979	1.979	1.964	1.941
0.000	0.000	0.006	0.002
0.000	0.000	0.004	0.000
1.006	1.006	1.001	1.022
0.000	0.000	0.002	0.000
3.000	3.000	3.000	3.000
1.979	1.979	1.964	1.941
0.000	0.000	0.000	0.010
0.000	0.001	0.001	0.000
0.008	0.007	0.008	0.002
0.005	0.004	0.005	0.024
0.008	0.009	0.022	0.024
2.000	2.000	2.000	2.000
0.998	0.998	0.979	0.998
0.000	0.000	0.002	0.000
0.002	0.002	0.009	0.000
0.000	0.000	0.004	0.000
0.000	0.000	0.006	0.002
1.000	1.000	1.000	1.000
3.000	3.000	3.000	3.000

ILMENITE formulae recalculated on the basis of 3 oxygen equivalents
Fe^{II}/Fe^{III} allocated assuming 2 cations per formula unit (Droop 1987)

	33	36	39	48	19	20	21
Sample	NP-020	NP-020	NP-020	NP-020	NP-009	NP-009	NP-009
Suite	Old	Old	Old	Old	Young	Young	Young
Petrology	medium-grained gabbro	medium-grained gabbro	medium-grained gabbro	medium-grained gabbro	medium-grained Amp-Bt tonalite	medium-grained Amp-Bt tonalite	medium-grained Amp-Bt tonalite
SiO_2	b.d.l.	b.d.l.	0.075	0.062	b.d.l.	b.d.l.	b.d.l.
TiO_2	50.049	49.041	49.293	49.387	52.275	52.389	51.771
V_2O_3	b.d.l.	b.d.l.	b.d.l.	0.444	b.d.l.	b.d.l.	b.d.l.
Fe_2O_3	4.719	5.480	5.558	5.241	0.570	0.000	0.849
MgO	0.223	0.051	0.158	0.040	0.050	b.d.l.	b.d.l.
CaO	b.d.l.	b.d.l.	b.d.l.	b.d.l.	0.233	0.136	0.096
MnO	0.876	0.899	0.848	0.831	4.763	6.847	5.842
FeO	43.735	43.111	43.289	43.585	41.810	39.820	40.529
Σ	99.602	98.582	99.221	99.590	99.701	99.192	99.087
Si	0.000	0.000	0.002	0.002	0.000	0.000	0.000
Ti	0.955	0.947	0.945	0.944	0.995	1.002	0.992
V	0.000	0.000	0.000	0.009	0.000	0.000	0.000
Fe^{III}	0.090	0.106	0.107	0.100	0.011	0.000	0.016
Mg	0.008	0.002	0.006	0.002	0.002	0.000	0.000
Ca	0.000	0.000	0.000	0.000	0.006	0.004	0.003
Mn	0.019	0.020	0.018	0.018	0.102	0.147	0.126
Fe^{II}	0.928	0.926	0.922	0.926	0.884	0.847	0.863
Σ.atoms	2.000	2.000	2.000	2.000	2.000	2.000	2.000

ESM 6: Whole-rock trace-element analyses from the AFMC (ppm)

	NP-020	*NJ-58*	NP-013	NP-012	*NJ-59*	NP-011	NP-018	NP-014	*NJ-57*	NK-29
Groups	Old	*Old*	Old	Old	*Old*	Old	Old	Old	*Old*	Old
Rock type	medium-grained gabbro	*v. coarse-grained honblendite*	v. coarse-grained honblendite	Amp-Bt tonalite	*Amp-bearing QtzD*	Amp-bearing QtzD	Bt augengneiss	v. coarse-grained Bt augengneiss	*v. coarse-grained Bt augengneiss*	orthogneiss with red Kfs, intruded by NJ-62
Lab	ACME	*ACME†*	ACME	ACME	*ACME†*	ACME	ACME	ACME	*ACME†*	UB
Rb	14.8	*37.0*	27.6	32.9	*72.4*	93.8	118.0	175.0	*118.6*	199.1
Cs	6.6	*6.7*	5.3	8.0	*4.5*	5.4	6.4	11.8	*2.3*	6.5
Ba	95	*156*	129	128	*538*	637	1205	850	*996*	648
Sr	573.1	*118.0*	113.6	700.2	*458.3*	411.8	503.2	266.3	*271.4*	165.3
Be	< 1	*3*	2	7	*1*	1	3	3	*1*	n.d.
Ga	23.6	*18.3*	18.0	22.6	*19.9*	21.4	21.1	19.5	*11.1*	n.d.
Th	< 0.2	*0.7*	0.3	0.7	*4*	6.7	11.7	41.3	*9.2*	35.36
U	< 0.1	*0.3*	0.2	0.4	*0.6*	0.7	1.8	3	*0.7*	4.3
Zr	21.2	*80.0*	44.6	363.5	*184.4*	195.7	268.1	369.9	*78.0*	295.3
Hf	1.0	*2.7*	1.8	9.0	*4.8*	5.1	7.4	9.2	*2.2*	8.9
Nb	2.2	*8.6*	6.7	5.3	*8.5*	8.3	12.7	27.5	*3.5*	12.6
Ta	0.1	*0.4*	0.3	0.3	*0.4*	0.5	1.1	2.3	*0.1*	n.d.
Sc	32.0	*6.2*	53.0	21.0	*5.6*	15.0	11.0	6.0	*1.6*	5.7
Ni	30.2	*101.2*	100.3	30.2	*14.4*	33.8	31.0	29.6	*3.9*	9.0
Co	58.9	*18.4*	53.3	17.6	*18.2*	19.3	14.5	7.2	*3.5*	27.7
V	446	*57*	263	94	*91*	127	110	40	*22*	35
Pb	3.6	*0.8*	1.4	22.1	*2.4*	3.0	4.7	14.4	*8.6*	30.4
Zn	31	*44*	33	20	*66*	78	90	64	*28*	72
Cu	97.4	*38.8*	76.7	20.9	*7.5*	13.7	13.5	12.1	*5.9*	2.0
Sn	< 1	*5*	3	3	*3*	2	3	3	*1*	n.d.
W	< 0.5	*0.1*	< 0.5	1.7	*0.1*	< 0.5	0.7	< 0.5	*0.1*	n.d.
Sb	< 0.1	< 0.1	< 0.1	< 0.1	< 0.1	< 0.1	< 0.1	< 0.1	< 0.1	n.d.
Mo	0.2	*0.2*	0.2	0.3	*0.1*	0.4	0.7	1.5	*0.1*	n.d.
Y	14.3	*46.6*	35.7	32.2	*26.6*	18.0	27.2	40.0	*6.7*	29.1
La	6.9	*11.1*	10.0	10.9	*21.8*	26.3	48.5	86.5	*23.4*	74.7
Ce	17.0	*45.7*	37.5	30.8	*53.9*	51.2	101.0	171.2	*46.5*	152.6
Pr	2.88	*7.47*	7.18	5.60	*6.93*	6.63	13.47	20.24	*4.63*	17.84
Nd	14.1	*36.7*	35.3	26.3	*27.7*	26.3	50.3	69.1	*16.5*	64.6
Sm	3.44	*9.05*	8.20	6.81	*5.93*	4.79	8.71	11.19	*2.34*	12.58
Eu	1.01	*1.99*	1.84	1.64	*1.54*	1.27	1.82	1.61	*0.85*	1.51
Gd	3.30	*8.59*	7.44	6.64	*5.78*	4.08	6.90	9.02	*1.72*	9.59
Tb	0.46	*1.49*	1.11	1.00	*0.93*	0.59	0.98	1.31	*0.25*	1.38
Dy	2.71	*8.53*	7.14	6.09	*5.17*	3.26	5.45	7.54	*1.37*	6.83
Ho	0.53	*1.64*	1.33	1.15	*0.96*	0.61	1.03	1.39	*0.23*	1.23
Er	1.46	*4.63*	3.71	3.26	*2.63*	1.64	2.80	4.02	*0.64*	3.48
Tm	0.20	*0.69*	0.52	0.46	*0.39*	0.25	0.41	0.58	*0.09*	0.44
Yb	1.30	*4.11*	3.43	2.94	*2.37*	1.62	2.68	3.92	*0.53*	3.03
Lu	0.18	*0.59*	0.49	0.42	*0.34*	0.25	0.40	0.55	*0.08*	0.45
ΣREE	55.5	*142.3*	125.2	104.0	*136.4*	128.8	244.5	388.2	*99.1*	350.2
La_N/Yb_N	3.6	*1.8*	2.0	2.5	*6.2*	10.9	12.2	14.9	*29.8*	16.6
La_N/Sm_N	1.3	*0.8*	0.8	1.0	*2.3*	3.5	3.5	4.9	*6.3*	3.7
Eu/Eu*	0.92	*0.69*	0.72	0.75	*0.80*	0.88	0.72	0.49	*1.30*	0.42
Yb_N	6.2	*19.7*	16.4	14.1	*11.3*	7.8	12.8	18.8	*2.5*	14.5

	NJ-05	**NP-009**	**NP-007**	***NK-42***	**NP-008**	**NP-021**	**NK-16**	***NJ-62***	**NP-010**
Groups	*Young*	Young	Young	*Young*	Young	Young	Young	*Young*	Young
Rock type	*(quartz) dioritic dyke*	medium-grained Amp-bearing tonalite	medium-grained Bt-Amp granodiorite	*medium-grained Bt-Amp granodiorite*	coarse-grained leucogranite	coarse-grained Bt granite	coarse-grained Bt granite	*Ms-Bt granite*	fine-grained Ms-Bt leucogranite
Lab	*ACME†*	ACME	ACME	*UB†*	ACME	ACME	UB	*ACME†*	ACME
Rb	*49.0*	86.0	124.6	*125.7*	139.1	212.0	236.7	*248.5*	243.4
Cs	*13.6*	7.6	16.0	*12.5*	3.2	11.4	16.1	*7.3*	7.6
Ba	*271*	411	1015	*632*	691	427	439	*314*	261
Sr	*338.1*	242.6	224.0	*218.6*	209.2	111.1	112.3	*67.7*	52.9
Be	*< 1*	2	4	*n.d.*	2	4	n.d.	*3*	2
Ga	*18.9*	19.7	17.6	*n.d.*	14.9	18.6	n.d.	*18.9*	19.7
Th	*4.5*	5.7	1.5	*9.58*	7.2	11.2	12.85	*15.3*	5.1
U	*1.2*	1.4	1.4	*1.84*	2.5	3.9	5.83	*5.7*	3.1
Zr	*209.8*	103.8	203.4	*50.7*	87.8	111.6	132.2	*101.5*	62.6
Hf	*5.6*	3.1	5.6	*1.9*	2.9	3.8	4.6	*3.6*	2.3
Nb	*12.5*	8.2	10.6	*11.3*	5.7	10.2	13.8	*14.9*	13.0
Ta	*0.8*	0.7	1.2	*n.d.*	0.7	1.2	n.d.	*1.7*	2.2
Sc	*8.5*	23.0	11.0	*12.4*	4.0	5.0	4.7	*0.4*	2.0
Ni	*1.5*	14.3	9.8	*n.d.*	11.0	10.6	n.d.	*10.2*	11.8
Co	*13.0*	21.6	9.1	*27.3*	2.9	2.5	24.7	*2.0*	1.4
V	*55*	165	53	*59*	17	14	21	*3*	< 8
Pb	*2.7*	4.4	6.1	*16.1*	29.3	3.1	31.2	*6.3*	6.4
Zn	*57*	66	64	*64*	27	45	61	*51*	42
Cu	*4.1*	17.2	3.7	*0.7*	3.1	2.1	3.0	*3.4*	4.0
Sn	*1*	3	3	*n.d.*	1	8	n.d.	*7*	13
W	*0.1*	1	0.7	*n.d.*	<0.5	0.6	n.d.	< 0.1	2.1
Sb	< 0.1	< 0.1	< 0.1	*n.d.*	< 0.1	< 0.1	n.d.	< 0.1	< 0.1
Mo	*0.3*	0.4	0.4	*n.d.*	0.2	0.2	n.d.	*0.4*	0.3
Y	*31.2*	24.5	22.3	*29.2*	14.0	13.3	15.7	*10.1*	7.3
La	*21.4*	18.0	6.6	*32.0*	14.6	23.0	31.7	*22.9*	11.2
Ce	*52.6*	39.1	15.0	*62.0*	28.2	45.9	65.6	*55.7*	22.8
Pr	*6.76*	5.24	2.47	*7.18*	3.48	6.10	7.68	*6.46*	3.00
Nd	*28.4*	21.9	11.9	*27.0*	12.7	22.9	28.2	*23.7*	10.6
Sm	*6.31*	4.40	3.43	*5.87*	2.49	4.53	6.11	*5.32*	2.73
Eu	*1.63*	1.15	1.15	*1.35*	0.86	0.79	0.84	*0.53*	0.43
Gd	*6.31*	4.57	3.97	*5.65*	2.44	3.74	4.84	*3.91*	2.90
Tb	*1.03*	0.74	0.65	*0.92*	0.40	0.51	0.72	*0.58*	0.45
Dy	*5.82*	4.66	4.01	*5.76*	2.43	2.84	3.54	*2.17*	1.77
Ho	*1.17*	0.89	0.78	*1.15*	0.45	0.48	0.60	*0.31*	0.22
Er	*3.39*	2.69	2.31	*3.33*	1.44	1.28	1.65	*0.77*	0.49
Tm	*0.49*	0.37	0.32	*0.47*	0.24	0.19	0.21	*0.11*	0.06
Yb	*2.97*	2.49	2.04	*3.11*	1.54	1.25	1.49	*0.67*	0.30
Lu	*0.46*	0.37	0.30	*0.45*	0.25	0.18	0.21	*0.09*	0.04
ΣREE	*138.7*	106.6	54.9	*156.2*	71.5	113.7	153.4	*123.2*	57.0
La_N/Yb_N	*4.9*	4.9	2.2	*6.9*	6.4	12.4	14.3	*23.0*	25.2
La_N/Sm_N	*2.1*	2.6	1.2	*3.4*	3.7	3.2	3.3	*2.7*	2.6
Eu/Eu*	*0.79*	0.78	0.95	*0.72*	1.07	0.59	0.47	*0.36*	0.47
Yb_N	*14.2*	11.9	9.8	*14.9*	7.4	6.0	7.1	*3.2*	1.4

10.01.2023

	NK-28	NP-017	NP-016	NJ-54
Groups	Unclear	Unclear	Unclear	Unclear
Groups	Ambiguous	Ambiguous	Ambiguous	Ambiguous
Rock type	quartz diorite dyke	fine-grained quartz diorite dyke	medium-grained gray granite, intrudes OS orthogneisse	pink Ms granite
Lab	ACME	ACME	ACME	ACME
Rb	66.7	87.8	202.7	225.7
Cs	3.1	3.7	3.1	4.3
Ba	777	956	541	236
Sr	921.5	881.0	109.7	53.0
Be	n.d.	2	5	n.d.
Ga	n.d.	22.4	18.4	n.d.
Th	3.25	4.1	13.3	5.12
U	1.99	2	3.4	6.22
Zr	70.7	151.9	121.1	79.5
Hf	2.0	4.2	3.8	2.8
Nb	9.0	8.1	10.6	14.5
Ta	n.d.	0.6	0.8	n.d.
Sc	5.1	3.0	4.0	1.3
Ni	8.0	30.8	22.8	0.0
Co	33.1	13.4	3.8	32.0
V	135	108	20	15
Pb	12.4	7.9	7.9	28.5
Zn	122	89	60	62
Cu	23.6	39.4	2.4	1.3
Sn	n.d.	1	6	n.d.
W	n.d.	2.1	<0.5	n.d.
Sb	n.d.	< 0.1	< 0.1	n.d.
Mo	n.d.	0.7	0.7	n.d.
Y	9.8	8.2	12.3	8.8
La	22.4	23.6	24.4	13.4
Ce	49.3	49.3	52.8	28.7
Pr	6.43	6.72	7.06	3.51
Nd	27.0	27.4	26.5	13.1
Sm	5.58	4.87	6.04	3.84
Eu	1.84	1.40	0.83	0.49
Gd	4.29	3.70	5.09	3.63
Tb	0.57	0.43	0.66	0.58
Dy	2.73	1.90	2.95	2.61
Ho	0.39	0.25	0.40	0.32
Er	0.97	0.50	0.89	0.71
Tm	0.08	0.06	0.13	0.07
Yb	0.54	0.38	0.78	0.45
Lu	0.06	0.05	0.11	0.05
ΣREE	122.2	120.6	128.6	71.4
La_N/Yb_N	28.0	41.9	21.1	20.1
La_N/Sm_N	2.5	3.0	2.5	2.2
Eu/Eu*	1.15	1.01	0.46	0.40
Yb_N	2.6	1.8	3.7	2.2

Laboratories: ACME: ACME Labs/Bureau Veritas Commodities (Vancouver, Canada); UB: University of Bergen
†, italics: data for samples discussed by Konopásek et al. (2016)

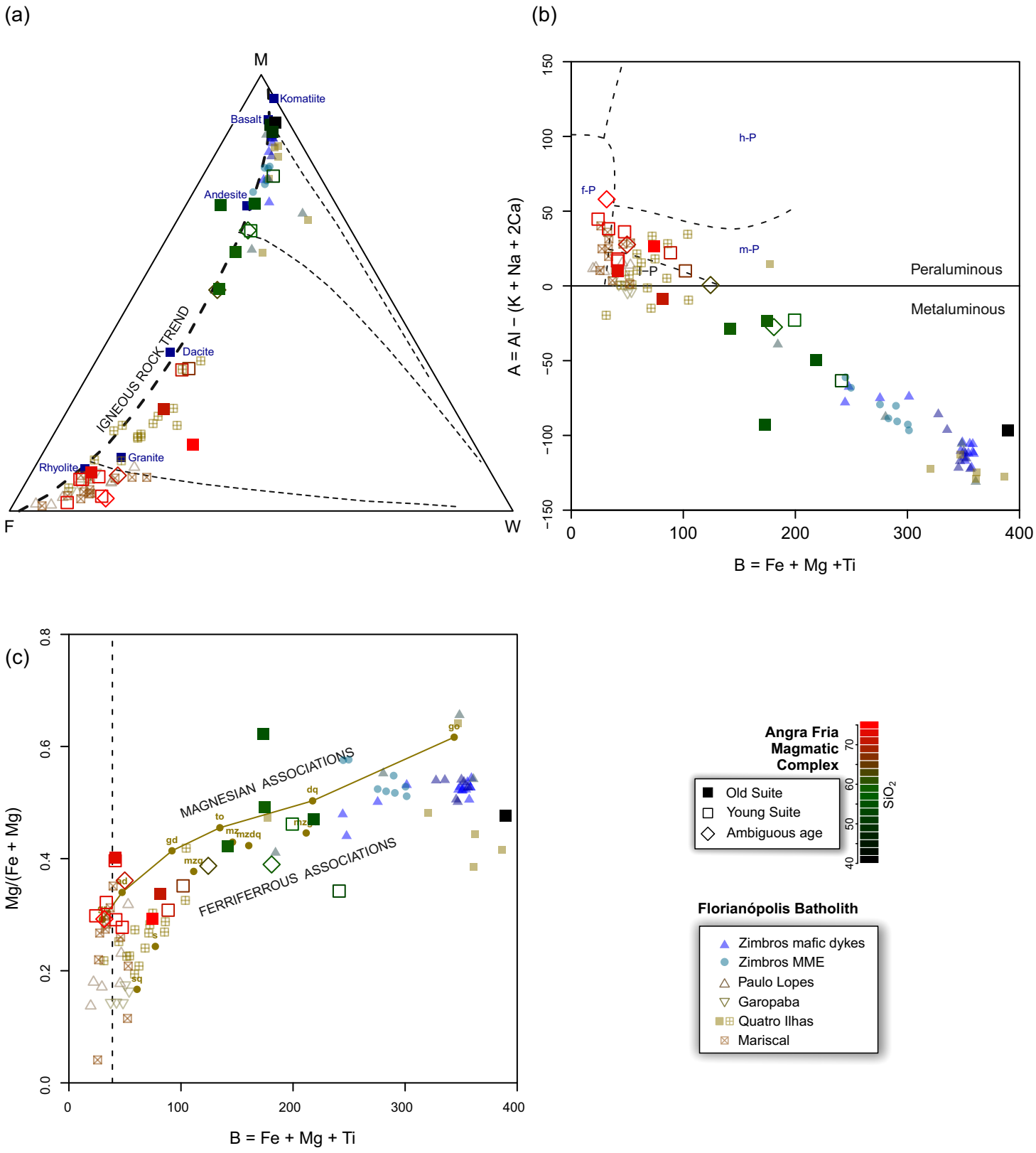
(a)
M
F
W
Komatiite
Basalt
Andesite
Dacite
Granite
Rhyolite
IGNEOUS ROCK TREND
(b)
A = Al − (K + Na + 2Ca)
B = Fe + Mg +Ti
h-P
f-P
m-P
I-P
Peraluminous
Metaluminous
(c)
Mg/(Fe + Mg)
B = Fe + Mg + Ti
MAGNESIAN ASSOCIATIONS
FERRIFERROUS ASSOCIATIONS
go
dq
to
mz
mzdq
gd
mzg
fd
s
sq
Angra Fria Magmatic Complex
Old Suite
Young Suite
Ambiguous age
SiO2
Florianópolis Batholith
Zimbros mafic dykes
Zimbros MME
Paulo Lopes
Garopaba
Quatro Ilhas
Mariscal

Table 1 Summary of the amphibole-derived melt parameters (Ridolfi and Renzulli, 2012)

Sample	**NP-020**[1]	**NP-013**[1]	**NP-011**	**NP-012**	**NP-013 high Si**	**NP-012 high Si**	**NP-009**	**NP-007**
n	**9**	**16**	**12**	**9**	**12**	**13**	**14**	**6**
Suite	OS	OS	OS	OS	OS	OS	YS	YS
Rock	gabbro	hornblendite	quartz diorite	tonalite	hornblendite	tonalite	tonalite	granodiorite
Whole-rock SiO_2 (wt. %)	40.7	49.9	59.7	54.7	49.9	54.7	57.2	67.2
Amphibole classification[1]	tschermakite	magnesiohornblende	pargasite > tschermakite >> ferropargasite, magnesiohornblende	magnesiohornblende	magnesiohornblende > actinolite	magnesiohornblende >>> actinolite	ferrohornblende >>> ferrotschermakite, magnesiohornblende	ferropargasite
T (°C)	796 ± 28[3]	757 ± 24	772 ± 15	726 ± 26			729 ± 29	739 ± 14
H_2O_melt (wt. %)	16.1 ± 2.1	9.7 ± 0.7	10.9 ± 0.5	11.3 ± 0.7			10.8 ± 1.1	13.0 ± 1.0
log fO_2	–14.1 ± 0.9	–13.5 ± 0.8	–13.6 ± 0.6	–15.2 ± 0.7			–16.3 ± 0.7	–15.6 ± 0.7

[1] cumulate

[2] Leake et al. (1997)

[3] median ± 1σ

Table 2

Sample	Lab	Groups	Age	Rock type	SiO_2 (wt. %)	Rb (ppm)	Sr (ppm)	$^{87}Rb/^{86}Sr$	$^{87}Sr/^{86}Sr$	2 s.e.	$^{87}Sr/^{86}Sr_i$	Sm (ppm)	Nd (ppm)	$^{147}Sm/^{144}Nd$	$^{143}Nd/^{144}Nd$	2 s.e.Nd.	$^{143}Nd/^{144}Nd_i$	εNd_i	TDM_{1stg}	TDM_{2stg}
NP-018	CGS	Old	626	Bt augengneiss	59.89	118.0	503.2	0.6791	0.712981	0.000009	0.70692	8.71	50.3	0.1047	0.511999	0.000008	0.511570	-5.1	1.53	1.67
NP-014	CGS	Old	626	Bt augengneiss	70.01	175.0	266.3	1.9049	0.723097	0.000010	0.70609	11.19	69.1	0.0979	0.512077	0.000003	0.511676	-3.0	1.35	1.51
NJ-57	*UB* †	*Old*	*626*	Bt augengneiss	*73.78*	*121.3*	*270.8*	*1.2974*	*0.719309*	*0.000009*	*0.70773*	*2.58*	*16.6*	*0.0938*	*0.511973*	*0.000006*	*0.511589*	*-4.7*	*1.43*	*1.64*
NK-29	UB	Old	630	Bt augengneiss	74.12	212.2	164.3	3.7495	0.739066	0.000009	0.70537	13.45	71.8	0.1132	0.512120	0.000006	0.511652	-3.4	1.48	1.54
NP-020	CGS	Old	630	Amp gabbro	40.69	14.8	573.1	0.0747	0.706737	0.000009	0.70607	3.44	14.1	0.1475	0.512237	0.000008	0.511628	-3.9	1.94	1.58
NJ-58	*UB* †	*Old*	*622*	*hornblendite*	*49.23*	*35.6*	*112.5*	*0.9163*	*0.715108*	*0.000009*	*0.70698*	*9.66*	*36.7*	*0.1594*	*0.512282*	*0.000006*	*0.511632*	*-4.0*	*2.21*	*1.58*
NP-013	CGS	Old	622	hornblendite	49.90	27.6	113.6	0.7035	0.712568	0.000008	0.70633	8.20	35.3	0.1404	0.512239	0.000008	0.511667	-3.3	1.76	1.53
NP-012	CGS	Old	622	Bt–Amp quartz diorite	54.65	32.9	700.2	0.1360	0.708702	0.000010	0.70750	6.81	26.3	0.1565	0.512233	0.000009	0.511595	-4.7	2.23	1.64
NJ-59	*UB* †	*Old*	*620*	*Bt–Amp quartz diorite*	*55.41*	*74.7*	*473.5*	*0.4568*	*0.711879*	*0.000009*	*0.70784*	*6.68*	*29.8*	*0.1356*	*0.512167*	*0.000006*	*0.511616*	*-4.4*	*1.79*	*1.61*
NP-011	CGS	Old	626	Bt–Amp tonalite	59.69	93.8	411.8	0.6596	0.713518	0.000010	0.70763	4.79	26.3	0.1101	0.512084	0.000009	0.511632	-3.9	1.49	1.58
NJ-05	*UB* †	*Young*	*584*	*(quartz) dioritic dyke*	*52.02*	*50.9*	*351.1*	*0.4196*	*0.715243*	*0.000009*	*0.71175*	*6.99*	*30.6*	*0.1380*	*0.511985*	*0.000006*	*0.511456*	*-8.4*	*2.19*	*1.90*
NP-009	CGS	Young	586	Amp–Bt tonalite	57.17	86.0	242.6	1.0272	0.719398	0.000009	0.71081	4.40	21.9	0.1215	0.512126	0.000006	0.511659	-4.4	1.60	1.58
NP-007	CGS	Young	586	Amp–Bt granodiorite	67.16	124.6	224.0	1.6127	0.725068	0.000008	0.71159	3.43	11.9	0.1742	0.512251	0.000007	0.511582	-5.9	3.04	1.70
NK-42	*UB* †	*Young*	*586*	*Amp–Bt granodiorite*	*70.53*	*131.6*	*206.9*	*1.8445*	*0.728083*	*0.000009*	*0.71267*	*5.99*	*29.1*	*0.1245*	*0.512011*	*0.000005*	*0.511533*	*-6.8*	*1.83*	*1.78*
NP-008	CGS	Young	586	Ms–Bt granite	72.06	139.1	209.2	1.9284	0.728321	0.000009	0.71221	2.49	12.7	0.1185	0.512038	0.000005	0.511583	-5.9	1.68	1.70
NP-021	CGS	Young	580	Ms–Bt granite	72.39	212.0	111.1	5.5495	0.756827	0.000009	0.71093	4.53	22.9	0.1196	0.512047	0.000010	0.511593	-5.8	1.69	1.69
NK-16	UB	Young	580	Ms–Bt granite	72.45	259.4	113.2	6.6697	0.767786	0.000009	0.71263	6.29	29.6	0.1286	0.512051	0.000006	0.511563	-6.4	1.85	1.74
NJ-62	*UB* †	*Young*	*575*	*Ms–Bt granite*	*72.55*	*243.9*	*65.2*	*10.9309*	*0.799878*	*0.000009*	*0.71026*	*5.73*	*25.2*	*0.1373*	*0.512216*	*0.000006*	*0.511699*	*-3.9*	*1.74*	*1.54*
NP-010	CGS	Young	575	Ms–Bt leucogranite	73.51	245.0	56.0	12.7965	0.815762	0.000009	0.71085	2.73	10.6	0.1557	0.512166	0.000008	0.511579	-6.2	2.36	1.72
NK-28	UB	Unclear	580	quartz diorite dyke	58.33	70.2	923.6	0.2200	0.707047	0.000008	0.70523	5.44	27.2	0.1209	0.512311	0.000005	0.511852	-0.8	1.30	1.30
NP-017	CGS	Unclear	580	tonalitic dyke	62.35	87.8	881.0	0.2884	0.707056	0.000009	0.70467	4.87	27.4	0.1074	0.512281	0.000008	0.511873	-0.3	1.19	1.26
NP-016	CGS	Unclear	580	medium-grained gray granite	71.83	202.7	109.7	5.3713	0.752239	0.000011	0.70782	6.04	26.5	0.1378	0.512179	0.000007	0.511655	-4.6	1.82	1.60
NJ-54	UB	Unclear	580	Ms granite	75.96	223.5	50.0	13.0755	0.820496	0.000009	0.71236	4.14	14.8	0.1690	0.512183	0.000006	0.511541	-6.8	2.93	1.77

† *(italics) published by Konopásek et al. (2016)*

Subscripts 'i' indicate initial values recalculated to the age given

T^{DM}_{Nd} are two-stage Nd model ages calculated after Liew and Hofmann (1988)